Nonlinear Optical Effect in Laser Trapping of Dielectric and Metallic Particles under Femtosecond Pulsed Excitation: Theory and Experiment

Anita Devi

A thesis submitted for the partial fulfillment of the degree of Doctor of Philosophy

Department of Physical Sciences

Indian Institute of Science Education and Research Mohali
Knowledge city, Sector 81, SAS Nagar, Manauli PO,
Mohali 140306, Punjab, India.

February 2020

Dedicated to

My Parents and Brother

Declaration

The work presented in this thesis has been carried out by me under the guidance of **Dr. Arijit Kumar De** at the Indian Institute of Science Education and Research Mohali. This work has not been submitted in part or in full for a degree, a diploma, or a fellowship to any other university or institute. Whenever contributions of others are involved, every effort is made to indicate this clearly, with due acknowledgement of collaborative research and discussions. This thesis is a bona fide record of original work done by me and all sources listed within have been detailed in the bibliography.

Anita Devi
(Candidate)

In my capacity as the supervisor of the candidate's thesis work, I certify that the above statements by the candidate are true to the best of my knowledge.

Dr. Arijit K. De
(Supervisor)

Certificate of Examination

This is to certify that the thesis titled *"Nonlinear Optical Effect in Laser Trapping of Dielectric and Metallic Particles under Femtosecond Pulsed Excitation: Theory and Experiment"* submitted by **Ms. Anita Devi** (Reg. No. MP13001) for the partial fulfillment of Doctor of Philosophy programme of the Institute, has been examined by the thesis committee duly appointed by the Institute. The committee finds the work done by the candidate satisfactory and recommends that the report be accepted.

Dr. Abhishek Chaudhuri Dr. Sabyasachi Rakshit Dr. Arijit K. De
(Supervisor)

Acknowledgement

It is a pleasure to express my thanks to all those who contributed in many ways to the successful completion of this thesis.

Firstly, I would like to express my deep gratitude and sincere regards to my thesis supervisor, Dr. Arijit K. De, for the continuous support of my Ph.D. study and related research, for his patience, motivation, and immense knowledge. I would also like to thank him for being supportive of every crazy idea that I had presented him during our innumerable discussions. His guidance helped me in all the time of research and writing of this thesis.

I would like to thank Prof. N. Sathyamurthy (former), Prof Devi Sarkar (former), Prof. Arvind (former), Prof. Siva Umapathy (former), and Prof. Jayaraman Gowrishankar (current), directors of IISER Mohali for providing the infrastructure and all the necessary facilities to work in this institute.

I am grateful to MHRD, Government of India for a fellowship during my graduate studies.

I am thankful to my doctoral committee members, Dr. Abhishek Chaudhuri, Dr. Sabyasachi Rakshit for their valuable comments.

I am grateful to Prof. Jasjeet Singh Bagla, Dr. K. P. Yogendran, Dr. Abhishek Chaudhuri, Dr. Kavita Dorai, Prof. Sudeshna Sinha and other members of physics department for their kind support in administrative and academic aspects whenever I needed them. I am thankful to our lab assistants - Tarun pal, Manoj, Rajender for their help whenever needed. I also acknowledge all the facility that has been provided to us here at IISER Mohali. I feel privileged to be part of IISER Mohali community. I must thank the technical and office staff, Dr. Paramdeep Singh Chandi, Garima, Sunny, Ramshankar, Deepika, Anuj, Brijesh, Santosh and Satinder. I express my heartfelt gratitude to hostel cleaning staff. I also acknowledge my neighbours for their constant support and cooperation during the stay at IISER Mohali.

I would also like to express my deep gratitude to Dr. Adrene Freeda D'cruz for helping me in English.

I would like to thank my batch-mates: Atul Singh Arora, Kishor Bharti, Vivek

Singh, Joydeep, Biplop Nandi, Hemanshu, Samridhi, Jaskeran, Mirtunjay, Ayushi, Pooja for their kind support during course work.

I would like to thank my lab mates: Dr. Arindam Das, Dr. Subhash Chander, Ms. Yogita Silori, Ms. Monika Dahiya, Ms. Shaina Dhamija, Ms. Samita Mishra, Mr. Sumit Yadav, Ms. Garima Bhutani, Ms. Sakshi Chawla, Mr. Subho Mitra, Mr. Dharm Singh Yadav, Mr. Ajay Jayachandran, Ms. Dipali Singh, Ms. Umang Gupta, Dr. Somrita Mondal, Mr. Anuj K. Pennathur, Ms. Anusree PV, Mr. Meghnad Kayanattil, Ms. Pragya Verma, Ms. Shreya Khandal, Mr. Ajeet Kumar, Ms. Shruthi S. Nair and Mr. Pankaj Seliya for their continuous support and helpful discussion. I would like to acknowledge separately Sumit, Samita, Sakshi, Monika and Yogita for being a friend before a labmate.

I would like to thanks my friends Kiran Sharma, Poonam Sharma, Manvendra Pratap (Manu), Vivek Singh (Uranium), Smriti Thakur (Shopping brand), Dr. Nisha Gupta, Sumit Mishra, Samita Mishra, Sakhsi Chawla, Garima Bhutani, Dharm Singh Yadav for their moral support and delightful discussions.

My heartiest thanks to my close friends Dr. Gopal Verma, Hemanshu Dua (Helium), Gyanendra Yadav (Takki), Sumit Yadav (Tau), Vinay Tomar, with whom I have shared valuable moments and has been a constant support in good and bad times. I owe a lot of gratitude for them for always being there for me during my Ph.D. journey. A special thanks to my friend Ankit Tomar for his unconditional support, and encouragement. He was always around at times I thought that it is impossible to continue, he helped me to keep things in perspective. I greatly value his contribution and deeply appreciate his belief in me. I have and will always cherish the warmth and affection shown by all of them.

Finally, I feel a deep sense of gratitude for my parents (Basant Kumar Rathi and Suman Rathi) and my younger brother (Rishav Rathi), who unconditionally supported me all these years and without their encouragement, love and understanding it would have been impossible for me to finish this work. Their support and infallible love has always been my strength. During my Ph.D., either good or bad time, my parents have always been a motivational source to me. I consider myself the luckiest in the world to have such a supportive family, standing behind me with their love and support.

Publications

Journal

1. Anita Devi and Arijit K. De, Theoretical investigation on nonlinear optical effects in laser trapping of dielectric nanoparticles with ultrafast pulsed excitation, Optics Express **24 (9)**, 21485-21496, 2016.
   https://doi.org/10.1364/OE.24.021485
2. Anita Devi and Arijit K. De, Theoretical investigation on optical Kerr effect in femtosecond laser trapping of dielectric microspheres, Journal of Optics (IOP Publishing) **19 (6)**, 065504 (1-6), 2017.
   https://doi.org/10.1088/2040-8986/aa698c
3. Anita Devi and Arijit K. De, Theoretical estimation of nonlinear optical force on dielectric spherical particles of arbitrary size under femtosecond pulsed excitation, Physical Review A **96 (2)**, 023856 (1-9), 2017.
   https://doi.org/10.1103/PhysRevA.96.023856
4. Anita Devi and Arijit K. De, An alternate analytic formulation of optical force on a dielectric sphere in the ray optics limit, Journal of the Optical Society of America B **35 (2)**, 244-250, 2018.
   http://doi.org/10.1364/JOSAB.35.000244
5. Anita Devi and Arijit K. De, Harnessing optical nonlinearity to control reversal of trapping force: A theoretical investigation, Journal of Optics (IOP Publishing) **21**, 065502 (1-8), 2019.
   https://doi.org/10.1088/2040-8986/ab162a
6. Anita Devi and Arijit K. De, Simultaneous detection of two-photon fluorescence and back-scattered signal of optical trapping of dielectric nanoparticles under femtosecond pulsed excitation, Journal of Nanophotonics (JNP Letters) **13 (2)**, 020501 (1-8), 2019.
   http://dx.doi.org/10.1117/1.JNP.13.020501
7. Anita Devi, Shruthi S. Nair and Arijit K. De, Disappearance and reappearance of optical trap for silver nanoparticles under femtosecond pulsed excitation: A theoretical investigation, EPL (Europhysics Letters) **126**, 28002 (1-7), 2019.
   http://dx.doi.org/10.1209/0295-5075/126/28002

Refereed proceedings

1. Anita Devi and Arijit K. De, Generalized Lorentz-Mie theory of optical Kerr effect in femtosecond laser trapping of dielectric nanoparticles, **13th International Conference on Fiber Optics and Photonics, OSA Technical Digest (online) (Optical Society of America, 2016)**, paper Th4A.3, 2016. (Invited paper)
   http://doi.org/10.1364/PHOTONICS.2016.Th4A.3
2. Anita Devi, Shaina Dhamija, and Arijit K. De, Optical trapping with femtosecond laser pulses, **Proceedings of SPIE** 10347, 1034737 (1-5), 2017.
   http://dx.doi.org/10.1117/12.2273839
3. Anita Devi, Sumit, and Arijit K. De, Optical trapping dynamics probed by simultaneous detection of two-photon fluorescence and back-scatter, **PHOTONICS-2018: International Conference on Fiber Optics and Photonics** (ISBN 978-93-88653-41-1), Paper No. TP075, 2018.
4. Pragya Verma, Anita Devi and Arijit K. De, Probing ultrafast relaxation dynamics of a thermal lens in a transparent medium by non-resonant pump/non-resonant probe Z-scan technique, **PHOTONICS-2018: International Conference on Fiber Optics and Photonics** (ISBN 978-93-88653-41-1), Paper No. FP024 (2018).
5. Anita Devi, Shruthi S. Nair and Arijit K. De, Nonlinear splitting of optical trap of metallic nanoparticles, **CLEO/Europe-EQEC**, Paper No: EG-P1130, 2019.
   https://doi.org/10.1109/CLEOE-EQEC.2019.8871799
6. Anita Devi and Arijit K. De, Generalized Lorentz Mie Theory of reversal of optical trapping force, **CLEO/Europe-EQEC**, Paper No: CD-P1174, 2019.
   https://doi.org/10.1109/CLEOE-EQEC.2019.8873069
7. Anita Devi and Arijit K. De, Optical trapping dynamics probed by real-time back-scatter imaging, **Proceedings of SPIE** 11075, Novel Biophotonics Techniques and Applications V, 110750Z, 2019.
   https://doi.org/10.1117/12.2526378

Bulletin

1. Anuj K. Pennathur, Anita Devi and Arijit K. De, Probing Ultrafast Energy Transfer Dynamics: From Ensemble to Single Particle Measurements, ISRAPS Bulletin **28 (3)**, 24-32, 2016. (Invited article)

Under consideration

1. Anita Devi, Sumit Yadav, and Arijit K. De, Mapping nonlinear optical potential from on-the-fly dynamics of dielectric microspheres inside a femtosecond laser trap.
2. Anita Devi, Sumit Yadav, and Arijit K. De, A table-top portable multimodal nonlinear laser tweezer.
3. Anita Devi, and Arijit K. De, Harnessing optical nonlinearity to control reversal of trapping force under pulsed excitation using Generalized Lorentz Mie Theory.
4. Anita Devi, and Arijit K. De, A general theoretical investigation of dielectric nanoparticles in optical trapping under femtosecond pulsed excitation.
5. Anita Devi, and Arijit K. De, Theoretical investigation of nonlinear effects in optical trapping of arbitrary size dielectric particle with ultrafast pulsed excitation using Exact Mie Theroy.
6. Anita Devi, Sumit Yadav, and Arijit K. De, Mapping nonlinear optical potential for optical trapping of dielectric microspheres by simultaneous backscatter and video microscopy.
7. Anita Devi, Shruthi S. Nair, and Arijit K. De, Harnessing optical nonlinearity in dielectric-metallic hybrid nanoparticles under pulsed excitation using Dipole approximation.

Abbreviations

AFM	:	Atomic Force Microscopy.
BBO	:	Beta Barium Borate.
BSC	:	Beam Shaping Coefficient.
CCD	:	Charge-Coupled Device.
CMOS	:	Complementary Metal-Oxide Semiconductor.
CW	:	Continuous Wave.
EMCCD	:	Electronic Multiplier Charge-Coupled Device.
EMT	:	Exact Mie Theory.
ET	:	Electromagnetic Tweezer.
FFT	:	Fast Fourier Transform.
fps	:	frames per second.
FWHM	:	Full Width Half Maxima.
GLMT	:	Generalized Lorenz Mie Theory.
GO	:	Geometric Optics.
LASER	:	Light Amplification by Stimulated Emission of Radiation.
LMT	:	Lorentz Mie theory.
MASER	:	Microwave Amplification by Stimulated Emission of Radiation.
MSC	:	Mie Scattering Coefficient.
MSD	:	Mean Square Displacement.
MT	:	Magnetic Tweezers.
NA	:	Numerical Aperture.
NAC	:	Nonlinear Absorption Coefficient.
NP	:	Nanoparticles.
NRI	:	Nonlinear Refractive Index.
OKE	:	Optical Kerr Effect.
OT	:	Optical Tweezer.
PMT	:	Photo-multiplier Tube.
PS	:	Particle Size.
RI	:	Refractive Index.
SHG	:	Second harmonic Generation.
SPR	:	Surface Plasmon Polariton.
TPF	:	Two-photon Fluorescence.
TPA	:	Two-photon Absorption.

Symbols

λ	:	Wavelength of light.
τ	:	Pulse width.
RR	:	Repetition rate.
c	:	Speed of light.
n^w	:	RI of the medium.
n^p	:	RI of the particle.
n^c	:	RI of the core medium.
n^s	:	RI of the shell medium or silver nanopaticles.
n_2^w	:	Second order NRI of the medium.
n_2^p	:	Second order NRI of the particle.
n_2^c	:	Second order NRI of the core medium.
n_2^s	:	Second order NRI of the shell medium or silver nanopaticles.
ϵ_∞	:	Background permittivity.
ω_p	:	Plasma frequency.
γ_c	:	Collision damping frequency.
n_4^s	:	Fourth order NRI of the silver medium.
n_6^s	:	Sixth order NRI of the silver medium.
σ	:	Absorption coefficient.
σ_2^s	:	Second order NAC of the silver medium.
σ_4^s	:	Fourth order NAC of the silver medium.
σ_6^s	:	Sixth order NAC of the silver medium.
μm	:	micrometer.
nm	:	nanometer.

Abstract

There is presently an increased research activity in understanding the nature of optical force when ultrashort pulsed excitation is used to trap and manipulate objects with sizes ranging from micrometers down to nanometers. Such a "femtosecond laser tweezer" is peculiarly promising because the nature of the force can be dramatically tuned owing to optical nonlinearity. In this thesis, we have studied the role of optical Kerr effect in laser trapping theoretically as well as experimentally.

In the first part of this thesis, we have shown numerical simulations using different theories such as dipole approximation formulation, geometric optics formulation, generalized Lorenz Mie theory (using localized approximation), and exact Mie theory under both continuous-wave (CW) and pulsed excitation for dielectric as well as metallic particles. It has been shown that owing to optical nonlinearity, the escape potential (the height of the axial trapping potential barrier along the beam propagation direction), not absolute potential (the absolute depth of the axial trapping potential), is the relevant parameter for stability of an optical trap created by a train of femtosecond laser pulses. We have optimized the average power and particle size by fixing the other parameters in numerical simulations for micron to nanometer-sized particles. Also, we have demonstrated that the optical trapping force/potential can be reversed (from repulsive to attractive), upon switching from CW to pulsed excitation. The results open up the possibility of utilizing optical nonlinearity for facile optical manipulation/sorting by controlled reversal of optical force. Later, we have extended our study from dielectric to metal nanoparticles and observed that the initial disappearance of trapping potential well along the axial direction with an increase in laser power but subsequent reappearance at higher laser power. These studies show how one can harness optical Kerr effect to fine-tune the stability of an optical trap and thereby have controlled optical manipulation.

In the second part of this thesis, we have performed experiments to test the theoretical results. We have designed and built a complete table-top optical tweezer set-up with versatile detection modalities: *wide-field detection mode* using camera

required for spatial resolution and *point detection mode* using photomultiplier tubes for temporal resolution. To quantify the pulse-width at the sample position of optical tweezer set-up, we have used collinear two-photon fluorescence (TPF) autocorrelation. Firstly, we have explored the physics of the nonlinear nature of optical trapping force/potential under ultra-short pulsed excitation for micron-sized particles. Thus, we have presented the very first attempt in building a bridge between nonlinear optical phenomena and optical trapping by a combination of theory and experiment. Here, we have provided a model to elucidate sequential events (drag, adjustment, equilibration, fluctuation and ejection) in optical trapping dynamics and showed how we can map the highly asymmetric axial potential created by a femtosecond pulse-train. Later, we have extended our study from micron to nanometer-sized dielectric particles. We have shown that while TPF signal decays over time due to photobleaching but this signal is useful to know whether a particle is dragged towards the trap, in contrast, backscattered signal provides detailed information about the particle's dynamics inside the optical trap. Therefore, a simultaneous detection set-up is essential to capture the trapping events of fluorescent particles.

Considering fine-tuning of trap-stiffness through optical nonlinearity, we envision far-reaching applications of using ultra-short pulsed excitation in laser trapping and manipulation.

Contents

General introduction 1

The interaction of light with matter gives rise to the exciting effects that have captured the imagination of man over centuries. Research in optics encompasses a very diverse field ranging from something as trivial as refraction through a lens to as intricate ideas as using light to trap atoms and small particles. Optical trapping is one of the fascinating techniques that is used to trap and manipulate objects with sizes ranging from micrometers down to nanometers. It works on the principle that light carries momentum and can, therefore, exert force on objects. There is presently an increased research activity in understanding the nature of optical force when ultrashort pulsed excitation is used. This thesis endeavors to construct a bridge between relevant concepts of optical trapping and nonlinear optical phenomena. So first, I will discuss the basics of optical tweezer in detail and then its history followed by mathematical formulation.

1.1 Introduction of optical tweezer

Optical tweezer is a versatile technique that finds numerous applications in the field of chemistry, biology, plasmonics, colloidal science, and nanophotonics for solving various problems. Optical tweezer is typically a modified version of optical microscopes. The progress of optical tweezer from an elementry microscope to a state of the art instrument which can control the dynamics of single particle. It can measure the force that is of the order of pN and displacement of the order of nm. The basic principle of this technique is based on radiation pressure. Trillions of photons every second bombard us, but we are too massive to be pushed or pulled by the tiny momenta of the photons. However, when it is all about atoms, molecules, and particles of colloidal dimension, the force is significant. In recent years many researchers are investigating different techniques such as single and dual-beam optical trap [1], magnetic tweezer [2], acoustic tweezer [3], dielectrophoretic trapping [4], hydrodynamic trapping with microfluidic valving [5] to capture the dynamics of micron and nano-sized particles in the various field of sciences. All these techniques have their advantages and disadvantages according to the requirements. Over the decades, single-beam optical tweezer has become a known technique for manipulating viruses and bacteria [6], yeast cell, blood cell, protozoa [7, 8], chromosomes [9], bacterial flagella [10], internal cell surgery [11], sperm cells [12, 13], motor molecules driving mitochondrion and latex spheres along microtubules [14, 15], vesicle [16–18], DNA [19], dielectric

[1, 20, 21], metallic particles [22–26], etc. Optical tweezer can also be used for [21] cooling down atoms and molecules from temperatures ranging several hundreds of degrees kelvin to nanokelvin.

1.2 The journey of implementing the radiation pressure concept in optical tweezer

Although Optical tweezer was invented in the 20th century, the origin of this concept can be traced back to the observation of Halley's comet as early as the 15th century where for the first time, 21 comets were seen together [27, 28]. This marked the beginning of comet tail science, and researchers started exploring the science behind the comet tail. In 1531, Peter Apian a German astronomer, observed that independent of the direction of motion of planets or weather, the comet tails always point away from the Sun. In 1577, Tycho Brahe observed this phenomenon night after night but was not able to comment on the motion of the comet tail because the trajectory of the moon and Sun around the earth was not very clear at that point in time [29]. In 1609, Johannes Kepler, a great mathematician took this challenging problem and elucidated Tycho Brahe's observations [30]. Although Johannes Kepler lived in an era where there was no distinction between astrology and astronomy, there was a clear difference between astronomy and physics. To determine the trajectory of the comet tail, he faced many hurdles. Therefore, Johannes Kepler presumed that earth follows an elliptical path and the comet motion follows a straight line in the solar system. Alongside, he referred the 1607 the comet database and solved the problem qualitatively. In 1623, Galileo argued that the comets were optical phenomena and Descartes thought that the comets were bodies that travels from one galaxy system to another. Both theories were not accepted because no appropriate explanation was found. Later in the century, the path of the comet's tails was agreed to be elliptical or parabolic instead of a straight line. Still, no conclusive evidence was found. In 1687, Newton introduced the comet as a member of the solar system and proposed that the comet's trajectory is the same as other planets in solar system. He investigated the occurrence of the comet tail based on four fundamental assumptions [29, 31]: (1) thick atmosphere exists around the comets, (2) comet tail rises from the comet's atmosphere, (3) comet tail is pointing away from the Sun due to solar heat, and (4) comets are moving in ambient ether medium. In 1705, Edmond Halley took this challenging problem as a mission and incorporated Newton's

idea along with all the existing database from previous centuries and observed that comet was appearing in 1533, 1607, and 1682 was following the same path. Subsequently, he concluded that comets are moving along the parabolic path and along with this he also predicted that the next comet tail will appear in 1758. The comet came to be known as Halley's comet because according to his prediction, comet appeared in 1758 (on a Christmas Day), but unfortunately, he died in 1742. Then researchers focused on the other parameters of Halley's comet-like mass, and frequency of appearance, etc. Later in 1811, Heinrich Olbers proposed that pressure of light could be responsible for pointing the comet tail away from the Sun. Following this proposal in 1836, a German astronomer and mathematician Friedrich Bessel started working on this. They determined that a repulsive force opposite to the direction of Sun's radiation is experienced by the particles. In 1876, Italian physicist Adolfo Bartoli also explained radiation pressure in terms of the second law of thermodynamics [32]. Feodor Bredikhin further revised the theory in 1877 and introduced a new concept depending on the repulsive force. In 1900, Svante Arrhenius identified the repulsive force acting on the dust particle as radiation pressure by sunlight. In 1901, the same concept of radiation pressure was modified by Karl Schwarzschild. In 1873, James Clerk Maxwell Scottish physicist gave a fantastic theory which is known as Theory of Electromagnetism "*In a medium in which the waves are propagated, there is a pressure in the direction normal to the wave, and numerically equal to the energy contained in unit volume*". This theory contributed significantly to solve the problem [33, 34]. Till that time no experimental evidence was observed for radiation pressure. Later in the beginning of 19th century in 1901 an experimental evidence of radiation pressure was found by Pyotr Nikolaevich Lebedev using a torsional pendulum at the University of Moscow [35]. Later in the same year, Ernest Fox Nichols and Gordon Ferrie Hull also demonstrated radiation pressure and the transfer of momentum between light and matter at Dartmouth University, where they used high gas pressure and silver glass vanes. In contrast, P. N. Lebedev used low gas pressure, and they concluded that both experiments could verify the existence of radiation pressure qualitatively [36, 37]. In 1903 the same group published quantitative evidence of radiation pressure [38]. The LASER was invented in 1960s, and Arthur Ashkin was the first in that century to give a qualitative and quantitative existence of radiation pressure concept by accelerating and trapping of microsphere using argon laser having wavelength 514.5 nm along with TEM_{00} mode (Gaussian) beam profile [1] in 1970. Sixteen years later, in 1986, he

successfully invented the technique called Optical Tweezer by trapping a single particle using a highly focused Gaussian beam [39]. Very recently in 2018, Arthur Ashkin has been awarded Nobel prize in Physics for his pioneering research.

1.3 Early development in optical tweezer

Arthur Ashkin is known as the father of optical tweezer [1, 21, 39]. His work started around the era of the Second World War when he was pursuing his graduation from Columbia University. He joined the Columbia radiation lab because he was fascinated by the field of radiation pressure. During this time, he learned about MASER. Later the concept of MASER was implemented to LASER [40]. This work played a crucial role in developing the field of optical trapping. In 1947, he received his Bachelor's degree in Physics from Columbia University. Then he moved to Cornell University for pursuing a Ph.D. in nuclear physics, and in 1952 he received his doctorate. Afterward, Sidney Millman recommended him to join the Bell Laboratories because of his remarkable work. To explore the Johannes Kepler and James Clerk Maxwell radiation pressure concept [41], he designed a simple experiment using MASER having a wavelength around 3 cm along with megawatt magnetrons. His idea worked extremely well, and it became experimental evidence of radiation pressure in magnetrons. Later on, in 1960, Theodore H. Maiman invented LASER at Hughes Research Laboratories [42].
During the next decade, A. Ashkin observed an unfamiliar motion of dust particles within the resonant cavity of the visible laser. He hypothesized that particles are drawn towards the beam center and move along the direction of propagation due to the radiation pressure of the light. To quantify this phenomenon, he came up with a straightforward experiment with a micron-sized transparent sphere using a focused laser beam. In this experiment, he had used a glass coverslip for the sample. After that, he thought about a way to replace this glass coverslip with any other counter-propagating wall (which need not necessarily be a physical wall). Consequently, he came up with an idea of using another laser beam, which propagates opposite to the direction of propagation of the first laser. In 1970, his idea worked successfully, and trapping of the particle was detected using a dual-beam optical trap which paved the way to levitation traps. The basic idea behind this experiment was that if light exerts a force on the particle, it results in canceling the scattering force acting on the particle. The particle can be confined in the vicinity of focal volume forever due to the counter-propagation

of the second laser beam. Now, the question is whether it is possible to trap a single particle using a single beam instead of dual-beam [21] because the main challenge in the dual-beam optical trap is coinciding the focal plane of both the counter-propagating laser beams to trap the object within the focal plane. In a single beam optical tweezer, the scattering force (acting along the direction of propagation of laser beam) pushes the particle away from the trap while the gradient force (acting along all the three direction) pulls the particle towards the trap.

A stimulating personal experience may be found in references [6, 8, 43, 44]. His first groundbreaking work was published in "Physical Review Letter (PRL)" [1]. He tried to apply this concept in biophysics like bacteria, live cell [6, 8, 44], etc. For later research, he approached Jim Gordon who developed MASER and Jim Gordon found his work interesting and agreed with the results [45–47]. They collaborated and explicated the "Optical Earnshaw Theorem" which explained the optical gradient and scattering force [48].

In 1984 Steven Chu arrived at Holmdel from the Bell Labs in Murray Hill and collaborated with John Bjorkholm, Leo Holberg and Arthur Ashkin on the project. Afterward, the breakthrough discovery of the century in this field came up, which is atom cooling and trapping. This discovery was awarded Nobel prize in 1997 to Steven Chu of Stanford University, Claude Cohen-Tannoudji of the Collège de France and Ecole Normale Supérieure, Paris, and William Phillips of the National Institute of Standards and Technology (NIST) in Maryland [49]. The importance of atom cooling and trapping technique is that we can cool down the atom to few microkelvins while a single beam trap can cool down the atom to a few Kelvin. This breakthrough changed the perspective of the scientific community, and the discovery of LASER-cooled Bose-Einstein Condensation (BEC) came up [50–53]. In 1986, Arthur Ashkin could witness the big moment of his experiment, and an optical tweezer was discovered (single-beam gradient force trap). The particles were indeed getting dragged towards the focal volume because of the huge gradient force that acts on the particle with a single, tightly focused laser beam. Subsequently, he gave a theoretical model for his experimental evidence. He elucidated that two kinds of forces are acting on the particle: one is scattering force along the direction of propagation, and the other is the gradient force acting along all the three directions [39]. Eventually, optical tweezer opened up many different applications in different fields of science.

1.4 Work done so far in optical tweezer

Optical tweezer is a powerful technique to study light-matter interaction, and due to its remarkable property of manipulating the micron to nanometer-sized object, this technique is unique as compared to others. It has potential applications in the field of research as well as real-life applications in measuring the force, elasticity, torsion, and position of a trapped object. Arthur Ashkin showed, for the first time, a single-beam optical trap in 1986 using polystyrene particles [39]. Later on, he showed the application of optical tweezer in the manipulation of complex biological compounds [6, 8, 13, 14]. In 1993, Steven Block and his collaborators performed the first direct measurement of the movement of individual kinesin [54]. The basic optical tweezer technique was eventually integrated with a quadrant photodiode (QPD) to measure sub-nanometer displacement and to enhance the spatial-temporal resolution of trapped objects [55]. In 1994, an advanced technique of optical tweezer known as "Optical spanner" was proposed, which can be used to manipulate the rotational degrees of freedom. Miles Padgett implemented this idea and Les Allen from the University of St. Andrews in Scotland [56] in optical tweezer in 1996, which leads to the discovery of optical spanner. However, an optical spanner works only with a special type of laser beam called a Laguerre-Gaussian beam or higher-order Gaussian beam because they have a helical wave-front and their Poynting vector spirals about the axis of the beam which helps to rotate the particle [57]. Optical tweezer was integrated with Raman spectroscopy to measure the chemical composition and physical properties of a single trapped particle via molecular vibrational spectroscopy known as Raman tweezers [58–60]. Raman spectra, along with the optical trapping, were first time measured from the levitation glass sphere and quartz microcrystals in the air in 1984 [61]. Later on, this technique was applied for biological compounds [62–64] due to its unique property of collecting Raman spectrum during the experiment because, during the experiment, cells or spores can grow, change and reproduce in buffer liquid or air. Laser Trapping Raman Spectroscopy (LTRS) helps to understand the dynamics of these cells. Afterward, enhancement in the Raman scattering was observed for bacterial spores using optical trapping [65]. In 2002, Holographic Optical Tweezer (HOT) was developed by David G. Grier. Interaction dynamics of the trapped particle can be studied using HOT in which HOT uses computer-generated hologram (experimentally can be implemented by spatial light modulator or diffractive optical element) to split a single collimated laser beam into several beams [66]. In 2004 Kishan

Dholakia used pulsed excitation instead of continuous-wave excitation and found the experimental evidence of optical trapping using femtosecond laser pulses, which are known as femtosecond optical tweezers for the first time [67, 68]. To study the plasmonic effect in metallic particle/rod through optical tweezer was modified to surface plasmon optical tweezers [69–71]. Thermal [72] and magnetic [55] tweezer were also developed to study the heating and magnetic effect of trapped particles, respectively. Continuous advancements in this field have been useful to study micro to nano-size particles both theoretically and experimentally. As a result, in 2011 single protein molecule of Bovine Serum Albumin (BSA) having a hydrodynamic radius of 3.4 nm was trapped [73]. Very recently, a hypothetical model was proposed by our group, which suggested that in the case of femtosecond optical tweezers, peak power is very high as compared to the average power of CW laser; consequently, the potential created in the focal plane has a steep well depth. The generation of the potential well depends upon the repetition rate of pulses, and steepness depends on the pulse width [74]. These advancements in the field of optical tweezer are used by few researchers to detect the early stages of certain diseases like malarial/cancer infection with a minimal amount of blood sample. Red Blood Cells (RBCs) are trapped in optical tweezer, which show the Brownian motion. The two samples were taken: infected RBCs and normal RBCs. The Brownian motion of the infected RBCs was different from that of normal RBCs. It was observed that the Brownian fluctuations were expressed as the corner frequency. The corner frequency of the infected RBCs was more than that of the normal RBCs [75, 76].

Recently, the role of low-power high-repetition-rate ultrafast pulsed excitation on trapping efficiency has been investigated for larger dielectric particles having diameter greater than 0.5 μm [13, 68, 77–81]. Such excitation results in stable trapping of individual dielectric nanoparticles with diameter $\leq$ 0.1 μm for example, trapping of 100 nm diameter latex nanosphere [82, 83] and 10-20 nm diameter Cd-Se quantum dots [74, 83]. Stable trapping is confirmed by sensitive measurement of precise step-wise rise in two-photon fluorescence and/or scattering signal. The small dimension of nanoparticles leads to faster diffusion; however, the high pulse peak power results in a steep trapping potential to overcome these challenges associated. Also, the high pulse repetition-rate restricts diffusion of the trapped particle out of focus during the dead-time between consecutive pulses [74, 82, 83]. A phenomenological description has been put forward to capture the underlying physics behind the enhanced trapping efficiency with such excitation

[74]. The repetitive instantaneous momentum transfer by a train of pulses with typically 100 fs pulse-width at 100 MHz repetition rate (i.e., with the 10 ns time lag between consecutive pulses) ensures that the trap is stable. But the response of the particle to an instantaneous momentum transfer is dictated by the trapped particle's inertial time (which is inversely related to the particle size). Thus, a smaller particle having a diameter of ≤ 0.1 μm can respond to this impulsive force. However, for a larger particle with diameter ≥ 0.5 μm, the typical inertial time is several tens of nanoseconds; As a result, the particle always respond to cumulative momentum transfer by several pulses in the pulse train such that the trapping efficiencies turn out to be the same under pulsed and continuous-wave (CW) excitation [13, 68, 77–80]. In addition to that, even after chirping the pulse-width remains too small to have any effect such that the trapping efficiency turns out to be independent of femto- to pico-second pulse-chirping [77].

In the case of such high peak-power pulsed excitation combined with the tight-focusing condition, the nonlinear optical effects become non-negligible, and the role of these nonlinear effects in determining the trapping efficiency has not yet been explored well. We have theoretically shown that for a dielectric particle, the OKE always has a stabilizing effect on the radial component of trapping potential, but it significantly modulates the axial component. At lower power level, the fine balance between the gradient force and the scattering force along axial direction renders the trap progressively more stable upon increasing the power; however, above a critical power level, the trend is reversed leading to an unstable trap along the axial direction. With an increase in power, the trapping potential along axial direction becomes more asymmetric, and to quantify the trapping efficiency, the appropriate quantity is the height of the potential barrier along beam propagation direction and not the absolute depth of the trapping potential which is contrary to the common understanding in existing literature regarding the stability of an optical trap. We have also discussed under what optimal excitation parameters the dipole trap is most stable.

In the recent years, trapping of nanoparticles ($\leq$ 100 nm; latex bead, CdS, ZnS, core-shell, hollow sphere, and metallic particles) have gained attention due to its numerous applications in nanophotonics [6, 83, 84]. As particle size decreases, diffusivity increases and Brownian fluctuations become larger in amplitude, which makes trapping more challenging. These Brownian fluctuations can be controlled by using high repetition rate ultrafast pulsed excitation instead of continuous wave (CW) excitation for stable trapping of nanoparticles. The nature of the

potential well must be much steeper than that of conventional trapping potential needed to trap micron-sized particles. A shallower potential leads to a large amplitude motion of the trapped nanoparticle inside the potential well. On the other hand, a steeper potential leads to stable spatial confinement of the nanoparticle [74]. In a recent study of high repetition rate ultrafast pulsed excitation (chapter 1 to 6), it was shown that nonlinearity exhibits a significant effect that is not observed in the continuous wave (CW) excitation. Including the nonlinearity shows that for stable trapping, there should be a balance between the scattering and gradient forces, and any further increase in the scattering force will destabilize the trap. Nonlinear effects bring a significant change at a similar power level under CW and pulsed excitation. However, still, it is not clear why femtosecond should be advantageous over CW excitation because trapping can be done even by a simple laser. One possible explanation could be that high repetition rate ultrafast pulsed excitation offers a very steep potential, which helps in the trapping of very small size particle because of its high peak power. However, there is no concrete evidence behind this hypothesis. Many researchers have modulated the potential well using higher-order Gaussian beam, Bessel beam, etc. This technique opened a new world of single-molecule spectroscopy that resulted in some landmark research work.

1.5 Importance of optical tweezer over other techniques

Number of techniques such as Optical tweezer (OT), magnetic tweezer (MT) [2, 55], electromagnetic tweezer (ET) [85], atomic force microscopy (AFM) [55], micro-needle manipulation [86], bio-membrane force probe [87], flow-induced stretching, [88, 89] electrophoresis, and micropipette [90] has been developed simultaneously or over time to understand the dynamics of a single particle or molecule. Each one of them has its own advantages and disadvantages (as listed in Table 5.1) [55, 90, 91] depending upon certain condition. Based on what we want to study, the researchers have to compromise one aspect of the chosen technique over the other. Among these techniques, Optical tweezers provide higher resolution spatially and temporally as compared to other techniques. The optical tweezer technique is limited by thermal heating. When the trapping beam is focused, the typical intensity is 10^9-10^{12} W/cm^2 at the focal plane, which results in a significant chnage in temprature [92, 93]. The optical tweezer technique

Techniques	OT	MT	AFM	ET
Type	Non-Contact	Non-Contact	Contact	Non-contact
Spatial Resolution (nm)	0.1-2	5-10	0.5-1	2-10
Temporal Resolution (s)	10^{-4}	10^{-1}-10^{-2}	10^{-3}	10^{-4}
Stiffness (pN/nm)	0.005-1	10^{-3}-10^{-6}	10-10^{5}	10^{-4}
Force (pN)	0.1-1000	0.001-100	10-10000	0.01-10000
Displacement Range (nm)	0.1-100000	5-10000	0.5-10000	5-100000
Probe size (μm)	0.25-15	0.5-5	100-250	0.5-5
Energy Dissipation	Yes	No	No	No
Surface Considerations	No	No	Yes	No
Low Cost	Yes	Yes	No	Yes
Features	Low noise and low drift	Force-clamp, Bead rotation, and specific interaction	High-resolution imaging	Force-clamp, Bead rotation
Limitations	Photo-damage, Sample heating, and Non-specific	No controlled manipulation of dielectric particles	High stiffness probe and minimal force nonspecific	Force hysteresis

Tab. 1.1.: Comparison of force spectroscopy technique.

allows heat dissipation, but laser heating can be minimized by using a modified profile of trapping beam both spatially and temporally. It can also be minimized if we use a pulsed laser rather than a CW laser. In the case of pulse excitation, there is a time interval between two consecutive pulses, depending upon the

repetition rate. Therefore, laser heating can be dissipated to the surrounding medium, which prevents the sample from radiation damage and minimizes the accumulation of heating effects. From the above discussion, we can say that optical tweezer is one of the best techniques to study the dynamics of a single particle or a single molecule. It opens up a whole new world for biological complex compounds; few are listed here: force estimation for Kinesin motors, microtubules, cytoplasm of cells, other molecular motors, mechanical studies of bacterial flagella, chromosome manipulation during mitosis, chromosome dissection, microsurgery and manipulation of cells in vivo, controlled cell fusion, kinetic studies of DNA and RNA, etc.

1.6 Thesis at a glance

In this thesis, we have studied the role of optical Kerr effect (OKE) in laser trapping theoretically as well as experimentally under both CW, and pulsed excitations for dielectric and metallic particles and optical trapping dynamics of micron to nano-sized particles is studied while the particle is confined within the optical trap. The experimental results are compared with our theoretical model. The specific question which we have asked is: Does femtosecond pulse excitation provides a better or worse or similar trapping efficiency (stability) than CW excitation at similar average power level?

My thesis is divided into two part: *part A: Theory (chapter 2 to 7) and part B: Experiment (chapter 8 to 10)*.

Part A: Theory: In **chapter 2**, detailed mathematical formulations are given for dipole approximation, geometric optics (GO) approximation, Generalized Lorenz Mie Theory (GLMT), and exact Mie theory (EMT) for trapping including optical nonlinearity.
In **chapter 3**, we have studied the effect of OKE in laser trapping using dipole approximation under both CW and pulsed excitation. A tight focusing condition under pulsed excitation results in a significant contribution of the nonlinear effect, which cannot be ignored. However, under CW excitation, these effects can be ignored. Under pulsed excitation, with an increase in laser power, the radial component of the trapping potential becomes progressively more stable, but the axial component is dramatically modulated due to the significant contribution of OKE. We have justified that the relevant parameter to quantify the trapping

efficiency is escape potential (the height of the potential barrier along the beam propagation direction), not the absolute potential (absolute depth of the global potential minimum). We have also discussed the optimal excitation parameters leading to the most stable dipole trap. In addition, we have demonstrated that the nature of the force/potential curves is highly dependent on the relative refractive index of the particles. At similar conditions, CW excitation shows repulsive force while pulsed excitation shows attractive force because under pulse excitation overall relative refractive index is modulated by the notable contribution of the nonlinear refractive index. Thus, the relative refractive index value for any material with significant optical nonlinearity can be controlled by changing the average power (hence, the peak power) of the laser beam. Therefore, both CW and pulsed excitations have their pros and cons depending upon the linear and nonlinear refractive indexes of the dielectric nanoparticles and surrounding medium. Similar results are obtained for metamaterials as well. Our results show excellent agreement with previous experiments. With these results, we have contradicted the notion earlier believed: *The optical potential created by the tightly focused laser is quite skewed along axial direction*. As scattering force is a dominant factor for the occurrence of asymmetry in the potential well, hence, the optical potential is anharmonic under both CW and pulsed excitation. Therefore, the ejection of the particle is always along the axial direction.Later, using dipole approximation, we have theoretically demonstrated that for hollow-core polystyrene nanoparticles, the optical trapping force/potential can be reversed from repulsive to attractive, upon switching from CW to pulsed excitation. The results open up the possibility of utilizing optical nonlinearity for facile optical manipulation/sorting by controlled reversal of optical force. Considering wide-ranging applications of hybrid and hollow-core nanoparticles, we envision the far-reaching application of facile optical sorting/manipulation in a user-defined way.

A theoretical underpinning is yet to be established whether the effect of optical nonlinearity is omnipresent across different particle sizes or not. This issue has been investigated in **chapter 4**. Here we have demonstrated the role of OKE for arbitrary sized conventional, hybrid, and hollow-core nanoparticles under both CW and pulsed excitation using GLMT with localized approximation. First, we have analyzed the nature of force/potential for spherical particles and provided a detailed comparative discussion between this generalized scattering formulations with dipole scattering formulation for dielectric nanoparticles. Later, we have extended the study to find the role of OKE in hybrid nanoparticles using GLMT

with localized approximation which is compared with dipole approximation and obtained similar results as discussed in **chapter 3**.

In **chapter 5**, we have studied the effect of OKE on a micron-sized spherical dielectric particles. The optical force on a micrometer-sized dielectric sphere in a single-beam gradient laser trap was formulated by considering the 2D distribution of rays for a plane-wave excitation using GO approximation. We have shown how the inclusion of OKE results in the significant change of the force curves along axial direction under femtosecond pulsed excitation compared with CW excitation. Most importantly, similar to the optical trapping of nanoparticles under ultrafast pulsed excitation, we have shown that the escape potential also governs the efficiency of trapping of micron-sized particles (and not by the absolute potential) of the axial trapping potential. Firstly, we explained formulation for flat-top beam profile, but laser beams usually have a Gaussian transverse intensity profile, which, upon tight focusing, leads to a 3D optical trap. Later, we have systematically formulated a generalized ray/GO formalism for estimating force/potential for both flat-top and Gaussian laser beams using the 2D distribution of light rays as well as the 3D distribution of light cones. We have also compared our method with the EMT. Also, we have presented a detailed discussion on the nature of force/potential considering the OKE under pulsed excitation and showed that GO approximation is dependent on the particle size, which was earlier believed to be independent of particle size.

Ashkin compared different theories and concluded that EMT holds the overall regime and yields better results than others. But this presents some problems when confronted with the phenomenon of bending of light in a medium. In **chapter 6**, the definition of bending of light inside the medium is reformulated, and then using this new definition, we compared EMT with GO approximation and dipole approximation. It is found that dipole approximation and GLMT using localized approximation do not match with EMT, while GO does stand in agreement with EMT under CW excitation. When nonlinearity is incorporated, GO results deviate from those of EMT. So, in these two particular limits, EMT cannot be used for an accurate qualitative or quantitative prediction of force under pulse excitation, but it holds for Mie regime.

In addition to this, metallic nanoparticles have gained a lot of attention in the field of optical trapping because of their intrinsic behavior of surface plasmon resonance effects, which arise upon interaction with electromagnetic radiation that enables a large number of nano-optical applications of high current interest.

In **chapter** 7, we have extended our study from dielectric to metal nanoparticles and found quite interesting results. We have observed that the initial disappearance of trapping potential well along the axial direction with an increase in laser power but subsequent reappearance at higher laser power. This shows how one can harness OKE to fine-tune the stability of an optical trap and thereby have controlled optical manipulation.

Part B: Experiment: To perform experiments to test the theoretical results, we have designed and built a complete table-top optical tweezer set-up with versatile detection modalities: *wide-field detection mode* using camera (with CMOS detector) required for spatial resolution and *point detection mode* using photomultiplier tubes (PMTs) for temporal resolution. In wide-field detection, we can capture dark-field images to record either two-photon fluorescence (TPF) image (for fluorophore coated particles) or back-scatter images (for both coated and uncoated particles); alternatively, we can use white-light illumination to capture transmitted bright-field images. In point detection mode, we can simultaneously detect both TPF and back-scatter. In **chapter** 8, we have discussed the experimental set-up, which is used while performing the experiment followed by the characterization of laser pulses, preparation of the sample, data analysis, etc. The quantification of pulse width at the sample position of optical tweezer set-up using second harmonic generation (SHG), autocorrelation is challenging. Thus, we have performed free-space measurement of pulse width using both SHG and TPF autocorrelation, and obtained similar pulse width. Therefore, we have measured pulsed use TPF signal from Rhodamin6G to measure pulse width at the sample position of the optical tweezer set-up.
In **chapter** 9, we have explored the physics of the nonlinear nature of optical trapping force/potential under ultra-short pulsed excitation for micron-sized particles. Here, we have also developed a generalized theory to numerically estimate trapping force/potential including optical nonlinearity, and implement a variety of detection modalities to capture particle's real-time trajectories under ultra-short pulsed excitation. By a combination of theory and experiment, we provide a model to elucidate sequential events (drag, adjustment, equilibration, fluctuation, and ejection) in optical trapping dynamics and showed how we could map the highly asymmetric axial potential created by a femtosecond pulse-train. Considering fine-tuning of trap-stiffness through optical nonlinearity, we envision far-reaching applications of using ultra-short pulsed excitation in laser trapping

and manipulation.

In **chapter 10**, high-repetition-rate ultrafast pulse excitation has been identified to play a vital role in stable trapping of dielectric nanoparticles assisted by optical nonlinearity due to its high peak power. We have demonstrated the trapping of 100-nm fluorescent polystyrene particles by simultaneous detection of both TPF and back-scattered signals. Here, we have shown that TPF signal decays over time due to photo-bleaching, but this signal is useful to know whether a particle is dragged towards the trap. In contrast, the back-scatter signal provides detailed information about the particle's trapping dynamics inside the optical trap. We have also discussed pros and cons of the moving-averaging method and concluded that the number of points for moving point averaging should be chosen judiciously in such a way that our signal should be smoothened enough to extract the information about the particles' trapping dynamics but not at the expense of losing it.

In **chapter 11**, we have discussed the overall conclusion and future aspects of this work.

Part A: Theory

2 A detailed mathematical description of different theories

2.1 Introduction

Here, we have considered that the particle to be isotropic, homogeneous, non-magnetic, and spherical.

Optical tweezer is characterized into three different regimes based on the scaling between the wavelength of the trapping beam (λ) and particle size (d is the diameter of the particle): Dipole/Rayleigh where the particle size is approximately ten times smaller than the wavelength of the trapping beam ($\lambda \gg d$) [94], geometric optics (GO)/ray optics [95, 96] where the particle size is approximately ten times greater than the wavelength of the trapping beam ($\lambda \ll d$) and Mie regime where the particle size is approximately equal to the wavelength of the trapping beam ($\lambda \approx d$) [94].

The confinement of the particle within the optical trap depends on the RI of the particle and the surrounding medium. Figure 2.1 shows the schematic diagram for the forces acting on a particle where RI plays an important role. A classical model can explain it following Snell's law. When a light ray falls at point A, some part of it gets reflected, and the rest gets refracted based on the material properties of the particle. If n_1 (RI of the particle) is greater than n_2 (RI of the surrounding medium), the ray bends toward the normal (figures 2.1a and 2.1b) and if n_1 is less than n_2, the ray bends away from the normal (figures 2.1c and 2.1d). Similarly, refracted light falls at point B, and the ray bend towards or away from the normal depending upon the RI of the particle and surrounding medium. Thus there is a change in the direction of propagation of light and hence a change in its momentum. According to Newton's second law, the change in momentum is equal to the force. However, Newton's third law says there is an equal and opposite reaction resulting in a force (known as gradient force) that acts on the particle. The trapping beam contains billions of rays following distribution according to its respective beam profile. For instance, in the case of the Gaussian beam, central rays are more intense as compared to the terminal rays, whereas for a flat-top beam profile, all rays are equally intense. As shown in figure 2.1a, for a Gaussian beam profile, the magnitude of the force F_1 is less

than that of F_2. Consequently, there is a net force dragging the particle towards the focal volume.

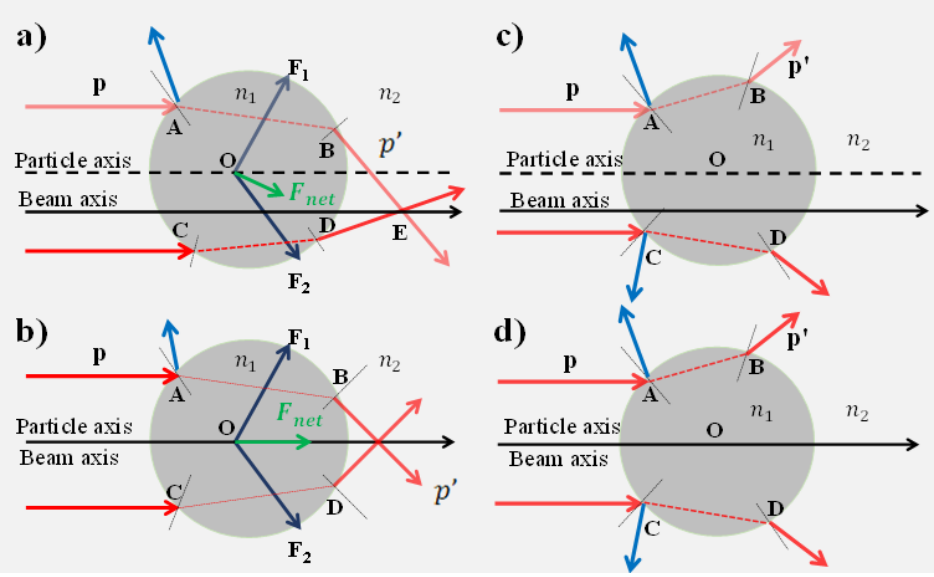

Fig. 2.1.: Ray diagram for large size particles. When particle is lying (a and c) before the focus and off from the beam axis, (b and d) before the focus and on the beam axis. The RI of the particle is (a and b) greater than the surrounding medium, (c and d) less than the surrounding medium. The dashed line passes through the center of the particle, parallel to the beam axis (solid line).

On the other hand, in figure 2.1b, the RI of the particle is less than that of the medium; therefore, the rays diverge, and a net repulsive force acts on the particle which tries to pull the particle away from the optical trap. Figures 2.1a and 2.1c show when particle is off-axis whereas figures 2.1b and 2.1d show when particle is on-axis of the trapping beam. Thus it can be inferred that if the RI of the particle is more as compared to the medium, then the particle will always get dragged towards the focal volume due to the gradient force acting on it. However, if the RI of the particle is less than the medium, the trapping is difficult. Apart from this, there is another kind of force acting on the particle due to the radiation pressure, which is known as scattering force. Earlier studies established that for getting a stable trap, gradient force should dominate over the scattering force. But this observation has left many questions unanswered such as:

Is it always necessary that for getting stable trapping, gradient force should be dominant over scattering force?

Can't we get stable trapping for the particle having RI less than the RI of the medium?

To answer these questions, we will first discuss the fundamental processes in-

volved in optical trapping and then analyze analytical forces (scattering and gradient) acting on the particle separately for all three regimes.

2.2 Dipole approximation

When the particle size is of the order of few nanometers, it behaves as a point dipole, and the shape of the particle does not matter since the dimension is much smaller than the wavelength. However, trapping depends strongly on the particle type, which could be a dielectric, magnetic, or metallic. For instance, in the case of metallic particles, plasmonic effects become dominant, which causes enhancement of the optical forces [97]. Here, we will focus on the effect of light electric field on dielectric particles (since the particle is assumed to be non-magnetic).

2.2.1 Gradient Force

This force is due to the Lorentz force acting on the dipole, induced by the electromagnetic field. The direction of the electric field is from positive to negative charge. Due to this applied electric field, the nucleus experiences a force in the direction of the electric field, and the electron cloud experiences it in the opposite direction (if the field is too high, it can ionize the atom and substance will then become a conductor). So, it also depends upon the strength of the electric field. However, an equilibrium is established soon between positive and negative charge clouds. The mutual attraction between the two clouds holds the atom together with the positive cloud shifted slightly in the direction of the electric field, and the negative cloud shifted in the opposite direction. The atom now has a tiny dipole moment in the direction of the electric field known as the induced dipole moment, which is proportional to the applied field $\vec{p} = \alpha\vec{E}$; here $\vec{p}$ is the induced dipole moment, and α is atomic polarizability (dipole moment per unit volume). In the uniform electric field, the force acting on both positive and negative ends are exactly equal. Nevertheless, if the applied field is non-uniform, the force experienced by the two ends is slightly different, and there is an infinitesimally small distance $\delta r = r_+ - r_-$ between both the ends. The force applied on a single charge in an inhomogeneous electromagnetic field is given by the Lorentz force, *i.e.*, $\vec{F} = q(\vec{E} + \vec{v} \times \vec{B})$ where, q is induced charge, $\vec{B}$ is the magnetic field and $\vec{v}$ is the velocity of the charged particle. The above equation can be rewritten as $\vec{F} = q\left(\vec{E} + \frac{d\vec{x}}{dt} \times \vec{B}\right)$. Here, the net electric field is $\vec{E} = \vec{E}(r_+) - \vec{E}(r_-)$; distance can be considered as $r_\pm = r \pm \frac{1}{2}\delta r$, so we may

expand the difference between the electric fields into a power series in δr by using Taylor expansion [98]:

$$\begin{aligned} f(x+a) &= f(x) + a.f'(x) + \frac{1}{2!}a^2 f''(x) + ... \\ &= f(x) + a.(\nabla f(x)) + \frac{1}{2!}a^2\nabla^2 f(x) + ... \end{aligned} \tag{2.1}$$

Neglecting higher order terms

$$f(x \pm a) = f(x) \pm (a.\nabla)f(x) + \frac{1}{2}(a.\nabla)^2 f(x) + ... \tag{2.2}$$

$$\begin{aligned} \vec{E} &= \vec{E}\left(r + \frac{1}{2}\delta r\right) - \vec{E}\left(r - \frac{1}{2}\delta r\right) \\ &= (\delta r.\nabla)\vec{E}(r) \end{aligned} \tag{2.3}$$

Using this, force can be written as:

$$\vec{F} = q\left((\delta r.\nabla)\vec{E} + \frac{d\delta\vec{r}}{dt} \times \vec{B}\right) = \left((p.\nabla)\vec{E} + q\frac{d\delta\vec{r}}{dt} \times \vec{B}\right) \tag{2.4}$$

By using a vector inequality:

$$\nabla(\vec{A}.\vec{B}) = \vec{A} \times (\vec{\nabla} \times \vec{B}) + \vec{B} \times (\vec{\nabla} \times \vec{A}) + (\vec{A}.\vec{\nabla})\vec{B} + (\vec{B}.\vec{\nabla})\vec{A} \tag{2.5}$$

It can be expressed as:

$$\nabla(\vec{E}.\vec{E}) = \vec{E} \times (\vec{\nabla} \times \vec{E}) + \vec{E} \times (\vec{\nabla} \times \vec{E}) + (\vec{E}\vec{\nabla})\vec{E} + (\vec{E}.\vec{\nabla})\vec{E} \tag{2.6}$$

$$(\vec{E}.\vec{\nabla})\vec{E} = \frac{1}{2}\vec{\nabla}(\vec{E}.\vec{E}) - \vec{E} \times (\vec{\nabla} \times \vec{E}) \tag{2.7}$$

$$\begin{aligned} \vec{F} &= \left(\alpha(\vec{E}.\nabla)\vec{E} + q\frac{d\delta\vec{r}}{dt} \times \vec{B}\right) \\ &= \left(\alpha\frac{1}{2}\vec{\nabla}(\vec{E}^2) - \alpha\vec{E} \times (\vec{\nabla} \times \vec{E}) + \alpha\frac{d\vec{E}}{dt} \times \vec{B}\right) \end{aligned} \tag{2.8}$$

using Maxwell equation

$$\vec{F} = \left(\alpha\frac{1}{2}\vec{\nabla}(\vec{E}^2) - \alpha\vec{E}\times(-\frac{d\vec{B}}{dt}) + \alpha\frac{d\vec{E}}{dt}\times\vec{B}\right) \tag{2.9}$$

The last two terms in the above expression are the time derivative of the Poynting vector (power per unit area passing through the surface). Since the power of laser beam is constant over time, this term goes to zero and force expression reduces to $\vec{F} = \left(\alpha\frac{1}{2}\vec{\nabla}(\vec{E}^2)\right)$ which is the gradient force.
The electric field for the Gaussian beam can be written as (detail discussion given in appendix A)

$$E(x,y,z) = E_0\frac{\omega_0}{\omega(z)}e^{-\frac{x^2+y^2}{\omega(z)^2}}e^{-\iota\frac{k(x^2+y^2)}{2\omega(z)^2}}e^{-\iota kz}e^{\iota\phi(z)} \tag{2.10}$$

here, $\omega(z) = \omega_0\sqrt{1+(2\tilde{z})^2}$. Using this intensity can be written as:

$$\begin{aligned} I(r) &= \langle S(r,t)\rangle_T \\ &= \langle E(r,t)\times H(r,t)\rangle_T \\ &= \left(\frac{2P_{peak/average}}{\pi\omega_0^2}\right)\left(\frac{1}{1+(2\tilde{z})^2}\right)e^{-\frac{2\tilde{r}^2}{1+(2\tilde{z})^2}} \end{aligned} \tag{2.11}$$

where $P = \frac{\pi\omega_0^2 n_w\epsilon_0 cE_0^2}{4}$ is the average power, n_w is the RI of medium (water), ω_0 is the spot-size *i.e.* Gaussian beam radius at focus, and NA is the numerical aperture of the objective and the reduced coordinates are given by: $\tilde{r} = \frac{r}{w_0}$, $\tilde{z} = \frac{z}{k\times w_0^2}$.
Force can be written as:

$$F = \alpha\left(\frac{1}{2}\nabla\left(\frac{2}{n_m\epsilon_0 c}I\left(r\right)\right)\right) \tag{2.12}$$

here, $\alpha = V\alpha_e$ is polarizability and α_e is polarizability per unit volume which can be expressed as (detail discussion given in appendix B):

$$\alpha_e = \frac{3\epsilon_0}{N}\left(\frac{m^2-1}{m^2+2}\right) \tag{2.13}$$

here, m is relative RI of the particle. This is known as the Clausius-Mossotti relation. In the field of the laser, the gradient force on an induced dipole is:

$$\begin{aligned} F_{gradient} &= 4\pi\epsilon_0 a^3 n_m^2 \left(\frac{m^2-1}{m^2+2}\right)\left(\frac{1}{2}\nabla\left(\frac{2}{n_m\epsilon_0 c}I\left(r\right)\right)\right) \\ &= \frac{2\pi n_w a^3}{c}\left(\frac{m^2-1}{m^2+2}\right)\nabla I\left(r\right) \end{aligned} \tag{2.14}$$

2.2.2 Scattering Force

In general, when unpolarized light interacts with an object, scattering can have two components one is due to reflection (which is polarized), and refraction (which is partially polarized) from the surface of the object and the other is due to diffraction from the rearrangement of the wave-front. The reflection and refraction of direct light are equal in all directions, whereas the diffraction pattern is predominately in the forward direction depending on the particle geometry [99].

The scattering force acting on the particle is due to the radiation pressure, and

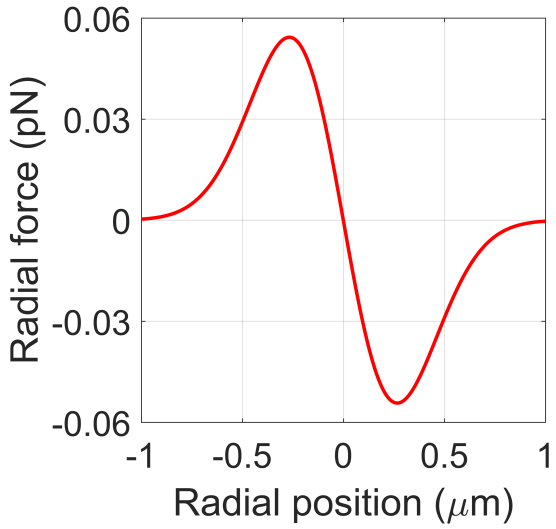

Fig. 2.2.: The plot of trapping force along radial direction at 100 mW average power under CW excitation for 40 nm polystyrene nanoparticle

depending upon the material properties, it can be absorbed and isotropically re-emitted by the particle. Consequently, two impulsive forces act on the particle one in the direction of propagation of the beam, and the other is in the opposite direction of the emitted photon. Since photon emission has a random direction

which results in a net force acting in the direction of propagation. Radiation pressure in terms of the electromagnetic wave can be written as:

$$P = \frac{\langle S \rangle}{c} = \frac{I(r)}{c} = \frac{F}{\sigma} \implies F = \frac{I(r)}{c}\sigma \tag{2.15}$$

here, σ is cross sectional area of particle which is [39, 94]:

$$\sigma = \frac{8}{3}\pi\,(ka)^4\,a^2\left(\frac{m^2-1}{m^2+2}\right)^2 \tag{2.16}$$

In the field of the laser, the scattering force on an induced dipole is along direction of propagation, which can be written as:

$$F_{scattering} = \frac{8\pi\,(ka)^4\,a^2}{3c}\left(\frac{m^2-1}{m^2+2}\right)^2 I\,(r) \tag{2.17}$$

Hence, we have computed the magnitude of the total force around the geometrical focus for nanoparticles.

Figure 2.2 shows the plot for the trapping force along the radial direction at 100

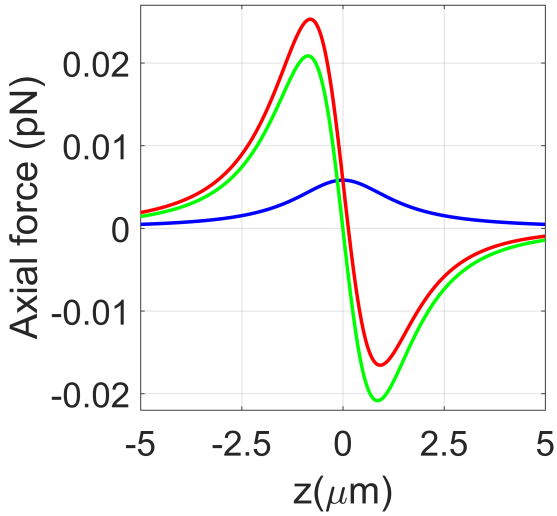

Fig. 2.3.: The plots of trapping force along the axial direction at 100 mW average power under CW excitation for 40 nm polystyrene nanoparticle. Color: green/blue/red curve corresponds to gradient/scattering/total force.

mW average power under CW excitation for 40 nm (radius) particle size. This force acting on the particle is enough to trap it for a considerable amount of time. In Figure 2.3 we describe the axial force, where the blue/green/red curves correspond to the scattering/gradient/total force acting on the particle along the axial direction at 100 mW average power under CW excitation for 40 nm (radius)

particle size. It can be seen that there is an asymmetry in peak to valley height about the axis for the total force acting on the particle. In contrast, the gradient force is symmetric about the axis. Consequently, this asymmetry in total force is owing to the scattering force acting on the particle.
The essential condition for trapping is the dominance of gradient force over scattering force, but not sufficient condition for stable trapping. The additional condition required for stable trapping is that the potential well due to gradient force should be much larger than kinetic energy [39] of the particles i.e., Boltzmann factor $exp\left(-\frac{U}{k_BT}\right) \ll 1$, where U is energy, k_B is the Boltzmann constant and T is temperature.

2.3 GO approximation

When $\lambda \ll$ d, the trapping phenomenon can be explained by using the ray optics approximation. In this approximation, the trapping depends upon the shape of the particle, as the focal spot dimensions are smaller than the dimensions of the particle; we will limit our discussion only to spherical particles. The core concept is that light carries momentum, and due to this change in momentum, a force experienced by the particle *i.e.* $F = Q\left(n_m P/c\right)$. Here, Q is defined as the trapping efficiency, and it is a dimensionless quantity [95]. The ray optics approximation is valid, where it is assumed that the beam is divided into many different rays.
When a ray is incident on the particle, it shows the reflection and refraction phenomenon due to change in the medium, as shown in figure 2.4. To conserve momentum, an equal and opposite force acts on the particle, which is responsible for dragging the particle inside the optical trap. The total force has two components [95, 96]:

$$F_{gradient} = \frac{n^w P_{ray}}{c} \times \left(R^{'} sin2\theta_i - \frac{T^{'2}\left(sin\left(2\theta_i - 2\theta_r\right) + R^{'} sin2\theta_i\right)}{1 + R^{'2} + 2R^{'} cos\left(2\theta_r\right)} \right) \tag{2.18}$$

$$F_{scattering} = \frac{n^w P_{ray}}{c} \times \left(1 + R^{'} cos2\theta_i - \frac{T^{'2}\left(cos\left(2\theta_i - 2\theta_r\right) + R^{'} cos2\theta_i\right)}{1 + R^{'2} + 2R^{'} cos\left(2\theta_r\right)} \right) \tag{2.19}$$

where n^w is the RI of the medium, P_{ray} is the average power of a single ray, c is speed of light, $R^{'}$ and $T^{'}$ are the Fresnel reflection and transmission coefficients for p- and s-polarized light (or, equivalently, the absolute coefficients for a circu-

larly polarized light) [100, 101]:

$$R_p = Abs\left(\frac{n^w cos\left(\theta_r\right) - n^p cos\left(\theta_i\right)}{n^w cos\left(\theta_r\right) + n^p cos\left(\theta_i\right)}\right)^2$$

$$R_s = Abs\left(\frac{n^w cos\left(\theta_i\right) - n^p cos\left(\theta_r\right)}{n^w cos\left(\theta_i\right) + n^p cos\left(\theta_r\right)}\right)^2$$

$$R' = \frac{R_p + R_s}{2} \tag{2.20}$$

$$T^{'} = 1 - R' \tag{2.21}$$

The scattering and gradient components of the total force acting on the particle along axial (Z) direction is given by:

$$F_{gradient,ray}\left(z\right) = -F_{gradient} sin\varphi \tag{2.22}$$

$$F_{scattering,ray}\left(z\right) = F_{scattering} cos\varphi \tag{2.23}$$

Total gradient and scattering force is summed over all the rays, can be expressed as:

$$F_{gradient/scattering} = \sum_{ray} F_{gradient/scattering,ray}\left(z\right) \tag{2.24}$$

In figure 2.4 the radius of particle chosen is 4 μm (for validity of GO approxima-

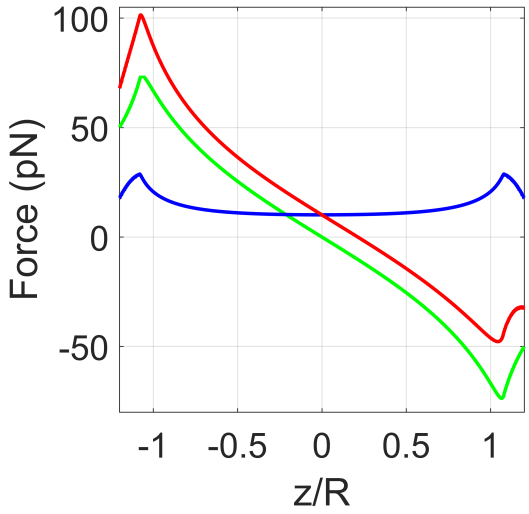

Fig. 2.4.: Plots of trapping force along the axial direction at 100 mW average power under CW excitation in GO regime for 4 μm polystyrene microsphere. Color: green/blue/red curve corresponds to gradient/scattering/total force.

tion), and we have shown axial force for the plane wave where the blue/green/red curves correspond to the scattering/gradient/total force acting on the particle at 100 mW average power under CW excitation. It can be seen that gradient force is dominating over the scattering force causing the particle to be dragged inside the potential well.

2.4 Generalized Lorenz Mie Theory

The Generalized Lorentz Mie Theory (GLMT) is a general theory applicable to all particle size limits. However, the particle should not be too small that it owns a bulk microscopic character or not so large because an infinite dimension does not exist. So the nature of particle should be chosen in a careful manner such that the method of separation variable can be used, as this method is a key factor to solve GLMT. G. Gouebest *et. al.* and a few other researchers are working on this since the last few decades and have made a significant contribution to this field. GLMT was formulated in 1978 [102]. Later in 1982, GLMT on-axis partial wave expansion for the spherical particle was studied by Bromwich formalism using the Gaussian beam [103], here particle considered was spherical, isotropic, homogenous and non-magnetic. To define the profile of the trapping beam, beam shape coefficients (BSCs) were defined, and these expressions were approximately similar to Lorentz Mie Theory (LMT), which was earlier reported by Kerker [104]. It has been proved that the LMT is a special case of GLMT. In 1985 existing Gaussian beam formulation was modified for low order Davis beam coefficient known as order L beam; here, L stands for the lower order of approximation [105]. Later L^{-} approximation was developed, which is solved for lower than the lowest order and compared with earlier developed models [106, 107]. The numerical evaluation by quadrature method to calculate the BSC was very time consuming, which takes more than 2-3 hours for one BSC. However, we have to calculate hundreds or thousands depending upon the particle size and other parameters. To reduce the computational time, the same formulation was done by the finite series method instead of the quadrature method (Appendix C shows the BSCs for Quadrature and finite series for the reference), and not much success was found concerning the time taken for evaluation [107]. Eventually, another method was discovered, which was valid for the Gaussian beam, and the advantage of this method was that it reduces the computational time to 30 sec for one BSC, and this approximation was termed as localized approximation or

interpretation. This method was developed based on the inspiration of the famous principle of localization of Van de Hulst [99, 107, 108]. Afterward, L, L^{-}, and localized approximations were compared, and it was concluded that "localized approximation can be used in the vast domain for the Gaussian beam without any error" [109]. All these formulations are well explained in GLMT book by G. Gouesbet [107]. The expression for on-axis force along the axial direction is [39, 94]:

$$F_{axial}^{GLMT}(z) = \left(\frac{n^{w}}{c}\right) \times \left(\frac{2P}{\pi w_0^2}\right) \times C_n^{pr}(z) \tag{2.25}$$

On-axis is a special case for GLMT where x=y=0 for which $g_{n,m}^{TM} = g_{n,m}^{TE} = g_n$ (BSC) and $C_n^{pr}(z)$ is the pressure cross section given by [109]:

$$C_n^{pr}(z) = \left(\frac{\lambda^2}{2\pi}\right) \sum_n \left[\left(\frac{2n+1}{n(n+1)}\right) |g_n|^2 S_{n,GLMT}^{(1)} + \left(\frac{n(n+2)}{n+1}\right) Re\left[g_n g_{n+1}^{*} S_{n,GLMT}^{(2)}\right]\right] \tag{2.26}$$

where, $S_{n,GLMT}^{(1)}$ and $S_{n,GLMT}^{(2)}$ corresponds to scattering and gradient force respectively.

$$S_{n,GLMT}^{(1)} = Re\left(a_n + b_n - 2a_n b_n^{*}\right) \tag{2.27}$$

$$S_{n,GLMT}^{(2)} = \left(a_n + b_n + a_{n+1} + b_{n+1} - 2a_n a_{n+1}^{*} - 2b_n b_{n+1}^{*}\right) \tag{2.28}$$

here, a_n and b_n are scattering coefficients which can be written as:

$$\begin{aligned} a_n &= \left(\frac{\psi_n(\alpha)\,\psi_n'(\beta) - m\psi_n'(\alpha)\,\psi_n(\beta)}{\varrho_n(\alpha)\,\psi_n'(\beta) - m\varrho_n'(\alpha)\,\psi_n(\beta)}\right) \\ b_n &= \left(\frac{m\psi_n(\alpha)\,\psi_n'(\beta) - \psi_n'(\alpha)\,\psi_n(\beta)}{m\varrho_n(\alpha)\,\psi_n'(\beta) - \varrho_n'(\alpha)\,\psi_n(\beta)}\right) \end{aligned} \tag{2.29}$$

Scattering coefficients depends on the spherical Bessel function of positive and negative half-integer order and Ricatti-Bessel functions [107, 110]:

$$\begin{aligned} \psi_n^1(x) &= \left(\frac{\pi}{2x}\right)^{\frac{1}{2}} J_{n+\frac{1}{2}}(x) \\ \psi_n(x) &= x \times \psi_n^1(x) \\ \varrho_n(x) &= \psi_n(x) + i(-1)^n \times \left(\frac{\pi x}{2}\right)^{\frac{1}{2}} J_{-n-\frac{1}{2}}(x) \end{aligned} \tag{2.30}$$

where the variable x is either $\alpha = k \times a$ or $\beta = m \times \alpha$.
So the force expression for GLMT becomes:

$$F_{axial}^{GLMT}(z) = \left(\frac{n^w}{c}\right) \times \left(\frac{2P}{\pi w_0^2}\right) \times \left(\frac{\lambda^2}{2\pi}\right) \sum_n \left[\left(\frac{2n+1}{n(n+1)}\right)|g_n|^2 S_n^{(1)} + \left(\frac{n(n+2)}{n+1}\right) Re\left[g_n g_{n+1}^* S_n^{(2)}\right]\right] \tag{2.31}$$

For calculating the BSC (g_n), we have chosen localized approximation (L- approximation) because this theory reduces computation time as mentioned in the above discussion and corresponding expression for the on-axis calculation is [110]:

$$g_n = iQexp\left[-iQ\left(\frac{\rho_n}{\omega_0}\right)^2\right] \times exp\left[ikz_0\right] \tag{2.32}$$

where $Q = \frac{1}{i+2\frac{z-z_0}{l}}$, $l = k \times \omega_0^2$ is the spreading length, and we have taken $z_0 = 0$ and $\rho_n = \left(\frac{n+1/2}{2\pi}\right)\lambda$.

2.5 Exact Mie Theory

Exact Mie Theory (EMT) is applicable for all size limits. Since the particle size is approximately equal to the wavelength ($d \approx \lambda$), we have employed EMT to calculate force and potential along axial direction only where the force expression is [111]:

$$F = \frac{n_w}{c} P_{peak/avg} Q \tag{2.33}$$

where Q is the trapping efficiency which can be written as a combination of Q_e (which includes the product of incident field to the scattered field) and Q_s (which includes all rest of the terms in Maxwell Stress Tensor (MST)):

$$Q = Q_e + Q_s \tag{2.34}$$

$$Q_e = \frac{4\gamma^2}{A} Re\left[\sum_n (2n+1) S_{n,EMT}^{(1)} G_n G_n'^*\right] \tag{2.35}$$

$$Q_s = -\frac{8\gamma^2}{A} Re\left[\sum_n \left(\frac{n(n+2)}{n+1} S_{n,EMT}^{(2)} G_n G_{n+1}^* + \frac{2n+1}{n(n+1)} S_{n,EMT}^{(3)} G_n G_n^*\right)\right] \tag{2.36}$$

where A is the fraction of the power which enters through the objective (at 800 nm, A=0.85), γ is the ratio of the objective focal length to the beam waist which

can be calculated as $\gamma = \sqrt{-\frac{Log(1-A)}{2*sin^2(\phi_{max})}}$; where ϕ_{max} is focusing angle with the beam axis. a_n and b_n are the Mie scattering coefficients (MSCs) [107]. $S^{(1)}_{n,EMT}$, $S^{(2)}_{n,EMT}$, and $S^{(3)}_{n,EMT}$ can be expressed as:

$$S^{(1)}_{n,EMT} = (a_n + b_n) \tag{2.37}$$

$$S^{(2)}_{n,EMT} = \left(a_n a^*_{n+1} + b_n b^*_{n+1}\right) \tag{2.38}$$

$$S^{(3)}_{n,EMT} = a_n b^*_n \tag{2.39}$$

G_n is the beam shape coefficient (BSC) which can be expressed as:

$$G_n = \int_0^{\phi_{max}} d\phi sin\phi \sqrt{cos\phi} e^{-\gamma^2 sin^2\phi + i\delta cos\phi} d^n_{1,1}(\phi) \tag{2.40}$$

$$G'_n = -i\frac{\partial G_n}{\partial \delta} \tag{2.41}$$

with $\delta = k \times z$ and $d^n_{1,1}(\phi)$ are the matrix elements of the finite rotations can be written as [112]:

$$d^n_{1,1}(\phi) = \frac{1}{(2n+1)}\left(\frac{P_{n-1}(cos\phi) - P_{n+1}(cos\phi)}{1 - cos^2\phi}(1 - cos\phi) + (2n+1)P_n(cos\phi)\right) \tag{2.42}$$

where, $P_j(cos\phi)$ is Legendre function of first kind. The MSCs represent the functions of the negative and the positive half integer spherical Bessel and Ricatti-Bessel functions:

$$\psi_n(x) = \left(\frac{\pi x}{2}\right)^{\frac{1}{2}} J_{n+\frac{1}{2}}(x) \tag{2.43}$$

$$\varrho_n(x) = \left(\frac{\pi x}{2}\right)^{\frac{1}{2}} J_{n+\frac{1}{2}}(x) + i(-1)^n \times \left(\frac{\pi x}{2}\right)^{\frac{1}{2}} J_{-n-\frac{1}{2}}(x) \tag{2.44}$$

here, $\psi'_n(\beta)$ and $\varrho'_n(\alpha)$ can be calculated as $\frac{d}{dx}\psi_n(x)|_{x=\beta}$ and $\frac{d}{dx}\varrho_n(x)|_{x=\alpha}$, respectively.

2.6 Time averaging of force and potential

The expressions for potential are obtained by numerical integration of the analytical expressions for force:

$$U_{radial}\left(r; z=0\right) = -\int F_{radial}\left(r; z=0\right) dr \tag{2.45}$$

$$U_{axial,gradient/scatter}\left(z; r=0\right) = -\int F_{axial,gradient/scatter}\left(z; r=0\right) dz \tag{2.46}$$

The average force acting on the particle over one duty cycle of the pulse is obtained by time-averaging the instantaneous force (or potential) acting on the particle:

$$\begin{aligned}\langle F_{pulsed}\rangle &= \frac{1}{T}\int_{-\frac{\tau}{2}}^{\frac{\tau}{2}} F_{pulsed} dt = F_{pulsed}\frac{1}{T}\int_{-\frac{\tau}{2}}^{\frac{\tau}{2}} dt \\ &= F_{pulsed} \times \left(\frac{1}{T} \times \tau\right) = F_{pulsed} \times (f \times \tau)\end{aligned} \tag{2.47}$$

Here, the instantaneous force is independent of time since the peak intensity is assumed to be constant throughout the pulse. If we ignore Kerr effect the instantaneous force is only linearly proportional to the peak intensity (as the terms involving $m = \frac{n^p}{n^w} = \frac{n_0^p}{n_0^w}$ do not depend on peak intensity) for which we have:

$$\begin{aligned}\langle F_{pulsed}\rangle &= constant \times I_{peak} \times (f \times \tau) \\ &= constant \times I_{average} \equiv F_{CW}\end{aligned} \tag{2.48}$$

Thus, trapping efficiency would be identical under pulsed and CW excitation, as observed under low power excitation for which the Kerr effect is negligible. On the other hand, if we take the Kerr effect into account, the term involved

$$m = \frac{n^p}{n^w} = \frac{(n_0^p + n_2^p \times I_{peak})}{(n_0^w + n_2^w \times I_{peak})} \tag{2.49}$$

depends on the peak intensity, introducing a nonlinear dependence on the peak power for the instantaneous force:

$$\langle F_{pulsed}\rangle \neq F_{CW} \tag{2.50}$$

and the obtained results are very different.

2.6.1 Excitation parameters

The peak-power/-intensity to average-power/-intensity ratio values for a commercial Titanium:sapphire oscillator is given by:

$$\frac{P_{peak}}{P_{average}} \equiv \frac{I_{peak}}{I_{average}} = \frac{1}{f \times \tau} \approx 10^5 \tag{2.51}$$

Here, τ and f are the pulse-width and repetition-rate (f , i.e. the inverse of the time lag between consecutive pulses, T) respectively. Such a definition assumes the peak-power/-intensity to be constant throughout the pulse, or in other words, the pulse has a rectangular temporal envelope. The explicit time dependence of the envelope of the pulse has been safely neglected here.

2.7 Optical Kerr effect

The Kerr effect is a phenomenon that is observed in optical materials, and it is an instantaneous process that occurs when a strong electric field (intense light) is applied to the optical materials. An applied electric field leads to a change in the refractive index of the material. Kerr effect is of two types, namely, electro-optic (DC Kerr effect) and OKE (AC Kerr effect). In 1875, Scottish physicist John Kerr first obtained the electro-optic Kerr effect also known as quadratic electro-optic (QEO) effect, in which a varying DC electric field is applied to the optical medium, and a change is perceived in the refractive index of the material [113, 114]. Thus, the material acts as a wave-plate that polarizes light in the desired direction. On the other hand, in 1961, Peter Franken *et al.* discovered OKE, which refers to nonlinear effects which arise when intense light propagates through a medium [115]. All materials that tend to modify the properties of the light beam, as it propagates through the medium, show OKE (nonlinear effects). Inside the propagating medium, these nonlinear effects are manifested as self-focusing, self-phase modulation and modulation instability, etc. The physical origin of this instantaneously occurring nonlinear response is due to the generation of a nonlinear polarization. The total polarizability can be written as a sum of linear and nonlinear terms: $P^T = P^L + P^{NL}$.

$$P^L = \epsilon_0 E \chi^{(1)} \tag{2.52}$$

$$P^{NL} = \epsilon_0 \left(\chi^{(2)} |E|^2 + \chi^{(3)} |E|^3 + \ldots \right) \tag{2.53}$$

Considering the system to be isotropic and homogenous in nature, the second-order nonlinear processes do not contribute to the polarization because of the inherent symmetry within the system [116]. To make it simple, the higher-order terms can be neglected and the above expressions can be rewritten as follows $P^T = \epsilon_0 E \chi^T = \epsilon_0 E \left(\chi^{(1)} + 3\chi^{(3)} |E|^2 \right)$ where $\chi^{(1)} = \epsilon^{(1)} - 1$ which implies $\epsilon = \epsilon^{(1)} + 3\chi^{(3)} |E|^2$. Using $n = \sqrt{\epsilon}$, refractive index term can be written as $n = \sqrt{\epsilon^{(1)} + 3\chi^{(3)} |E|^2}$. According to the standard definition of intensity ($I = 2 n_0 \epsilon_0 c |E|^2$), the refractive index can be expressed as follows:

$$n = n_0 \sqrt{1 + \frac{2 n_2 I}{n_0}} \approx n_0 \left(1 + \frac{1}{2} \times \frac{2 n_2 I}{n_0} + \ldots \right) \approx n_0 + n_2 I \tag{2.54}$$

where, n_2 is the nonlinear RI $\left(n_2 = \frac{3\chi^{(3)}}{4 n_0 \epsilon_0 c} \right)$ [116].

Parameters used in calculations

Table 2.1 lists the values of all the parameters which have been used in numerical simulations.

Parameters used	Values
Central wavelength	$800\ nm$
Speed of light	$3 \times 10^8 m/s$
Repetition rate (RR)	$76MHz$
Pulse width	$120fs$
RI of medium [117]	1.329
RI of polystyrene [117]	1.578
RI of CdS [117]	2.386
RI of ZnS [117]	2.313
RI of air [117]	1.00
2^{nd} order NRI of polystyrene [118]	$5.9 \times 10^{-17} m^2/W$
2^{nd} order NRI of water [119]	$2.7 \times 10^{-20} m^2/W$
2^{nd} order NRI of silica [120]	$2.48 \times 10^{-20} m^2/W$
2^{nd} order NRI of CdS [121]	$1.68 \times 10^{-18} m^2/W$
2^{nd} order NRI of ZnS [121]	$3.80 \times 10^{-19} m^2/W$
2^{nd} order NRI of air [122]	$3.01 \times 10^{-23} m^2/W$
Background permittivity [123]	2.5
Plasma frequency [123]	1.37×10^{16} Hz
Collision damping frequency [123]	3.226×10^{13} Hz
2^{nd} order NRI of silver NP [124]	$7.5 \times 10^{-20} m^2/W$
4^{th} order NRI of silver NP [124]	$5 \times 10^{-35} m^4/W^2$
6^{th} order NRI of silver NP [124]	$7.5 \times 10^{-51} m^6/W^3$
2^{nd} order NAC of silver NP [124]	$13.2 \times 10^{-14} m/W$
4^{th} order NAC of silver NP [124]	$9 \times 10^{-29} m^3/W^2$
6^{th} order NAC of silver NP [124]	$7 \times 10^{-44} m^5/W^3$

Tab. 2.1.: List of the parameters.

3 Force and potential on dielectric, hybrid, and hollow-core polystyrene nanoparticles using dipole approximation

3.1 Introduction

In this chapter, we address the issue considering nonlinear trapping force/potential on a variety of nanoparticles core type (CdS, ZnS, and polystyrene), core-shell type (CdS-ZnS, polystyrene-CdS) and hollow-core type (polystyrene and CdS) because they are dielectric and exhibit good nonlinear optical properties. We begin by first studying the effect of nonlinearity in CdS, ZnS, and polystyrene nanoparticle, followed by the study of nonlinear effects in core-shell (CdS-ZnS and polystyrene-CdS) nanoparticles. Further, we have explored the same in the hollow nanosphere of CdS and polystyrene, and here we observed clear evidence for the advantage of high repetition rate ultrafast pulsed excitation over CW excitation. In our knowledge, this is one of the first evidence for the advantage of using femtosecond laser over CW excitation in the trapping of a core-shell and hollow sphere particles.

Although the explicit nature of the force (and potential) differs with particle size, the essential physics remains unchanged and, our model nicely explains few puzzling observations that were found experimentally: 1) for larger colloidal particles (diameter $\geq 0.5\ \mu$m), if we keep on increasing the power under pulsed excitation, trapping is destabilized around few tens of milli-Watt power level (the particle first moves laterally toward trap center and then is ejected out of the trap axially, as observed by video microscopy) but this is not observed under CW excitation at similar power level [77, 80, 81] and 2) 100 nm (diameter) polystyrene beads were reported to be optically trapped for few seconds under pulsed excitation at power levels slightly over 30 mW but no stable trapping was observed at higher power level [82, 83].

The rigorous mathematical formulation of dipole approximation discussed in chapter 1. In 2015, Harada and Asakura [94] discussed the conditions for the

validity of the dipole approximation and then compared it with GLMT. They found tremendous agreement for both the theories within dipole regime and appropriate condition of validity is $d = 2a \leq \frac{\lambda}{10}$ (here d is the diameter and a is the radius of the particle). Therefore, depending on the choice of the wavelength of the trapping beam, the range of particle changes for the validity of dipole approximation. Although GLMT is a more rigorous method for estimating trapping force (or potential), we show that the simpler theoretical treatment under dipole approximation yields very accurate estimates of trapping force (or potential) reported in earlier experiments. Also, in this size limit, Rayleigh scattering expression is more useful as there is, in principle, no restriction on the NA of the focusing objective, which is often a problem to deal with in GLMT. For realistic estimation, we consider typical values for commercial oil-immersion objectives as NA=1.4 & NA=1.3 (with typical refractive index (RI) of immersion oil being 1.515); these values are 0.924 & 0.858 and 1.228 & 1.140 in air and water, respectively.

3.2 Core-type nanoparticles

All the parameters used in numerical simulations are listed in table 2.1. Nonlinear optical effects arise when electronic motion in a strong electromagnetic field cannot be considered harmonic. Here we are incorporating nonlinear effects into account through the OKE, which is rigorously discussed in chapter 2. Thus, the intensity-dependent nonlinear refractive indices of both polystyrene and water can be expressed as:

$$n^{w/p} = n_0^{w/p} + n_2^{w/p} * I\,(r, z) \tag{3.1}$$

The values of n_2^w and n_2^p were reported at 532 nm and we ignore the wavelength dependence of these quantities. This is a reasonable approximation at 800 nm, as the difference is negligible. The second order nonlinear RI for water is very small. The magnitudes of the nonlinear terms ($n_2^{w/p} * I$) with respect to the linear terms ($n_0^{w/p}$) around geometric focus, $I\,(r = z = 0) = \frac{2P}{\pi w_0^2}$ under tight-focusing condition for NA equal to 1.4 is negligible. The peak intensity at 100 mW average power is approximately $2.27 \times 10^{12}\ W/cm^2$, which is less than the femtosecond optical breakdown of dielectric ($10^{14}\ W/cm^2$) [125]. Thus, no dielectric breakdown occur at 100 mW average power.

Under CW excitation, the terms $n_2^{p/w} * I_{average}$ are much smaller than $n_0^{w/p}$ such that $n^{w/p} \approx n_0^{w/p}$; for example, even at average power level as high as 100 mW the

values for $n_2^{p/w} * I_{average}$ are only 1.3x10^{-5} and 6.0x10^{-9} for polystyrene and water respectively. Contrary to this, under pulsed excitation, $n_2^p * I_{peak}$ is non-negligible compared with n_0^p ; for example, at 100 mW average power $n_2^p * I_{peak} \approx 1.4$ which is comparable with $n_0^p = 1.578$. However, even at this high peak intensity, $n_2^w * I_{peak}$ is only about 6.6×10^{-4}. So $n^w \approx n_0^w$ for all excitation conditions and non-linear beam propagation effects inside water can be ignored ($k = \frac{2\pi * n^w}{\lambda} \approx \frac{2\pi * n_0^w}{\lambda}$).

Since nonlinear optical effects are instantaneous, to include OKE under pulsed excitation, we first calculate the instantaneous force (or potential), which readily yields the time-averaged force (or potential) just after multiplication by $(f * \tau)$. ***The NA is chosen as 1.4, average power 100 mW under both CW and pulsed excitation, and the particle radius as 40 nm unless otherwise mentioned.***

3.2.1 Along radial direction

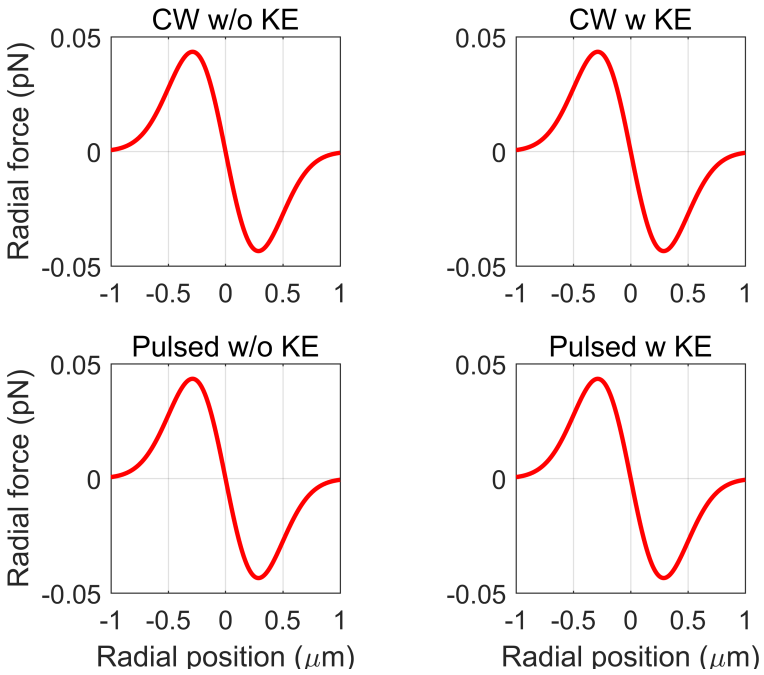

Fig. 3.1.: Plots of trapping force along radial direction for silica nanoparticles under CW and pulsed excitation ignoring and including OKE.

Figures 3.1 and 3.2 show the trapping force along radial direction for silica and polystyrene nanoparticles respectively. It can be observed that including OKE under both CW and pulsed excitations for silica nanoparticle does not show any change in nature and magnitude of the force acting on the particle from the case without including OKE. However, for polystyrene nanoparticles, the inclusion of OKE increases the maximum of (radial component) the gradient force under

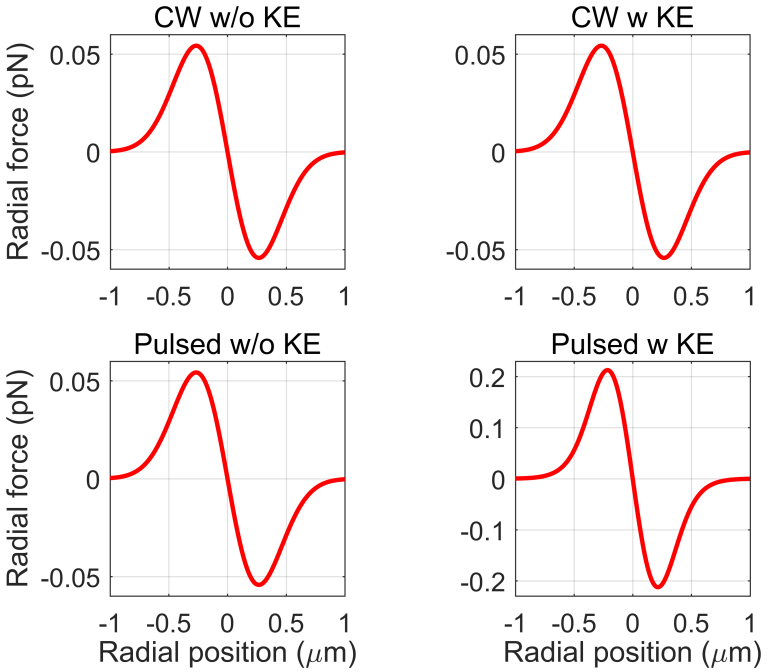

Fig. 3.2.: Plots of trapping force along radial direction for polystyrene nanoparticles under CW and pulsed excitation ignoring and including OKE.

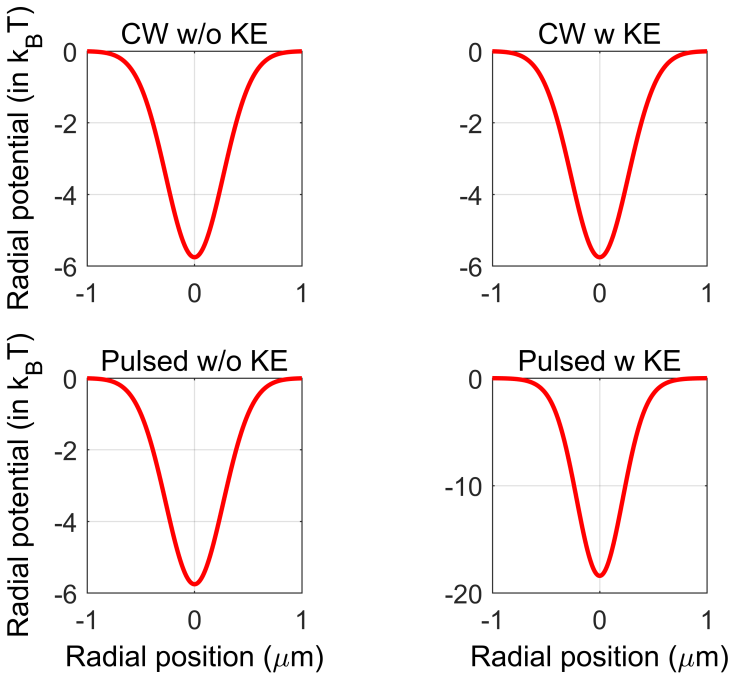

Fig. 3.3.: Plots of trapping potential along radial direction for polystyrene nanoparticles under CW and pulsed excitation ignoring and including OKE.

pulsed excitation by a factor of ~ 4. In addition, the maxima shift a bit from the classical turning points ($r = \pm\frac{w_0}{2}$). As a result of OKE, the lateral trap becomes more stable (~ 3 times), which is evident from the corresponding plots

of trapping potential along the radial direction, as shown in figure 3.3.
Also, in case of polystyrene, a significant change in order of magnitude of force and potential under pulsed excitation with OKE, while no significant change is observed for silica nanoparticles because the nonlinear RI for silica is 1000 times smaller than polystyrene, therefore, nonlinear RI does not contribute significantly, can be seen from comparison of figures 3.1, 3.4 and figures 3.2, 3.5.

3.2.2 Along axial direction

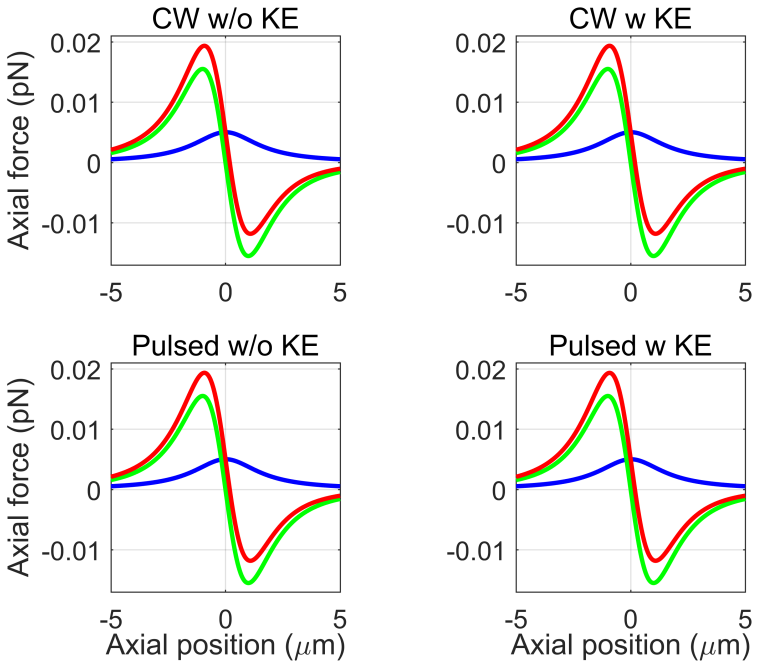

Fig. 3.4.: Plots of trapping force along axial direction for silica nanoparticles under CW and pulsed excitation ignoring and including OKE. Color: blue/green/red curve corresponds to scattering/gradient/total force.

Figures 3.4 and 3.5 show the trapping force along axial direction for silica and polystyrene nanoparticles respectively; here, the blue/green/red curves correspond to scattering/gradient/total force. Like before, silica does not show any change in the nature of the curve or magnitude of force/potential with the inclusion of the OKE. Whereas for polystyrene, as before, incorporation of OKE increases the maximum of (axial component) the gradient force under pulsed excitation by a factor of ~ 4.2.However, the maximum of the scattering force is increased by a factor of ~ 23.4. Here, also the maxima shifts a bit from the classical turning points for the gradient force ($z = \pm\frac{kw_0^2}{2\sqrt{3}}$) and away from the focal plane for the scattering force ($z = 0$). The corresponding plots of trapping potential along axial direction are shown in figure 3.6 ; here, the blue/green/red

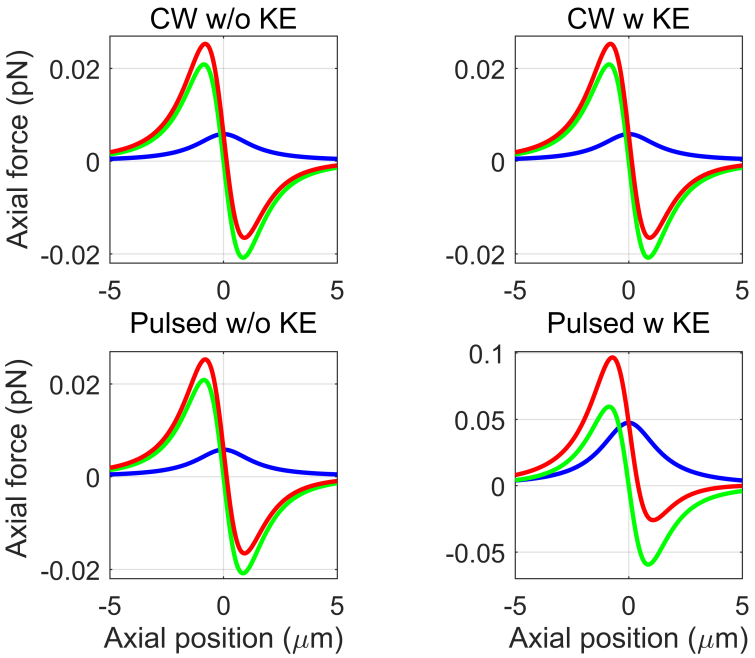

Fig. 3.5.: Plots of trapping force along axial direction for polystyrene nanoparticles under CW and pulsed excitation ignoring and including OKE. Color: blue/green/red curve corresponds to scattering/gradient/total force.

curves correspond to scattering/gradient/total potential.

The nonlinear RI of the water cannot be neglected in comparison to silica

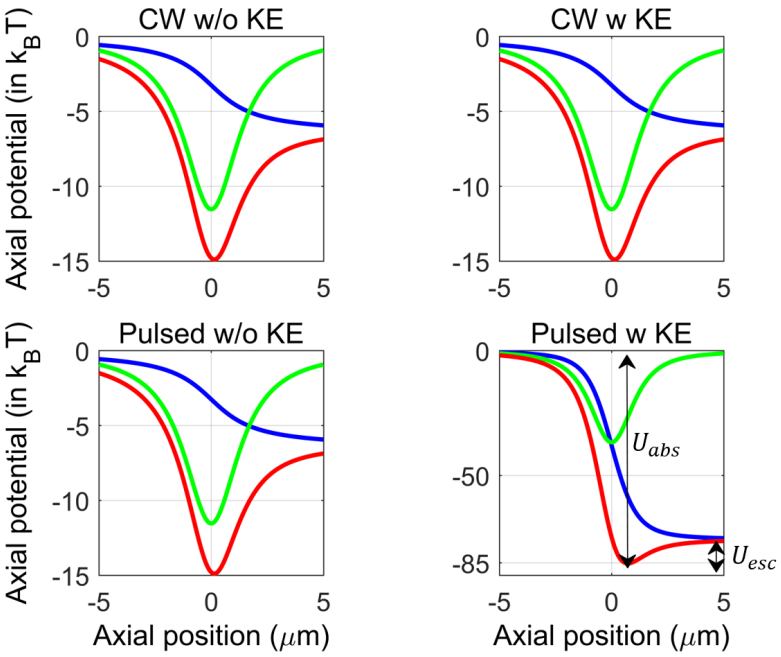

Fig. 3.6.: Plots of trapping potential along axial direction for polystyrene nanoparticles under CW and pulsed excitation ignoring and including OKE.Color: blue/-green/red curve corresponds to scattering/gradient/total potential.

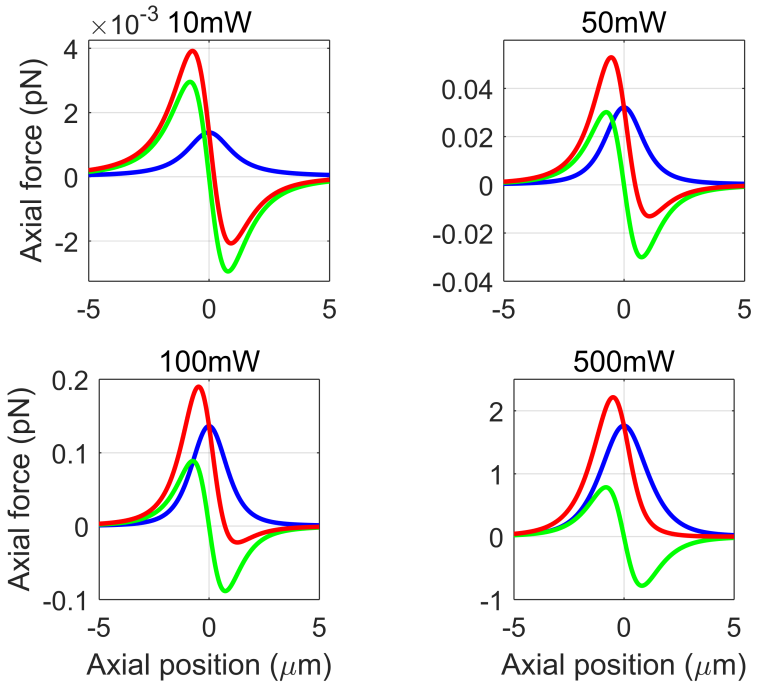

Fig. 3.7.: Plots of trapping force along axial direction at different average power under pulsed excitation including OKE.Color: blue/green/red curve corresponds to scattering/gradient/total force.

nanoparticles as they are of a similar order of magnitude. The nonlinear effects of silica become significant at very high average power. The pulse-chirping experiment on silica microspheres [77] did not reveal this owing to the very low Kerr nonlinearity of silica. Hereafter, all the simulations are done for polystyrene nanoparticles in this chapter, unless otherwise mentioned.

3.2.2.1. Dependence on power:

Along radial direction, the trapping force and potential increases with increasing average power because only gradient force contributes, however, along axial direction there is the contribution from both scattering and gradient forces, and the nature of total force curve changes along the axial direction. From now on, we will restrict our discussion to trapping along axial direction under pulsed excitation only for which the Kerr effect significantly modulates the potential. In figure 3.6, the longer double-headed arrow corresponds to the absolute depth of the global potential minimum, U_{min} . However, the potential well is highly asymmetric, and the smaller double-headed arrow indicates the potential barrier for the particle to come out of this potential well, U_{esc} along beam propagation

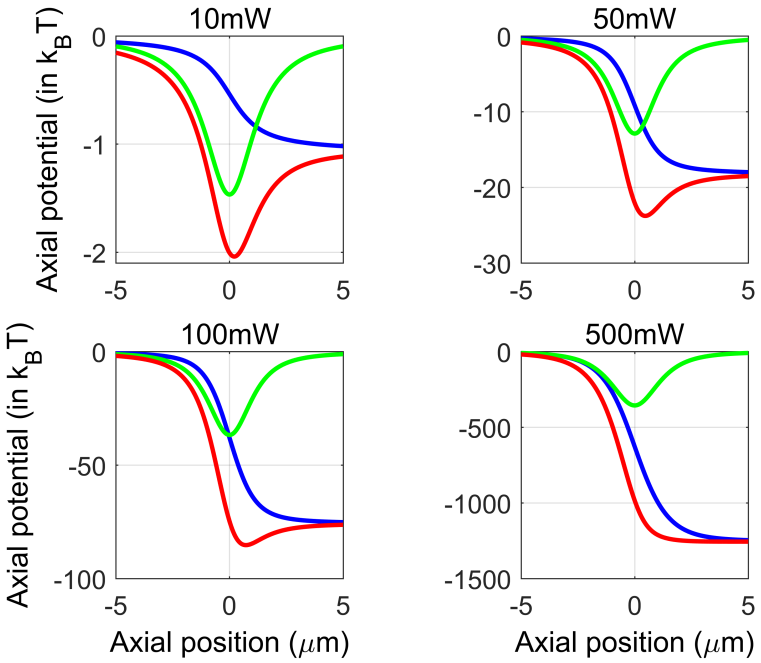

Fig. 3.8.: Plots of trapping potential along axial direction at different average power under pulsed excitation including OKE.Color: blue/green/red curve corresponds to scattering/gradient/total potential.

direction (*i.e.* positive z-direction). Introduction of OKE increases U_{min} by a factor of ~ 15.7 while it increases U_{esc} by a factor of ~ 1.1 only.

Upon increasing the power, a point is reached when there is no restoring force along beam propagation direction; as shown is figure 3.7; where, the blue/-green/red curves correspond to scattering/gradient/total force, which is already reached at 500 mW power. At this power level, although U_{min} is very high, $U_{esc} = 0$ *i.e.* the axial trapping potential becomes unbound as depicted in figure 3.8.

Figures 3.9 and 3.10 show the 3D plots of trapping force and potential along axial direction at different average power, which shows a significant change in potential well while including OKE. So, the particle is initially dragged towards the trap center but eventually propelled along axial direction which is consistent with the well-known observation of axial ejection for larger colloidal particles (diameter ≥ 0.5 μm) upon increasing the power under pulsed excitation only [77, 80, 81]. Therefore, the more relevant parameter to quantify the trapping efficiency is U_{esc} and not U_{min} .

To have a better insight into the nature of these two types of potential, U_{min} and U_{esc} , we plotted them separately with increasing power shown in figure 3.11. U_{min} increases monotonically with power, but U_{esc} increases reaching a maximum

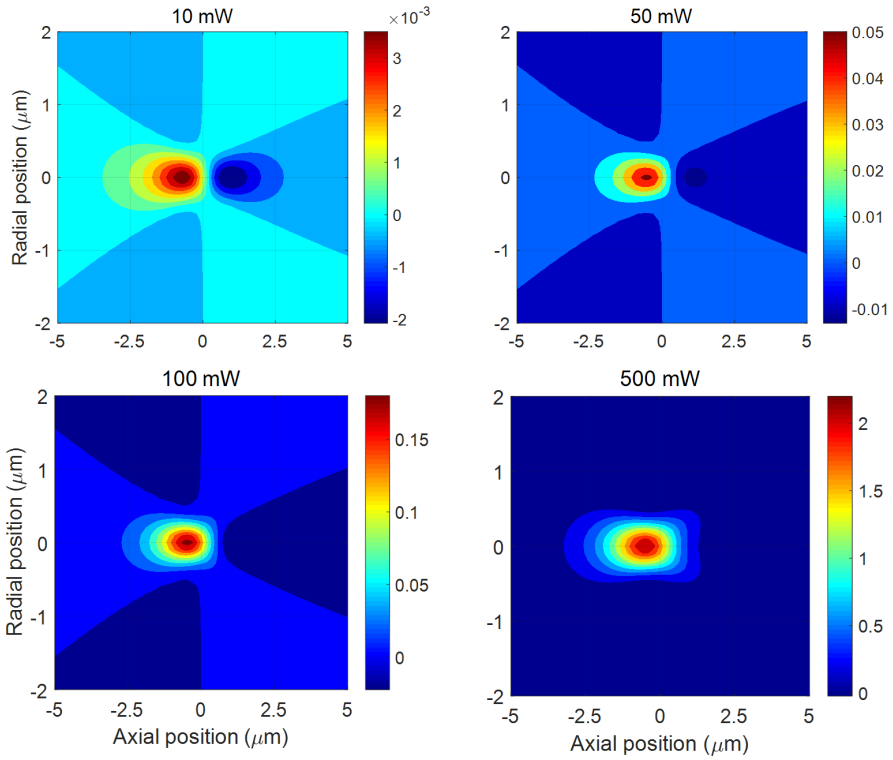

Fig. 3.9.: 3D plots of trapping force (total force) along axial direction at different average power under pulsed excitation including OKE.

before dropping off. This means there is an optimal average power corresponding to which the trap is most stable. This optimal power is about 150 mW for the 40 nm particle when using a 1.4 NA objective. This is quite a remarkable observation as we can theoretically predict the optimal excitation parameters for having the most stable dipole trap. Figure 3.12a shows the variation of the shift in axial equilibrium position with increasing power; we note that the most stable trap around 150 mW corresponds to a trapping center away from the geometrical focus (z=0). Figure 3.12b shows the gradient and scattering potential at the location corresponding to this axial equilibrium position, we have noticed an initial dominance of the gradient potential which, upon increasing power, is reversed around 40 mW (zoomed within inset); also note that the gradient potential goes through a maximum around 250 mW. Thus, contrary to common understanding, the trap is neither destabilized due to pushing the particle away from focus by scattering potential, nor it is stabilized by maximizing gradient potential alone. Figure 3.12c, shows the absolute trapping potential at the the axial equilibrium position (U_{min}) along with the asymptotic value of the scattering potential ($U_{axial,scatter}\,(z \to \infty)$). The separation (zoomed within inset) between these two potential is maximum around 150 mW (when the trap is most stable), and they

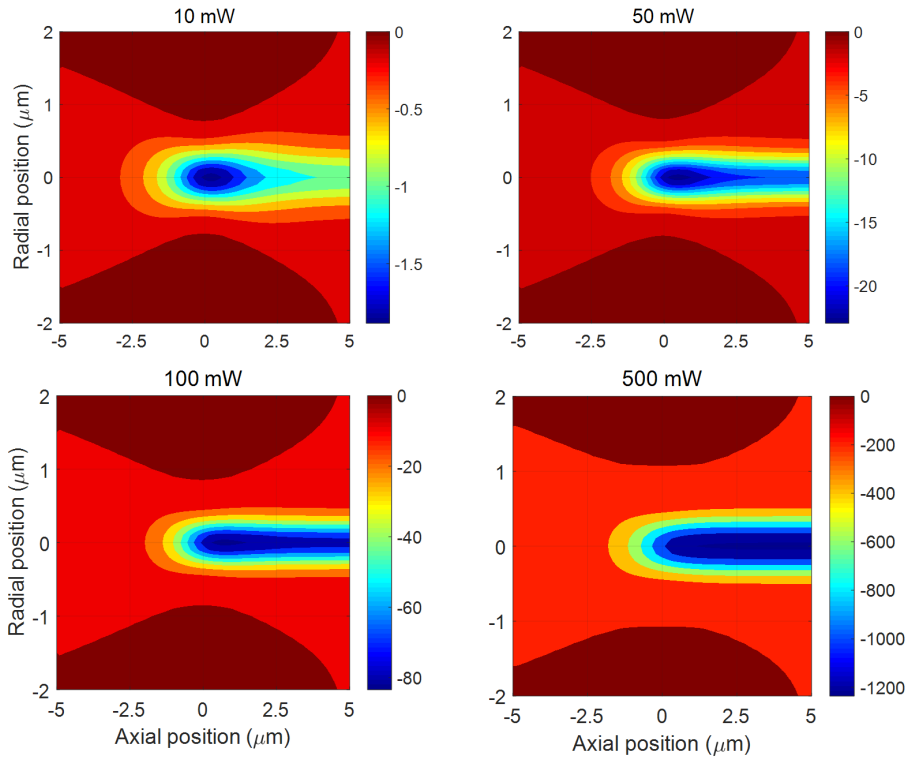

Fig. 3.10.: 3D plots of trapping potential (total potential) along axial direction at different average power under pulsed excitation including OKE.

are merging near 400 mW (when the potential is unbound). Thus, trapping efficiency is indeed subtly controlled by a delicate balance between these potentials. The above results indicate that for particles having linear refractive indices less than the surrounding medium, which is 'repelled' by single beam trapping potential, there is a possibility of observing OKE assisted stable trapping (depending on the strength of Kerr nonlinearity). We have noted an earlier theoretical work in literature [13] that discussed the role of OKE, resulting only in a slight increase in trapping force under CW excitation. However, for an idealized nanoparticle with quite high Kerr nonlinearity ($1.8 \times 10^{-12}\, m^2W^{-1}$) and without any detailed analysis on the exact nature of trapping force and potential.

3.2.2.2. Dependence on NA

Figure 3.13 indicates that U_{esc} is decreased by a factor of about 1.5 when the NA is switched from 1.4 to 1.3; the power corresponding to maxima of U_{esc} is also increased but only slightly (140 mW to 150 mW). For stable trapping, a 'rule of thumb' is that a minimum of $10k_BT$ barrier height is required, so the trap becomes thermally unstable when NA is changed to 1.3.

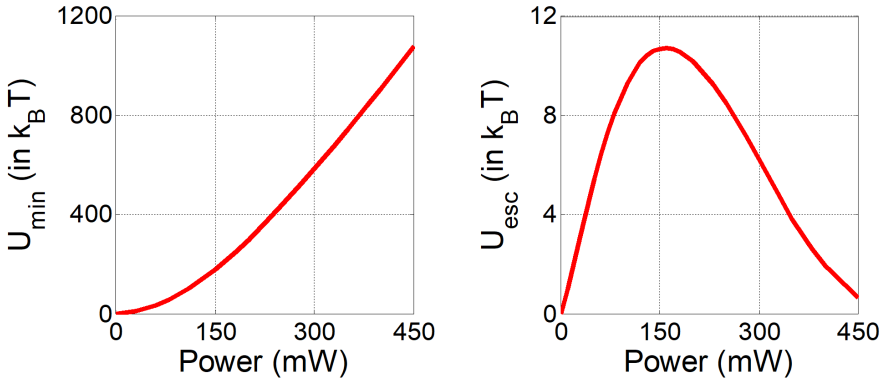

Fig. 3.11.: Plots of the absolute depth of the trapping potential (left) and escape potential (right) along axial direction at different average power levels.

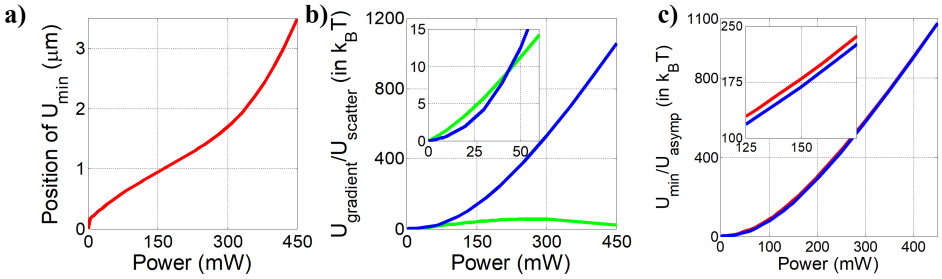

Fig. 3.12.: Plots of a) position of the minima for absolute trapping potential along axial direction, b) the gradient and the scattering potential (green and blue lines, respectively) corresponding to this minima at different average power levels, and c) absolute depth of the trapping potential and the asymptotic scattering potential (red and blue lines, respectively) for the same.

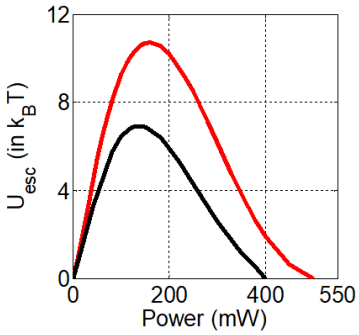

Fig. 3.13.: Plots of the escape potential with 1.4 NA (red line) and 1.3 NA (black line) at different average power levels.

3.2.2.3. Dependence on particle size

It is interesting to explore the optimal average power and the corresponding U_{esc} for particles with different radius (each satisfying the criterion, $d = 2a \leq \frac{\lambda}{10}$), for example, 40 nm and 35 nm without changing the focusing condition (NA$= 1.4$

). As shown in the left panel of figure 3.14, while the optimal average power is 150 mW for the 40 nm particle, it is around 500 mW for the 35 nm particle, which means it requires more power for stable trapping of the smaller particle. The maximum height of the potential barrier increases by a factor of about 2.6 for the smaller particle, which means the smaller particle can be trapped with more stability. This is a very promising finding considering the direct trapping of dielectric nanoparticles. Also, the threshold power ($U_{esc} = 0$) decreases with increasing particle size. A small change in particle size results in a significant change in the optimal average power level which is a consequence of higher power dependence of force on the radius of the particle.
Although 50 nm polystyrene beads do not strictly satisfy the dipole limit, we are still intrigued to find the optimal power level for such particles. As shown in right panel of figure 3.14, the optimal power is $\sim$ 40 mW for which U_{esc} is just about $2.7k_{\mathrm{B}}T$; this means the particle is trapped but only for a while (considering the 'rule of thumb' of minimum $10k_{\mathrm{B}}T$ barrier height for stable trap). All these quantitatively agree with the experimental findings.

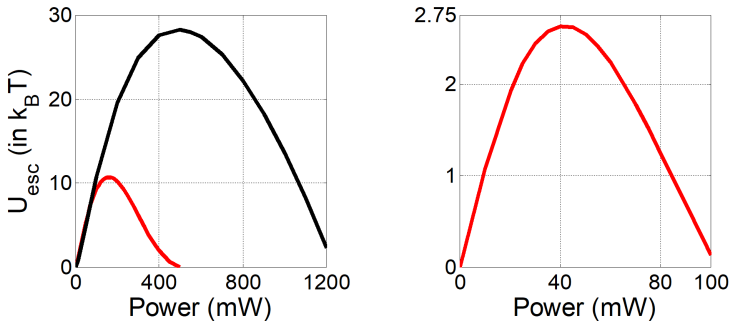

Fig. 3.14.: Left: Plot of escape potential on an 40 nm particle (red line) and on a 35 nm particle (black line) at different average power levels. Right: The same for a 50 nm particle.

3.2.2.4. Dependence of RI with NA, particle size

From the above discussion, it can be concluded that nonlinear RI for water can be neglected. Thus, here onward, simulations have been done by ignoring OKE under CW excitation and including OKE under pulsed excitations. Also, if RI value is negative which implies that material is meta-material.

CW excitation

Figure 3.15 shows the trapping force and potential curve for 40 nm (radius) polystyrene particle under CW excitation. Figure 3.15a shows the trapping force around the geometric focus for both axial ($r = 0$) and radial ($z = 0$) directions; here, green/blue/red curves correspond to gradient/scattering/total force along axial direction and black curve corresponds to gradient or total force along radial direction. Figure 3.15b shows the 3D force curve, and Figure 3.15c shows the corresponding potential, where U_{abs} represents the absolute height of the potential well whereas U_{esc} represents the escape potential.

To study the behavior of trapping force depending on particle RI, Figure 3.16

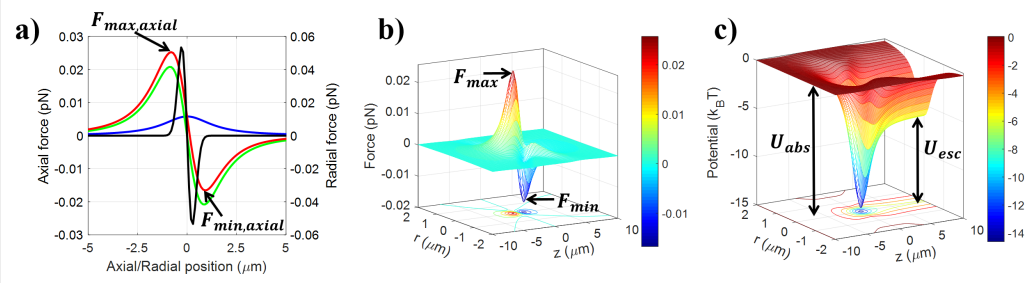

Fig. 3.15.: Plots of trapping force and potential for under CW excitation for fixed NA=1.4 a) forces along radial as well as axial direction around geometric focus, b) 3D force and c) corresponding potential.

shows the plots of trapping force for 40 nm particle along axial and radial direction under CW excitation, and RI of the particle equal to 1.32, 1.33, and 1.34 respectively; here, green/blue/red curves correspond to gradient/scattering/total force along axial direction, and black curve corresponds to gradient or total force along radial direction. The medium is considered to be water having RI equal to 1.33. Figure 3.16a shows the trapping force for $n_p < n_w$, where the particle experiences a repulsive force. Figure 3.16b shows the force curve for $n_p = n_w$, the particle does not experience any net force acting on it. Figure 3.16c shows the force for $n_p > n_w$, where the particle experiences an attractive force. It can be observed that under CW excitation, there is a sudden change in the nature of the force curve from repulsive to attractive as the RI of particle changes. Figure 3.17 shows the plots of trapping force maxima ($F_{max,axial}$) and minima ($F_{min,axial}$) shown using an arrow in figure 3.15a versus particle RI along the axial direction under CW excitation for fixed NA=1.4. To confine the particle within the optical trap, the force must be attractive and $F_{max,axial}$ >0 and $F_{min,axial}$ <0 are the required conditions. From figures 3.17a and 3.17b, it can be observed that for all sized particles if RI lies between 0 to $\pm$ 1.33, $F_{max,axial}$ <0 and $F_{min,axial}$

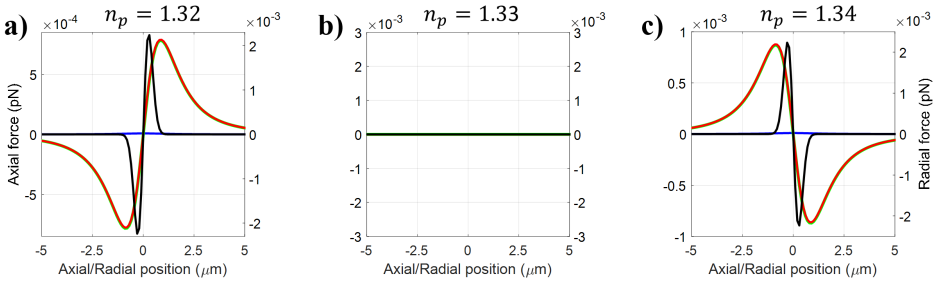

Fig. 3.16.: Plots of trapping force for along axial and radial direction under CW excitation for fixed NA=1.4 and particle RI a) 1.32, b) 1.33, and c) 1.34. Color: green/blue/red curve corresponds to gradient/scattering/total force along the axial direction, and black curve corresponds to gradient or total force along the radial direction.

>0, which implies that force is repulsive; here, red/green/blue/black curve corresponds to 10/20/30/40 nm particle size. Consequently, the particle cannot be trapped within this RI range under CW excitation as shown in Figure 3.17a inset. For n_p =± 1.33, the particle RI is balanced by medium RI and $F_{max,axial}$ = $F_{min,axial}$ =0 which results in, no net force acting on the particle as shown in Figure 3.17 (marked by A and B). The $F_{max,axial}$ >0 is true only if n_p >1.33, whereas $F_{min,axial}$ <0 for 10 nm, 20 nm and 30 nm particle size, and this satisfies both the required condition for the attractive force acting on the particle. Quite interestingly, there is a small deviation in the nature of force curve with an increase in particle size, for example, 40 nm particle, RI range fulfills only one condition, i.e., $F_{max,axial}$ >0. $F_{min,axial}$ <0 is valid only for the certain range i.e. ± 1.33< n_p <± 3.49 which results in an attractive force in the specific range of RI of the particle. However, within this range of RI, first ($F_{min,axial}$) decreases then increases, which implies that first it stabilizes the trap (a balance between both scattering and gradient force) and further increase in RI destabilizes the trap (scattering force dominates over gradient force) and eventually it becomes unbound (gradient force contribution is negligible compared to scattering force) for n_p >± 3.49. From here we can observe that particle having RI ± 2.04, can be trapped most stable at 100 mW average power under CW excitation at fixed NA=1.4. From the figure 3.17a inset, it can be observed that trapping force maxima of RI range from $0 < n_p < 1.33$ shows a similar trend for 10 nm, 20 nm, and 30 nm sized particles; however, a slight deviation in the nature of the curve for 40 nm sized particle. This is because for small-sized particles, within this RI regime, gradient force dominates over scattering force, consequently, decreasing RI monotonically decreases $F_{max,axial}$. However, for the 40 nm particle, decreasing

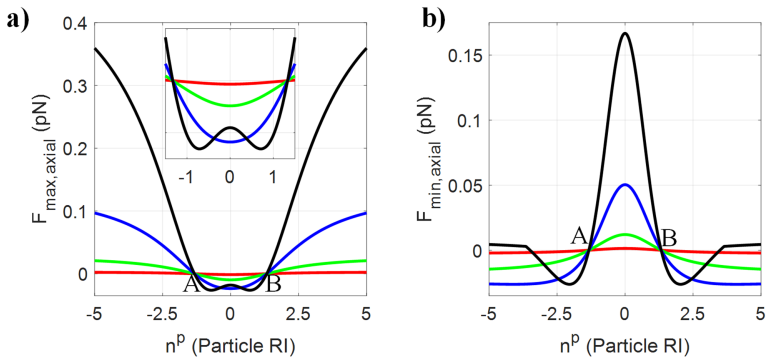

Fig. 3.17.: Plots of trapping force a) maxima, and b) minima (shown in figure 15) versus particle RI for a different particle size under CW excitation for fixed NA=1.4. Color: red/green/blue/black curve corresponds to 10/20/30/40 nm particle size.

RI monotonically decreases $F_{max,axial}$ and reaches to a minimum value of $F_{max,axial}$. The RI value corresponds to this minimum of $F_{max,axial}$ is the value till gradient force dominates over scattering force. Further decrease in the RI value shows a reverse trend for $F_{max,axial}$ because scattering dominates over gradient force, and a similar trend observed in negative RI range as well.

Thus, depending upon the range of RI, the nature of forces can be characterized to be attractive or repulsive, and we have broadly categorized them into four regimes: repulsive, intermediate (transition from repulsive to attractive), attractive, and unbound forces. The range of RI that characterizes all these regimes strongly depends upon the values of NA and average power. In the repulsive regime, the particle experiences an outward force that pushes it away from the trap. In the intermediate regime, it experiences both attractive and repulsive forces, and the stability of the trap depends upon their relative magnitudes. The attractive forces are responsible for dragging the particle towards the trap. The unbound regime, complete destabilization of the trap due to the increased scattering forces. Figure 3.18 shows the plot of trapping force maxima ($F_{max,axial}$) and minima ($F_{min,axial}$) versus varying particles RI along the axial direction under CW excitation for a 40 nm particle. From table 3.1, it can be observed that an increase in NA leads to increasing the upper bound of the RI range, thereby increasing the attractive force RI range. However, the repulsive force RI range remains unchanged. The value of optimal RI corresponding to optimal (stable) trap is also increased for fixed average power and particle size. A similar effect can be observed for other sized particles as well, and a decrease in particle size results in shifting RI values

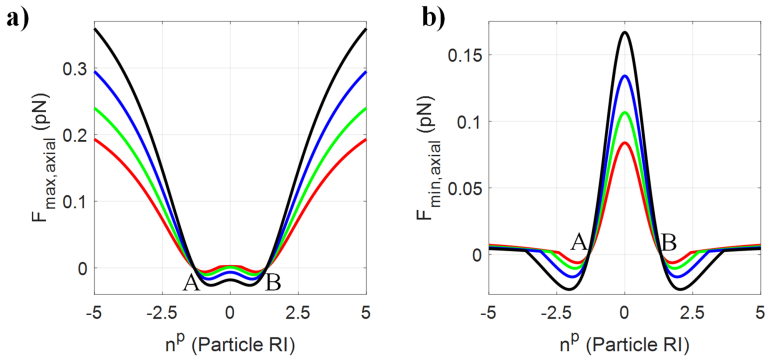

Fig. 3.18.: Plots of trapping force a) maxima, and b) minima (shown in figure 15) versus particle RI for different NA under CW excitation. Color: red/green/blue/red curve corresponds to 1.1/1.2/1.3/1.4 NA.

towards higher RI.

NA	Repulsive force	Attractive force	Unbound force	Optimal
1.1	$0 < n_p > 1.33$	$1.33 < n_p < 2.34$	$n_p \geq 2.34$	$n_p = 1.74$
1.2	$0 < n_p > 1.33$	$1.33 < n_p < 2.61$	$n_p \geq 2.61$	$n_p = 1.83$
1.3	$0 < n_p > 1.33$	$1.33 < n_p < 2.98$	$n_p \geq 2.98$	$n_p = 1.92$
1.4	$0 < n_p > 1.33$	$1.33 < n_p < 3.49$	$n_p \geq 3.49$	$n_p = 2.04$

Tab. 3.1.: RI limits variation with NA, for repulsive, attractive, unbound, and optimal (stable trapping) values under CW excitation.

NA	Repulsive force	Attractive force	Unbound force	Optimal
1.1	$-1.33 < n_p > 0$	$-2.34 < n_p < -1.33$	$n_p \leq -2.34$	$n_p = -1.74$
1.2	$-1.33 < n_p > 0$	$-2.61 < n_p < -1.33$	$n_p \leq -2.61$	$n_p = -1.83$
1.3	$-1.33 < n_p > 0$	$-2.98 < n_p < -1.33$	$n_p \leq -2.98$	$n_p = -1.92$
1.4	$-1.33 < n_p > 0$	$-3.49 < n_p < -1.33$	$n_p \leq -3.49$	$n_p = -2.04$

Tab. 3.2.: RI limits variation with NA, for repulsive, attractive, unbound, and optimal (stable trapping) values under CW excitation for meta-materials.

On comparison of tables 3.1 and 3.2, it can be seen that the range of RI for repulsive, attractive, and unbound forces are similar for meta-materials, and optimal trap values for fixed NA is also same in magnitude.

It is a bit difficult to get optimal RI values for particle size less than 30 nm because decreasing particle size results in shifting the stable trap RI towards higher values. From figure 3.19, it can be seen that after a particular value of particle RI, polarizability saturates, consequently, it is difficult to optimize RI value under CW excitation for small particle size; here, blue/green/red/black curves correspond to 10 nm/20 nm/30 nm/40 nm particle size.

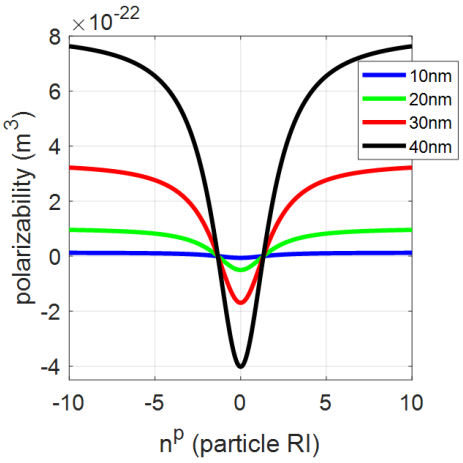

Fig. 3.19.: Plots of the polarizability against particle RI for different particle size under CW excitation.

From the above discussion, it can be observed that under CW excitation, the force is directly proportional to the average power, and any change in average power leads to a change in the order of magnitude while the nature of force curve remains the same which implies that upper and lower bound of RI range remains the same for repulsive, attractive, unbound, and stable trap forces for different average power at fixed particle size and NA. Irrespective of all the parameters, repulsive force RI limit remains the same under these conditions, however upper bound of attractive and unbound regimes increases with decreasing particle size.

Pulsed excitation

Under pulsed excitation, we have considered pulse width as 120 fs and repetition rate as 76 MHz. OKE can be taken into account using two different methods, which are described very rigorously in the appendix D. In the following simulations, we have used the second method in which nonlinearity is incorporated through a modified RI, which can be written as: $n^p = n_0^p + n_2^p I$; where n_0 is linear RI and n_2 is second order nonlinear RI of the particle.

Figure 3.20 shows the trapping force and potential curve for 40 nm polystyrene particle under pulsed excitation. Figure 3.20a shows the trapping force around the geometric focus for both axial ($r = 0$) and radial ($z = 0$) directions. Including nonlinearity gives a significant change in the order of magnitude as well as the nature of force curves, as compared to CW excitation at similar average power. Figure 3.20b shows the 3D force curve, and figure 3.20c shows the corresponding potential.

Nonlinearity plays a crucial role, with an increase in average power. To compare

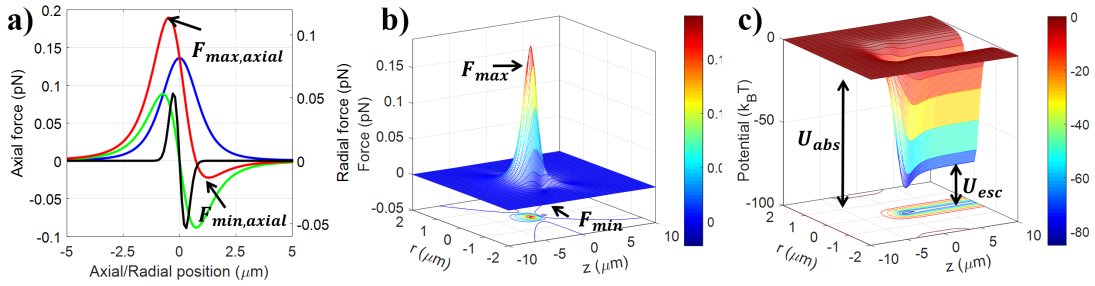

Fig. 3.20.: Plots of trapping force and potential under pulsed excitation for fixed NA=1.4 a) forces along radial as well as axial direction around geometric focus, b) 3D force and c) corresponding potential. Color: green/blue/red curves correspond to gradient/scattering/total force along the axial direction, and black curve corresponds to a gradient or total force along the radial direction.

with CW excitation, we have considered the average power as 1 mW because, at low average power, nonlinear effects do not contribute significantly. Figure 3.21 shows the plot of trapping force for 40 nm particle along the axial and radial directions at 1 mW average power under CW excitation for fixed NA=1.4, and the RI of the particle equal to 1.31, 1.32, and 1.33 respectively. Here, we have considered second-order nonlinear RI (n_2^p) as 5.9×10^{-17}. Figures 3.21a-c shows the nature of resultant force curves as repulsive, both attractive and repulsive, and repulsive, respectively. It can be seen that when RI of the particle is equal to RI of the medium, the nature of the force curve is attractive. However, under CW excitation, the forces are repulsive in nature, as shown in figure 3.16. Quite interestingly, the change in the nature of the force curve from repulsive to attractive is not sudden change under pulsed excitation due to the effect of nonlinearity, and this transformation is shown in figures 3.21d and 3.21h (red rectangular box). Depending upon the average power, NA, and particle size these RI ranges are different as can be seen from table 3.3.

From table 3.3, under pulsed excitation, the repulsive regime, at low average power (1 mW), the range of RI is approximately similar to CW excitation because nonlinear effects are not contributing significantly. With increasing power, the upper bound of RI decreases for fixed NA. Similarly, for a fixed power where nonlinearity contributes significantly, the upper bound of RI decreases with increasing NA. However, at high average power and high NA, repulsive forces are not present.

In the intermediate regime, although both the upper and lower bound decreases, the RI range increases significantly with increasing average power and increases slightly with increasing NA. The RI range values for repulsive and intermediate

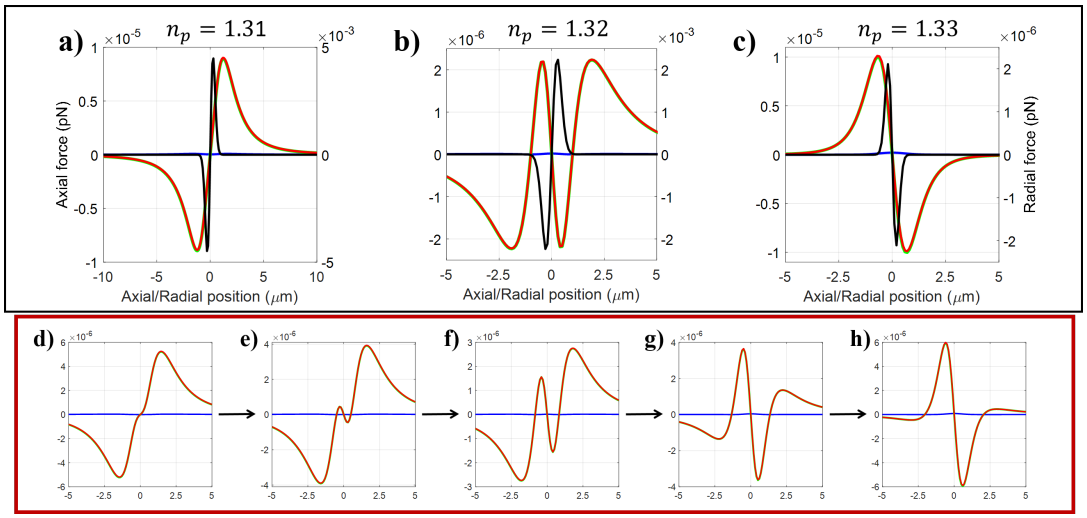

Fig. 3.21.: Plots of trapping force along axial and radial direction under CW excitation for fixed NA=1.4 and particle RI a) 1.31, b) 1.32, c) 1.33, d) 1.315, e) 1.317, f) 1.319, g) 1.322, and h) 1.325.Color: green/blue/red curves correspond to gradient/scattering/total force along the axial direction, and black curve corresponds to a gradient or total force along the radial direction.

P (mW)	NA	Repulsive force	Repulsive to Attractive	Attractive force	Unbound force	Most stable trap
1	1.1	$0 < n_p \leq 1.315$	$1.315 < n_p < 1.33$	$1.33 \leq n_p < 2.32$	$n_p \geq 2.32$	$n_p = 1.74$
	1.2	$0 < n_p \leq 1.315$	$1.315 < n_p < 1.33$	$1.33 \leq n_p < 2.6$	$n_p \geq 2.6$	$n_p = 1.82$
	1.3	$0 < n_p \leq 1.315$	$1.315 < n_p < 1.33$	$1.33 \leq n_p < 2.92$	$n_p \geq 2.92$	$n_p = 1.92$
	1.4	$0 < n_p \leq 1.315$	$1.315 < n_p < 1.33$	$1.33 \leq n_p < 3.47$	$n_p \geq 3.47$	$n_p = 2.03$
10	1.1	$0 < n_p \leq 1.22$	$1.22 < n_p < 1.3$	$1.3 \leq n_p < 2.28$	$n_p \geq 2.28$	$n_p = 1.64$
	1.2	$0 < n_p \leq 1.2$	$1.2 < n_p < 1.3$	$1.3 \leq n_p < 2.55$	$n_p \geq 2.55$	$n_p = 1.76$
	1.3	$0 < n_p \leq 1.17$	$1.17 < n_p < 1.3$	$1.3 \leq n_p < 2.9$	$n_p \geq 2.9$	$n_p = 1.84$
	1.4	$0 < n_p \leq 1.16$	$1.16 < n_p < 1.28$	$1.28 \leq n_p < 3.41$	$n_p \geq 3.41$	$n_p = 1.95$
50	1.1	$0 < n_p \leq 0.7$	$0.7 < n_p < 1.15$	$1.15 \leq n_p < 2.11$	$n_p \geq 2.11$	$n_p = 1.44$
	1.2	$0 < n_p \leq 0.6$	$0.6 < n_p < 1.15$	$1.15 \leq n_p < 2.35$	$n_p \geq 2.35$	$n_p = 1.48$
	1.3	$0 < n_p \leq 0.5$	$0.5 < n_p < 1.12$	$1.12 \leq n_p < 2.66$	$n_p \geq 2.66$	$n_p = 1.51$
	1.4	$0 < n_p \leq 0.4$	$0.4 < n_p < 1.05$	$1.05 \leq n_p < 3.13$	$n_p \geq 3.13$	$n_p = 1.56$
100	1.1	$0 < n_p \leq 0.1$	$0.1 < n_p < 1.0$	$1.0 \leq n_p < 1.95$	$n_p \geq 1.95$	$n_p = 1.15$
	1.2	$0 < n_p \leq 0.04$	$0.04 < n_p < 0.95$	$0.95 \leq n_p < 2.14$	$n_p \geq 2.14$	$n_p = 1.13$
	1.3	No	$0 < n_p < 0.85$	$0.85 \leq n_p < 2.41$	$n_p \geq 2.41$	$n_p = 1.09$
	1.4	No	$0 < n_p < 0.75$	$0.75 \leq n_p < 2.82$	$n_p \geq 2.82$	$n_p = 1.08$

Tab. 3.3.: RI limits variation with NA, for repulsive, attractive, and unbound force values for 40 nm particle at different average power under pulsed excitation for fixed 40 nm particle size.

regimes remain unchanged for different sized particles within the dipole limits. In an attractive regime, the lower and upper bound of the RI range decreases significantly with increasing average power and NA. Within this range, the value

P (mW)	NA	Repulsive force	Repulsive to Attractive	Attractive force	Unbound force	Most stable trap
1	1.1	-1.333 $< n_p \leq$ 0	-1.343$< n_p <$-1.333	-2.333 $\leq n_p \leq$ -1.343	$n_p \leq$-2.333	$n_p =$ -1.743
	1.2	-1.333$< n_p \leq$0	-1.343$< n_p <$-1.333	-2.603$< n_p \leq$-1.343	$n_p \leq$-2.603	$n_p =$ -1.843
	1.3	-1.333$< n_p \leq$0	-1.346$< n_p <$-1.333	-2.973$< n_p \leq$-1.346	$n_p \leq$-2.973	$n_p =$ -1.933
	1.4	-1.333$< n_p \leq$0	-1.348$< n_p <$-1.333	-3.493$< n_p \leq$-1.348	$n_p \leq$-3.493	$n_p =$ -2.053
10	1.1	-1.36$< n_p \leq$0	-1.45$< n_p <$-1.36	-2.37$< n_p \leq$-1.45	$n_p \leq$-2.37	$n_p =$ -1.80
	1.2	-1.36$< n_p \leq$0	-1.46$< n_p <$-1.36	-2.66$< n_p \leq$-1.46	$n_p \leq$-2.66	$n_p =$ -1.90
	1.3	-1.36$< n_p \leq$0	-1.48$< n_p <$-1.36	-3.03$< n_p \leq$-1.48	$n_p \leq$-3.03	$n_p =$ -2.01
	1.4	-1.36$< n_p \leq$0	-1.50$< n_p <$-1.36	-3.56$< n_p \leq$-1.50	$n_p \leq$-3.56	$n_p =$ -2.14
50	1.1	-1.45$< n_p \leq$0	-1.95$< n_p <$-1.45	-2.57$< n_p \leq$-1.95	$n_p \leq$-2.57	$n_p =$ -2.04
	1.2	-1.48$< n_p \leq$0	-2.0$< n_p <$-1.48	-2.89$< n_p \leq$-2.00	$n_p \leq$-2.89	$n_p =$ -2.18
	1.3	-1.50$< n_p \leq$0	-2.10$< n_p <$-1.50	-3.30$< n_p \leq$-2.10	$n_p \leq$-3.30	$n_p =$ -2.34
	1.4	-1.52$< n_p \leq$0	-2.20$< n_p <$-1.52	-3.86$< n_p \leq$-2.20	$n_p \leq$-3.86	$n_p =$ -2.52
100	1.1	-1.55$< n_p \leq$0	-2.52$< n_p <$-1.55	-2.85$< n_p \leq$-2.52	$n_p \leq$-2.85	$n_p =$ -2.33
	1.2	-1.60$< n_p \leq$0	-2.65$< n_p <$-1.60	-3.21$< n_p \leq$-2.65	$n_p \leq$-3.21	$n_p =$ -2.53
	1.3	-1.7$< n_p \leq$-0.6	-2.86$< n_p <$-1.7 -0.6$< n_p <$0	3.66$< n_p \leq$-2.86	$n_p \leq$-3.66	$n_p =$ -2.76
	1.4	-1.8 $< n_p \leq$ -0.4	-3.10 $\leq n_p \leq$ -1.8 -0.4 $< n_p <$ 0	-4.27$< n_p \leq$-3.10	$n_p \leq$-4.27	$n_p =$ -3.01

Tab. 3.4.: RI limits variation with NA, for repulsive, attractive, and unbound force values for 40 nm particle at different average power under pulsed excitation for fixed 40 nm particle size for meta-materials.

of axial force minima first decreases and reaches a minimum and then increases with increasing RI and the RI corresponding to the minima is where the trap is most stable under these conditions. This optimal RI increases with increasing NA and decreases with increasing average power. However, there is a small deviation from this trend with increasing NA for high average power which is highlighted in table 3.3, where optimal RI decreases with increasing NA because, at 100 mW average power, nonlinearity leads to destabilizing of the trap where scattering force dominates over the gradient force.

In the unbound regime, only the lower bound of RI exists, and this value increases with increasing NA for fixed average power. However, it decreases with increasing average power for fixed NA. Similarly, from table 3.4, it can be seen that under pulsed excitation, at low average power (1 mW), the range of RI is approximately similar to CW excitation because nonlinear effects are not contributing significantly. With increasing power, the lower bound of RI is decreasing for fixed NA. Similarly, for fixed power where nonlinearity contributes significantly, the lower bound of RI decreases with increasing NA. In terms of the magnitude of RI, the

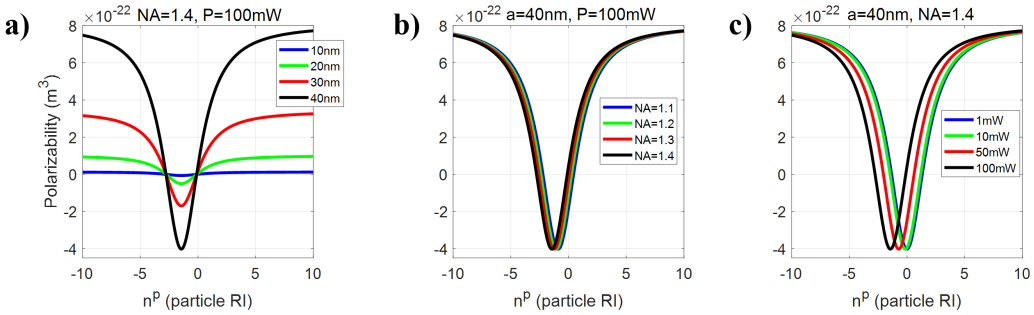

Fig. 3.22.: Plots of polarizability against particle RI for a) NA=1.4 and 100mW average power, b) 40 nm particle and 100mW average power, c) 40 nm particle size and NA=1.4 under pulsed excitation.

behavior of intermediate, attractive, and unbound forces are similar to that of a particle having positive RI. However, in an intermediate regime, at high average power and high NA, the transition from repulsive to attractive force lies in two different regimes due to the significant contribution of nonlinear RI, which is highlighted in the table 3.3. In an attractive regime, the lower and upper bound of the RI range decreases significantly with increasing average power and NA. However, within this range, the value of axial force minima first decreases reaches a minimum and then increases with RI. The RI corresponding to the minima is where the trap is most stable under these conditions. This optimal RI decreasing with increasing NA and decreases with increasing average power.

For small particles, in the attractive and unbound regimes, defining the range is ambiguous because the polarizability saturates after a particular value of RI, which can be seen from figure 3.22a. Figure 3.22b shows that for fixed particle size and average power, the minima of polarizability is shifting towards lower RI value as per increase in NA. Similarly, an increase in average power for fixed particle size and NA results in shifting the polarizability minima towards lower RI value, as shown in figure 3.22c. The range of RI for repulsive regimes listed in the above tables 3.3 and 3.4 can also be mapped through the polarizability.

An interesting observation is that particles having RI less than the medium can be trapped using pulsed excitation but not using CW excitation. This is one instance where we can see the advantage of femtosecond pulsed excitation over CW excitation. Under pulsed excitation, increasing average power contributes significantly to the nonlinearity resulting in unstable trapping for particles having higher RI, whereas, in the case of CW excitation, it can be trapped. However, for metamaterial particles, there is a specific range of RI, where particles can be trapped. The particles having a RI less than the medium cannot be trapped using

pulsed excitation but can be trapped using CW excitation. It can be observed

	Optimal power (mW)				$U_{esc}(k_BT)$			
NA / PS (nm)	1.1	1.2	1.3	1.4	1.1	1.2	1.3	1.4
40	103	117	134	160	2.62	4.40	7.00	10.78
39	119	135	155	189	3.06	5.09	8.08	12.56
38	137	156	182	228	3.57	5.90	9.40	14.81
37	159	182	217	281	4.16	6.87	11.05	17.68
36	185	216	250	363	4.86	8.05	13.12	21.77
35	219	261	335	482	5.70	9.55	16.05	28.29
34	261	322	444	783	6.75	11.52	19.96	39.36
33	318	415	653	1808	8.08	14.24	26.56	67.01
32	399	571	1165	–	9.86	18.34	39.93	–
31	524	870	–	–	12.39	25.47	–	–
30	726	1846	–	–	16.39	41.99	–	–
29	1211	–	–	–	23.92	–	–	–
28	3243	–	–	–	45.00	–	–	–

Tab. 3.5.: Optimal power and corresponding escape potential values for different particle size variation with NA under pulsed excitation.

that nanoparticle having a high RI (quantitatively listed in tables 3.1, 3.2, 3.3 and 3.4) than the surrounding medium cannot be trapped using both CW and pulsed excitations. Because they scatter more, which results in the domination of scattering force over gradient force. Therefore, trap destabilizes. In order to trap very high RI nanoparticles, we require antireflection coating on top of particle surface so that scattering force can be minimized [126, 127]. Under pulsed excitation, optimal power can be calculated for fixed sized particles by measuring U_{esc} with an increase in average power, which can be seen from table 3.5. The optimal power and U_{esc} increases, with a decrease in particle size for fixed NA. Similarly, optimal power and U_{esc} increase with an increase in NA for fixed particle size. Interestingly, it can be observed that after a specific particle size limit, getting optimal power for a fixed NA is difficult, and the particle size limit is different for different NA. This is because the increase in average power contributes significantly to nonlinear RI, which results in an increase in the total RI. Consequently, polarizability increases initially and then saturates, which can

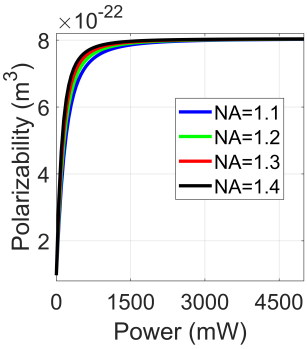

Fig. 3.23.: Plots of polarizability against average power for 40nm polystyrene particle size under pulsed excitation.

be seen from both figure 3.23 and table 3.6. When it reaches saturation, it is not very easy to get optimal power for fixed particle size and NA.

From table 3.5, it can be seen that by fixing the particle size and NA, varying

Power (mW)	$m = \frac{n_p}{n_w}$	$\alpha = \frac{m^2-1}{m^2+2}$
100	2.2736	0.5816
500	6.6182	0.9345
1000	12.0489	0.9796
2000	22.9103	0.9943
3000	33.7717	0.9974
4000	44.6331	0.9985
5000	55.4945	0.9990

Tab. 3.6.: Polarizability variation with average power and NA under pulsed excitation.

the average power in order to calculate the optimal power, it fails after a certain limit due to the saturation of polarizability. Therefore, we have used another method to calculate the optimal parameter for stable trapping, where average power and NA are fixed, and the particle size is varying. U_{esc} initially increases, followed by a maximum and then decreases. The particle size corresponding to the maxima results in stable trapping for a particular average power, which is listed in tables 3.7 and 3.8. It is also observed that the initial increase in average power results in a rapid decrease in optimal particle size. Whereas approaching towards smaller sized particles, there is a range of average power for which an optimal particle can be stably trapped, and this range increases as particle size decrease. The salient point here is that in the earlier method (fixing the particle size and varying the average power), optimal average power for fixed particle size can be calculated till 33 nm, 32 nm, 30 nm, and 28 nm which corresponds to NA 1.4, 1.3, 1.2, and 1.1 respectively. However, using this method (fixing power and varying particle size), optimal particle size for fixed average power

can be calculated till 23 nm, 24 nm, 25 nm, and 26 nm, which corresponds to 1.4, 1.3, 1.2, and 1.1 NA, respectively. Still, it is challenging to calculate optimal parameters for further smaller particles. There is yet another way to estimate the parameters which depend on the average power. We can predict whether it creates a stable or unstable trap by measuring U_{esc} , and match it with the thumb of rule condition *i.e.* if U_{esc} is $> 10k_BT$, it will create a stable trap. So, according to the available parameters like average power, pulse width, repetition rate, and nonlinear refractive indices of particle and medium, we can predict whether the particle can be trapped or not.

Figure 3.24 shows the optimal power and U_{esc} against pulse width for 40 nm

NA=1.1			NA=1.2		
OP (mW)	PS (nm)	$U_{esc}(k_BT)$	OP (mW)	PS (nm)	$U_{esc}(k_BT)$
50	40	5.45	100	34	7.96
100	35	10.71	200	30	16.00
150	33	16.12	300	29	24.43
200	31	21.69	400	28	33.10
250-300	30	27.41-33.17	500-600	27	41.85-50.76
350-400	29	39.12-45.03	700-1300	26	59.62-113.00
450-750	28	50.92-57.00	1400-onward	25	121.89-onward
800-1400	27	92.95-164.74	–	–	–
1450-onward	26	176.54-onward	–	–	–

Tab. 3.7.: Optimal particle size and corresponding escape potential values for different average power with NA (1.1 and 1.2) under pulsed excitation. OP: optimal power, PS: particle size.

NA=1.3			NA=1.4		
OP (mW)	PS (nm)	$U_{esc}(k_BT)$	OP (mW)	PS (nm)	$U_{esc}(k_BT)$
100	33	5.76	100	33	4.05
200	30	11.49	200	29	8.03
300	28	17.52	300	27	12.18
400	27	23.70	400	26	16.45
500-600	26	30.00-36.35	500-600	25	20.81-25.21
700-1200	25	42.78-74.86	700-1000	24	29.70-43.11
1300-onward	24	81.35-onward	1100-onward	23	47.61-onward
–	–	–	–	–	–
–	–	–	–	–	–

Tab. 3.8.: Optimal particle size and corresponding escape potential values for different average power with NA (1.3 and 1.4) under pulsed excitation. OP: optimal power, PS: particle size.

particle size under pulsed excitation at fixed NA 1.4. It can be observed that optimal power and U_{esc} varies linearly with pulse width. This is useful for achieving realistic parameter according to the experimental scenario, for example, optimal

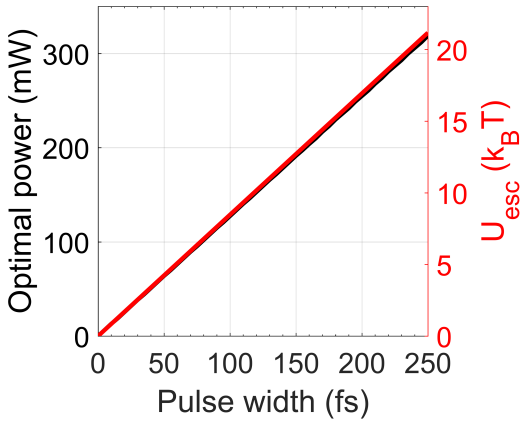

Fig. 3.24.: Plot of optimal power and escape potential vs pulse width under pulsed excitation for fixed NA 1.4.

power for 120 fs pulse width is 1000 mW, but to get a more realistic parameter, the same conditions are achievable if we choose average power equal to 100 mW for 12 fs pulse width. Similar behavior is obtained for different particle size and NA as well.

In addition, we have explored the effect of OKE in CdS, ZnS, and compared with polystyrene since CdS, ZnS, and polystyrene have significant higher second-order nonlinear RI. The chosen parameters are 100 mW average power under both CW and pulsed excitation for fixed NA 1.4 unless mentioned. Figure 3.25 shows total (gradient only) force acting on the particle along the radial direction for both CW and pulsed excitation for 10 nm particle size.

Figure 3.26 shows the total force/potential acting on the particle along the axial direction for both CW and pulsed excitation for 10 nm particle size, where red, green, and black corresponds to CdS, ZnS and polystyrene respectively. It can be seen that the forces in the case of CdS and ZnS under CW excitation are comparable, while for polystyrene, it is relatively very less. This is because the linear RI of CdS and ZnS are comparable, but polystyrene has a very less linear RI. Nevertheless, upon including nonlinearity, there is a significant change in polystyrene, while corresponding changes in ZnS and CdS are minimal at the same average power. The change in the CdS curve is not significant, and for ZnS, there is almost no change. This is because, for both CdS and ZnS, the nonlinear RI is very small compared to that of polystyrene (CdS by a factor of $\sim$10 and ZnS by a factor of $\sim$ 100). The results obtained along the radial direction are qualitatively very similar but quantitatively different from that obtained in the case of the axial direction. This is because, for small particles, the contribution from the scattering force is insignificant. Hence, the results are dictated by gradient force,

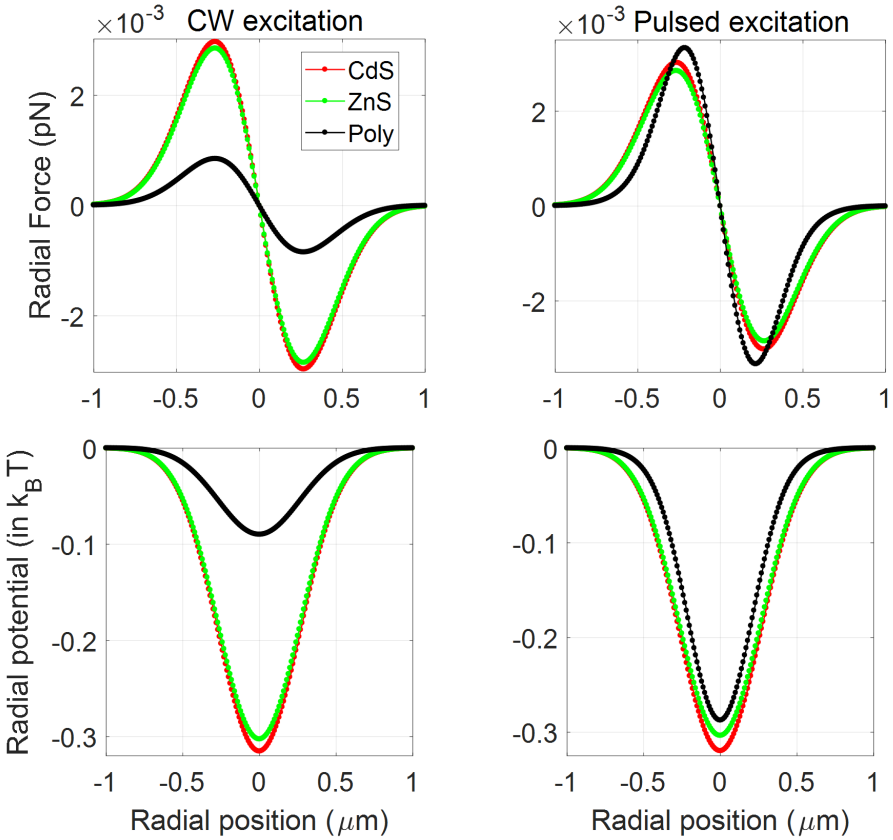

Fig. 3.25.: Plots of trapping force along radial direction for both CW and pulsed excitation at 100 mW average power for 10 nm particle size.

which is also the only force along the radial direction as well. Note that the radial potential is symmetric, while the axial potential is asymmetric about the axis due to contribution from the scattering force. In earlier chapters, we have defined the depth of the trapping potential as absolute potential (U_{abs}) and the height of the barrier to the positive z-axis as escape potential (U_{esc}) and identified U_{esc} as the crucial quantity to be considered for stability of an optical trap; these two potentials are shown in figure 3.26 (marked by blue arrow).

Figure 3.27 shows the plot of escape potential vs particle size under both CW and pulsed excitations. It can be seen that depth of potential decreases with decreasing particle size along the radial direction, whereas for axial direction, CdS and ZnS pass through maxima. At the same time, polystyrene does not reach maxima before 40 nm particle size (we did not attempt to simulate force/potential above 40 nm particle size since it lies beyond the validation of dipole approximation). Again including nonlinearity gives significant deviations in case of polystyrene compared with ZnS and CdS. As seen in figure 3.27, in the linear case, there is a well-defined maximum in the case of ZnS and CdS, but no such

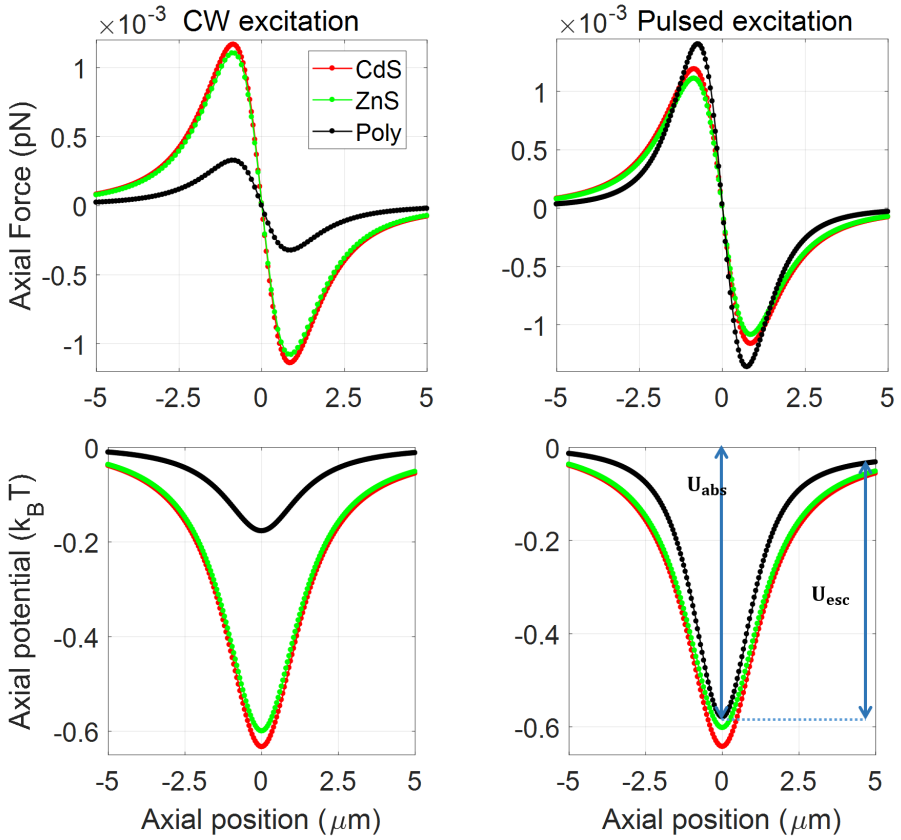

Fig. 3.26.: Plots of trapping force along axial direction for both CW and pulsed excitation at 100 mW average power for 10 nm particle size.

behavior is observed for polystyrene. This means that within the domain of CW excitation, stable trapping can be achieved for smaller particles of CdS and ZnS. However, for polystyrene, the corresponding size is much higher, which is off the scale for fixed average power. But the inclusion of nonlinearity brings about a shift in the peak for the case of polystyrene, indicating that even smaller particles can be trapped. So it can be concluded that for a fixed power, nonlinear contributions must be included to correctly predict the optimal size for stable trapping, particularly for particles having a high nonlinear RI like polystyrene. Another aspect of nonlinearity is portrayed in the average power dependence of stable trapping in the axial direction for 500 mW and 1000 mW average powers, as shown in figure 3.28. If only linear aspect (CW excitation) is considered, there is no shift in peaks (w. r. t. particle size) with a change in power because here, power is linearly dependent. Under pulsed excitation, a shift in the maxima towards smaller particle size is observed when the average power is increased. Again the change is very significant for polystyrene, smaller for CdS, and almost negligible for ZnS. In the radial direction, there is a change quantitatively with

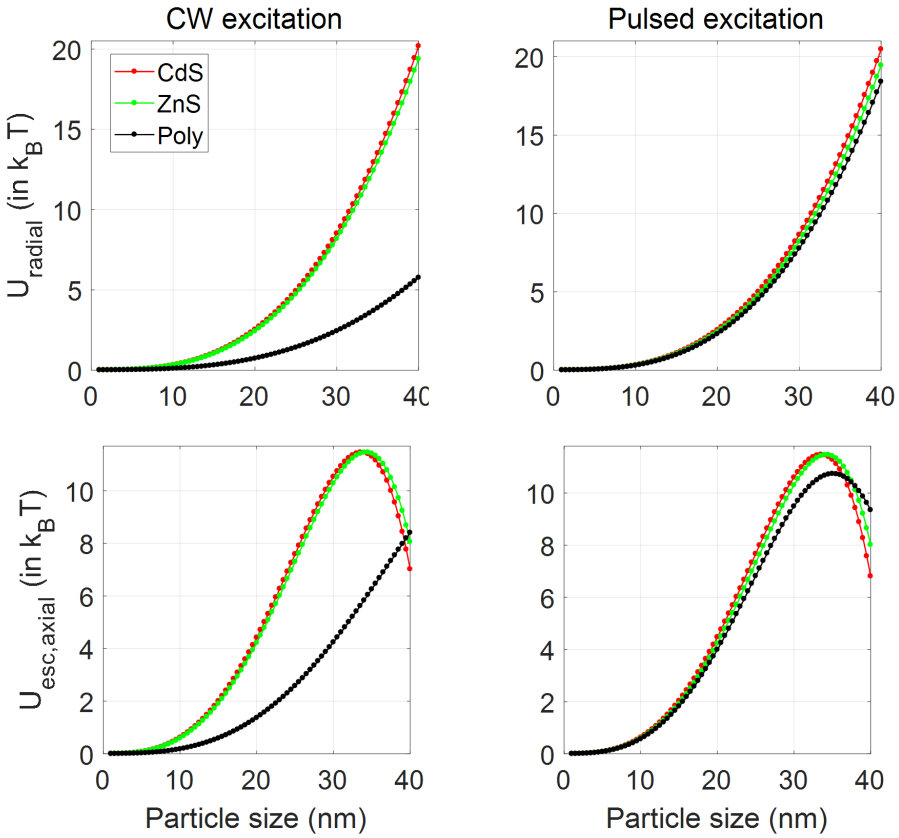

Fig. 3.27.: Plots of radial/escape potential against particle size under both CW and pulsed excitation.

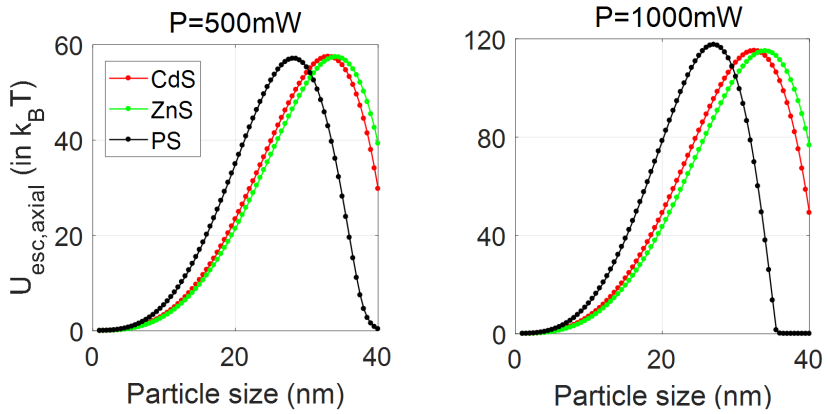

Fig. 3.28.: Plots of escape potential vs particle size under pulsed excitation at different average power.

the change in the order of magnitude. However, qualitatively there is no significant effect of including nonlinearity for different average power. As per particle size decreases, well depth also decreases, which implies that trapping is harder for smaller particles. So, the high average power is required to trap small size particle.

3.3 Core-Shell type nanoparticles

The mathematical formulation for dipole approximation discussed in chapter 1. All the parameters used in numerical simulations are listed in table 2.1. The method of calculating polarizability for core-shell and hollow-core type is different from that of core-type nanoparticles. There are two methods to calculate the polarizability: one is the average method, and another one is rigorous method (in which polarizability of each layer incorporated to make it more efficient). On comparison, both the methods give similar results for very small or quantum dot particles, but for few tens of nanometer-sized particles both show different results which explained briefly in this chapter.

3.3.1 Average method

In this method α is calculated by using the average RI of the particle.

$$\alpha = \left(\frac{m^2 - 1}{m^2 + 2}\right) \tag{3.2}$$

where $m = \frac{n_p}{n_w}$ is relative RI of the particle to the medium. Because of very small size, the shape is indistinguishable, hence, it can be treated as dipole with $n^p = \frac{n_c^p + n_s^p}{2}$, which is just an average of core (n_c^p) and shell (n_s^p) particle RI.

3.3.2 Rigorous method

In this method α is calculated by individually taking the polarizability factors for core and shell and can be written as [128]:

$$\alpha = \frac{\alpha'}{V} = \frac{(n_s^2 - n_w^2)(n_c^2 + 2n_s^2) + f^3(2n_s^2 + n_w^2)(n_c^2 - n_s^2)}{(n_s^2 + 2n_w^2)(n_c^2 + 2n_s^2) + f^3(2n_s^2 - 2n_w^2)(n_c^2 - n_s^2)} \tag{3.3}$$

where, n^c , n^s and n^w are RI of core, shell and water (medium) respectively, $f = \frac{a_c}{a_s}$ is the ratio of radius of core (a_c) to that of shell (a_s). In the limit $n^c = n^s = n^p$, we get back the polarizability per unit volume for single nanoparticle. This is more general method than average method to calculate the polarizability per unit volume and is more appealing because of its rigorous evaluation. V in above calculation is: $V = 4\pi n_w^2 \epsilon_0 a_s^3$.

We have calculated the forces for both CW excitation and pulsed excitation using both the methods. In case of CW excitation only linear RI is considered;

$n^{s/c/w/p} = n_0^{s/c/w/p}$ (excluding nonlinear RI factor), whereas in pulsed excitation, second order nonlinear RI factor $n_2^{s/c/w/p}$ is also incorporated giving $n^{s/c/w/p} = n_0^{s/c/w/p} + n_2^{s/c/w/p} * I(r,z)$. Here, we have chosen NA =1.4 and 100 mW average power under CW and pulsed excitation until mentioned otherwise.

3.3.3 Comparison of average and rigorous method

We now consider CdS-ZnS and polystyrene-CdS as core-shell particle immersed in water. These materials were chosen because for one of them (CdS-ZnS) RI of the core is greater than the shell $(n^c > n^s < n^w)$ and in other case (polystyrene-CdS) it is other way around ($n^c < n^s > n^w$).

Figure 3.29 shows the total force acting on core-shell particle for both methods

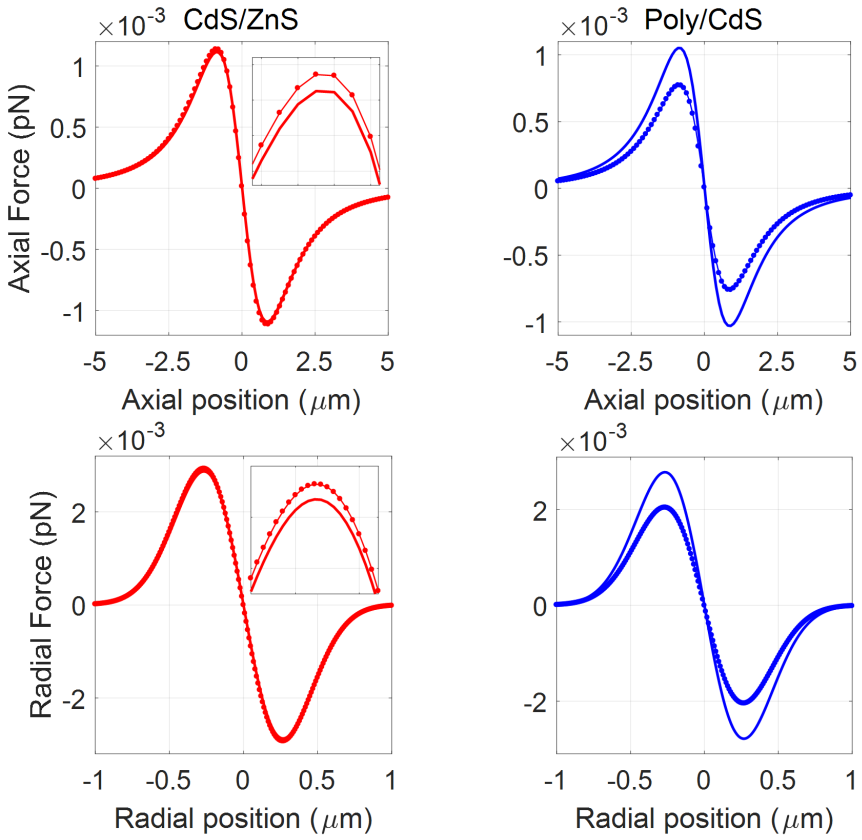

Fig. 3.29.: Plots of trapping force along axial and radial directions for (5 nm thick) core-shell under CW excitation. Color: red/blue curve corresponds to CdS-ZnS/Poly-CdS particles. The solid and dotted lines correspond to the rigorous formulation and average method of polarizability, respectively.

for calculating α under CW excitation, where the considered core radius is 5 nm and shell thickness is 5 nm for both radial as well as in axial direction. The solid line corresponds to the rigorous formulation, and the dotted circled line

corresponds to the average method, where the red and blue curves correspond to CdS-ZnS and polystyrene-CdS, respectively. It can be seen that in case of CdS-ZnS force acting on the particle is overestimated in the average method (shown in the inset of figure 3.29) as compared with the rigorous method however for polystyrene-CdS average method underestimates the force as compared with the rigorous method.

From now on, we consider simulations using the rigorous method to calculate polarizability α. Figure 3.30 shows the force/potential curves under pulsed

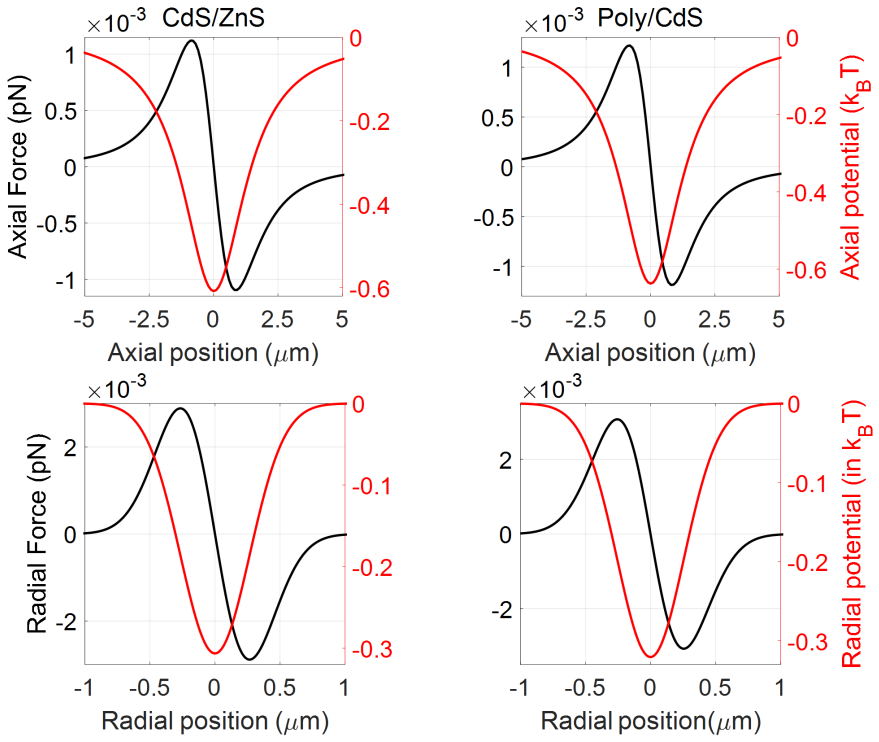

Fig. 3.30.: Plots of trapping force/potential along axial and radial direction at 100 mW average power for 5 nm core and 5 nm shell under pulsed excitation.

excitation for 5 nm core radius and 5 nm shell thickness along axial as well as radial direction. It can be seen that including nonlinearity gives rise to a significant change in magnitude not in the nature of force and potential curve for polystyrene-CdS while no significant change in CdS-ZnS.

Quite interestingly, there is a critical dependence on the core radius and shell thickness. As in the example in figure 3.29, we find that for the case of core radius as 5 nm and shell thickness as 5 nm, the average method overestimates force for CdS-ZnS and underestimates for polystyrene-CdS. This is in contrast to 12 nm as the core, and 3 nm as shell case, wherein both average method and rigorous method give qualitatively similar results for polystyrene-CdS. However,

for CdS-ZnS case average method again overestimates the force. In yet another case considered, with 17 nm as core and 3 nm as shell thickness, the average method predicts more force for both polystyrene-CdS and CdS-ZnS. Therefore, it follows that while the average method always overestimates force for CdS-ZnS, it may overestimate or underestimate force or give a comparable prediction as compared to the rigorous method in case of polystyrene-CdS. This variation can be attributed to the fact that CdS and ZnS have comparable linear refractive indices, whereas polystyrene and CdS have significantly distinct linear refractive indices. In figure 3.31, the left panel shows the variation of shell radius against escape

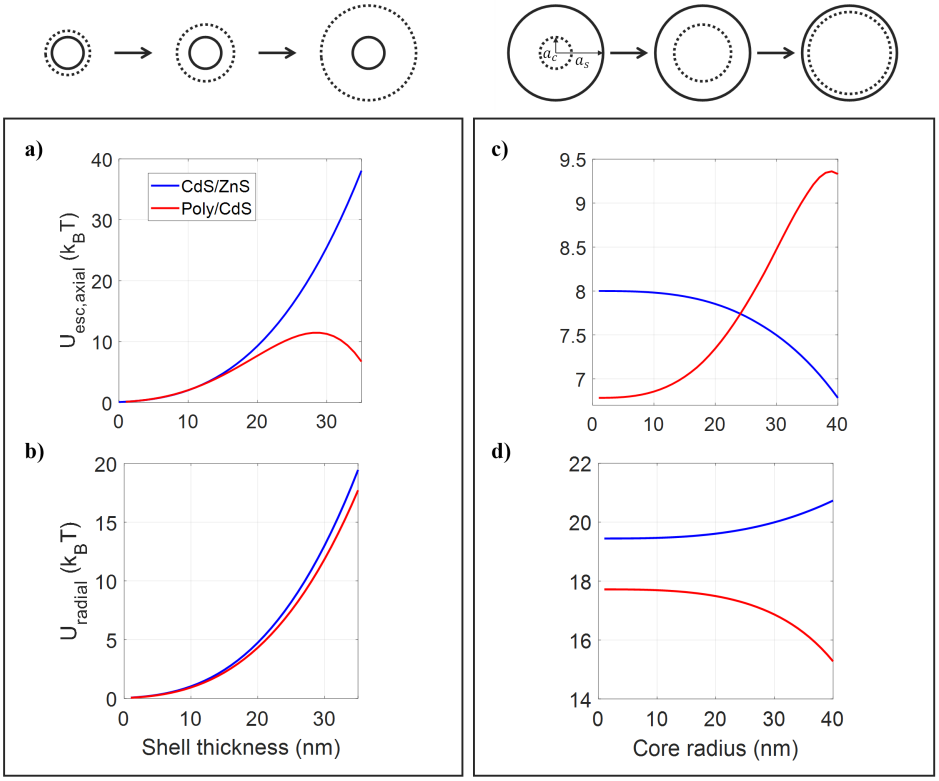

Fig. 3.31.: Plots of escape potential vs core and shell radius variation along radial as well as axial direction under pulsed excitation.Color: black/red curve corresponds to force/potential.

potential by fixing the core radius at 5 nm, and the right panel shows the variation of core radius against escape potential by fixing shell radius at 40 nm for both axial and radial directions under pulsed excitation. Here blue curve corresponds to CdS-ZnS and red curve corresponds to the polystyrene-CdS. From figure 3.31a, it can be seen that as shell thickness increases, escape potential increases because increasing shell thickness implies that the overall radius of core-shell nanoparticle increasing, which results in a continuous increase in escape potential height

Particle type	a_c (nm)	a_s (nm)	f = $\frac{a_c}{a_s}$	α (at focus)		
				1 mW	100 mW	1000 mW
CdS/ZnS	5	10	0.50	0.4058	0.4095	0.4414
		20	0.25	0.4034	0.4060	0.4293
		30	0.167	0.4031	0.4057	0.4281
		40	0.125	0.4030	0.4056	0.4278
	5	40	0.125	0.4030	0.4056	0.4278
	15		0.375	0.4042	0.4072	0.4334
	25		0.625	0.4085	0.4133	0.4542
	35		0.875	0.4180	0.4267	0.4980
poly/CdS	5	10	0.50	0.3943	0.4570	0.6285
		20	0.25	0.4241	0.4376	0.5339
		30	0.167	0.4241	0.4376	0.5339
		40	0.125	0.4247	0.4372	0.5316
	5	40	0.125	0.4247	0.4372	0.5316
	15		0.375	0.4124	0.4454	0.5742
	25		0.625	0.3634	0.4756	0.7046
	35		0.875	0.2396	0.5375	0.8894

Tab. 3.9.: Table for polarizability values of CdS-ZnS and polystyrene-CdS at different average power for varying core radius and shell thickness. Here a_c: core radius; a_s: shell radius.

for CdS-ZnS along axial direction whereas in case of polystyrene-CdS passes through a maximum. However, along the radial direction for both CdS-ZnS and polystyrene-CdS, escape potential increases as shell thickness increases because the potential is stabilizing more and more with increasing overall particle size can be seen from figure 3.31b.

In the case of variation of the thickness of core with a fixed particle size (40 nm), it can be seen that escape potential height decreases with an increase in core radius for CdS-ZnS. However, it is significantly small in quantity as compared with shell thickness variation case because, in case of core thickness variation, the overall particle size is fixed. But in the case of polystyrene-CdS, escape potential height passes through a maximum, with increasing core thickness (figure 3.31c) because, for CdS-ZnS, RI of the core is higher as compared to the shell, as opposed to polystyrene-CdS (figure 3.31d). An increase in the core radius leads to an increase in the quantity (in polarizability expression) f for both CdS-ZnS and

Particle type	a_c (nm)	a_s (nm)	f = $\frac{a_c}{a_s}$	α (at focus)		
				1 mW	100 mW	1000 mW
Hollow CdS	35	36	0.9722	-0.1010	-0.0988	-0.0773
		37	0.9460	-0.0439	-0.0398	-0.0015
		38	0.9211	0.0043	0.0098	0.0603
		39	0.8974	0.0455	0.0520	0.1116
		40	0.875	0.0809	0.0883	0.1548
Hollow poly	35	36	0.9722	-0.1440	-0.0588	0.7152
		37	0.9460	-0.1214	0.0276	0.8338
		38	0.9211	-0.1014	0.0966	0.8806
		39	0.8974	-0.0835	0.1529	0.9056
		40	0.875	-0.0674	0.1996	0.9212

Tab. 3.10.: Table for polarizability values of CdS and Polystyrene hollow sphere at different average power for varying core radius and shell thickness. Here a_c: core radius; a_s: shell radius.

polystyrene-CdS. This increase in f causes an increase in polarizability in CdS-ZnS and a decrease in polystyrene-CdS because the second term in the numerator and denominator in equation 3.3 gives a positive contribution for CdS-ZnS while the corresponding contributions have a negative sign for polystyrene-CdS which can be seen from table 3.9. It is also observed that at 1 mW average power CdS-ZnS polarizability value decreases with increasing shell thickness and increases with increase in core radius whereas in case of polystyrene-CdS this trend is reversed (highlighted in table 3.9). However, this behavior will change (shift the peak towards left) for polystyrene-CdS at high average power and remain the same for CdS-ZnS because at high average power, the contributions from nonlinear RI become quite significant. For CdS-ZnS there is no such reversal of behavior.

3.4 Hollow-core type nanoparticles

For hollow-core type particles results are surprisingly very different from those in case of core-shell nanoparticles.

Figure 3.32 shows the axial and radial force curves under CW excitation. It can be seen that the nature of force shows the repulsive nature instead of attractive. The thickness of the shell considered is 3 nm; the inner radius of the hollow nanosphere is 37 nm. A small change in thickness of the shell leads to a significant

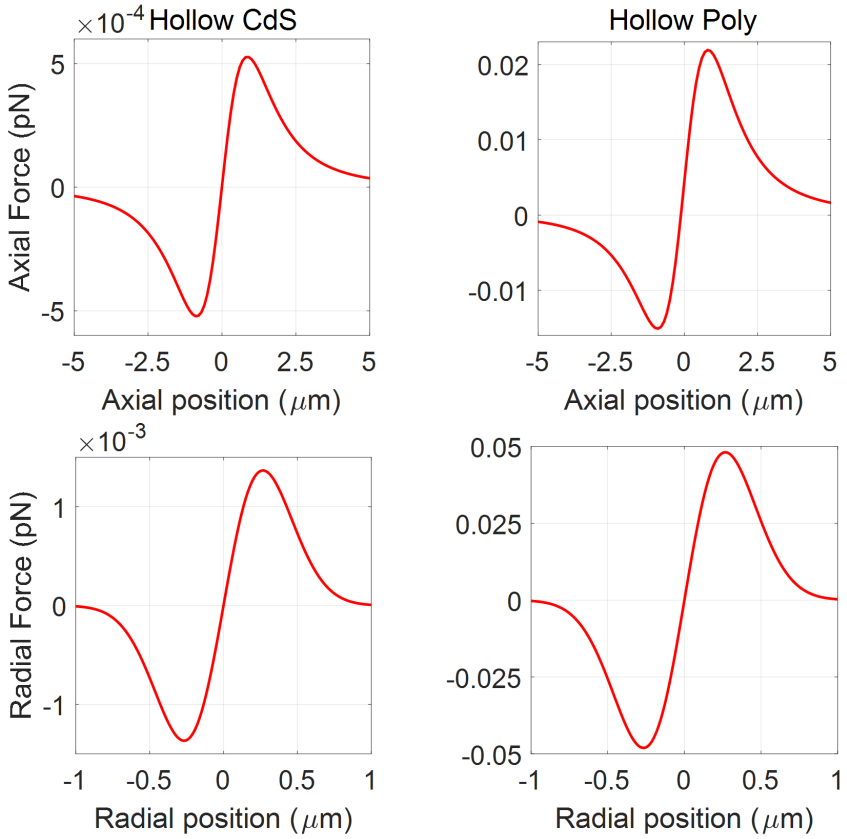

Fig. 3.32.: Plots of trapping force along axial and radial direction for hollow CdS and polystyrene for 3 nm shell thickness (inner and outer radius as 37 nm and 40 nm) under CW excitation.

change in the force curve quantitatively as well as qualitatively. For example, if we consider the radius of the inner core as 37 nm and outer as 40 nm, it results in a repulsive force. However, at the same time, if we consider inner and outer radius as 37 nm and 42 nm, we will get the attractive instead of repulsive force. From this, we can say if the thickness of the CdS and polystyrene shell is greater than 4 nm and 10 nm, respectively. It will result in an attractive force, but shell thickness less than this gives a resulting repulsive force. From table 3.10, it can be seen that an increase in the thickness of the shell changes the polarizability sign from positive to negative for both CdS and polystyrene hollow sphere. It can also be observed that at 1 mW average power, a particle having an inner radius 35 nm and outer radius more than 38 nm shows attractive force for the CdS hollow sphere, however, repulsive for polystyrene because for CdS the linear RI is more as compared to polystyrene. On the other hand, at high average power, this transition occurs earlier in polystyrene as compared to CdS because polystyrene

has a higher nonlinear RI as compared to CdS.

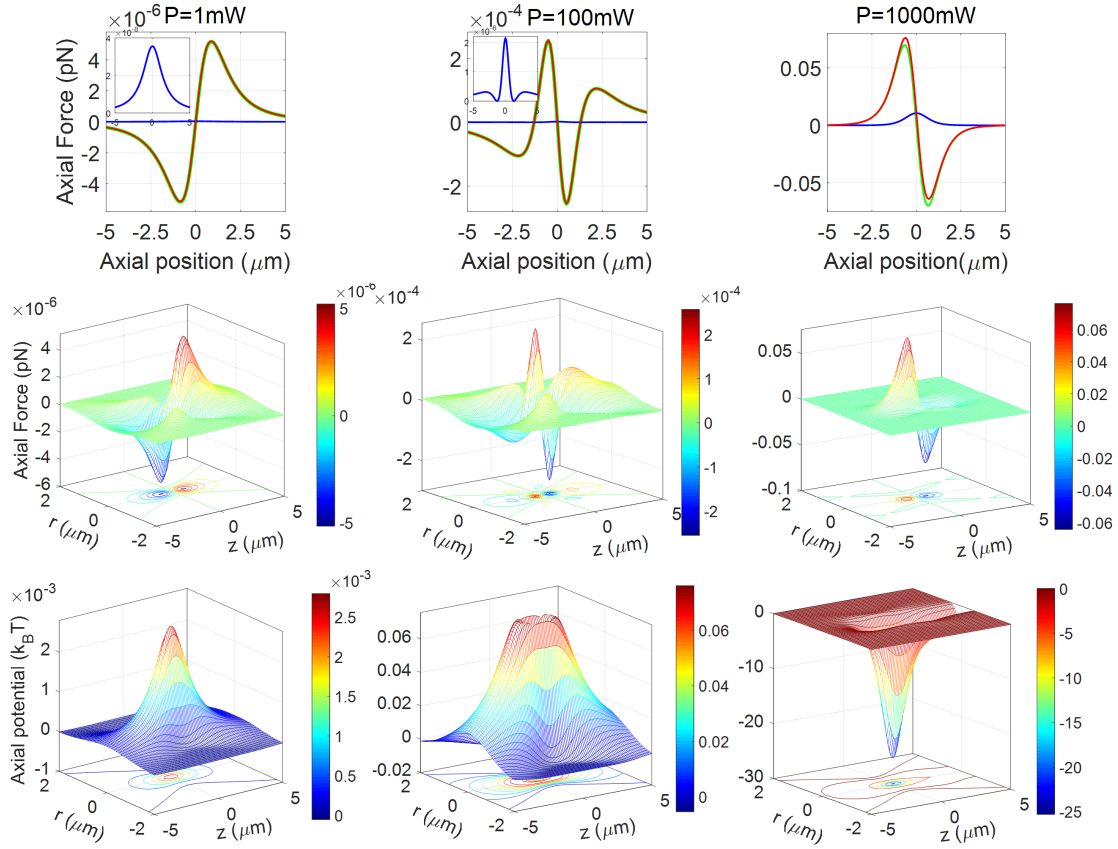

Fig. 3.33.: Plots of trapping force along axial direction for hollow CdS for 3 nm shell thickness (inner and outer radius as 37 nm and 40 nm) under pulsed excitation. Color: green/blue/red curve corresponds to gradient/scattering/total force.

Figure 3.33 shows the effect of nonlinearity on the hollow CdS nanosphere for different average power under pulsed excitation, although it has a very small nonlinear RI compared to polystyrene. As average power is increased, nonlinearity contributes more significantly, which results in to change in the nature of a force curve from repulsive to attractive. This change in the nature of force can be seen from figure 3.33, where increasing in average power contributes significantly to scattering and gradient forces, which leads to change in the nature of the total force curve. From the earlier discussion, we know that polystyrene shows a significant nonlinear effect as compared to CdS and ZnS due to higher second-order RI. So, this change in the nature of the force curve from repulsive to attractive can be seen very clearly at low average power in the hollow polystyrene nanosphere from figure 3.34. For CdS-ZnS and polystyrene-

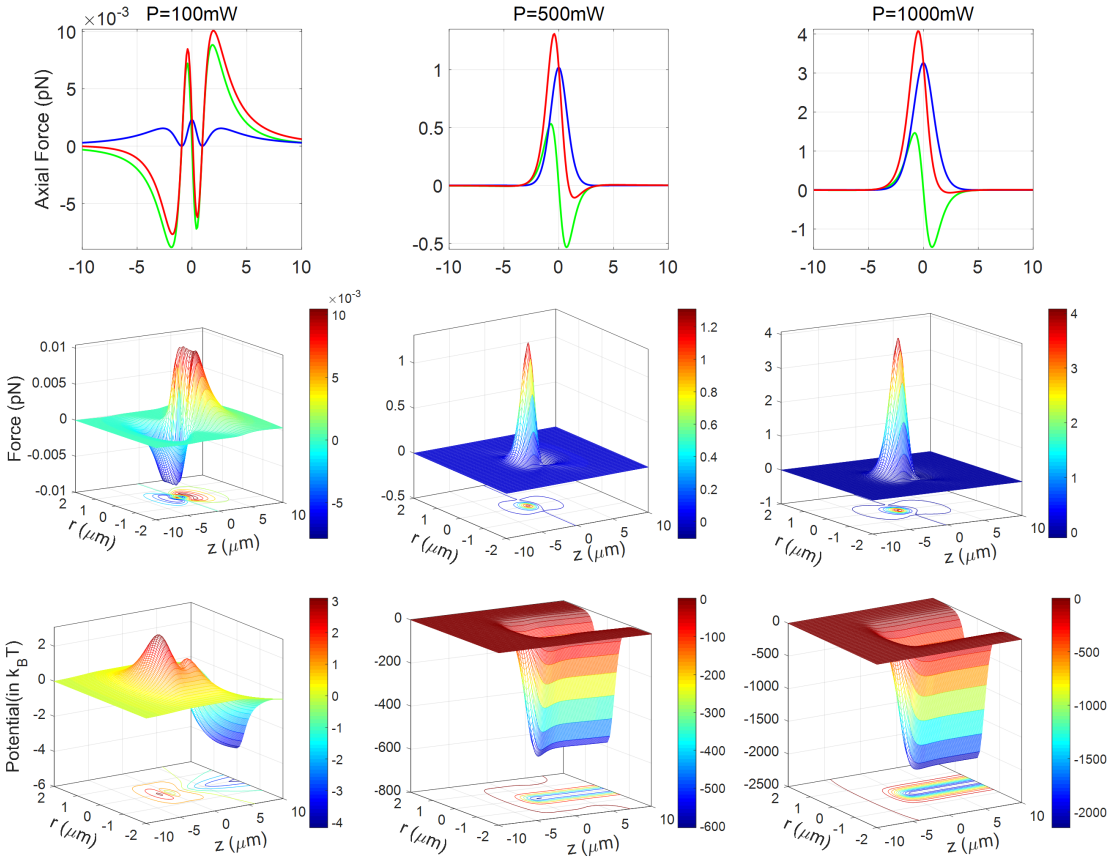

Fig. 3.34.: Plots of trapping force along axial direction for hollow polystyrene for 3 nm shell thickness (inner and outer radius as 37 nm and 40 nm) under pulsed excitation. Color: green/blue/red curve corresponds to gradient/scattering/-total force.

CdS under CW excitation, we observe that the forces are repulsive (figure 3.32), whereas under pulsed excitation, they become attractive (figures 3.33 and 3.34) at 100 mW average power. The increase in average power, it converts from the unstable (repulsive) trap (due to a thickness of shell and RI of the material) to a stable (attractive) trap (nonlinearity contributes in a significant amount leading to increase in the RI of the material). Further increase in average power destabilizes the trap along axial direction due to dominance of scattering force over gradient force while along the radial direction, further increase in power results in stabilizing the trap as there is no contribution from scattering force. This is a clear advantage of pulsed excitation.

Figure 3.35 shows the transformation of repulsive to attractive potential through the splitting of potential as the average power is increased for both CdS and polystyrene hollow nanosphere. It can be seen that with an increase in average power, nonlinear RI contributes significantly to the linear RI which results in a

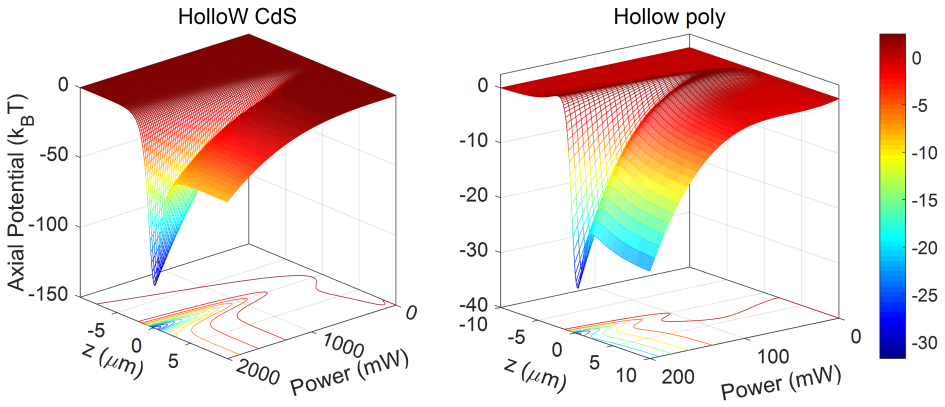

Fig. 3.35.: Plots of trapping force along axial and radial direction for hollow CdS and polystyrene for 3 nm shell thickness (inner and outer radius as 37 nm and 40 nm) under pulsed excitation.

change of repulsive potential to the splitting of potential and is eventually to attractive potential, any further increase in average power leads to an unstable trap due to scattering force. Figure 3.36 shows the change in escape potential

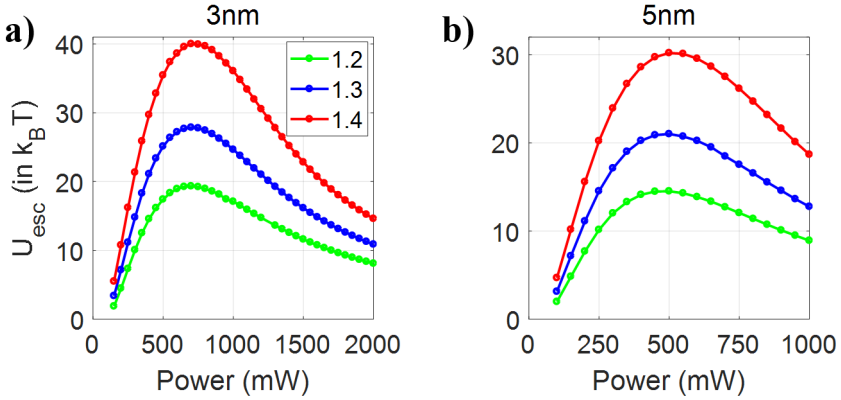

Fig. 3.36.: Plots of escape potential vs average power along axial direction for hollow polystyrene nanosphere having thickness a) 3nm and b) 5nm under pulsed excitation.

with average power for polystyrene hollow nanosphere for different NA *i.e.* 1.2, 1.3 and 1.4 respectively. It can be seen that with an increase in average power, escape potential first increases, then reaches to maxima and eventually decreases. The average power corresponding to the maximum escape potential is optimal power for the most stable trap. It is also observed that a small change in the thickness of the polystyrene hollow nanosphere (from 3 nm to 5 nm) results in shifting the optimal average power (from 700 mW to 500 mW) under pulsed excitation for fixed NA and corresponding escape potential height decreases significantly. This implies that the optimal power decreases with an increase in

the thickness of the hollow nanosphere shell, consequently with an increase in thickness, the particle can be trapped easily at low average power. Similarly, it can be done for CdS hollow sphere as well.
Changing the wavelength of the trapping beam results in a change in the nature and magnitude of trapping force and potential; accordingly, the range of particle size for dipole approximation also changes. In addition, the effect of polarization can be seen if we consider circular or elliptical polarization instead of plane-polarized light. Similar force reversal effects are presumed to be observed for materials with high nonlinear refractive indices, in particular, low-dimensional materials. However, analytic modeling of nonlinear force/potential for two-dimensional materials is very different from nanosphere [129].
Note that this reversal of force is solely due to the nonlinear nature of gradient force at an excitation wavelength far from resonance and not due to the scattering force; hence, this should not be confused with Fano resonance which arises due to interference between background and resonance scattering amplitudes leading to asymmetric spectral profiles [130, 131]. A detailed discussion is given in appendix E for the probability of occurrence of Fano-resonance in core-shell and hollow-core type nanoparticles.

3.5 Conclusion

We have shown that under high-repetition-rate ultrafast pulsed excitation, in addition to repetitive instantaneous trapping, how OKE dramatically modulates the efficiency of optical trapping of dielectric nanoparticles. We have correctly identified the height of the potential barrier along beam propagation direction to be the most relevant quantity considering trapping efficiency which nicely correlates with previous experimental findings. We have estimated the optimal average power levels that lead to most stable dipole trap which is extremely important in direct trapping of dielectric nanoparticles. We also predict OKE assisted stable trapping of nanoparticles that are difficult to trap otherwise.
From the above discussion, we have concluded that particles having RI less than the surrounding medium show repulsive nature of force/potential curve under CW excitation, but show attractive nature of force/potential under pulsed excitation for similar conditions. Under CW excitation, change in the RI of the particle results in a sudden change in the nature of force/potential curve from repulsive to attractive. However, under pulsed excitation, this transformation occurs gradually. Consequently, it can be observed that there is a certain regime

of RI where CW excitation is unable to trap while pulsed excitation is able to trap the nanoparticles under similar conditions. The case is reversed when RI of the particle is greater than the surrounding medium. Along with this, if particle has RI much higher than the surrounding medium, it cannot be trapped under both CW and pulsed excitation because scattering force dominates over gradient force and results in destabilizing the trap. Therefore, both CW and pulsed excitations have their own advantages and disadvantages depending upon the RI of the particle and surrounding medium. Similarly, for metamaterials, RI regimes exist corresponding to the different nature of force/potential curves. In comparison with dielectric particles, the range of RI is the same for metamaterial particles under CW excitation but different under pulsed excitation for all regimes.

Also, we have theoretically shown an advantage of pulsed excitation for stable trapping of different types of nanoparticles by utilizing optical nonlinearity. Considering the reversal of force for hollow-core nanoparticles, we envision far-reaching applications of this method for facile optical manipulation and optical sorting in a user defined way.

4 Force and potential on arbitrary sized dielectric particles using generalized Lorenz Mie theory

4.1 Introduction

Followed by the chapter 3, here, we have demonstrated the similar phenomena in hybrid nanoparticles using GLMT using localized approximation. Experimentally researchers have reported that trapping efficiency is better while using a pulsed laser rather than CW at similar average power [68, 77, 81]. It might appear puzzling at first glance because under pulsed excitation, the trap should appear and disappear depending upon the repetition rate of the laser beam, and this would seem a disadvantage. To explain the experimental observation, our group had proposed a model that under CW excitation, a potential well gets created, which is present as long as the laser beam is on. In contrast, under pulsed excitation, a steeper potential well gets created [74]. However, the time interval between two consecutive pulses is not enough for the trapped particles to diffuse out of the trap. Very recently, researchers have studied the bio-conjugated core-shell microparticles, and it was observed that they enhance trapping ability. Most importantly, high force experiments can be performed by tethering with biological complex compounds, and these particles exhibit higher trap stiffness compared to conventional beads [132]. In the field of optical tweezer, core-shell and hollow-core nanoparticle dynamics are still unexplored. Here in this chapter, we have rigorously studied the role of nonlinearity under pulsed excitation and demonstrated a potential advantage of pulsed excitation over CW excitation because hollow-core nanoparticles cannot be trapped under CW excitation. However, under pulsed excitation, the trapping force can be reversed by harnessing OKE, which can be utilized for controlled manipulation of hollow-core nanoparticles. This unique feature of controlling the reversal of trapping force/potential opens up a new world in biology for performing high force experiments and in performing medical therapies.

4.2 Core type nanoparticles

A mathematical formulation for GLMT using localized approximation was explained in chapter 2. Here, we are using the same formulation for both CW excitation (ignoring OKE) and pulsed excitation (including OKE). All the parameters used in force and potential simulations are listed in table 2.1. Note that the specific choice of particle size allows us to directly compare the GLMT results with dipole approximation because the effects of diffraction in GLMT can be ignored. Our method still holds for a range of particle size as long as these two conditions are met: $\alpha \ll 1$ and $\rho \ll 1$ [99]. Also, we neglect any possibility of Mie resonance as: although $\alpha \ll 1$, $(m-1) \ll 1$ [99]. Moreover, we do not take into account any other nonlinear effect (i.e., resonance and plasmonic effect) found for optical trapping of metallic nanoparticle [133]. Also, a force arising due to recoil effects from nonlinear scattering (hyper Raman scattering) and absorption (multiphoton absorption) is neglected. We have numerically evaluated the axial force/potential under CW excitation (ignoring OKE) and under pulsed excitation (including OKE, for polystyrene only).

4.2.1 Under CW excitation

Here, in figures 4.1 to 4.4, green/blue/red curves represent gradient/scattering/-total force/potential; the dotted curves represent force/potential evaluated using dipole approximation while the solid ones represents the same, evaluated using localized approximation.

In figure 4.1, we have shown force and potential curves at 100 mW average power under CW excitation. We see that there is a deviation for force/potential using these two methods, which increases with an increase in particle size. To quantify this deviation, we have calculated the potential values in the asymptotic region (z= 10 μm) for both methods shown in table 4.1. Note that we take the zero potential to be the potential at z= -10 μm. We have observed that in case of dipole approximation gradient force/potential is symmetric along the axial direction but in localized approximation gradient force/potential is asymmetric along the axial direction and this asymmetry increases with an increase in particle size. This is because, in dipole approximation, the particle is considered to be a point dipole. Hence, an increase in particle size increases only the polarizability volume (or the dipole moment), and the nature of the force/potential is not changed. In contrast, in GLMT, the force/potential depends on the particle size

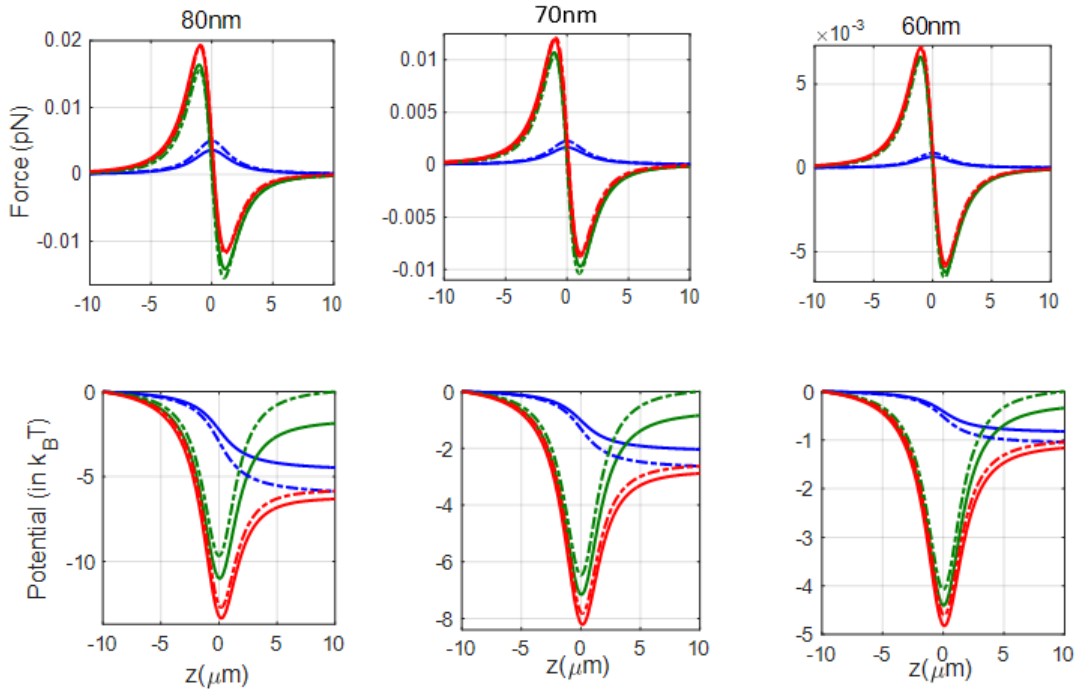

Fig. 4.1.: Plots of axial trapping force (top) and potential (bottom) at 100 mW average power under CW excitation.

through the scattering coefficients (a_n and b_n). Hence, an increase in particle size results in changing the nature of the force/potential.

Particle Size	80 nm		70 nm		60 nm	
Potential (in k_BT)	Dipole	GLMT	Dipole	GLMT	Dipole	GLMT
Scattering	-5.8625	-1.8544	-2.6311	-0.8450	-1.0434	-0.8234
Gradient	0	-4.4679	0	-2.0433	0	-0.3395
Total	-5.8625	-6.3223	-2.6311	-2.8883	-1.0434	-1.1629

Tab. 4.1.: Potential values in asymptotic regime (z=10 μm) at 100 mW average power under CW excitation.

4.2.2 Under pulsed excitation

In figure 4.2, we have shown force and potential curves at 100 mW average power under pulsed excitation. We have seen a similar deviation for force/potential using these two methods increases with an increase in particle size. However, quite interestingly, the deviation is almost negligible in the total asymptotic force/potential as the deviations contributed by scattering and gradient components compensate for each other. As before, we have calculated the asymptotic values of the potential, as shown in table 4.2. With the CW excitation, we observe

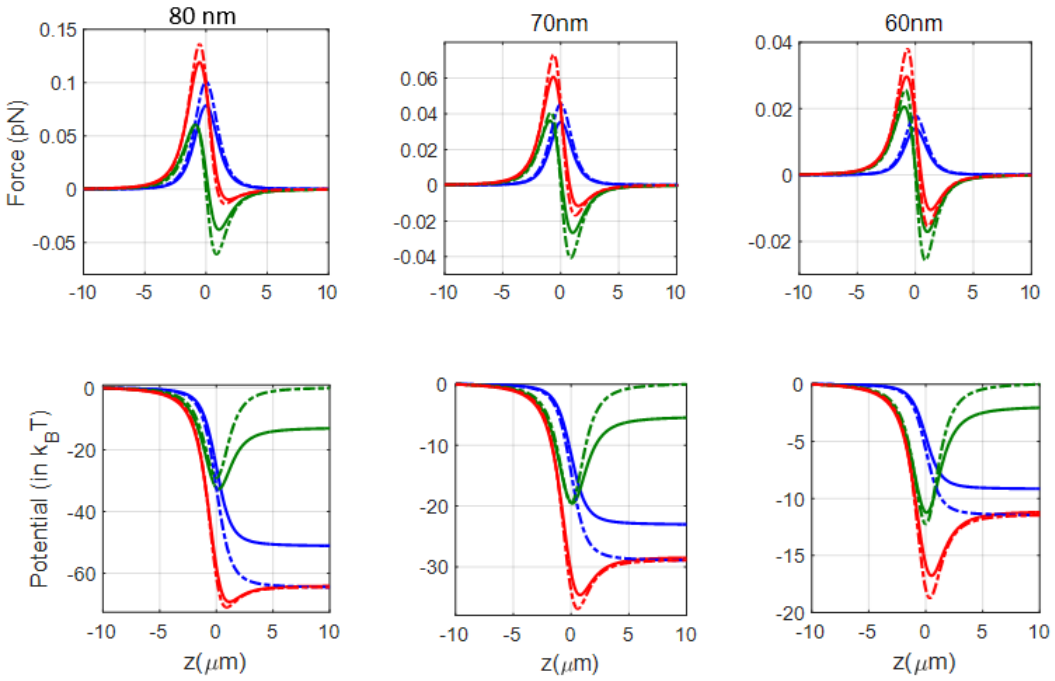

Fig. 4.2.: Plots of axial trapping force (top) and potential (bottom) at 100 mW average power under pulsed excitation.

that in case of dipole approximation gradient force/potential is symmetric about the axis, but in localized approximation gradient, force/potential is asymmetric. In the case of pulsed excitation, this asymmetry in gradient force/potential is more as compared to CW excitation at similar average power.

4.2.2.1. Variation of power

From figures 4.3 and 4.4, it can be seen that on increasing the power, the magnitude and nature of the force/potential curves change dramatically. Quite interestingly, the gradient force/potential exhibits oscillatory behavior near the focus, which increases with power for fixed particle size and increases with decreasing particle size for a fixed power.

4.2.2.2. Origin of deviation

Now, to explain the origin of this oscillatory nature of force/potential, let us focus on the expressions of force (equation 2.31). We see that the force depends on two parameters: beam shape coefficients (g_n) and scattering coefficients ($S_n^{(1)}$ and $S_n^{(2)}$).

In figures 4.5 to 4.7, we have plotted the relevant pairs of these coefficients according to expressions for force, *i.e.*, $|g_n|^2$ & $S_n^{(1)}$, $Re\left(g_n g_{n+1}^*\right)$ & $Re\left(S_n^{(2)}\right)$

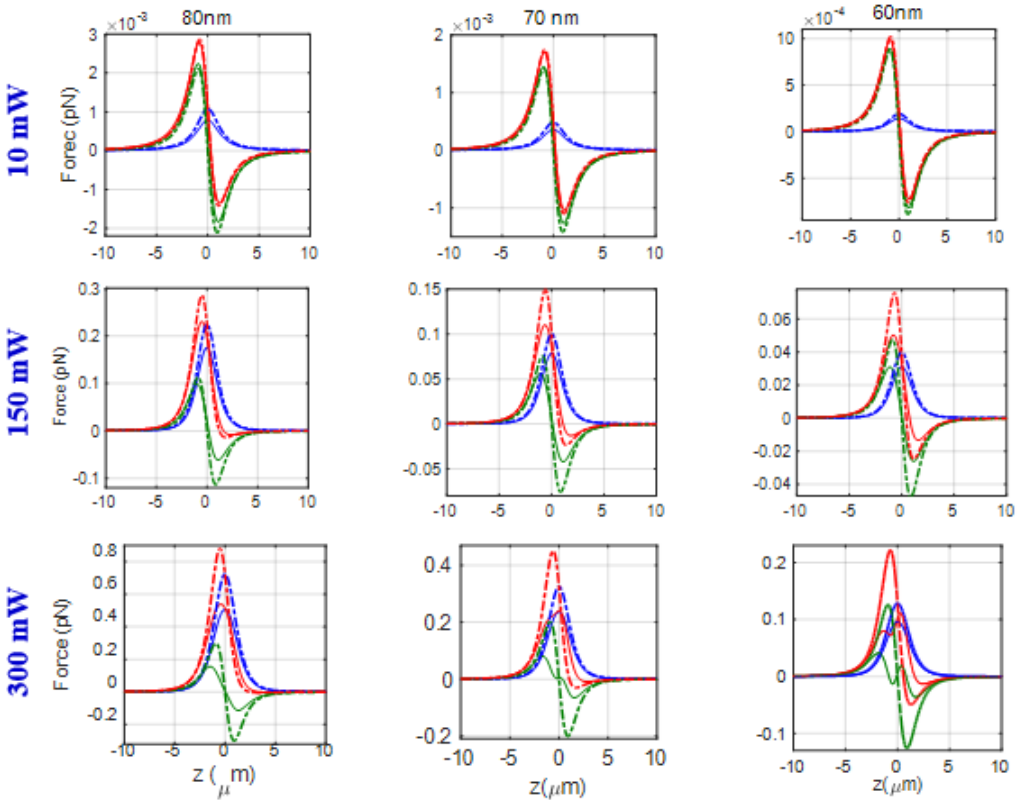

Fig. 4.3.: Plots of axial trapping force at three different average power under pulsed excitation.

Particle Size	80 nm		70 nm		60 nm	
Potential (in k_BT)	Dipole	GLMT	Dipole	GLMT	Dipole	GLMT
Scattering	-64.4205	-51.0458	-28.9116	-23.0138	-11.4655	-9.1570
Gradient	0	-13.0619	0	-5.4944	0	-2.0523
Total	-64.4205	-64.1077	-28.6116	-28.9116	-11.4655	-11.2093

Tab. 4.2.: Potential values in asymptotic regime (z=10 μm) at 100 mW average power under pulsed excitation calculated for different theories (Dipole approximation, GLMT approximation).

and $Im\left(g_n g_{n+1}^*\right)$ & $Im\left(S_n^{(2)}\right)$ for three leading terms, n = 1, 2 and 3 shown in figures 4.5, 4.6, and 4.7, respectively, as higher order terms contribute less to the total force; (Line color: purple/red/green/blue corresponds to scattering coefficient ($S_n^{(1)}, Re(S_n^{(2)})$ and $Im(S_n^{(2)})$)at 10/150/300/500 mW average power, respectively, and black for beam shape coefficient ($BSC : |g_n|^2, Re(g_n g_{n+1}^*)$ and $Im(g_n g_{n+1}^*)$). Note that the beam coefficient is a constant of power which we plot as black curves in the leftmost column in each figure. We have plotted the scattering coefficients in the next three columns for three different particle sizes;

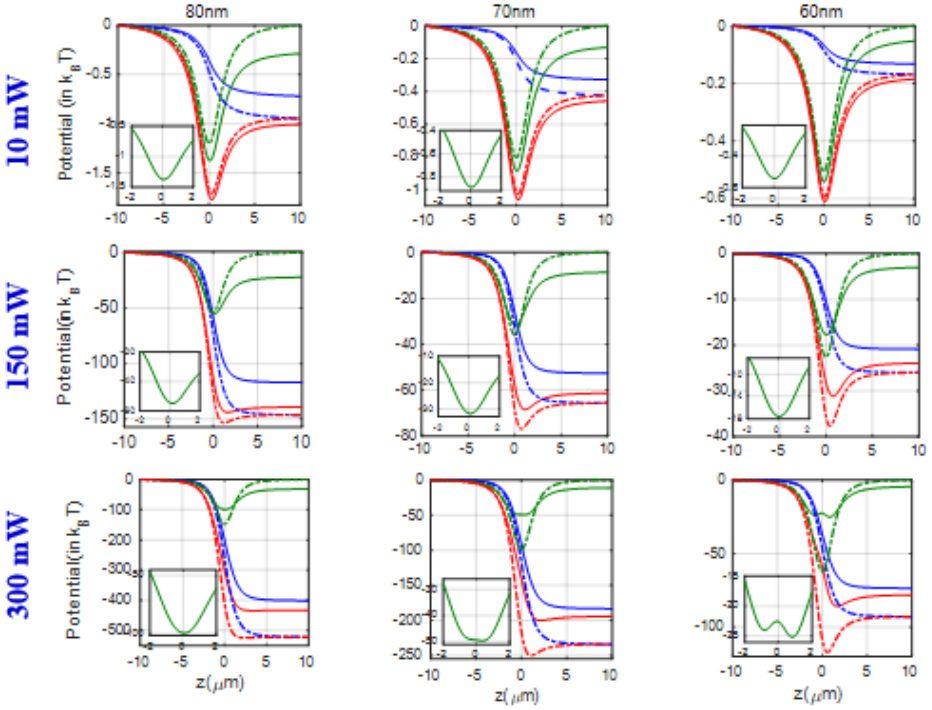

Fig. 4.4.: Plots of axial trapping potential at three different average power under pulsed excitation. The insets show the zoomed-in region of bottom of the gradient potential as well.

here purple, red, green and blue correspond to 10 mW, 150 mW, 300 mW and 500 mW average power, respectively. For any particle, for a specific power, the three relevant product terms are readily obtained by choosing the corresponding pairs; for example, if we want to explore the nature of axial scattering force for a 70 nm diameter particle at 150 mW average power, we have to consider the pair $|g_n|^2$ & $S_n^{(1)}$ (since, according to equation 2.31, product of these terms gives rise to axial scattering force) in the top row where $|g_n|^2$ is plotted in the leftmost column and $S_n^{(1)}$ is plotted as a red curve (150 mW) in the third column (70 nm particle). We have observed that the oscillatory behavior is contributed by both $S_n^{(1)}$, $S_n^{(2)}$.

4.2.2.3. Nature of potential

Based on previous experimental findings [13, 68, 74, 77, 80–83], it has recently been established that the stability of an optical trap under pulsed excitation depends on U_{esc} rather than U_{min} [99, 109]. In figure 4.8, we have compared the power variation of the minimum potential (U_{min}) and the escape potential (U_{esc}) calculated using the dipole approximation and GLMT for different particle size. In order to quantify the deviation between the numerical values of U_{min}

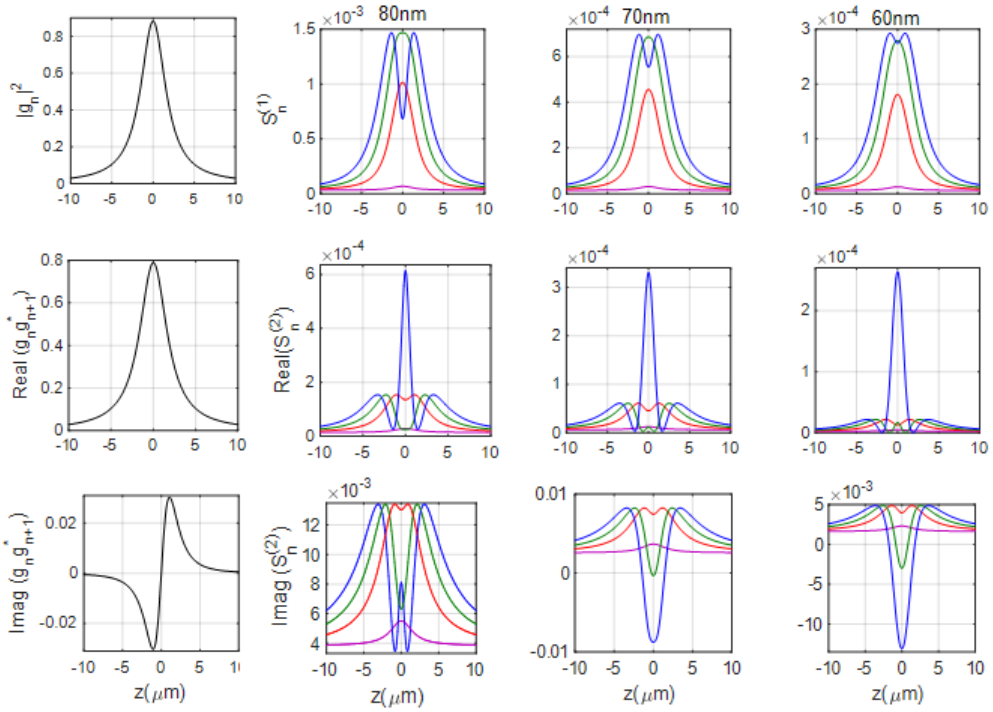

Fig. 4.5.: Plots of beam shape coefficients (BSC) and scattering coefficients at different average power under pulsed excitation for n=1.

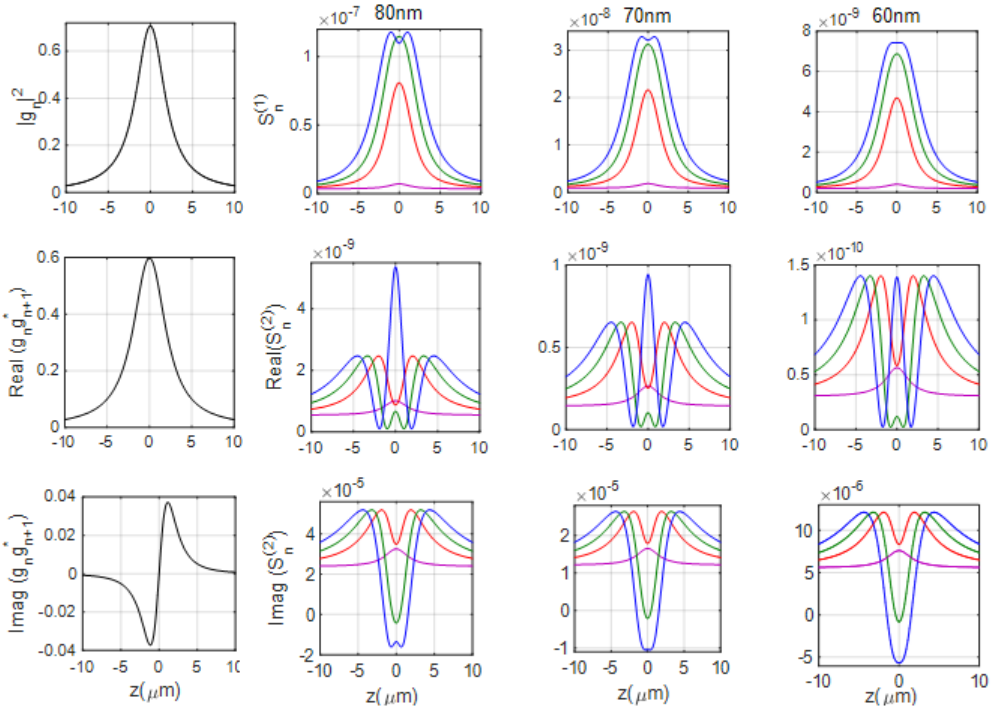

Fig. 4.6.: Plots of beam shape coefficients (BSC) and scattering coefficients at different average power under pulsed excitation for n=2.

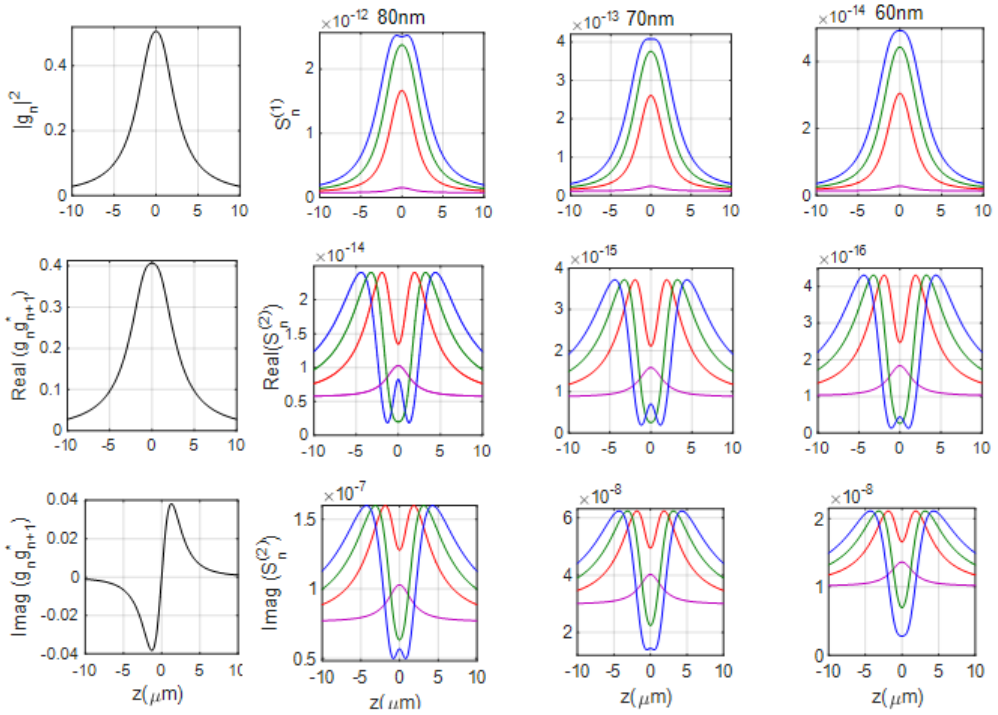

Fig. 4.7.: Plots of beam shape coefficients (BSC) and scattering coefficients at different average power under pulsed excitation for n=3.

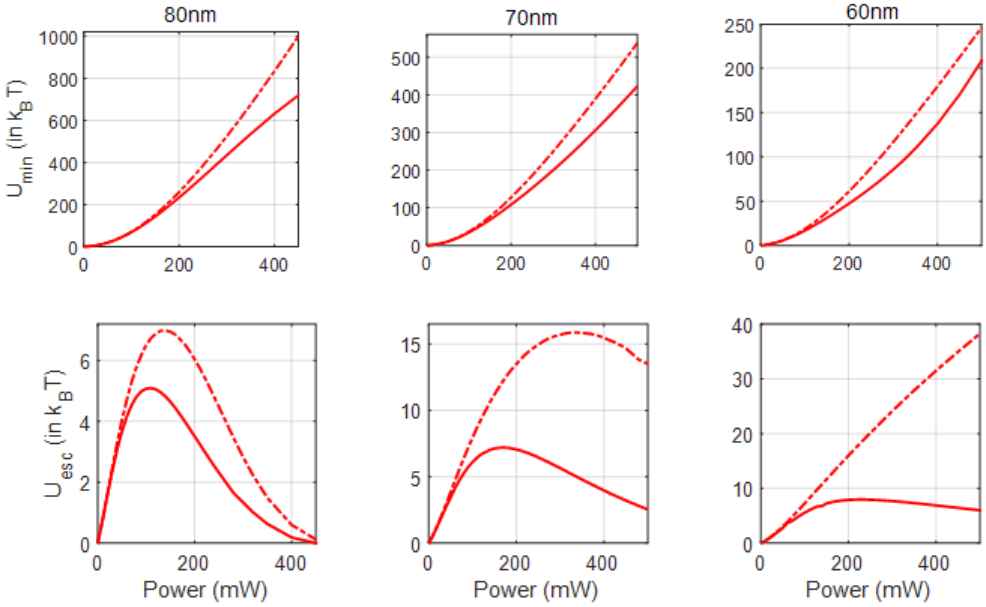

Fig. 4.8.: Plots of minimum potential (U_{min}) (top panel) and the escape potential (U_{esc}) (bottom panel) at different average power under pulsed excitation.

calculated using these two methods, we have compared the values at different power, as shown in table 4.3. It can be seen that with a decrease in the particle size, the deviation in U_{min} calculated using these two methods decreases.
Now, to quantify the deviation between the numerical values of U_{esc} calculated

using these two methods, we have compared the maxima of U_{esc}, the numerical values as well as the corresponding power. The difference increases with decreasing particle size, as shown in table 4.4. Also, we have explored the effect

Particle Size	80 nm			70 nm			60 nm		
Power (mW)	Dipole	GLMT	Diff.	Dipole	GLMT	Diff.	Dipole	GLMT	Diff.
10	1.71	1.77	-0.07	1.03	1.06	-0.04	0.59	0.61	-0.02
30	8.18	8.35	-0.17	4.70	4.75	-0.05	2.61	2.61	0.004
50	19.48	19.63	-0.15	10.78	10.62	0.15	5.8	5.62	70.18
80	46.38	45.86	0.52	24.6	23.59	1.01	12.75	11.79	0.96
100	70.93	69.18	1.75	36.86	34.62	2.24	18.7	16.8	1.9
120	100.45	96.56	3.89	51.3	47.2	4.12	25.7	22.3	3.4
150	153.2	143.8	9.38	76.82	68.49	8.34	37.69	31.21	6.48
180	214.73	196.64	18.08	106.13	91.92	14.21	51.33	40.77	10.55
200	259.96	234.11	25.85	127.44	108.48	18.96	61.19	47.47	13.72
450	998.53	718.85	279.68	462.75	363.27	99.48	212.62	170.36	42.26

Tab. 4.3.: Comparison between absolute potential maxima (unit in k_BT) at different average power for both GLMT using localized approximation and Dipole approximation.

Particle Size	80 nm			70 nm			60 nm		
Max.	Dipole	GLMT	Diff.	Dipole	GLMT	Diff.	Dipole	GLMT	Diff.
$U_{esc}(k_BT)$	6.985	5.0957	1.88	15.864	7.192	8.672	—	7.963	—
Optimal Power (mW)	140	110	30	330	170	160	—	220	—

Tab. 4.4.: Comparison between power corresponding to maxima and maxima of escape potential for both GLMT using localized approximation and Dipole approximation.

of OKE in CdS and compared with polystyrene nanoparticles because CdS and polystyrene both have higher second-order nonlinear RI (can be seen from table 2.1).

Figure 4.9 shows the trapping force and potential curves for 40 nm CdS and polystyrene nanoparticles. Under CW excitation, the magnitudes of force and potential are higher for CdS than polystyrene because RI for CdS is higher than polystyrene. Under pulsed excitation, including OKE shows a significant enhancement in the magnitude of the force and potential curves for polystyrene, however,

change is negligible for CdS nanoparticle because polystyrene has higher non-linear RI as compared to CdS. In previous theoretical works, we had defined the absolute depth of axial trapping potential as *absolute potential* (U_{abs}) and height of the axial trapping potential barrier (along beam propagation direction) as *escape potential* (U_{esc}). In figure 4.9, U_{abs} and U_{esc} is represented by longer and smaller double-sided arrow respectively.

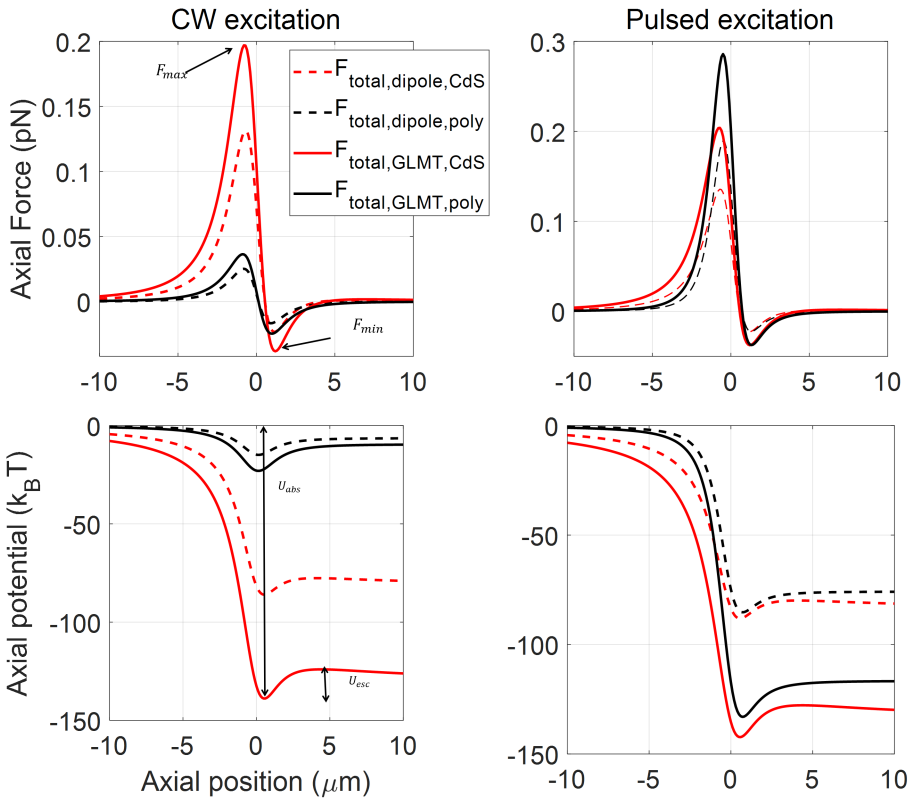

Fig. 4.9.: Plots of trapping force and potential for dipole and GLMT approximation under both CW and pulsed excitation.

A more rigorous analysis of force maxima, minima (shown in figure 4.9), and U_{esc} under both CW (tables 4.5 and 4.6) and pulsed (tables 4.7 and 4.8) excitations for different NA and particle size have been computed using both the theories for CdS and polystyrene. The force minima do not follow a similar trend throughout; thus, U_{esc} is the more appropriate quantity to characterize the stability of the optical trap. U_{esc} first increases with particle size then decreases, and there is a finite U_{esc} for all the particle sizes excepts NA is 1.1; eventually, it becomes unbound for larger particle size. Because for small-sized nanoparticles, the magnitude of the scattering force is less as compared to the gradient force, but increasing particle size increases the contribution of scattering force to the total force and a balance between both scattering and gradient force results in stabilization of the trap.

NA	PS (nm)	$F_{max}\ (pN)$			$F_{min}\ (pN)$			$U_{esc}\ (k_BT)$		
		Dipole	GLMT	Diff	Dipole	GLMT	Diff	Dipole	GLMT	Diff
1.1	10	4×10^{-4}	7×10^{-4}	2×10^{-4}	-4.3×10^{-4}	-6.7×10^{-4}	-2.4×10^{-4}	0.364	0.591	0.227
	20	0.004	0.006	0.002	-0.003	-0.005	-0.002	2.445	4.022	1.576
	30	0.018	0.029	0.011	-0.006	-0.010	-0.004	4.347	7.447	3.099
	40	0.065	0.104	0.039	8.5×10^{-4}	-4.1×10^{-5}	-8.9×10^{-4}	0.000	0.000	0.000
1.2	10	6×10^{-4}	10×10^{-4}	3×10^{-4}	-6.1×10^{-4}	-9.3×10^{-4}	-3.2×10^{-4}	0.442	0.706	0.265
	20	0.006	0.009	0.003	-0.004	-0.007	-0.002	3.053	4.943	1.891
	30	0.024	0.038	0.014	-0.010	-0.016	-0.006	6.198	10.376	4.179
	40	0.083	0.130	0.047	-0.004	-0.009	-0.004	0.000	0.000	0.000
1.3	10	9×10^{-4}	1.3×10^{-3}	4.2×10^{-4}	-8.5×10^{-4}	-1.3×10^{-3}	-4.1×10^{-4}	0.525	0.827	0.301
	20	0.008	0.011	0.004	-0.006	-0.009	-0.003	3.710	5.908	2.198
	30	0.032	0.048	0.017	-0.015	-0.023	-0.008	8.262	13.535	5.272
	40	0.105	0.161	0.056	-0.012	-0.021	-0.009	2.648	5.781	3.133
1.4	10	0.001	0.002	0.001	-0.001	-0.002	-0.001	0.615	0.951	0.336
	20	0.010	0.015	0.005	-0.008	-0.012	-0.004	4.420	6.907	2.486
	30	0.041	0.061	0.020	-0.022	-0.033	-0.011	10.535	16.883	6.348
	40	0.131	0.197	0.066	-0.023	-0.038	-0.015	7.020	12.760	5.740

Tab. 4.5.: The magnitude of force maxima, minima and escape potential under CW excitation at 100 mW average power for CdS.

NA	PS (nm)	$F_{max}\ (pN)$			$F_{min}(pN)$			$U_{esc}\ (k_BT)$		
		Dipole	GLMT	Diff	Dipole	GLMT	Diff	Dipole	GLMT	Diff
1.1	10	1.2×10^{-4}	1.9×10^{-4}	0.7×10^{-4}	-1.2×10^{-4}	-1.9×10^{-4}	-0.7×10^{-4}	0.105	0.169	0.065
	20	0.001	0.002	0.001	-0.001	-0.002	-0.001	0.798	1.296	0.498
	30	0.004	0.006	0.002	-0.003	-0.005	-0.002	2.355	3.865	1.509
	40	0.011	0.017	0.006	-0.005	-0.009	-0.003	4.095	6.987	2.892
1.2	10	1.8×10^{-4}	2.7×10^{-4}	9.2×10^{-5}	-1.7×10^{-4}	-2.7×10^{-4}	-9.1×10^{-5}	0.127	0.202	0.075
	20	0.001	0.002	0.001	-0.001	-0.002	-0.001	0.974	1.557	0.583
	30	0.005	0.008	0.003	-0.004	-0.006	-0.002	2.935	4.738	1.803
	40	0.015	0.022	0.008	-0.008	-0.013	-0.005	5.405	8.994	3.589
1.3	10	2.43×10^{-4}	3.6×10^{-4}	1.2×10^{-4}	-2.4×10^{-4}	-3.6×10^{-4}	-1.2×10^{-4}	0.150	0.236	0.085
	20	0.002	0.003	0.001	-0.002	-0.003	-0.001	1.162	1.828	0.666
	30	0.007	0.011	0.004	-0.006	-0.009	-0.003	3.563	5.650	2.087
	40	0.019	0.029	0.009	-0.012	-0.018	-0.006	6.843	11.128	4.285
1.4	10	3.3×10^{-4}	4.7×10^{-4}	1.5×10^{-4}	-3.2×10^{-4}	-4.7×10^{-4}	-1.4×10^{-4}	0.176	0.271	0.095
	20	0.003	0.004	0.001	-0.003	-0.004	-0.001	1.365	2.316	0.951
	30	0.010	0.014	0.004	-0.008	-0.012	-0.004	4.241	6.593	2.353
	40	0.025	0.036	0.011	-0.017	-0.025	-0.008	8.407	13.351	4.944

Tab. 4.6.: The magnitude of the force maxima, minima and the escape potential under CW excitation at 100 mW average power for polystyrene.

NA	PS (nm)	$F_{max}\,(pN)$			$F_{min}(pN)$			$U_{esc}\,(k_BT)$		
		Dipole	GLMT	Diff	Dipole	GLMT	Diff	Dipole	GLMT	Diff
1.1	10	4.5×10^{-4}	7.0×10^{-4}	2.5×10^{-4}	-4.4×10^{-4}	-6.8×10^{-4}	-2.4×10^{-4}	0.37	0.59	0.22
	20	0.004	0.007	0.003	-0.003	-0.005	-0.002	2.462	4.050	1.59
	30	0.018	0.030	0.012	-0.006	-0.010	-0.004	4.340	7.439	3.10
	40	0.066	0.106	0.040	0.001	0.000	-0.001	0.000	0.000	0.000
1.2	10	6.4×10^{-4}	9.7×10^{-4}	3.3×10^{-4}	-6.2×10^{-4}	-9.4×10^{-4}	-3.2×10^{-4}	0.045	0.71	0.26
	20	0.006	0.009	0.003	-0.004	-0.007	-0.003	3.079	4.986	1.907
	30	0.025	0.039	0.014	-0.010	-0.016	-0.006	6.205	10.392	4.187
	40	0.085	0.134	0.049	-0.004	-0.008	-0.004	0.000	0.000	0.000
1.3	10	8.8×10^{-4}	1.3×10^{-3}	4.1×10^{-4}	-8.6×10^{-4}	-1.3×10^{-3}	-4.0×10^{-4}	0.53	0.83	0.30
	20	0.008	0.012	0.004	-0.006	-0.009	-0.003	3.749	5.969	2.220
	30	0.033	0.050	0.017	-0.015	-0.024	-0.009	8.293	13.589	5.296
	40	0.108	0.166	0.058	-0.012	-0.021	-0.009	2.457	5.481	3.024
1.4	10	1.2×10^{-3}	1.7×10^{-3}	5.1×10^{-4}	-1.2×10^{-3}	-1.7×10^{-3}	-5×10^{-4}	0.62	0.95	0.33
	20	0.010	0.015	0.005	-0.009	-0.012	-0.003	4.474	6.991	2.517
	30	0.042	0.063	0.021	-0.022	-0.033	-0.011	10.597	16.987	6.390
	40	0.136	0.204	0.068	-0.023	-0.038	-0.015	6.808	12.441	5.633

Tab. 4.7.: The magnitude of the force maxima, minima and he escape potential under pulsed excitation at 100 mW average power for CdS.

NA	PS (nm)	$F_{max}\,(pN)$			$F_{min}(pN)$			$U_{esc}\,(k_BT)$		
		Dipole	GLMT	Diff	Dipole	GLMT	Diff	Dipole	GLMT	Diff
1.1	10	4.1×10^{-4}	6.4×10^{-4}	2.3×10^{-4}	-4×10^{-4}	-6.1×10^{-4}	-2.2×10^{-4}	0.264	0.423	0.159
	20	0.004	0.006	0.002	-0.003	-0.004	-0.001	1.824	2.951	1.127
	30	0.017	0.027	0.010	-0.006	-0.010	-0.004	3.904	6.533	2.629
	40	0.064	0.102	0.038	-0.004	-0.008	-0.004	2.636	5.191	2.555
1.2	10	6.4×10^{-4}	9.7×10^{-4}	3.3×10^{-4}	-6.2×10^{-4}	-9.3×10^{-4}	-3.1×10^{-4}	0.347	0.546	0.199
	20	0.006	0.009	0.003	-0.004	-0.007	-0.003	2.425	3.855	1.430
	30	0.026	0.040	0.014	-0.010	-0.015	-0.005	5.412	8.871	3.459
	40	0.095	0.148	0.053	-0.008	-0.014	-0.006	4.307	8.070	3.763
1.3	10	9.6×10^{-4}	1.4×10^{-3}	4.6×10^{-4}	-9.3×10^{-4}	-1.4×10^{-3}	-4.4×10^{-4}	0.446	0.687	0.241
	20	0.009	0.013	0.004	-0.007	-0.010	-0.003	3.146	4.905	1.759
	30	0.038	0.058	0.020	-0.015	-0.024	-0.009	7.261	11.664	4.403
	40	0.136	0.209	0.073	-0.013	-0.023	-0.010	6.514	11.744	5.230
1.4	10	1.4×10^{-3}	2.0×10^{-3}	6×10^{-4}	-1.4×10^{-3}	-1.9×10^{-3}	-5.8×10^{-4}	0.561	0.845	0.284
	20	0.012	0.018	0.006	-0.010	-0.014	-0.004	3.993	6.097	2.104
	30	0.054	0.080	0.026	-0.023	-0.035	-0.012	9.489	14.944	5.455
	40	0.190	0.286	0.096	-0.022	-0.037	-0.015	9.347	16.283	6.936

Tab. 4.8.: The magnitude of force maxima, minima and escape potential under pulsed excitation at 100 mW average power for polystyrene.

The further increase in particle size increases the scattering force, which results in the destabilization of the trap. Therefore, for a fixed average power and NA, there is a corresponding optimal particle size, which can be stably trapped. The trend for pulsed excitation is similar to CW excitation. However, the discrepancy between GLMT and dipole is more for polystyrene than CdS because nonlinear RI is more for polystyrene than CdS.

4.3 Mie Scattering Coefficient for hybrid nanoparticles

The mathematical formulation is discussed in chapter 2. The method for calculating the polarizability/Mie scattering coefficient (MSC) is different for core-shell and hollow-core type nanoparticles. MSC for core type particles can be calculated using [107, 134]:

$$a_n = \left(\frac{\psi_n(\alpha)\,\psi_n'(m\alpha) - m\psi_n'(\alpha)\,\psi_n(m\alpha)}{\varrho_n(\alpha)\,\psi_n'(m\alpha) - m\varrho_n'(\alpha)\,\psi_n(m\alpha)} \right) \tag{4.1}$$

$$b_n = \left(\frac{m\psi_n(\alpha)\,\psi_n'(m\alpha) - \psi_n'(\alpha)\,\psi_n(m\alpha)}{m\varrho_n(\alpha)\,\psi_n'(m\alpha) - \varrho_n'(\alpha)\,\psi_n(m\alpha)} \right) \tag{4.2}$$

where, $a = d/2$ is the radius of the core-type particle. For hybrid core-shell and hollow-core type nanoparticles, MSCs can be expressed as [99]:

$$a_n = \left(\frac{\psi_n(\alpha_2)\left[\psi_n'(m_2\alpha_2) - A_n\chi_n'(m_2\alpha_2)\right] - m_2\psi_n'(\alpha_2)\left[\psi_n(m_2\alpha_2) - A_n\chi_n(m_2\alpha_2)\right]}{\varrho_n(\alpha_2)\left[\psi_n'(m_2\alpha_2) - A_n\chi_n'(m_2\alpha_2)\right] - m_2\varrho_n'(\alpha_2)\left[\psi_n(m_2\alpha_2) - A_n\chi_n(m_2\alpha_2)\right]} \right) \tag{4.3}$$

$$b_n = \left(\frac{m_2\psi_n(\alpha_2)\left[\psi_n'(m_2\alpha_2) - B_n\chi_n'(m_2\alpha_2)\right] - \psi_n'(\alpha_2)\left[\psi_n(m_2\alpha_2) - B_n\chi_n(m_2\alpha_2)\right]}{m_2\varrho_n(\alpha_2)\left[\psi_n'(m_2\alpha_2) - B_n\chi_n'(m_2\alpha_2)\right] - \varrho_n'(\alpha_2)\left[\psi_n(m_2\alpha_2) - B_n\chi_n(m_2\alpha_2)\right]} \right) \tag{4.4}$$

$$A_n = \left(\frac{m_2\psi_n(m_2\alpha_1)\,\psi_n'(m_1\alpha_1) - m_1\psi_n'(m_2\alpha_1)\,\psi_n(m_1\alpha_1)}{m_2\chi_n(m_2\alpha_1)\,\psi_n'(m_1\alpha_1) - m_1\chi_n'(m_2\alpha_1)\,\psi_n(m_1\alpha_1)} \right) \tag{4.5}$$

$$B_n = \left(\frac{m_2\psi_n(m_1\alpha_1)\,\psi_n'(m_2\alpha_1) - m_1\psi_n(m_2\alpha_1)\,\psi_n'(m_1\alpha_1)}{m_2\chi_n'(m_2\alpha_1)\,\psi_n(m_1\alpha_1) - m_1\chi_n(m_2\alpha_1)\,\psi_n'(m_1\alpha_1)} \right) \tag{4.6}$$

here $\alpha_1 = k \times a_c$, $\alpha_2 = k \times a_s$, $m_1 = \frac{n^c}{n^w}$, and $m_2 = \frac{n^s}{n^w}$. We have calculated the force/potential for both CW excitation and pulsed excitation using both the methods. In case of CW excitation, only linear RI is considered; $n^{s/c/w/p} = n_0^{s/c/w/p}$, whereas in pulsed excitation, second-order nonlinear RI factor $n_2^{s/c/w/p}$ is also incorporated as $n^{s/c/w/p} = n_0^{s/c/w/p} + n_2^{s/c/w/p} \times I(r,z)$. Since the nonlinear RI for water and air is very less stable (refer to 2.1), it does not contribute to linear RI for 100 mW average power. Therefore, we can neglect it for pulsed excitation and can be approximated as $n^{w/air} \approx n_0^{w/air}$.

Hereafter, all the simulations are done by ignoring OKE under CW excitation and

NA	PS (nm)		$F_{max}\,(pN)$			$F_{min}(pN)$			$U_{esc}\,(k_BT)$		
	Core	Shell	Dipole	GLMT	Diff	Dipole	GLMT	Diff	Dipole	GLMT	Diff
1.1	5	10	1.7×10^{-4}	2.6×10^{-4}	9.5×10^{-5}	-1.6×10^{-4}	-2.6×10^{-4}	-9.3×10^{-5}	0.139	0.227	0.088
	10	20	0.001	0.002	0.001	-0.001	-0.002	-0.001	1.048	1.712	0.664
	15	30	0.005	0.008	0.003	-0.004	-0.006	-0.002	2.938	4.859	1.921
	20	40	0.016	0.025	0.009	-0.006	-0.010	-0.004	4.382	7.557	3.175
1.2	5	10	2.4×10^{-4}	3.6×10^{-4}	1.3×10^{-4}	-2.3×10^{-4}	-3.6×10^{-4}	-1.2×10^{-4}	0.169	0.271	0.102
	10	20	0.002	0.003	0.001	-0.002	-0.003	-0.001	1.281	2.062	0.781
	15	30	0.007	0.011	0.004	-0.005	-0.008	-0.003	3.703	6.024	2.321
	20	40	0.021	0.032	0.011	-0.010	-0.015	-0.005	6.067	10.197	4.130
1.3	5	10	3.3×10^{-4}	4.8×10^{-4}	1.6×10^{-4}	-3.2×10^{-4}	-4.8×10^{-4}	-1.6×10^{-4}	0.201	0.316	0.115
	10	20	0.003	0.004	0.001	-0.002	-0.004	-0.002	1.534	2.427	0.893
	15	30	0.010	0.015	0.005	-0.008	-0.011	-0.003	4.539	7.255	2.716
	20	40	0.028	0.042	0.014	-0.014	-0.022	-0.008	7.937	13.027	5.090
1.4	5	10	4.4×10^{-4}	6.3×10^{-4}	2×10^{-4}	-4.3×10^{-4}	-6.3×10^{-4}	-2×10^{-4}	0.235	0.363	0.128
	10	20	0.004	0.005	0.001	-0.003	-0.005	-0.002	1.804	2.805	1.001
	15	30	0.013	0.019	0.006	-0.010	-0.015	-0.005	5.438	8.530	3.092
	20	40	0.036	0.053	0.017	-0.020	-0.030	-0.010	9.998	16.032	6.034

Tab. 4.9.: The magnitude of the force maxima, minima and the escape potential under CW excitation at 100 mW average power for CdS-polystyrene.

including OKE under pulsed excitation along axial direction only, for both dipole and GLMT approximation. We choose NA=1.4 and the average power=100 mW under both CW and pulsed excitation unless mentioned otherwise. The mentioned dimension corresponds to the radius of the particle.

We will first mention the characteristic behavior that is observed in all systems and then elaborate on the individual behaviors that are unique to each system. In general, the magnitude of force/potential is higher for GLMT than the dipole for conventional, hybrid core-shell, and hollow nanoparticles under both CW and pulsed excitation. Although the nature of force and potential curves are the same for both dipole and GLMT approximations, there is a significant difference in the magnitudes. The magnitude of force maxima increases with an increase in particle size and NA. Consequently, the difference between force maxima (which quantifies the discrepancy between both the theories) calculated using GLMT and dipole also increases with increasing particle size and NA. In other words, the discrepancy is less for smaller sized nanoparticles.

4.4 Core-Shell type nanoparticles

Further, we consider hybrid core-shell nanoparticles immersed in water. We have chosen CdS-polystyrene and polystyrene-CdS because in CdS-polystyrene, RI of the core is greater than the shell $(n^c > n^s)$ and in polystyrene-CdS, it is other way around ($n^c < n^s$). In both systems, RI of the medium is less than the particle RI.

Figure 4.10 shows the trapping force and potential curves for hybrid core-shell

NA	PS (nm)		$F_{max}\,(pN)$			$F_{min}(pN)$			$U_{esc}\,(k_BT)$		
	Core	Shell	Dipole	GLMT	Diff	Dipole	GLMT	Diff	Dipole	GLMT	Diff
1.1	5	10	4.1×10^{-4}	6.5×10^{-4}	2.4×10^{-4}	-4.0×10^{-4}	-6.3×10^{-4}	-2.3×10^{-4}	0.338	0.55	0.212
	10	20	0.004	0.006	0.002	-0.003	-0.004	-0.001	2.299	3.791	1.492
	15	30	0.016	0.026	0.010	-0.006	-0.010	-0.004	4.382	7.534	3.152
	20	40	0.057	0.091	0.034	-0.001	-0.003	-0.002	0.000	0.000	0.000
1.2	5	10	5.8×10^{-4}	9×10^{-4}	3.13×10^{-4}	-5.7×10^{-4}	-8.7×10^{-4}	-3×10^{-4}	0.41	0.657	0.247
	10	20	0.005	0.008	0.003	-0.004	-0.006	-0.002	2.864	4.648	1.784
	15	30	0.022	0.034	0.012	-0.010	-0.015	-0.005	6.115	10.270	4.155
	20	40	0.074	0.115	0.041	-0.006	-0.012	-0.006	0.731	2.956	2.225
1.3	5	10	8×10^{-4}	1.2×10^{-3}	4×10^{-4}	-7.8×10^{-4}	-1.2×10^{-3}	-3.9×10^{-4}	0.487	0.769	0.282
	10	20	0.007	0.011	0.004	-0.006	-0.009	-0.003	3.474	5.543	2.069
	15	30	0.029	0.044	0.015	-0.014	-0.022	-0.008	8.044	13.213	5.169
	20	40	0.094	0.143	0.049	-0.014	-0.024	-0.010	4.248	8.812	4.564
1.4	5	10	4.4×10^{-4}	6.3×10^{-4}	2×10^{-4}	-4.3×10^{-4}	-6.3×10^{-4}	-2×10^{-4}	0.235	0.363	0.128
	10	20	0.004	0.005	0.001	-0.003	-0.005	-0.002	1.804	2.805	1.001
	15	30	0.013	0.019	0.006	-0.010	-0.015	-0.005	5.438	8.530	3.092
	20	40	0.036	0.053	0.017	-0.020	-0.030	-0.010	9.998	16.032	6.034

Tab. 4.10.: The magnitude of the force maxima, minima and the escape potential under CW excitation at 100 mW average power for polystyrene-CdS.

NA	PS (nm)		$F_{max}\,(pN)$			$F_{min}(pN)$			$U_{esc}\,(k_BT)$		
	Core	Shell	Dipole	GLMT	Diff	Dipole	GLMT	Diff	Dipole	GLMT	Diff
1.1	5	10	4.2×10^{-4}	6.4×10^{-4}	2.3×10^{-4}	-4×10^{-4}	-6.2×10^{-4}	-2.2×10^{-4}	0.278	0.446	0.168
	10	20	0.004	0.006	1.9×10^{-3}	-0.003	-0.004	-1.4×10^{-3}	1.916	3.110	1.194
	15	30	0.017	0.027	0.010	-0.006	-0.010	-3.7×10^{-3}	4.044	6.784	2.740
	20	40	0.064	0.102	0.038	-0.004	-0.007	-2.8×10^{-3}	2.249	4.510	2.261
1.2	5	10	6.4×10^{-4}	9.7×10^{-4}	3.3×10^{-4}	-6.2×10^{-4}	-9.3×10^{-4}	-3.2×10^{-4}	0.361	0.568	0.207
	10	20	0.006	0.009	2.8×10^{-3}	-0.004	-0.007	-2.7×10^{-3}	2.520	4.018	1.498
	15	30	0.026	0.040	0.014	-0.010	-0.016	-5.5×10^{-3}	5.590	9.199	3.609
	20	40	0.093	0.146	0.053	-0.007	-0.013	-6.1×10^{-3}	4.024	7.592	3.568
1.3	5	10	9.5×10^{-4}	1.4×10^{-3}	4.5×10^{-4}	-9.2×10^{-4}	-1.4×10^{-3}	-4.4×10^{-4}	0.458	0.707	0.249
	10	20	0.009	0.013	3.6×10^{-3}	-0.007	-0.010	-2.8×10^{-3}	3.235	5.061	1.826
	15	30	0.037	0.056	0.019	-0.015	-0.024	-8.7×10^{-3}	7.462	12.038	4.576
	20	40	0.132	0.202	0.070	-0.013	-0.023	-9.9×10^{-3}	6.374	11.532	5.158
1.4	5	10	1.0×10^{-3}	2×10^{-3}	9.7×10^{-4}	-1.0×10^{-3}	-1.9×10^{-3}	-9.1×10^{-4}	0.570	0.863	0.293
	10	20	0.012	0.018	5.6×10^{-3}	-0.010	-0.014	-3.9×10^{-3}	4.069	6.235	2.166
	15	30	0.053	0.077	0.024	-0.023	-0.035	-0.012	9.709	15.348	5.639
	20	40	0.183	0.273	0.090	-0.022	-0.037	-0.015	9.372	16.382	7.010

Tab. 4.11.: The magnitude of the force maxima, minima and the escape potential under pulsed excitation at 100 mW average power for CdS-polystyrene.

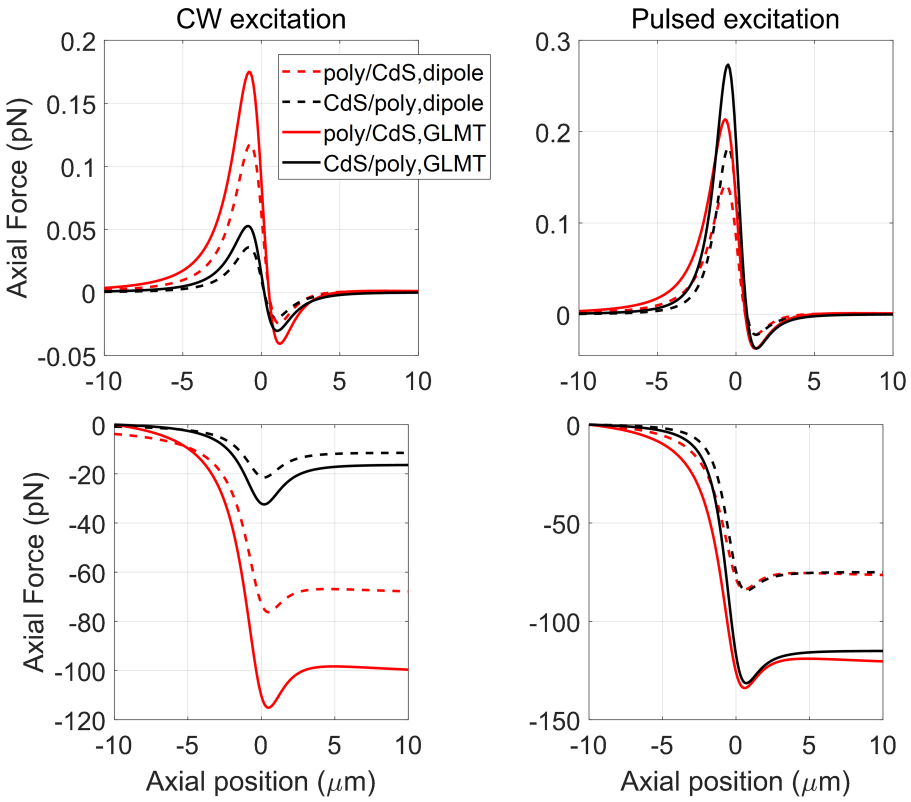

Fig. 4.10.: Plots of trapping force and potential for 20 nm core and 40 nm shell radius for dipole and GLMT approximation under both CW and pulsed excitation.

nanoparticles having core and shell radius equal to 20 nm and 40 nm, respectively. In force/potential calculations, the linear and nonlinear RI of the shell has a significant contribution as compared to the core. Therefore, under CW excitation, higher RI of shell results in a higher magnitude of the force, while under pulsed excitation, higher nonlinear RI of shell results in the higher magnitude of the force. This is because when the electromagnetic field is incident on the core-shell nanoparticles, it first interacts with the shell, which defines the angle of incidence for the inner core. If RI of the outer shell is more than that of the inner shell, then light bends toward the normal, and vice versa. When light bends towards the normal, gradient force is more as compared to when light bends away from the normal. Thus, under CW excitation, the magnitude of force and potential for polystyrene-CdS is higher than CdS-polystyrene. However, under pulsed excitation, the case is reversed due to the significant contribution of OKE, as nonlinear RI of the shell is higher in CdS-polystyrene as compared to polystyrene-CdS because nonlinear RI of polystyrene is higher than CdS by a factor of 10.

A meticulous analysis is performed by proportional variation of core-shell radii

NA	PS (nm)		$F_{max}\,(pN)$			$F_{min}(pN)$			$U_{esc}\,(k_BT)$		
	Core	Shell	Dipole	GLMT	Diff	Dipole	GLMT	Diff	Dipole	GLMT	Diff
1.1	5	10	4.5×10^{-4}	7×10^{-4}	2.5×10^{-4}	-4.3×10^{-4}	-6.7×10^{-4}	-2.4×10^{-4}	0.356	0.577	0.221
	10	20	0.004	0.006	0.002	-0.003	-0.005	-0.002	2.397	3.937	1.540
	15	30	0.018	0.029	0.011	-0.006	-0.010	-0.004	4.358	7.479	3.121
	20	40	0.066	0.105	0.039	0.000	-0.001	-0.001	0.000	0.000	0.000
1.2	5	10	6.4×10^{-4}	9.8×10^{-4}	-2.3×10^{-5}	-6.2×10^{-4}	-9.5×10^{-4}	5.4×10^{-5}	0.436	0.695	0.259
	10	20	0.006	0.009	0.003	-0.004	-0.007	-0.003	3.013	4.870	1.857
	15	30	0.025	0.039	0.014	-0.010	-0.016	-0.006	6.179	10.349	4.170
	20	40	0.086	0.135	0.049	-0.004	-0.009	-0.005	0.000	1.425	1.425
1.3	5	10	8.9×10^{-4}	1.3×10^{-3}	3.3×10^{-4}	-8.7×10^{-4}	-1.3×10^{-3}	-2.9×10^{-4}	0.523	0.821	0.298
	10	20	0.008	0.012	0.004	-0.006	-0.009	-0.003	3.691	5.863	2.172
	15	30	0.033	0.051	0.018	-0.015	-0.024	-0.009	8.239	13.492	5.253
	20	40	0.111	0.171	0.060	-0.012	-0.021	-0.009	3.223	7.000	3.777
1.4	5	10	1.2×10^{-3}	1.8×10^{-3}	7.6×10^{-4}	-1.2×10^{-3}	-1.7×10^{-3}	-7.1×10^{-4}	0.618	0.953	0.335
	10	20	0.011	0.015	0.004	-0.009	-0.013	-0.004	4.431	6.910	2.479
	15	30	0.044	0.065	0.021	-0.022	-0.033	-0.011	10.54	16.869	6.331
	20	40	0.142	0.213	0.071	-0.023	-0.037	-0.014	7.360	13.587	6.227

Tab. 4.12.: The magnitude of the force maxima, minima and the escape potential under pulsed excitation at 100 mW average power for polystyrene-CdS.

of nanoparticles for both CdS-polystyrene and polystyrene-CdS under both CW (tables 4.9 and 4.10) and pulsed (tables 4.11 and 4.12) excitation. Unlike the behavior of magnitude of force maxima, the trend shown by the magnitude of force minima is not uniform for CdS-polystyrene and polystyrene-CdS under both CW and pulsed excitation. The discrepancy in force minima between the two theories shows a similar trend for CdS-polystyrene under CW and pulsed excitation except at NA=1.1. However, for polystyrene-CdS, it shows a similar trend except at NA equal to 1.1 and 1.2. This is because, at low NA values, the beam is loosely focused, thereby reducing the magnitude of gradient force, which results in the destabilization of the trap. We have observed two trends in the behavior of U_{esc} : (i) U_{esc} increases with increasing particle size and NA, which means trap is getting stabilized, (ii) U_{esc} first increases, then decreases which means that the trap is getting stabilized first and then gets destabilized as elaborated in section 3.1.

Figure 4.11a shows the variation of U_{esc} against shell radius by fixing core radius as 5 nm. On comparison, the optimal particle size for CdS-polystyrene and polystyrene-CdS is different. It can be explained as follows: if RI of the shell is smaller, the stability of the optical trap is achieved at larger particle size due to an increase in the shell thickness that balances the bending of light, which results in stabilizing the trap. Figure 4.11b shows the variation of U_{esc} against core radius by fixing the shell radius to be 40 nm. The trend observed is remarkably different for CdS-polystyrene than polystyrene-CdS. We have already mentioned that shell nonlinearity contributes significantly to force/potential as compared

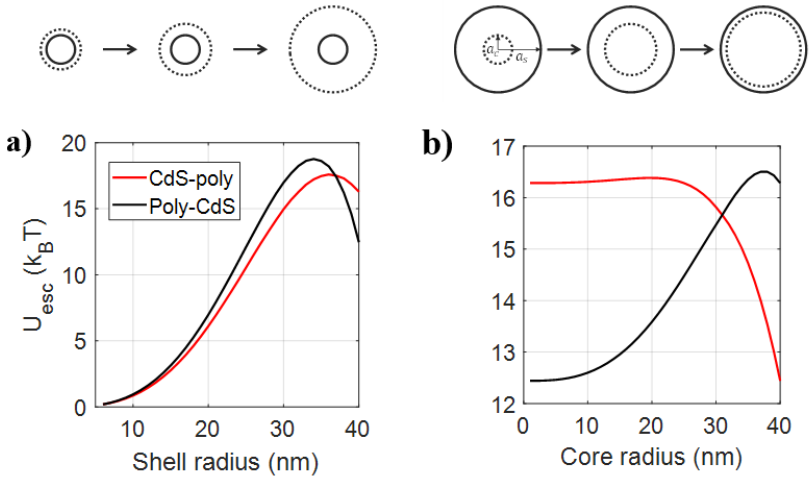

Fig. 4.11.: Plots of escape potential against core and shell radius variation under pulsed excitation.

to the core. So, in the case of CdS-polystyrene, the nonlinearity contribution decreases with increasing core radius, which results in rapid decrements in U_{esc}. However, in polystyrene-CdS, the case is reversed; increasing the core radius increases the contribution of nonlinearity, which results in increasing the U_{esc}. Thus, a particle having 20 nm CdS core and 40 nm polystyrene shell radius, can be trapped more efficiently than the 20 nm polystyrene core and 40 nm CdS shell radius (quantitatively can be seen from tables 4.5, 4.6, 4.7, and 4.8).

Figure 4.12 represents the trapping force for different core-shell sized nanopar-

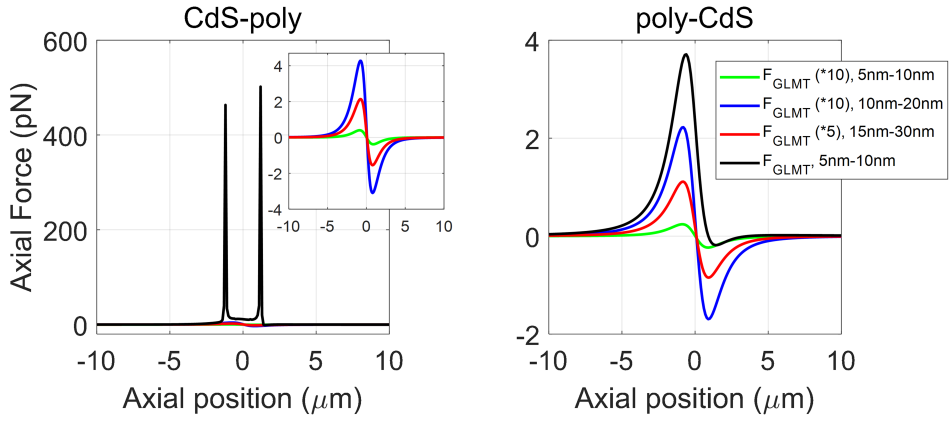

Fig. 4.12.: Plots of trapping force for different core and shell radius for GLMT approximation under pulsed excitation at 1000 mW average power. Just for clarity, we multiplied the force curves by constant factors. A factor of 10 multiplied to 5 nm - 10 nm, 10 nm - 20 nm core-shell and a factor of 5 to 15 nm - 30 nm core-shell nanoparticles.

ticles, calculated using GLMT approximation under pulsed excitation at 1000

mW average power. Under CW excitation, high average power results in the higher magnitude of the force; however, the nature of the force curve remains the same due to the linear proportionality of average power. Similar behavior is observed under pulsed excitation for polystyrene-CdS; however, for CdS-polystyrene increase in power leads to change in the magnitude as well as the nature of force curve. This change in the nature of the force curve is prominent in CdS-polystyrene than polystyrene-CdS. For CdS-polystyrene (20 nm core and 40 nm shell) at very high average power, gradient and scattering forces show spikes or oscillatory nature in force curves. Consequently, in the total force curve as well. The occurrence of these oscillations is due to MSC, which is discussed earlier in chapters 4 and 6, and this phenomenon could be due to Fano-resonance. Fano-resonance occurs due to the interference between background and narrow resonant mode. The MSC coefficient can be written as a summation of narrow resonance and slow varying background, which is equivalent to Fano-profile [130, 135]. It can also be understood in terms of excitation of anapole mode (anapole mode is non-radiative and emerges from the destructive interference of electric dipole and toroidal dipole, which results in enhancing the forward scattering efficiency) of the particle which is associated with Fano resonance. Consequently, backward scattering is reduced, which results in trapping the particles. These effects are prominent at high average power because at low average power, the optical transition between the discrete level is prominent, and background transitions are weak, which can be ignored. Continuous increases in average power saturate the discrete level transition after a threshold. However, continuum transition increases with average power, which results in appearing asymmetric line shape, which is known as Fano resonance [130, 135]. For a detailed discussion on Fano resonance, please refer to appendix E. Similar effects occur for smaller sized nanoparticles at very high average power. However, no such effect is observed in polystyrene-CdS due to less contribution of nonlinear RI from the outer layer. In contrast to this, no such effects are observed for dipole approximation because their force expression is described using polarizability, and no Fano-resonance occur under similar conditions.

4.5 Hollow-Core type nanoparticles

Figure 4.13 represents the trapping force and potential for hollow polystyrene (31 nm core and 40 nm shell) nanoparticles. Under CW excitation, particle shows the

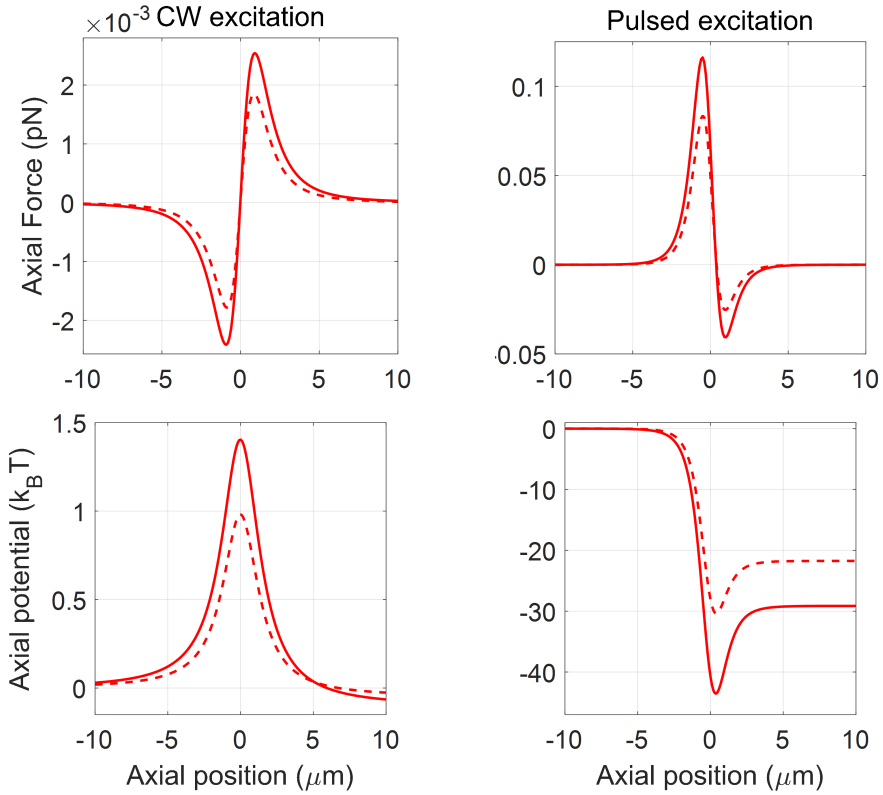

Fig. 4.13.: Plots of trapping force and potential for 31 nm core and 40 nm shell radius for dipole and GLMT approximation under both CW and pulsed excitation.

repulsive nature of force/potential curves while under pulsed excitation. It shows the attractive nature of force/potential curve under similar conditions due to the significant contribution of OKE. This reversal nature of force/potential signifies a clear advantage of pulsed excitation over CW excitation. Under CW excitation, even a small change in the thickness of the shell results in a drastic change in the nature of the force curve. The power variation of the potential curve for

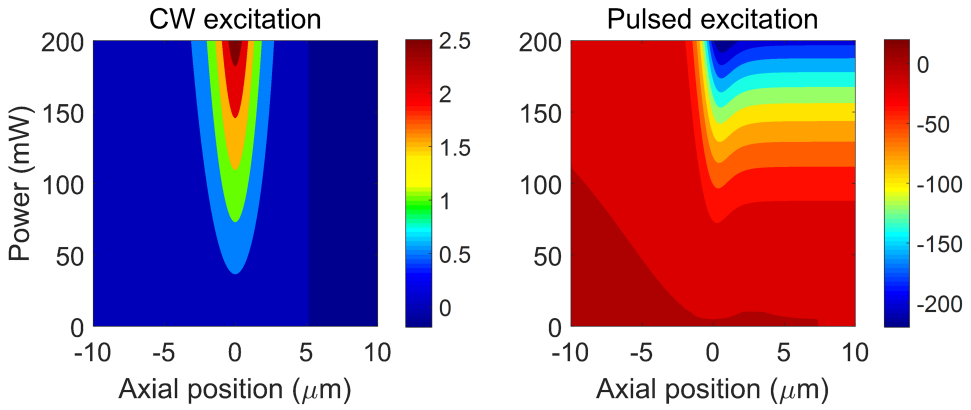

Fig. 4.14.: Plots of trapping potentials against axial position for 31 nm core and 40 nm shell under both CW and pulsed excitation at different average power.

31 nm core and 40 nm shell nanoparticles is shown in figure 4.14. Under CW excitation, although increasing power increases the magnitude of force/potential while the nature of potential becomes repulsive. Under pulsed excitation, at a very low average power, particle shows a repulsive potential curve. However, an increase in the power leads to a gradual change in the nature of the potential curve from repulsive to attractive. At very high average power (>1.5 W), hollow polystyrene nanoparticles also show a similar oscillatory or spike behavior in the force/potential curve, as shown in figure 4.12. Figure 4.15a shows plots of U_{esc}

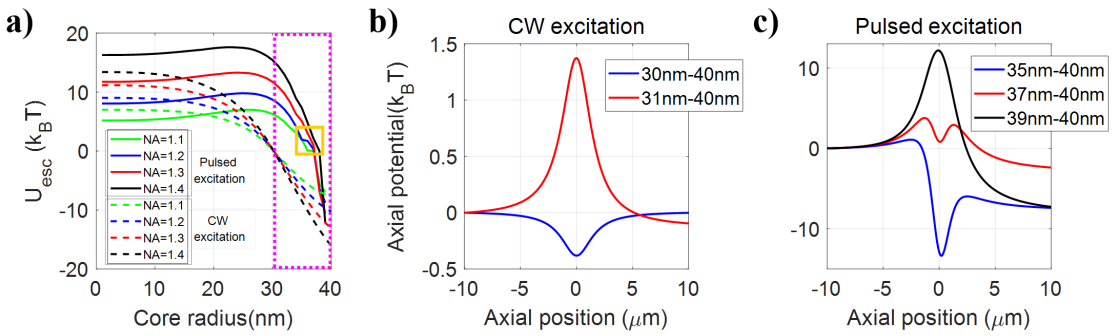

Fig. 4.15.: Plots of a) escape potential against core radius variation by fixing outer shell radius as 40 nm, b) trapping potential against axial position under CW excitation, and c) under pulsed excitation at 100 mW average power for fixed NA 1.4.

against core radius by fixing the shell radius to be 40 nm. Here, positive and negative values of U_{esc} indicate that the optical trap is attractive and repulsive, respectively. Under CW excitation, if the thickness of the shell is greater than 9 nm, the particle experiences an attractive force. Otherwise, force is repulsive (highlighted by the pink rectangle), which is independent of the average power and NA. The transition from repulsive to attractive is sudden, which can be seen from figure 4.15b. However, under pulsed excitation, under similar conditions, the force experienced by the particle is attractive rather than repulsive, and the yellow rectangle (figure 4.15a) shows the transition region where potential gradually changes from attractive to repulsive through the splitting of potential well as shown in figure 4.15c. It can be observed that at 100 mW average power and 1.4 NA, only 1 nm thickness of the shell shows repulsive force. For lower NA, if the thickness of the shell is less than 2 nm, it shows the repulsive nature of force, but an increase in average power results in an attractive force.

Further increase in average power shows no splitting behavior for similar particle size. This is because under pulsed excitation, increasing power shifts the maxima of U_{esc} towards the right, which results in stabilizing the trap even for very small-

sized hybrid nanoparticles. However, under CW excitation, an increase in average power results in increasing the magnitude of U_{esc}, but the nature of the curve remains the same.

Since polystyrene latex bead has vast applications in bio-conjugated experiments,

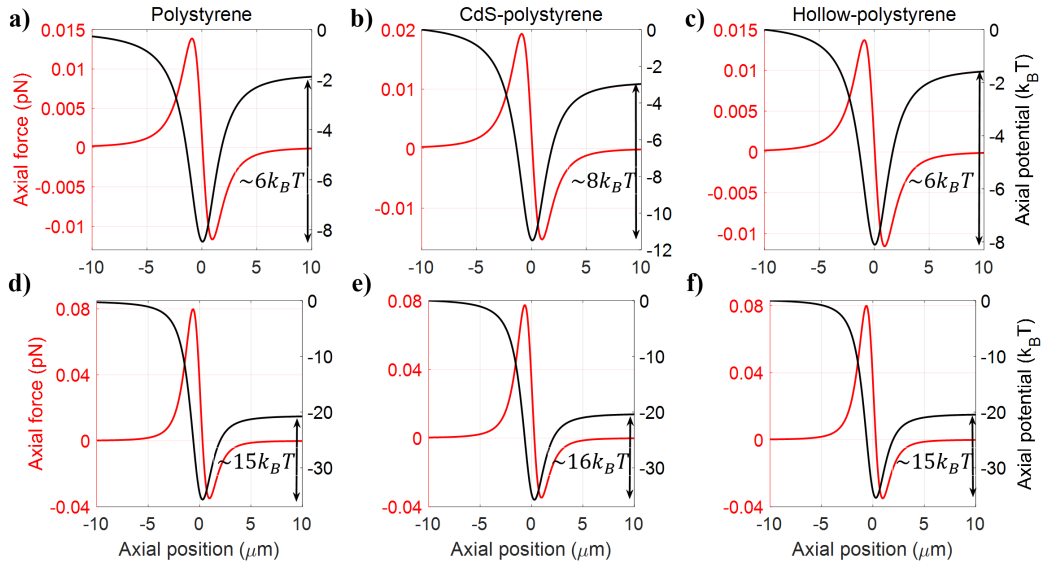

Fig. 4.16.: Plots of trapping force and potential under both CW (a-c) and pulsed (d-f) excitations, for 30 nm polystyrene (a, d), 15 nm -30 nm CdS-polystyrene (b, e), and 5 nm -30 nm hollow polystyrene nanoparticles (c, f).

in figure 4.16, trapping force and potential are calculated for the polystyrene (core-type), CdS-polystyrene (hybrid core-shell type), and hollow polystyrene nanoparticles having particle size equal to 30 nm under both CW (figure 4.16a-c) and pulsed (figure 4.16d-f) excitations. It can be observed that force experienced by the CdS-polystyrene is more than polystyrene, and corresponding U_{esc} is higher than polystyrene nanoparticle for both CW and pulsed excitations. However, hollow nanoparticle experiences the same force as experienced by polystyrene nanoparticle, but due to the hollow core, it has a potential application in drug delivery and cancer therapy. If we consider hollow nanoparticle of the size 25 nm - 40 nm, it experiences more force as compared to 40 nm polystyrene nanoparticle. From this discussion, we can conclude that by appropriate choice of the radius of core and shell, these nanoparticles can be used for high force experiments that can be performed by tethering with biological complex compounds and exhibit higher trap stiffness compared to conventional nanoparticles. Our results show an agreement with the established experimental results.

4.6 Conclusion

In summary, using GLMT (with L^{-} approximation), we have provided a generalized theory of OKE in laser trapping of dielectric spherical particles of arbitrary size and compared it with dipole approximation. We have found that the deviation between these two methods arises due to the incorporation of OKE, leading to the oscillatory nature of scattering coefficients in GLMT. Even though we have found quantitative disagreement between the two theories, both theories qualitatively predict that the axial trapping is destabilized with increasing power as a result of Kerr nonlinearity which was observed in experiments.

We have also theoretically investigated the trapping behavior of an optical trap for hybrid core-shell and hollow-core polystyrene nanoparticles using GLMT and compared with dipole approximation. The trapping force/potential is higher in GLMT than dipole approximation under both CW and pulsed excitation. In addition, the hybrid nanoparticles show higher trapping force/potential than conventional nanoparticles, which has a potential application for bio-conjugated complex compounds in which we tether the particles and perform high force experiments. The reversal of force for hollow-core nanoparticles shows an advantage of pulsed excitation for stable trapping of hollow nanoparticles by utilizing optical nonlinearity. Hollow nanoparticles are promising candidates for drug delivery in therapies. These results have potential applications in optical manipulation and optical sorting as well.

5 Force and potential on dielectric microspheres using geometric optics approximation

5.1 Introduction

In this chapter, extending our previous work to the geometric optics (GO) or ray optics limit ($\lambda \ll d$), we show how OKE plays an important role in the laser trapping under pulsed excitation, which is not observed under CW excitation at a similar power level. Note that the role of Kerr effect in optical trapping under CW excitation was discussed earlier, for an idealized particle with quite high Kerr nonlinearity ($6.5 \times 10^{-5} m^2 W^{-1}$) [136]. Although Kerr effect depends on peak intensity, changing the intensity by pulse-chirping did not reveal any effect on trapping of a silica microsphere [77] because silica particles have very low nonlinear refractive index *i.e.*, $2 \times 10^{-20} m^2 W^{-1}$ [137]. Estimating the force acting on the micron-sized particle by considering rays distribution on a 2D plane with equal power for each ray, which would be the case for a laser beam with a flat-top intensity profile. Whereas, in practice, researchers use the Gaussian beam profile for optical trapping, which is also discussed later in this chapter. Also, a focused beam can be better modeled as concentric 3D light cones instead of 2D rays. Therefore, we provide a systematic refinement of this model, taking into account specific transverse intensity distribution for both flat-top and Gaussian beam profile. To verify the 3D distribution of light cone method, we have also provided a comparison of this formalism with the EMT (mathematical formalism discussed in detail in chapter 2). We further apply this generalized formalism to account for an OKE, which is non-negligible under femtosecond pulsed excitation.

5.2 GO 2D distribution: flat-top beam profile

All the parameters used in force and potential simulations are listed in table 2.1. Here, we have numerically computed optical force and potential using plane wave approximation [95, 96]. The ray diagram for trapping of a particle in the absence and in presence of the particle is shown in figure 5.1a and figure 5.1b,

respectively. The trapping laser beam is considered to be made of many rays, all of which have the same power but different direction. Each ray makes a different angle (φ) w.r.t. the beam axis which varies from zero for the central ray ($\varphi = 0$) to a maximum angle for the terminal ray ($\varphi = \varphi_{max}$); φ_{max} can be calculated as: $\varphi_{max} = sin^{-1}\left(\frac{NA}{1.515}\right)$ where refractive index of oil is taken to be 1.515, and NA for oil-immersion objective is 1.4 (which is 0.924 in air and 1.228 in water) which yields $\varphi_{max} = 67.5 \times \pi/180$. We consider 101 different rays with different angles ranging from $\varphi = 0$ to $\varphi = \varphi_{max}$ at regular interval ($\Delta\varphi = \frac{\varphi_{max}}{100}$).

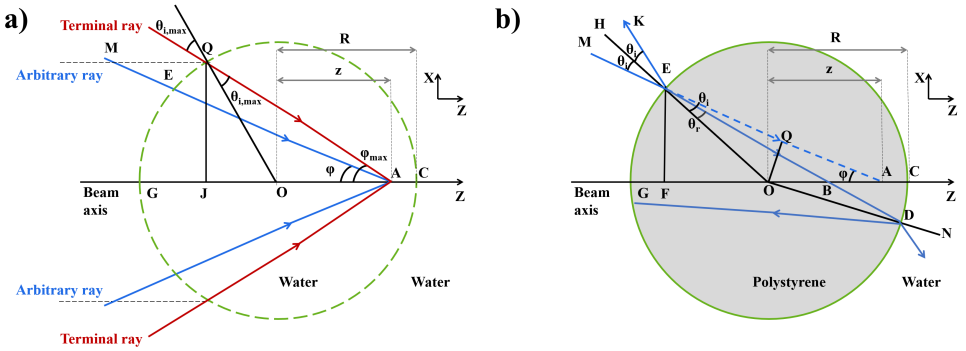

Fig. 5.1.: Ray diagram for trapping (a) in absence of particle and (b) in presence of a particle

Calculation of P_{ray}

The total power is equally distributed among these 101 rays: $P_{ray} = \frac{P_{total}}{101}$.
Note that in order to estimate the three-dimensional force/potential, we consider the rays to be distributed on a two-dimensional plane as such 2D distribution of rays is symmetric for rotation about the z-axis.
As shown in figures 5.1a and 5.1b, we define the distance between the center of the particle (point O) and the focal point in absence of the particle (point A) as a variable parameter (z), which we take positive if the center of the particle is towards the right of the focal point; note that, as shown in figure 5.1(a and b), z is negative in this convention. Figure 5.1b shows the path that the arbitrary ray of light follows when the particle is present. We account for multiple internal reflections. ME the path of the incident ray, EK the reflected ray, EBD the path of the refracted ray, OEH the normal to the surface, θ_i the angle of incidence and θ_r the angle of refraction; these angles are related by Snell's law: $n^w sin\theta_i = n^p sin\theta_r$ where n^w and n^p are the refractive indices of water and polystyrene respectively. We notice that: $\angle AEO = \theta_i, \angle EAO = \varphi, \angle OEB = \theta_r,\ \angle BEA = \theta_i - \theta_r$, and,

using exterior angle theorem, $\angle EBO = \varphi + (\theta_i - \theta_r)$, $\angle EOF = \varphi + \theta_i$. Now, by using the triangle property in Δ EOA (using OQ perpendicular to MEA), we get the relation between θ_i and φ : $Rsin\theta_i = -zsin\varphi$ where R is the radius of the particle. The area of the curved surface covered by laser beam falling on the particle can be calculated by integrating over the solid angle in spherical polar coordinate:

$$A_1 = |AQ|^2 \int_0^{2\pi} d\phi' \int_0^{\varphi_{max}} sin\varphi d\varphi = 2\pi |AQ|^2 (1 - cos\varphi_{max}) \tag{5.1}$$

Here, $|AQ|$ can be calculated from: $|AQ|sin\varphi_{max} = Rsin(\varphi_{max} + \theta_{i,max})$ where $Rsin\theta_{i,max} = -zsin\varphi_{max}$. Using this parameter, we define the intensity:

$$I(z;\varphi) = T' \times \left(\frac{P_{total}}{A_1 + A_0}\right) \tag{5.2}$$

where T' is the transmitted power inside the particle, P_{total} is the average power (for CW excitation) or peak power (for pulsed excitation) of the entire beam. $A_0 = \pi\omega_0^2$ is a constant equivalent to the area of diffraction-limited focal spot size; for plane wave, $\omega_0 = 0.61 \times \frac{\lambda}{NA}$ and for Gaussian beam $\omega_0 = 0.82 \times \frac{\lambda}{NA}$. Ideally, the area should vanish at the focal point, but in practice, this is not true. Therefore, A_0 denotes that constant area at the focal plane. This constant area term is phenomenological included to avoid the singularity in force/potential curves caused by vanishing area (and thereby blowing up the intensity) near $z/R = \pm 1$. The total force acting on the particle is the addition of scattering and gradient forces, which discussed in chapter 2. To calculate power for one single ray, P_{total} can be replaced by P_{ray} , where P_{ray} is the average power (for CW excitation) or peak power (for pulsed excitation) of a single ray. The scattering and gradient components of the total force acting on the particle along axial direction are:

$$F_{gradient,ray}(z) = -F_{gradient} sin\varphi \tag{5.3}$$

$$F_{scattering,ray}(z) = F_{scattering} cos\varphi \tag{5.4}$$

The expression for $F_{gradient}$ and $F_{scattering}$ can be seen from equations 2.19 and 2.18, respectively. The radius of the particle is taken to be 4 μm. Including Kerr effect, the refractive index is given by: $n^{w/p} = n_0^{w/p} + n_2^{w/p} \times I(z;\varphi)$. Here, the refractive index depends upon the intensity of the ray. In the case of CW excitation, the nonlinear RI term is not comparable with the linear RI term

at low average power, as discussed earlier in chapter 3. So we approximate $n^w \approx n_0^w$. To include the Kerr effect under pulsed excitation, we first calculate the instantaneous force, which readily yields the time-averaged force just after multiplication by $(f \times \tau)$ (discussed rigorously in Chapter 2). The cumulative force is calculated by summing over 101 different rays:

$$F_{cum}(z) = \sum_{ray(m)} F_{ray(m)}(z) \tag{5.5}$$

5.2.1 Force and potential simulations under CW excitation

Here, the total force along Z direction is plotted in red, whereas the gradient and scattering components are plotted in green and blue, respectively. In figure 5.2, we show force acting on the particle due to different rays along with the cumulative force at 10 mW average power. In figure 5.3, we show the cumulative force at different average power under CW excitation (ignoring the Kerr effect). Under CW excitation, the cumulative force is directly proportional to power. A change in the average power leads to a change in the magnitude of the force, whereas the nature of the force curve remains the same.

5.2.2 Force and potential simulations under pulsed excitation

Figure 5.4 shows force acting on the particle due to different rays along with the cumulative force at 10 mW average power under pulsed excitation (including the Kerr effect, equation 2.54). It can be observed that for the central ray ($\varphi = 0$), only scattering force is present under both CW and pulsed excitations. Whereas, with increase in φ , the gradient force increases, and maximizes for the terminal ray ($\varphi = \varphi_{max}$). This means that rays away from the beam axis are responsible for pulling the particle towards the trap center and the rays near the beam axis are responsible for pushing the particle away from the trap center.

Figure 5.5 shows the cumulative force at different average power under pulsed excitation and corresponding potentials shown in figure 5.6. Under pulsed excitation, the cumulative force and potential are non-linearly proportional to average power. A change in the average power results in a change in the magnitude and nature of the force curve. Note that near the surfaces (at $z/R = \pm 1$), the

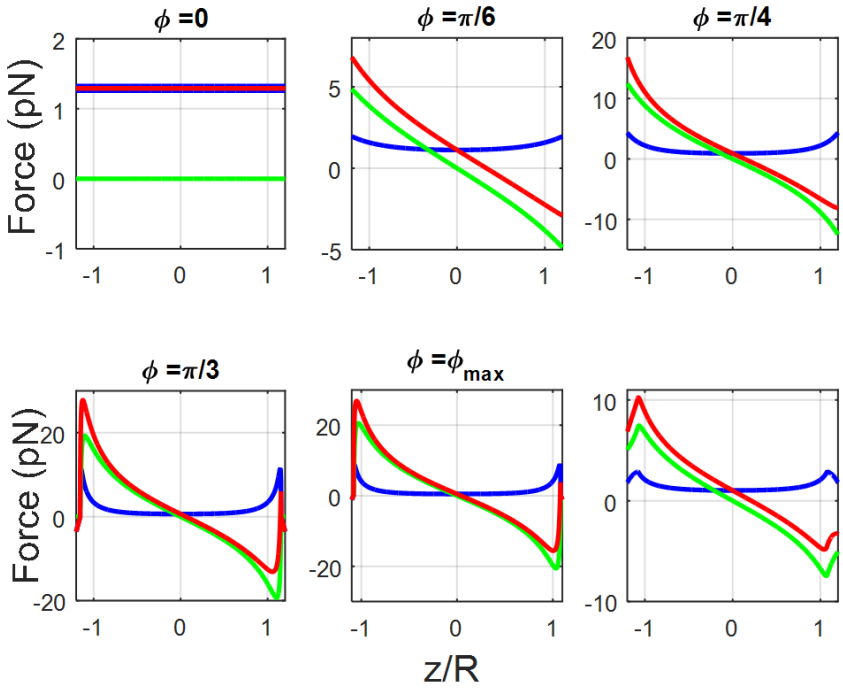

Fig. 5.2.: Plots of trapping force for different rays and the cumulative force at 10 mW average power under CW excitation. Color: green/blue/red curve corresponds to gradient/scattering/total force.

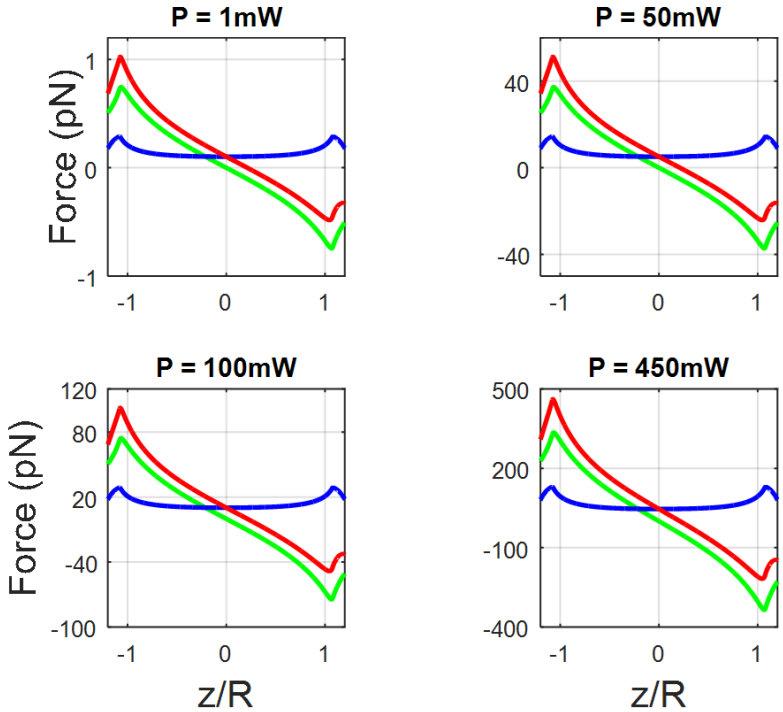

Fig. 5.3.: Plots of cumulative force at different average power under CW excitation. Color: green/blue/red curve corresponds to gradient/scattering/total force.

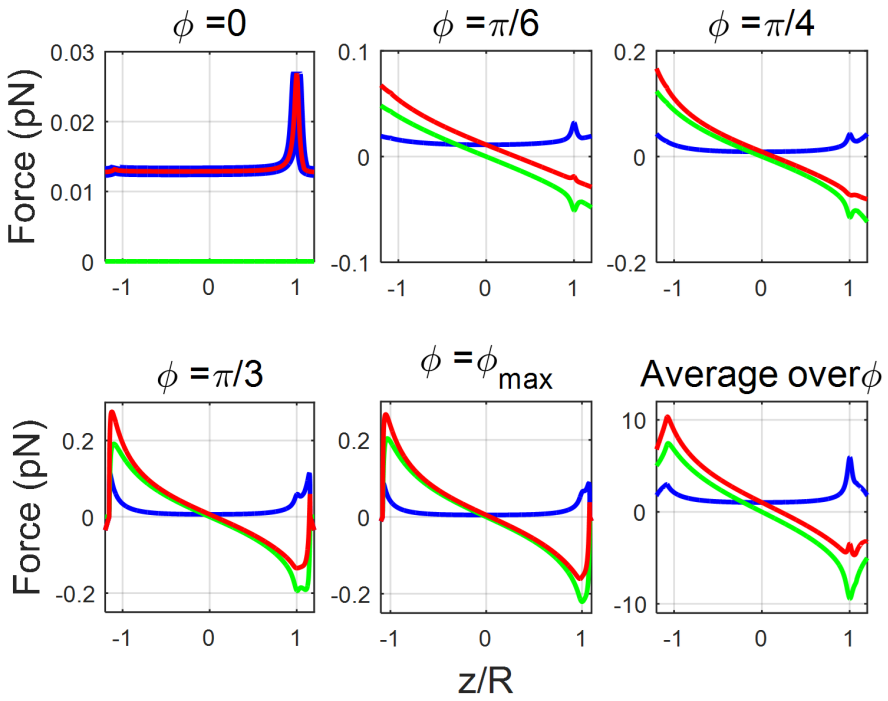

Fig. 5.4.: Plots of trapping force for different rays and the cumulative force at 10 mW average power under pulsed excitation. Color: green/blue/red curve corresponds to gradient/scattering/total force.

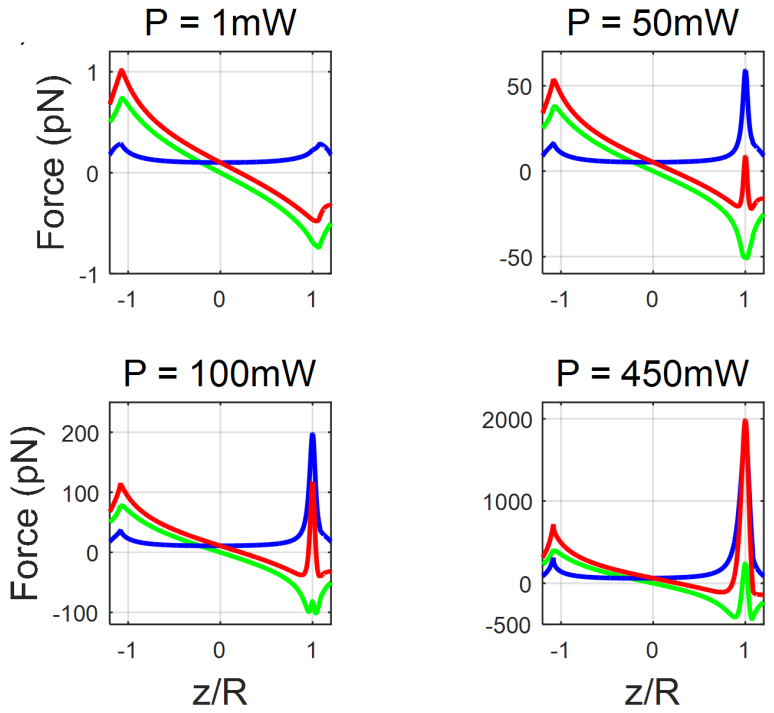

Fig. 5.5.: Plots of cumulative force at different average power under pulsed excitation. Color: green/blue/red curve corresponds to gradient/scattering/total force.

scattering force blows up due to vanishing area; consideration of the finite area ($A_0 = \pi\omega_0^2$) takes care of singularities at these points.

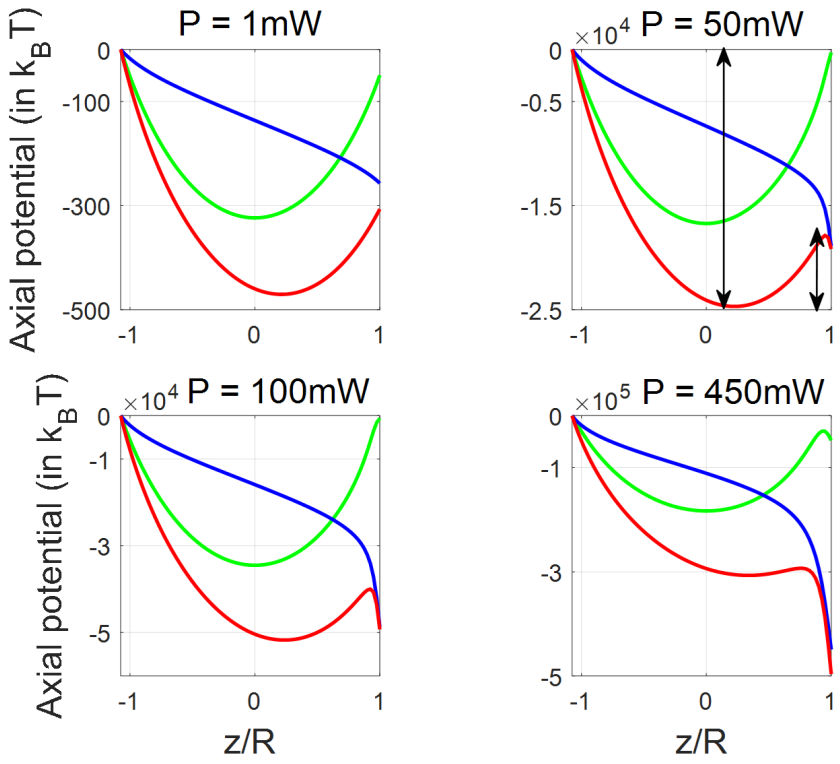

Fig. 5.6.: Plots of trapping potential for cumulative force at different average power under pulsed excitation. Color: green/blue/red curve corresponds to gradient/scattering/total potential.

5.2.2.1. Variation of power

In figure 5.6, the absolute depth of the trapping potential, indicated by longer double-headed vertical arrow (U_{min}) and the height of the potential barrier along beam propagation direction, indicated by shorter double-headed vertical arrow (U_{esc}). Figure 5.7 shows U_{min} and U_{esc} against average power, and it can be seen that absolute potential (U_{min}) increases monotonically with average power while the escape potential (U_{esc}) goes through a maximum corresponding to most stable trap and eventually becomes unbound. So U_{esc} turns out to be the appropriate quantity to quantify the trapping efficiency which was also observed in numerical simulation for trapping of nanoparticles using dipole approximation (discussed in chapter 3). This qualitatively explains one puzzling experimental observation: for larger colloidal particles ($d \geq 0.5\ \mu m$), trapping is destabilized upon increasing the power under pulsed excitation only [77, 80, 81]. Note that the depth of the potential well is too high, $O\left(10^4 k_B T\right)$, which is due to our

particular choice of choosing zero of potential located in the asymptotic region ($z \to \pm\infty$).

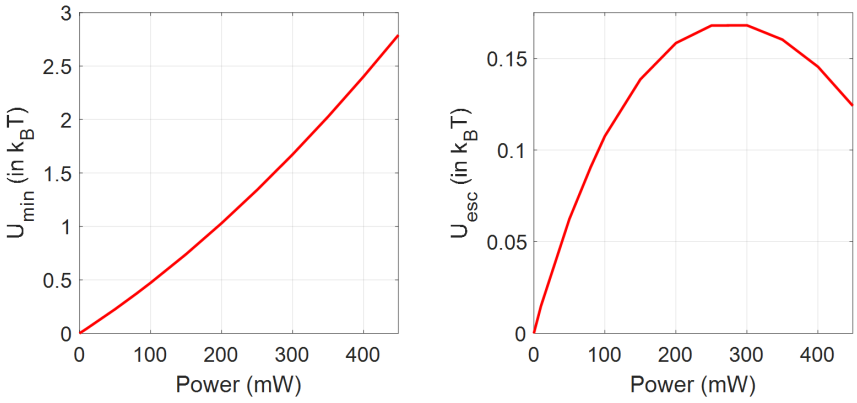

Fig. 5.7.: Plots of the absolute potential (left) and escape potential (right) along axial direction at different average power levels.

5.3 GO 2D distribution: Gaussian beam profile

The above discussion explains the force acting on the particle for the flat-top beam profile. The way of defining the average power of a single ray is different. Therefore, we will calculate the force acting on the particle for the Gaussian beam and then compare with flat-top beam profile using both 2D and 3D distribution of light ray and cone. The ray optics diagram considering trapping of a polystyrene microsphere in water is depicted in figure 5.8. In figure 5.8 MEA is the path of the arbitrary incident ray, EH and EBD are the reflected and refracted ray respectively, OEK is normal to the surface at point E, θ_i and θ_r are the angles of incidence and refraction at the surface; these angles can be related using Snell's law: $n^w sin\theta_i = n^p sin\theta_r$ where n^w and n^p are the refractive indices of water and polystyrene respectively. From 5.8, $\angle AEO = \theta_i, \angle EAO = \varphi, \angle OEB = \theta_r, \sim \angle BEA = \theta_i - \theta_r$. Using exterior angle theorem, $\angle EBO = \varphi + (\theta_i - \theta_r)$, $\angle EOF = \varphi + \theta_i$. Now, by using the triangle property in Δ EOA (using OI perpendicular to MEA), we get the relation between θ_i and φ : $Rsin\theta_i = -zsin\varphi$ where R is the radius of the particle. Note that, as shown in figure 5.1 z is negative, $\frac{z}{R}$ is $\sim$ 0 when the focus coincides with the particle center and it is 1 and $\sim$ -1 when the focus is on the back and front surface of the particle; the slight departure from 0 and 1 is due to refraction.

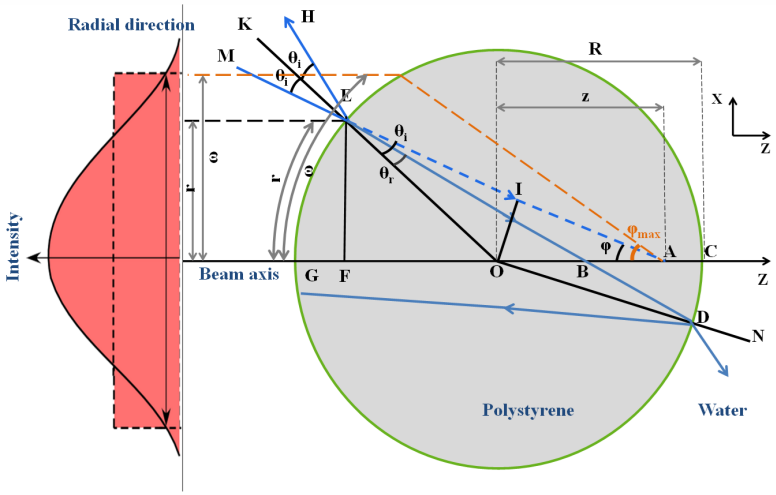

Fig. 5.8.: Ray optics diagram for trapping in the presence of a particle.

Calculation of P_{ray}

The reason for not using the Gaussian intensity profile in the ray optics regime in earlier work [81, 82] can be justified as follows [137]: being a diffractive beam, it converges inside an isotropic medium. The associated k-vector continuously changes direction leading to a changing momentum for each ray, which is conceptually inconsistent within the framework of ray optics. In accordance with the recommadation of reference [81], we calculate the power of a particular ray (P_{ray} using 5.1 and 5.2) according to the intensity distribution (flat top or Gaussian) in the far-field and consider the rectilinear convergence of the ray carrying the same power it had in the far-field.

Let us first consider a 2D distribution [81, 82], where the focused beam consists of light rays, as shown in figure 5.9. To calculate the force due to an arbitrary ray, we need to calculate the power carried by that ray (P_{ray}). We calculate P_{ray} at far-field by taking the product of intensity with the area; note that for a 2D distribution of rays the radial intensity distribution is one-dimensional (which is constant for a flat-top beam but varies for a Gaussian beam) and the area for each ray is the width, δr (which is same for every ray). From figure 5.8,

$$r = R\,(\theta_i + \varphi) \tag{5.6}$$

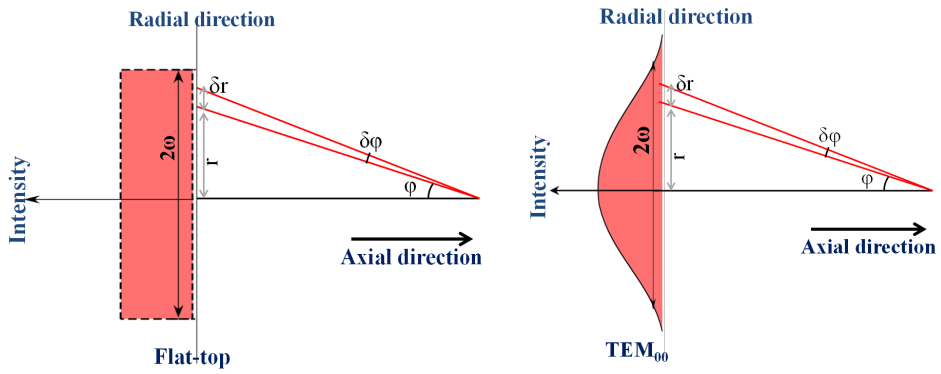

Fig. 5.9.: Distribution of light beam into rays in 2D along radial direction for flat top and Gaussian beam profile.

is the arc length corresponding to an arbitrary ray that makes an arbitrary angle φ with the beam axis. Therefore, the beam radius is:

$$\omega = R\left(\theta_{i,max} + \varphi_{max}\right) \tag{5.7}$$

is nothing but the arc length corresponding to the terminal rays. As the angle φ changes from 0 to $(N-1) \times \frac{\varphi_{max}}{N}$, an increment in the angle $\delta\varphi = \frac{\varphi_{max}}{N}$ increases the arc length by an amount $\delta r = \frac{\omega}{N}$. The total power, which is a measurable quantity, is obtained by integrating the intensity over the entire beam cross-section. The total power for a flat-top beam is

$$P_{total} = \int_0^{\omega} I_f dr = I_f \times \omega$$

which implies $I_f = \frac{P_{total}}{\omega}$; so, we can write power due to each ray ($P_{ray,f}$) as:

$$P_{ray,f} = I_f \times \delta r = \frac{P_{total}}{N} \tag{5.8}$$

Note that $P_{ray,f}$ is independent of the radial coordinate (r) which means that each ray has the same power. Similarly, for a Gaussian beam total power is

$$P_{total} = \int_0^{\infty} I_G dr = \int_0^{\infty} I_{0G} e^{\left(-\frac{2r^2}{\omega^2}\right)} dr \tag{5.9}$$

which implies $I_{0G} = \frac{2P_{total}}{\sqrt{\frac{\pi\omega^2}{2}}}$; so, we can write power due to each ray ($P_{ray,G}$) as:

$$P_{ray,G} = I_G \times \delta r = \frac{2P_{total}}{\sqrt{\frac{\pi}{2}} \times N} e^{-\left(\frac{2r^2}{\omega^2}\right)} \tag{5.10}$$

Note that $P_{ray,f}$ is independent of the radial coordinate (r) which means that each ray has the same power. Now we consider $z/R = 0$ for calculating the power corresponding to each ray for both flat-top as well as Gaussian beam profile shown in figure 5.10.

As the beam is focused, the beam radius (ω) (as well as the incremental

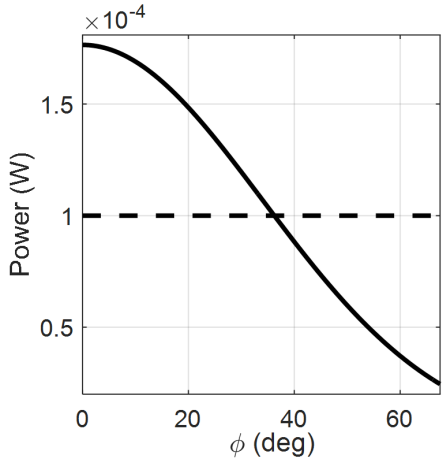

Fig. 5.10.: Power distribution of rays as a function of the angle ϕ for 2D distribution for 10 mW average power under CW excitation.

arc length, δr) decreases along the axial direction and drops to zero at the geometric focus. This leads to the undefined exponent in the power distribution for the Gaussian beam. To avoid this, we add the diffraction-limited beam waist $\omega_{0G} = \frac{0.82\times\lambda}{NA}$ and equally distribute this constant length among N rays as $\delta r_{0G} = \frac{\omega_{0G}}{N}$. Thus we re-define the total power as:

$$P_{total} = \int_0^{\infty} I_0 e^{-\left(\frac{2r^2}{\omega^2+\omega_{0G}^2}\right)} dr \tag{5.11}$$

which implies $I_0 = \frac{2P_{total}}{\sqrt{\frac{\pi\left(\omega^2+\omega_{0G}^2\right)}{2}}}$; so, P_{ray} for Gaussian beam as:

$$P_{ray,G} = I_0 e^{-\left(\frac{2\times r^2}{\omega^2+\omega_{0G}^2}\right)} \times (\delta r + \delta r_{0G}) \tag{5.12}$$

Note that the addition of this additional area is necessary for a Gaussian beam but not for a flat-top beam as the power is constant (and the same) for each ray. However, a vanishing beam radius leads to blowing up the intensity near $z/R = \pm 1$ for both types of the beam, which is crucial when the intensity-dependent nonlinear refractive index is taken into account. Therefore, in order

to keep the formulation consistent, we redefine the total power for the flat-top beam as:

$$P_{total} = \int_{0}^{\omega+\omega_{0f}} I_f dr = I_f \times (\omega + \omega_{0f}) \tag{5.13}$$

which implies $I_f = \frac{P_{total}}{\omega+\omega_{0f}}$; so, P_{ray} for a flat-top beam is expressed as:

$$P_{ray,f} = I_f \times (\delta r + \delta r_{0f}) \tag{5.14}$$

where $\delta r_{0f} = \frac{\omega_{0f}}{N}$ and the diffraction-limited beam waist is given by $\omega_{0f} = \frac{0.61\times\lambda}{NA}$. Note that here we consider the finite (non-vanishing) spot size at the geometric focus in an *ad hoc* to avoid the mathematical inconsistency and the most natural choice for that is the diffraction-limited spot size, which does not mean that we incorporate diffraction effect, as we develope the entire formalism within the ray optics framework.

5.3.1 Force and potential simulations under CW excitation

From here on, the flat-top and Gaussian beam intensity profiles are represented by the dotted and solid curves, respectively.

In figure 5.11 to 5.19, the green, blue and red curves represent the gradient, scattering and total force/potential along the axial direction, respectively.
Figures 5.11 and 5.12 show the force curves for CW excitation at 10 mW average power for five different rays and cumulative force. Since flat-top terminal rays are more intense as compared to Gaussian terminal rays, the gradient force acting on the particle is more in the case of the flat-top beam profile as compared to the Gaussian beam profile, which can be seen from table 5.1.

Beam profile / force (pN)	Flat-top	Gaussian
Scattering	2.9047	2.2578
Gradient	7.4412	4.9404
Total	10.3465	7.1983

Tab. 5.1.: Magnitude of force (at peak maxima) for flat-top and Gaussian beams under CW excitation at 10 mW average power for a 2D distribution.

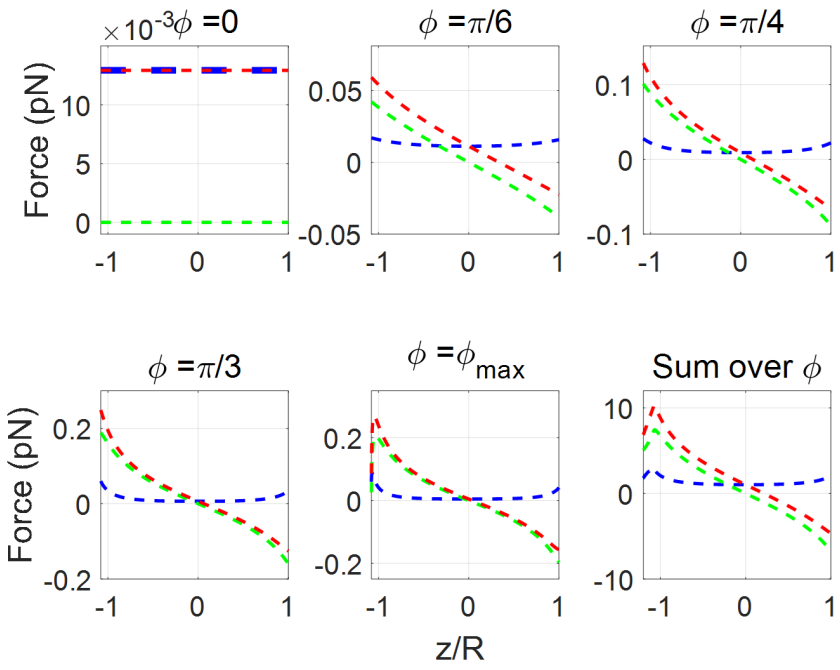

Fig. 5.11.: Plots of trapping force for different rays and the cumulative force for flat top beam profile at 10 mW average power under CW excitation for 2D distribution. Color: green/blue/red curve corresponds to gradient/scattering/total force.

5.4 GO 3D distribution: flat-top and Gaussian distribution

Let us now consider a 3D distribution where the focused beam consists of concentric light cones instead of rays, as shown in figure 5.13. To calculate the force due to an arbitrary cone, we need to calculate the power carried by that particular cone (P_{cone}), which is different for each cone for the Gaussian beam as well as for flat-top beam. We calculate P_{cone} at far-field by taking the product of intensity with the area; note that for a 3D distribution of cones, the radial intensity distribution is 2D (which is constant for a flat-top beam but varies for a Gaussian beam) and the area for each cone is the base area, $2\pi r\delta r$ (which is not same for every ray).

Calculation for P_{cone}

From the figure 5.13, $r = R(\theta_i + \varphi)$ is the base radius corresponding to an arbitrary cone that makes an arbitrary angle φ with the beam axis. Therefore, the beam radius $\omega = R(\theta_{i,max} + \varphi_{max})$ is nothing but the base radius corresponding

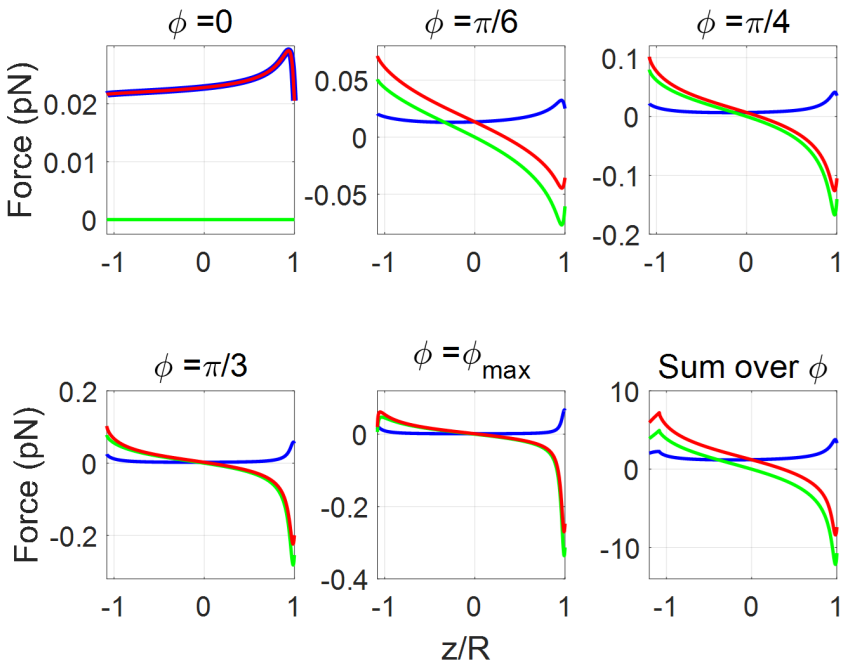

Fig. 5.12.: Plots of trapping force for different rays and the cumulative force for Gaussian beam profile at 10 mW average power under CW excitation for 2D distribution. Color: green/blue/red curve corresponds to gradient/scattering/total force.

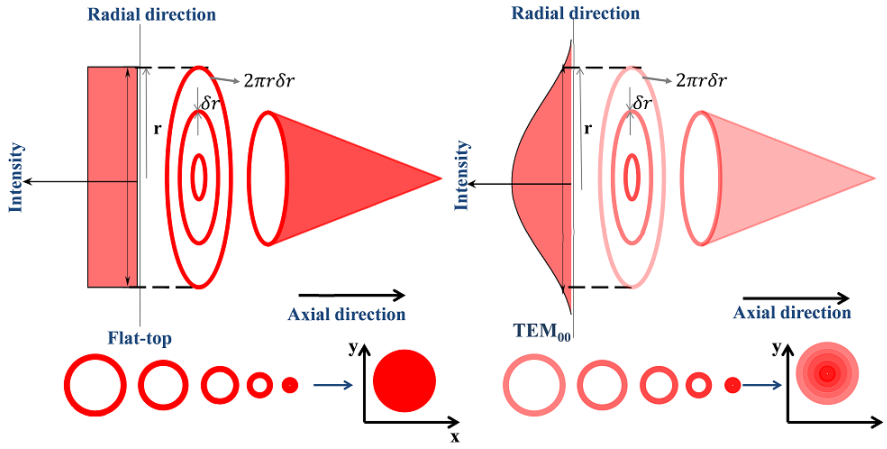

Fig. 5.13.: Distribution of light beam into light cone along axial as well as radial direction for flat-top and Gaussian beam profile.

to the terminal cones. As the angle φ changes from 0 to $(N-1)\times\frac{\varphi_{max}}{N}$, an increment in the angle $\delta\varphi=\frac{\varphi_{max}}{N}$ sweeps an incremental base radius of a cone by an amount $\delta r=\frac{\omega}{N}$. To avoid singularity near $z/R=\pm1$, we add the diffraction limited beam waist for flat-top as well as Gaussian beam profile. We calculate the P_{cone} for flat-top beam as $P_{cone,f}=I_f\times A_{cone,f}$ where I_f is the intensity of the flat top beam profile and $A_{cone,f}$ is the area of single light cone for flat top. The Flat

top intensity is defined as $I_f = \frac{P_{total}}{A_{total,f}}$ where, $A_{total,f} = \pi\omega^2 + \pi\omega_{0f}^2$ is the total area under the curve; so, we can rewrite the power of a single cone for a flat-top beam as:

$$P_{cone,f} = \frac{P_{total}}{A_{total,f}} \times A_{cone,f} \tag{5.15}$$

where, $A_{cone,f} = 2\pi r\delta r + \pi\left(\delta r\right)^2 + \frac{\pi\omega_{0f}^2}{N}$ is the area of single light cone for flat top beam profile. In a similar way a Gaussian beam intensity is expressed as $I_G = \frac{P_{total}}{A_{total,G}} \times e^{-\left(\frac{2r^2}{\omega^2+\omega_{0G}^2}\right)}$ where $A_{total,G} = \pi\omega^2 + \pi\omega_{0G}^2$ is the total area under the curve an $A_{cone,G} = 2\pi r\delta r + \pi\left(\delta r\right)^2 + \frac{\pi\omega_{0G}^2}{N}$ is the area of single light cone, we define the power of a single cone as:

$$P_{cone,G} = \frac{P_{total}}{A_{total,G}} \times e^{-\left(\frac{2r^2}{\omega^2+\omega_{0G}^2}\right)} \times A_{cone,G} \tag{5.16}$$

5.4.1 Force and potential simulations under CW excitation

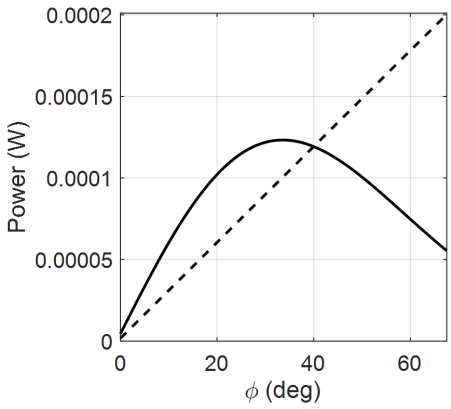

Fig. 5.14.: Power distribution of cones as a function of the angle ϕ for 3D distribution.

The power distribution for flat-top and Gaussian beams for 10 mW average power under CW excitation are plotted in figure 5.14. It is evident that each cone will have a different power for both beam profile at $\frac{z}{R} = 0$.

In figure 5.14, we show power distribution of cones. From figure 5.10, we observe that power is constant for each cone for a flat-top beam profile; however, for the Gaussian beam profile, the central cones are more intense as compared to terminal cones. In 3D distribution, power is proportionally increasing as we go towards the terminal cones for the flat-top profile, and it maximizes for a cone somewhere lying in the middle for the Gaussian beam profile, as shown in figure

5.14. This arises for a delicate balance between radially constant (for flat-top) or decreasing (for Gaussian) intensity and radially increasing annular base area of the light cone.

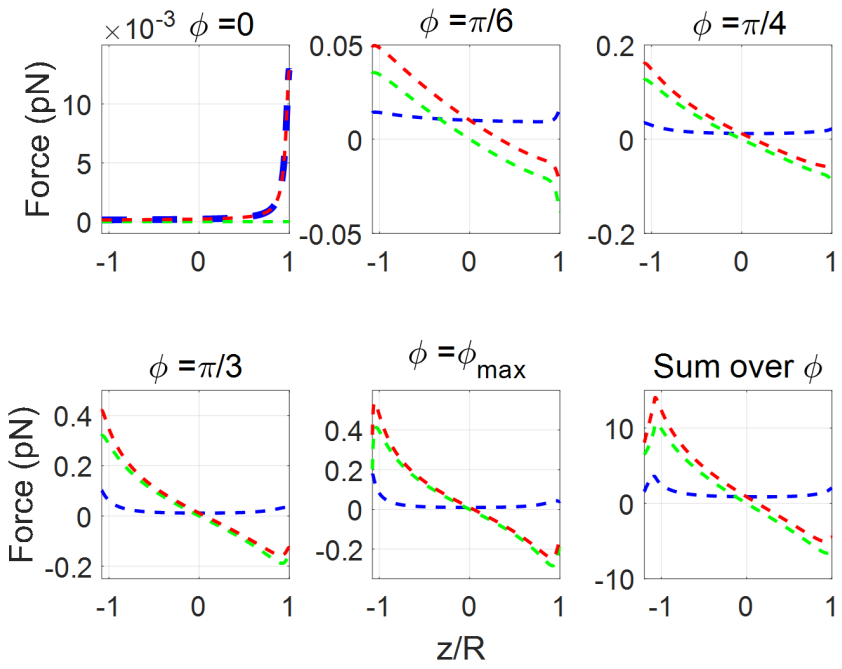

Fig. 5.15.: Plots of trapping force for different cones and the cumulative force for flat-top beam profile at 10 mW average power under CW excitation for 3D distribution. Color: green/blue/red curve corresponds to gradient/scattering/total force.

From figures 5.15 and 5.16, we show that the force plot for five different light cones and cumulative force for CW excitation at 10 mW average power. In the case of flat-top, power is continuously increasing towards the terminal cones. Since the terminal cones bend more than central cones, the gradient force is contributed more by the terminal cones. This is evident in table 5.2.

From tables 5.1 and 5.2, we can see dissimilarities between the magnitude of the

Beam profile / force (pN)	Flat-top	Gaussian
Scattering	3.6278	2.5826
Gradient	10.6351	7.1322
Total	14.0417	9.7148

Tab. 5.2.: Magnitude of cumulative force (at peak maxima) for flat-top and Gaussian beam profile for CW excitation for 3D distribution.

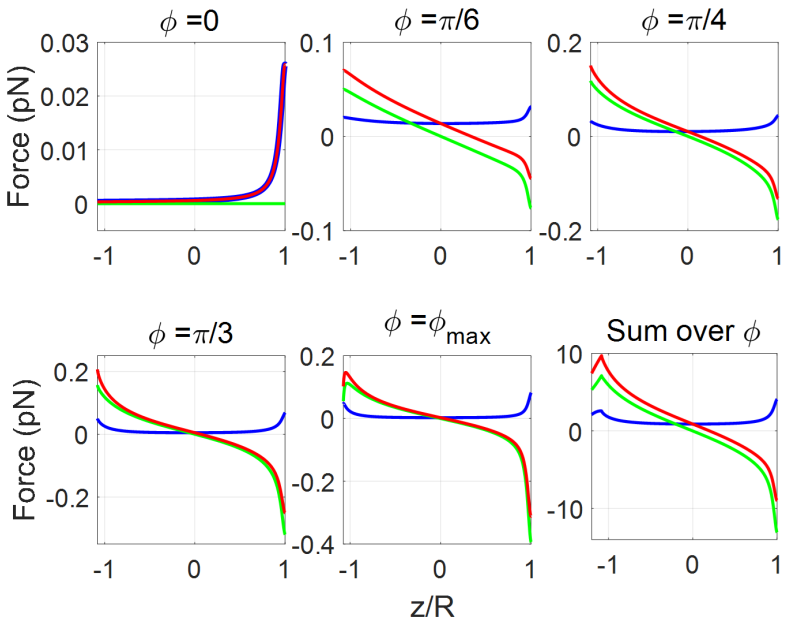

Fig. 5.16.: Plots of trapping force for different cones and the cumulative force for Gaussian beam profile at 10 mW average power under CW excitation for 3D distribution. Color: green/blue/red curve corresponds to gradient/scattering/total force.

forces (at peak maxima) for 2D and 3D distribution; it is less in 2D as compared to 3D for both flat top and Gaussian beam profiles.

5.4.1.1. Comparison of 2D and 3D distribution of rays using GO approximation with Exact Mie Theory

Note that there exist several other formalisms, for example, the Maxwell stress tensor method, T matrix method, and GLMT, which are more rigorous and accurate. Using Maxwell stress tensor method, one can estimate the total force distribution on the surface as well as in the bulk (although much of the discussion in literature mainly focused on the Abraham–Minkowski controversy, *i.e.* particle vs wave nature of light) [85, 138–140].

Here, we have intentionally chosen geometric/ray optics formulation, because it is much simpler to be applied compared to the more sophisticated methods. The entire goal was to improve the earlier formalism [95, 96] to include a more realistic situation (from a 2D model with a flat top transverse intensity profile to 3D model with Gaussian transverse intensity profile). Quite interestingly, even such a simple method yields excellent agreement with the EMT [111], which, as argued by Ashkin (for a detailed discussion on comparison between methods, see chapter 10 in reference [21]), is one of the most accurate methods. Intrigued

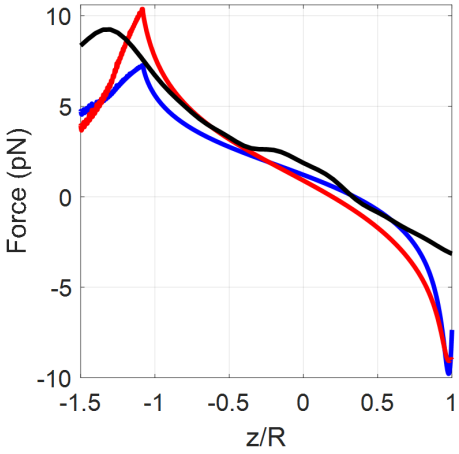

Fig. 5.17.: Plots of trapping force for the cumulative force at 10 mW average power under CW excitation for 2D distribution (blue), 3D distribution (red) and EMT (black).

by this, we further compared total force acting on the particle by three different methods: 2D formulation, 3D formulation, and the EMT for Gaussian beam profile; agreement can be seen from figure 5.17.

5.4.2 Force and potential simulations under pulsed excitation

Figures 5.18 and 5.19 show the cumulative force at different average powers under pulsed excitation including Kerr effect, with variation in power for both flat-top and Gaussian beam profiles. The force curves change, and their magnitude varies non-linearly. At high power, the scattering force dominates over the gradient force. Thus, there is a negligible resorting force acting on the particle. This destabilizes the trap, allowing the particle to escape. Figures 5.20 and 5.21 show the corresponding potential curves (for the force curves in figures 5.18 and 5.19).

5.4.2.1. Variation of power

Figure 5.22 corresponds to U_{min} and U_{esc} for the flat top beam profile and Gaussian beam profile with different particle sizes. Here we choose radius of the particle is $\geq 4\ \mu m$ to satisfy the ray optics limit ($d \gg \lambda$). Although the ray optics formulation is independent of particle size, we observe a clear dependence on size after considering OKE as evident from table 5.3.

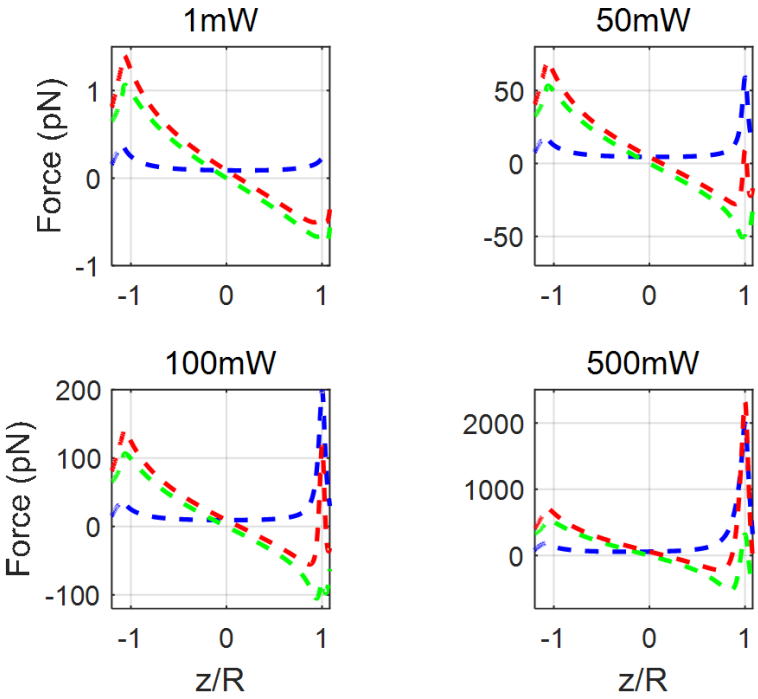

Fig. 5.18.: Plots of cumulative force at different average power for flat-top beam profile under pulsed excitation for 3D distribution. Color: green/blue/red curve corresponds to gradient/scattering/total force.

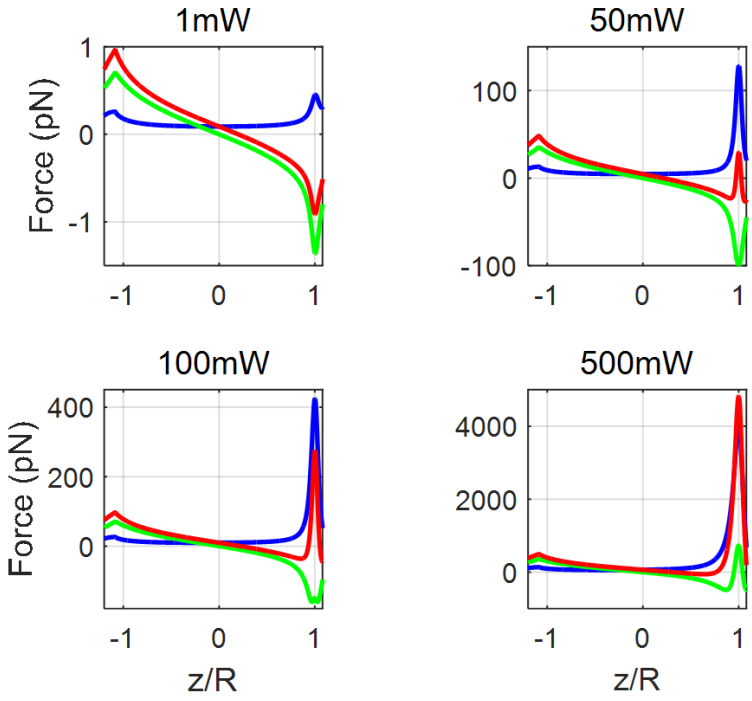

Fig. 5.19.: Plots of cumulative force at different average power for Gaussian beam profile under pulsed excitation for 3D distribution. Color: green/blue/red curve corresponds to gradient/scattering/total force.

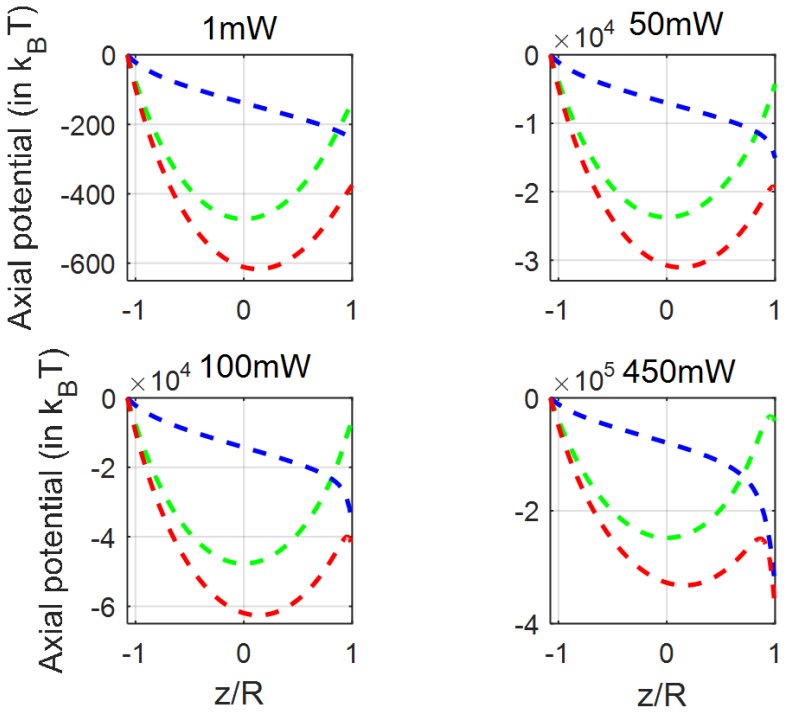

Fig. 5.20.: Plots of cumulative potential at different average power for flat-top beam profile under pulsed excitation for 3D distribution. Color: green/blue/red curve corresponds to gradient/scattering/total force.

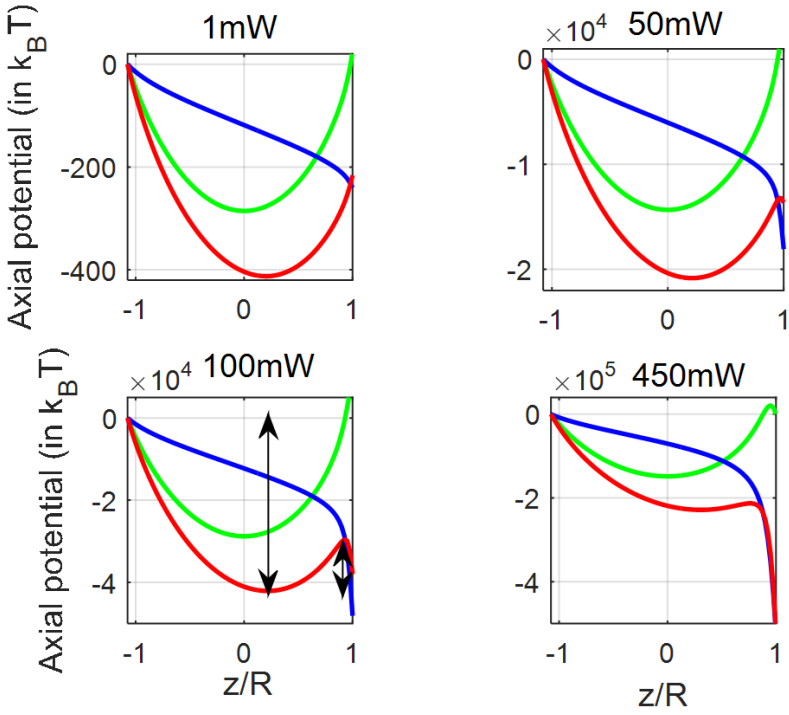

Fig. 5.21.: Plots of cumulative potential at different average power for Gaussian beam profile under pulsed excitation for 3D distribution. Color: green/blue/red curve corresponds to gradient/scattering/total potential.

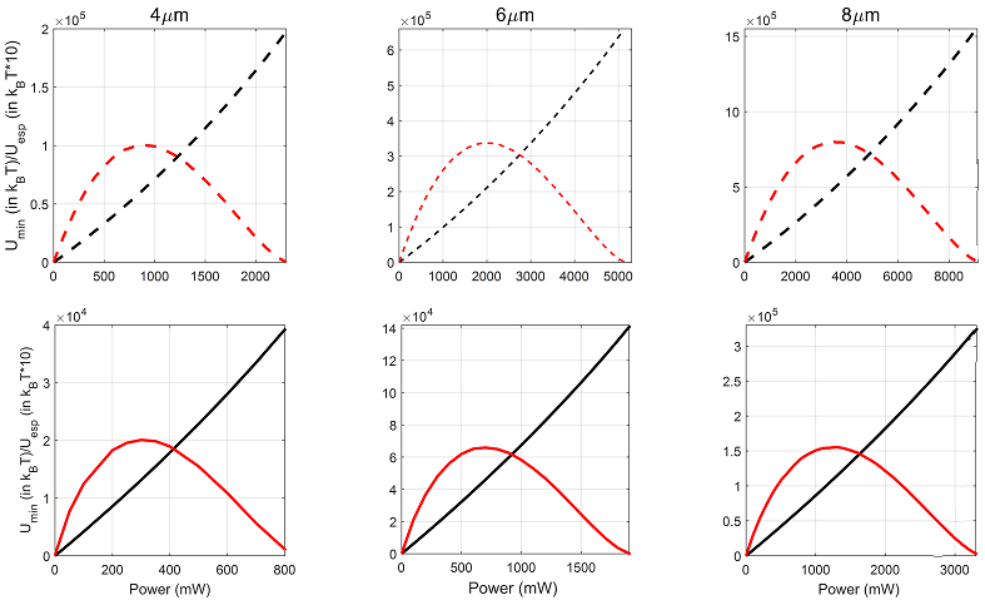

Fig. 5.22.: Plots of cumulative potential at different average power for Gaussian beam profile under pulsed excitation for 3D distribution.

Paricle size / Beam profile	4 μm	6 μm	8 μm
Flat-top	$\sim$ 900 mW	$\sim$ 2000 mW	$\sim$ 3450 mW
Gaussian	$\sim$ 300 mW	$\sim$ 700 mW	$\sim$ 1300 mW

Tab. 5.3.: Power (mW) corresponding to maximum escape potential for different particle sizes.

5.5 Conclusion

To conclude, we have shown how OKE changes the nature of the trapping force under high-repetition-rate ultrafast pulsed excitation, which nicely explains the earlier experimental findings. More importantly, we have demonstrated that the fact of the escape potential of the axial trapping potential being the relevant parameter to quantify optical trapping efficiency under ultrafast pulsed excitation, is universally held for all particle size limits. Along with this, we have systematically developed a general methodology for theoretically estimating optical force (and potential) in the geometric/ray optics limit using 3D distribution of light cones for flat-top as well as Gaussian transverse intensity profiles of the trapping laser beam, which circumvents the limitations of earlier theoretical formulation of using 2D distribution of light rays for plane-wave excitation only. Also, we have shown how an OKE plays a crucial role in modulating the trap stiffness under femtosecond pulsed excitation.

6 Force and potential on arbitrary sized dielectric particle using exact Mie theory

6.1 Introduction

As discussed in previous chapters 3 to 5, both dipole and geometric optics (GO) approximations have certain limitations depending upon the particle size, so we have explored the GLMT using localized approximation and compared the results with dipole approximation. We have found qualitative agreement (nature of force/potential are the same) between the theories but quantitatively (magnitude of force/potential) they disagree. We observed that GLMT with localized approximation might not be a good approximation. Apart from this, there exist several other methods like the Maxwell stress tensor or T matrix, discrete dipole approximation (DDA). These theories have their limitations. For accurate calculation of total force, the optimal agreement method was found by A. Ashkin, which is the exact Mie theory (EMT) [21]. In this chapter, the theoretical linear aspect of the problem is addressed using EMT, and we have found that the earlier done calculation for strongly focused light beyond the objective making an angle with beam axis is not appropriate, so here we redefine the calculation for bending of light inside the medium. By taking this redefined calculation along with EMT, the results are compared with GO 3D distribution of light cone for large-sized particles. For small-sized particles, results are compared with both dipole approximation and GLMT using localized approximation. Although in literature, it was mentioned that GLMT is applicable for all size limits, but we have observed that GLMT with localized approximation theory is applicable only for small-sized particles. Later the nonlinear aspect of the problem is studied using OKE by varying the numerical aperture (NA), particle size, and average power for pulsed excitation.

Mathematical formulation

A detailed mathematical formulation to calculate the force acting on the particle (using dipole approximation, 2D, and 3D distribution of geometric optics approx-

imation, GLMT using localized approximation and EMT [141]) is discussed in chapter 2. All the parameters used in numerical simulations are listed in table 2.1.

Figure 6.1 shows schematic diagram for calculating ϕ_{max}. In literature [142] , ϕ_{max} is calculated by using figure 6.1b, where at point A, the beam is transmitting from glass substrate (having RI 1.51) to oil (having RI 1.55); when beam is traveling from less to high dense medium using Snell's law the beam will bend towards the normal. However, at point B, the beam will bend away from the normal because the beam is traveling from high denser to less dense medium. At point C, the beam is travelling from glass substrate to water (having refractive index 1.33) so beam will bend away from the normal and eventually leads to focus on the beam axis and $\phi_{max} \approx sin^{-1}\left(\frac{NA}{n_{water}}\right)$. However, this definition does not seem feasible for high NA objective, for example, if we consider NA to be 1.4, ϕ_{max} will give a complex angle which cannot be possible, so we need to redefine this definition. Figure 6.1c, is the redefining of this definition and this can be done by making an assumption that these small deviations can be neglected; so, we have assumed that, this focusing persists throughout the medium and $\phi_{max} = sin^{-1}\left(\frac{NA}{n_{oil}}\right)$.

The notable point here is that in the old definition, for NA=1.33, the focusing

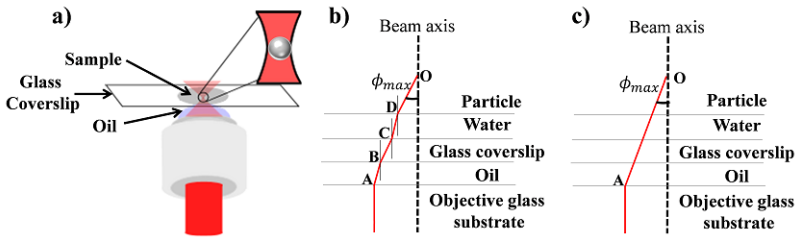

Fig. 6.1.: Schematic diagram for calculating ϕ_{max}.

beam axis angle is 90^0. This angle has no relevance because right angle rays will not give stable trapping (we can feasibly see that it is not possible at all). Another point is that nowadays, many researchers are using high NA objectives for a tight focusing condition like NA 1.4; in that case, this definition gives 90^0-18.51 i complex angle. But the redefined definition gives a relevant angle with the beam axis, for example, NA 1.3 and 1.4 makes 59.10° and 67.53°, respectively.

The force acting on the particle using the old definition of focusing angle, for NA 1.3, can be calculated (qualitatively and quantitatively, it might not be feasible), but for NA 1.4, it cannot be calculated because integrating over a complex angle is not possible. However, using the new definition, we can calculate the force

acting on the particle for both NA 1.3 and 1.4; discussed later in this chapter. Figure 6.2a shows the force acting on the 4 μm particle size (radius of the particle) with NA 1.3 from both old (circled line) and new definition (solid line) at 10 mW average power. It can be seen that the small change in the focusing angle gives a significant change in the force curve acting on the particle. Figures 6.2b and 6.2c are the schematic diagrams of the particle, which show that the beam is focusing on the front and back surfaces, respectively. At these points, scattering force is dominating over gradient force, which leads to a sharp peak at the back and the front surfaces of the particle. Nevertheless, according to the old definition, these peaks are lying inside the particle, and this cannot be possible because when the beam is focusing inside, the particle gradient force plays a significant role in the overall force. Note that according to this convention, z is negative, so for negative axial distance, this corresponds to z/R $\leq$ -1 (the focus is on the front surface of the particle). This is because for z/R = -1, the focus is still within the particle, so maximum repelling force exerted must be z/R<-1 (and not on the surface of the particle) due to refraction. It is due to the fact that the bending of light inside the medium might cause the deviation of the light beam from the actual focus position, so maximum force acting on the particle must lie on z/R>1. The overall conclusion is that when the beam is focusing outside the surface (back and front) of the particle then scattering is maximizing over gradient force which results in a sharp peak in the force curve and these positions must be z/R $\leq$ -1 and z/R $\geq$ 1.

In all the simulations from now onwards, we are using a new definition of ϕ_{max}.

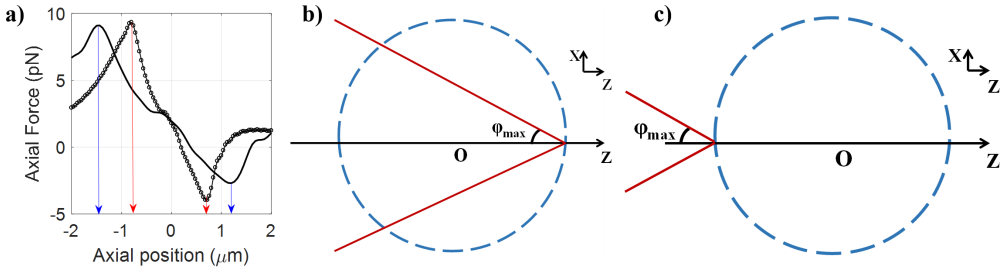

Fig. 6.2.: Plots of a) axial force using EMT for old and new definition of ϕ_{max} at 10 mW average power b) Schematic diagram when beam focus at $z/R = -1$ and c) when beam focus at $z/R = 1$.

OKE is incorporated through the second-order nonlinear refractive index which is discussed in chapter 2.

Before doing the comparative studies of different theories, we have rigorously analyzed the MSCs and BSCs, because in the case of GLMT and EMT theories,

these coefficient plays an important role in determining the force and potential calculations.

6.2 Mie Scattering Coefficients

MSC depends on the particle size and ratio of the refractive index of the particle to the medium through Bessel and Hankel functions (please see the equation 2.29). Therefore, a small change in these parameters leads to a significant change in the force acting on the particle.

6.2.1 CW excitation

Figure 6.3a shows plots of MSC against particle size till 10 μm for summed over n=150 terms (because all the MSC converges within this size limit for n=150). It can be seen that as per increase in particle size towards micron sized particle range, all the scattering coefficients (Re[a_n], Im[a_n], Re[b_n] and Im[b_n]) are contributing to the force calculation. However, for nano sized particle as shown in figure 6.3b, Im[a_n] is dominating over all the other terms in MSC. Interestingly in Rayleigh limit particle size MSC converges for n=10 terms. It can be clearly seen that only Im[a_n] is contributing mostly for very small sized particles.

Figure 6.4a shows the contribution of scattering coefficient in force calculations

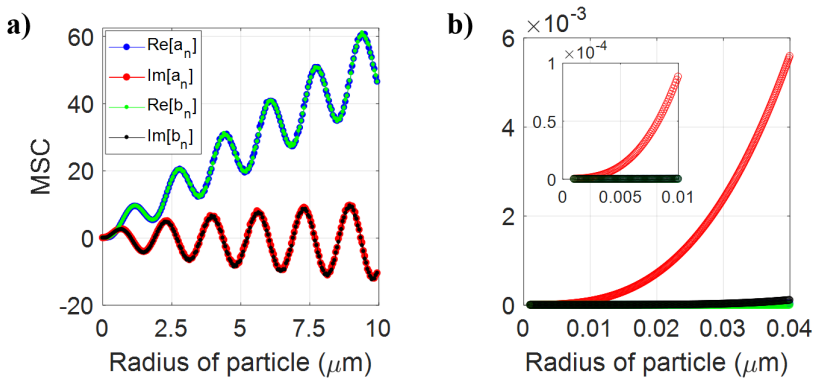

Fig. 6.3.: Plots of MSC against particle size under CW excitation.

for GLMT and EMT against particle size for n summed over 150 terms. It can be seen that contribution of MSC in GLMT is increasing as per increase in particle size but not following any trend for the curve whereas in case of EMT except $Im\left[S^{(3)}_{n,GLMT}\right]$ all are following a particular trend which shows a nice oscillatory behavior. However, figure 6.5b shows the contribution of scattering coefficient in force calculations for GLMT and EMT against particle size for n summed over 10 terms. It can be seen that for small sized particle $Im\left[S^{(2)}_{n,GLMT}\right]$ and $Im\left[S^{(1)}_{n,EMT}\right]$

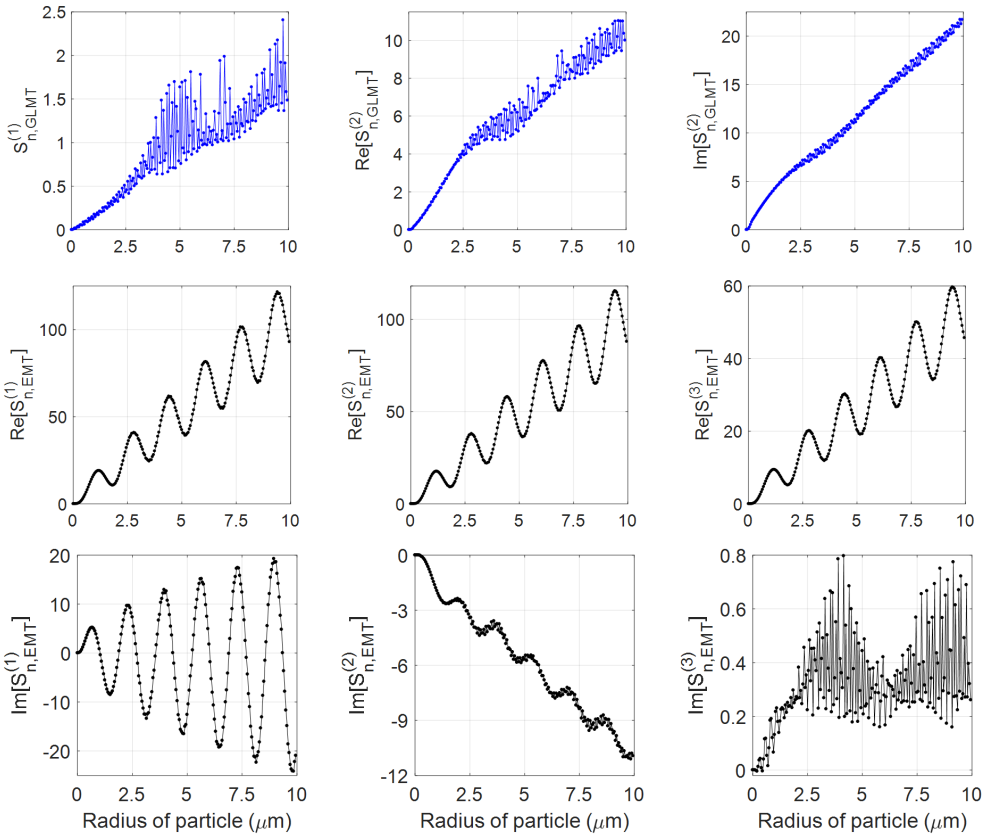

Fig. 6.4.: Plots of Scattering Coefficient Contribution (SCC) for force calculation in both GLMT and EMT against particle size under CW excitation.

mostly contribute to MSC for GLMT and EMT, respectively. In both these terms, dominancy comes from $Im\,[a_n]$ can be seen from figure 6.3.

6.2.2 Pulsed excitation

In the case of pulsed excitation, MSC depends on the axial position, NA, wavelength, and peak power of the trapping beam. Figures 6.6 and 6.7 show the MSC for three different planes (z=0 μm; focal plane, 1 μm and 4 μm) for fixed NA 1.3 at 10 mW, 100 mW and 200 mW average power, respectively. Figure 6.3 shows in the case of CW excitation, 6 maxima are appearing while in case of pulsed excitation at 10 mW average power for the focal plane (z=0 μm), 9 maxima are appearing. From figure 6.6, it is apparent that for a fixed power, the number of maxima is decreasing as we go away from the focal plane. For 4 μm plane, with an increase in average power from 10 mW to 100 mW, the number of maxima also increased from 6 to 11. However, for 1 μm plane at 10 mW average power, there is 8 number of maxima, but at 100 mW average power, they are

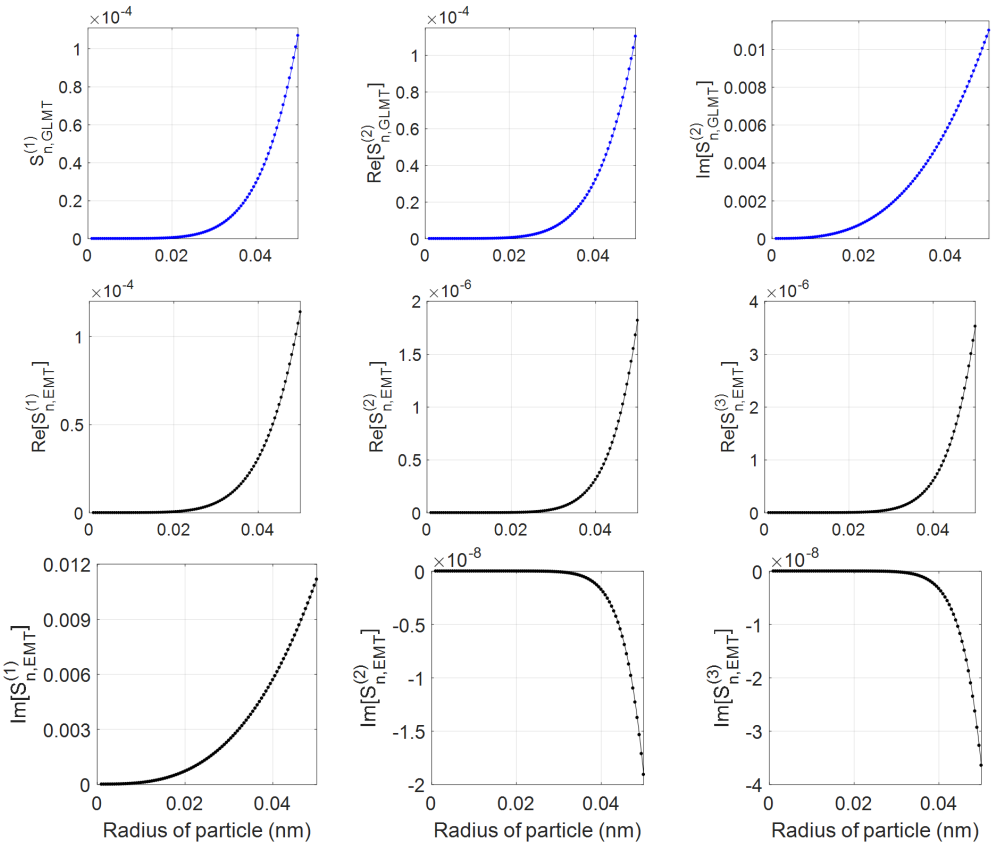

Fig. 6.5.: Plots of Scattering Coefficient Contribution (SCC) for force calculation in both GLMT and EMT against particle size under CW excitation.

very compact, so it is not straightforward to say in numbers. Furthermore, the increase in power gives the random appearance of maxima and minima without any pattern because maxima and minima start compensating each other result to distortion in the waveform like pattern. For z=0 μm at 10 mW average power, there are 9 maxima and 8 minima, whereas, for 100 mW average power, they are very compact and difficult to count but interestingly further increase in power leads to the appearance of patches. It is very clear from the figure 6.6 that small change in the average power leads to a drastic change in the pattern near the focus, while it is slowly changing as we go away from the focus. This is because near the focus, the intensity is very high as compared to 4 μm plane, and this behavior is symmetric about the focal plane. Far away from the focal (around $\pm$ 10 μm) plane behavior of the MSC coefficient is similar to CW excitation. Figure 6.7 shows the MSC against particle size within Rayleigh limit for three different planes (z=0 μm; focal plane, 1 μm and 4 μm) for fixed NA 1.3 at 10 mW, 100 mW and 200 mW average power under pulsed excitation, respectively. It can be seen that the nature of the force curve is similar for all three planes at different

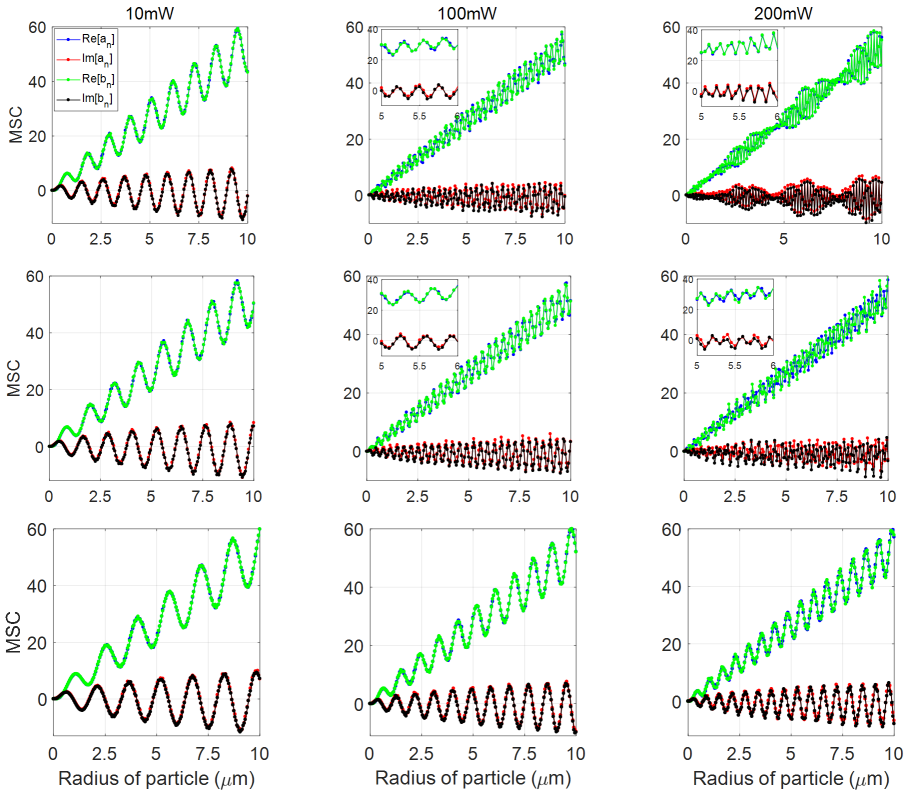

Fig. 6.6.: Plots of MSC against particle size under pulsed excitation for z=0 (focal plane; top panel), $z = 1\mu m$ (middle panel) and $z = 4\mu m$ (bottom panel).

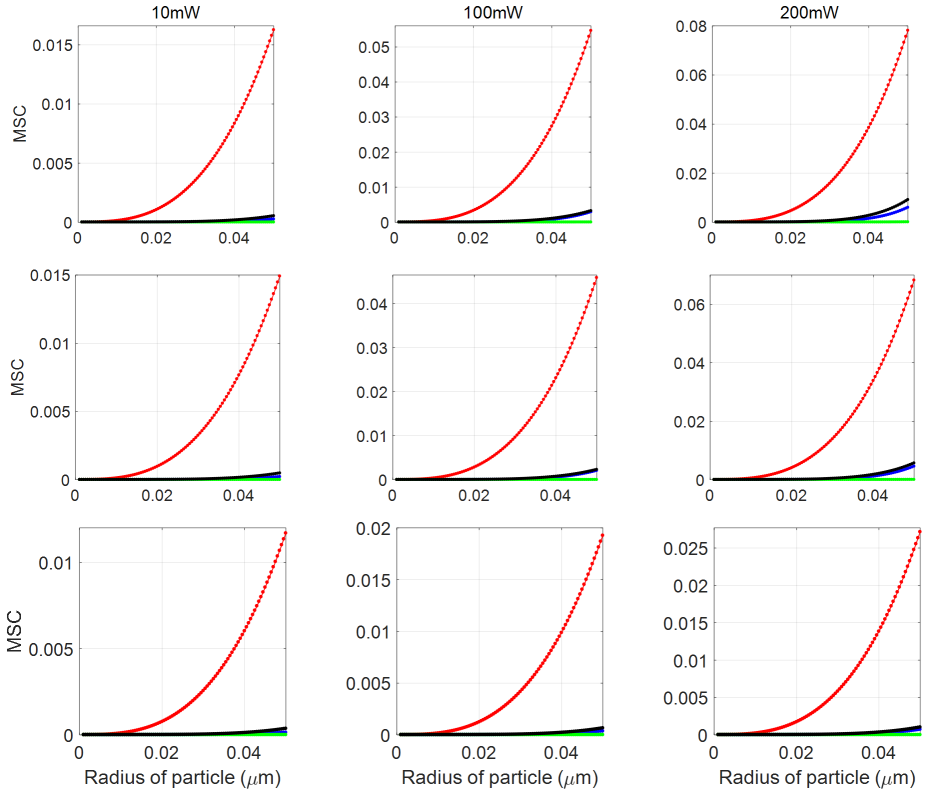

Fig. 6.7.: Plots of MSC against particle size (Rayleigh limit) under pulsed excitation for z=0 (focal plane; top panel), $z = 1\mu m$ (middle panel) and $z = 4\mu m$ (bottom panel). Color: blue/red/green/black curve corresponds to $Re[a_n]/Im[a_n]/Re[b_n]/Im[b_n]$.

average power but the change in the magnitude of force curve because MSCs are nonlinearly dependent upon the trapping beam average power. Hence, as per the increase in average power, there is a significant increment in the magnitude of force curve, and away from the focus, the intensity is decreasing that is why there is a significant decrease in the magnitude of force curve as we go from z=0 μm to 4 μm plane. It can be seen that for small-sized particle $Im[a_{\mathrm{n}}]$ contributes mostly and near the focus increasing power increases the magnitude of force curve and vice versa.

In conclusion, we can say that small change in axial position and average power of trapping beam leads to a significant change in the nature of the force curve, which implies that the contribution of MSC in GLMT and EMT also gives a significant change in nature of the curve.

6.3 Beam Shaping Coefficients

BSCs are independent of particle properties and average power of laser beam, and it depends upon focusing angle with beam axis, axial position, and summation over the number of terms for Legendre and exponential function in EMT and GLMT respectively. BSC plays a crucial role in force calculations, and these coefficients are the same for both CW and pulsed excitation. Figure 6.8 shows that the BSC for GLMT and EMT along axial direction for summation over 10 terms. It can be seen that for small-sized particles, the nature of the force curves is similar to the imaginary term of BSCs because the force is calculated by multiplication of MSC and BSC. The MSCs are constant values for fixed particle size and relative RI under CW excitation. However, in the case of pulsed excitation, MSCs are also axial position dependent, so the nature of the force curve strongly depends on the nature of BSC curves for CW excitation, however, for pulsed excitation it depends on both MSC as well as BSC. For large-sized particles, higher 'n' also contributes significantly, so summed over higher 'n' (150) terms leads to an increase in the magnitude of BSCs, not the nature of force curve. But for higher n, all BSC components contribute significantly, so the nature of the force curve depends on the nature of the BSCs curve for all the components.

For small-sized particles, the comparison is made for dipole approximation, GLMT using localized approximation and EMT. In the case of GLMT and EMT, MSC converges for summation over 10 values of n, therefore, in the force calculations, we considered initial 10 terms and all the calculations are done along the axial direction. In plots, the results corresponding to GLMT and dipole approxi-

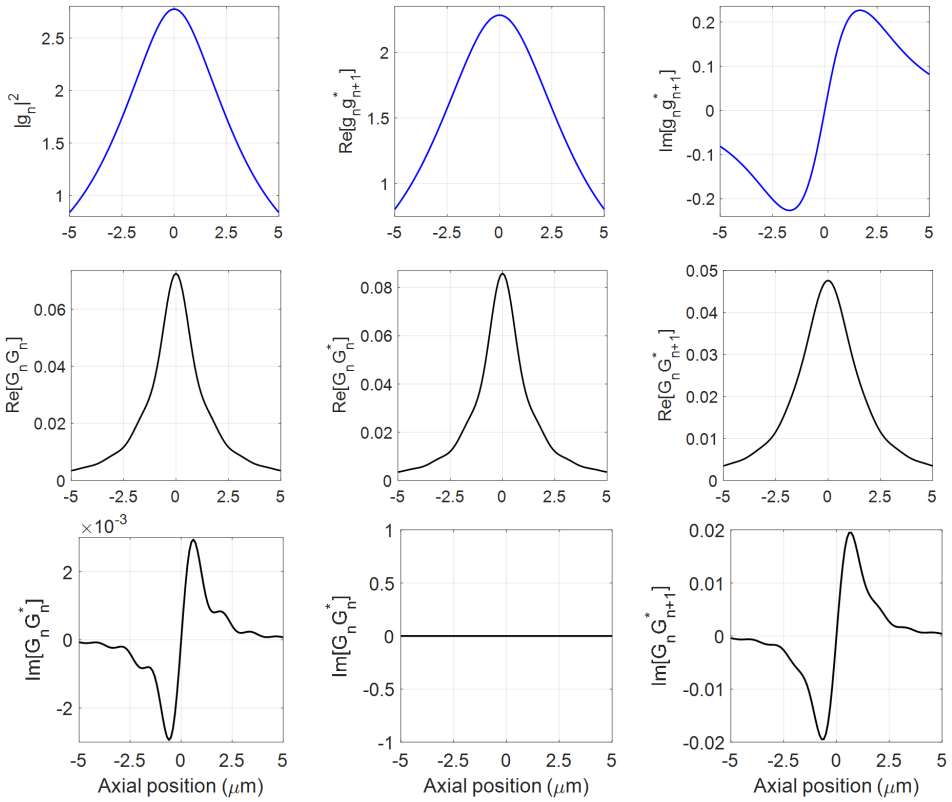

Fig. 6.8.: Plots of BSC for force calculation in both GLMT and EMT along axial direction for summed over 10 terms.

mation are multiplied by an additional factor of 10 for comparison because these approximations have a considerable difference in the magnitude as compared to EMT.

6.4 Comparison of dipole, GLMT and EMT in Rayleigh Regime

6.4.1 CW excitation

Figure 6.9 shows the force curve at 100 mW average power under CW excitation for EMT, GLMT, and dipole approximation. It can be seen that all three theories have significant differences in the magnitude of the force curve. However, for dipole and GLMT approximation nature of the force curve is similar, while the EMT nature of the force curve is very different from other theories. On comparing EMT with dipole and GLMT approximation, the difference is appearing because GLMT and Dipole approximation are valid under a paraxial approximation. However,

EMT formulation is applicable for tight focusing conditions. In the case of Dipole approximation, force is directly proportional to the particle size, whereas in the case of EMT and GLMT forces are an indirect function of particle size, that is why the increase in particle size leads to change in the magnitude of force curve. EMT force curve shows oscillation on the wings due to BSC (can be seen from figure 6.8) because it is a function of both exponential function and Legendre polynomial. The force acting on the particle is very confined due to tight focusing conditions in EMT. For small-sized particles, the EMT and dipole approximation show symmetric force about the axis. The increase in particle size results in a deviation from the symmetricity and becomes asymmetric about the axis. This is because for small-sized particles contribution of scattering force is negligible as compared to gradient forces. GLMT shows asymmetric force throughout the regime that can be seen from table 6.1. This asymmetry in all three theories increases with increasing NA for fixed particle size, while for fixed NA, the increase in particle size leads to more and more asymmetry in force curve about the axis. Under CW excitation, change (increase/decrease) in power leads to change (increase/decrease) in order of magnitude of force curve in the same proportion; no change in the nature of force curve because the analytical expression of forces is directly proportional to the average power.

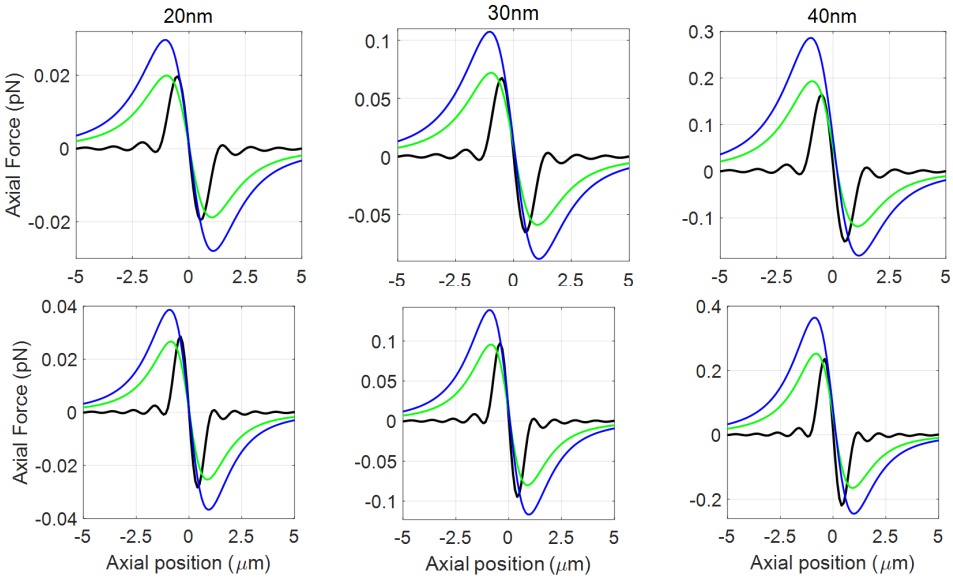

Fig. 6.9.: Plots of axial force top panel for NA=1.3 and bottom panel for NA=1.4. A factor of 10 is multiplied for GLMT and Dipole approximation. Color: black/blue/green curve corresponds to EMT/GLMT/Dipole approximation.

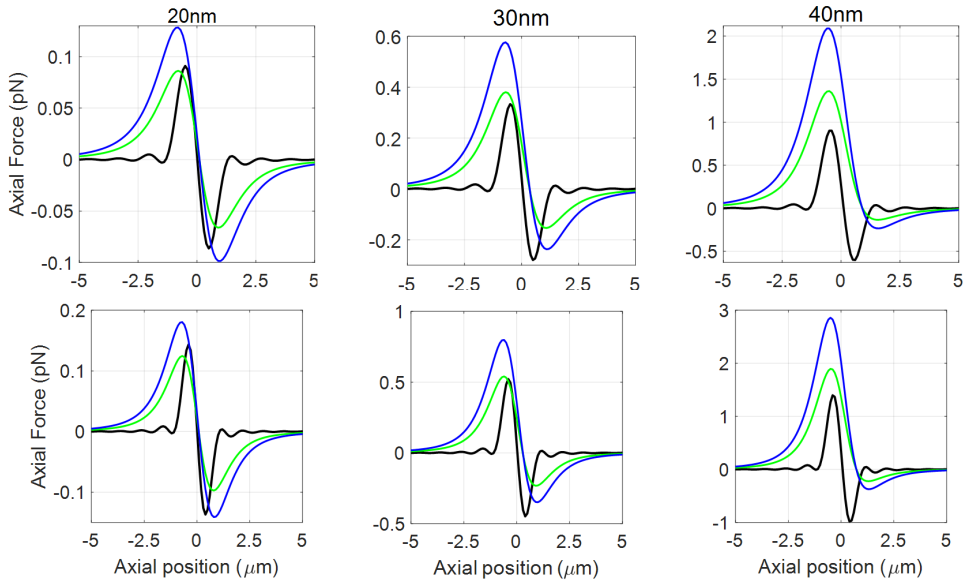

Fig. 6.10.: Plot of axial force top panel for NA=1.3 and bottom panel for NA=1.4 at 100 mW average power under pulsed excitation. A factor of 10 is multiplied for GLMT and Dipole approximation. Color: black/blue/green curve corresponds to EMT/GLMT/Dipole approximation.

NA	Theory	$F_{max}(pN)$			$F_{min}(pN)$		
		20 nm	30 nm	40 nm	20 nm	30 nm	40 nm
1.3	EMT	0.0197	0.0676	0.1044	-0.0195	-0.0650	-0.1504
	GLMT	0.0030	0.0107	0.0286	-0.0028	-0.0088	-0.0181
	Dipole	0.0020	0.0072	0.0193	-0.0020	-0.0059	-0.0118
1.4	EMT	0.0286	0.0975	0.2359	-0.0283	-0.0946	-0.2199
	GLMT	0.0038	0.0139	0.0365	-0.0036	-0.0117	-0.0246
	Dipole	0.0027	0.0096	0.0253	-0.0025	-0.0080	-0.0165

Tab. 6.1.: Force maxima and minima at peak for Gaussian beams under CW excitation at 100 mW average power for EMT, GLMT and dipole approximation.

6.4.2 Pulsed excitation

Figure 6.10 shows the force curve along axial direction at 100 mW average power under pulsed excitation for EMT, GLMT, and Dipole approximation with black, blue, and green colors, respectively. It can be seen that in pulsed excitation, there is a significant change in magnitude as well as in nature of force curve as compared to CW excitation for all three theories. Including OKE leads to more asymmetry in the force curve about the axis as compared to CW excitation for a fixed NA and fixed particle size in EMT, GLMT and dipole approximation can be

seen by comparing the table 6.1 and table 6.2. Increasing particle size increases the asymmetry about the axis, while for fixed particle size, on increasing NA, this asymmetry is also increasing in the force curves. Under pulsed excitation, forces are indirectly proportional to the average power. Consequently, the increase in the magnitude of force curve keeps on increasing with average power which results in nonlinear behavior in nature and magnitude of force curves.

Figure 6.11 shows the force curve for 40 nm particle size at different average

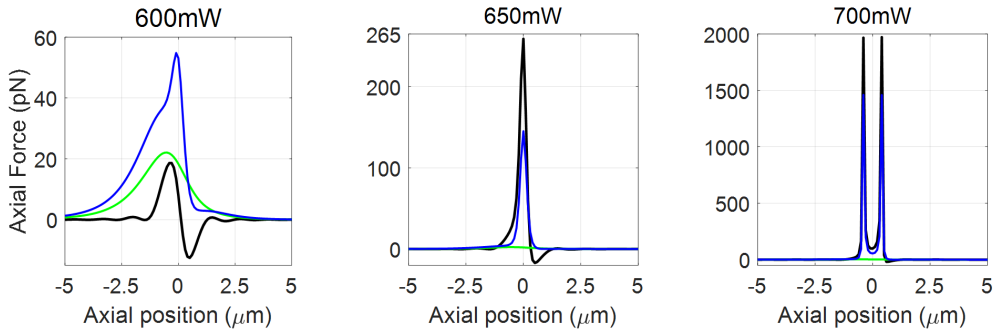

Fig. 6.11.: Plots of axial force for 40 nm particle size at different average power for NA=1.3. Color: black/blue/green curve corresponds to EMT/GLMT/Dipole approximation.

NA	Theory	$F_{max}(pN)$			$F_{min}(pN)$		
		20 nm	30 nm	40 nm	20 nm	30 nm	40 nm
1.3	EMT	0.0910	0.3330	0.9011	-0.0863	-0.2798	-0.6009
	GLMT	0.0128	0.0576	0.02089	-0.0098	-0.0267	-0.0234
	Dipole	0.0086	0.0380	0.1361	-0.0066	-0.0154	-0.0134
1.4	EMT	0.1433	0.5215	1.3961	-0.1370	-0.4492	-0.9858
	GLMT	0.0180	0.0798	0.2859	-0.0141	-0.0349	-0.0374
	Dipole	0.0125	0.0541	0.1896	-0.0097	-0.0233	-0.0223

Tab. 6.2.: Force maxima and minima at peak for Gaussian beams under pulsed excitation at 100 mW average power for EMT, GLMT and dipole approximation.

power for fixed NA 1.3. It can be seen that including OKE results in a nonlinear behavior in nature of force curve (spikes (fluctuations) appearing) at high average power in EMT and GLMT approximation. For fixed particle size, these spikes appear at low average power for high NA, while for fixed NA decreasing particle size results in the appearance of these spikes at high average power. In the case of GLMT approximation, these oscillations start appearing at less average power in gradient and scattering forces, which correspond to the distortion in the total

force acting on the particle as compared to EMT. It can be seen from the graph that at 600 mW average power, there are no oscillations or spikes in the case of EMT but present in GLMT.

Conclusively, we can say that for a small-sized particle (few of nanometer), all three theories have similar nature of curve for the force acting on the particle; however, they are very different in magnitude. As particle size increases within the Rayleigh limit, it leads to deviation in the nature of curve for GLMT and dipole approximation as compared to EMT because increasing particle size contributes a significant amount of scattering force as compared to gradient force. Quite interestingly, it can be seen that GLMT and dipole can be written in separate gradient and scattering forces, while EMT cannot be written as gradient and scattering forces. From figure 6.3 to 6.6, it can be seen that for small-sized particles $Im[a_{\mathrm{n}}]$ dominates over other MSC. Overall, these theories disagree quantitatively as well as qualitatively, but including OKE at high average power, these theories are not valid at all.

6.5 Comparison of ray optics, GLMT and EMT in GO regime

For large-sized particles, we have compared GO 3D distribution, GLMT, and EMT. Figure 6.3 shows for large-sized particle limit, all the MSC are contributing significantly in the force calculations. In the case of GLMT and EMT, the force calculation of large particle size converges for summation over n from 1 to 70, 1 to 100, and 1 to 110 for 4 μm, 6 μm and 8 μm (radius of particles) respectively. In GO 3D distribution, the force calculations of the large-sized particle are done for summation over 100 cones.

6.5.1 CW excitation

Figure 6.12a shows the comparison between EMT, GLMT, and GO 3D distribution for 4 μm sized particle with fixed NA 1.3 at 1 mW average power. It can be seen that force curves for EMT and GO 3D distribution are comparable while GLMT is not. Figure 6.12b shows the GLMT force curves where cyan, red, and blue corresponds to scattering, gradient, and total force acting on the particle. It can be seen that there is no splitting in the scattering force. The scattering force is maximum near the focus that could not be possible for large-sized particles because for large-sized particles, scattering is maximum at the surface of the particle, and gradient force is also not symmetric about the beam axis. Figure

6.12b (zoomed part) shows that locally the nature of total force acting on the particle is similar to EMT, but the order of magnitude and symmetry about both the beam and axial axis is very different from the EMT and GO 3D distribution. The noticeable point here is that near the focus, a hump is present in both GLMT and EMT because of MSC; however, no such local distortion is present in the GO 3D distribution curve. Here, it is apparent that GLMT using localized approximation is not a good theory/approximation to calculate the force acting on the particle for large-sized particle, that is why in further analysis for large-sized particle we have compared EMT and GO 3D distribution.

Figure 6.13 shows axial force calculations using EMT and compared with GO

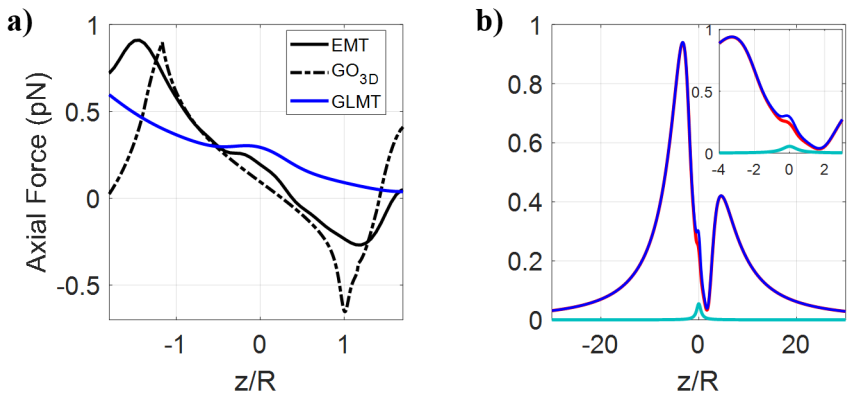

Fig. 6.12.: Plots of axial force a) total force for 2D/3D/GO approximation, and b) gradient, scattering, and total force using GLMT approxiamtion for NA=1.3 along axial direction at 1 mW average power under CW excitation. Here, solid/dotted line corresponds to EMT/ GO 3D distribution.

approximation for different radii of particles 4 μm, 6 μm and 8 μm having NA=1.3 (top panel) and NA=1.4 (bottom panel) at 1 mW average power under CW excitation for Gaussian beam profile; where solid and dotted lines correspond to the EMT and GO 3D distribution, respectively. Red and green are linear fits correspond to the GO 3D distribution and EMT, respectively. It can be seen from table 6.3 that the peak value of force is constant for GO 3D distribution for different particle sizes for fixed NA of 1.3 and 1.4, respectively. The comparison of NA 1.3 and 1.4 shows a small increment in peak value for NA 1.4 because, for NA 1.4, the beam is more tightly focused, which leads to high peak intensity compared to NA 1.3. On the other hand, if we look at EMT, it can be seen from table 6.3 that increase in particle size leads to decrease in the peak maxima for fixed NA, but for fixed particle size, with the increase in NA, peak maxima will increase due to tight focusing condition. The table 6.4 shows a negligible change in peak minima for different particle szie at fixed NA and same theory, which

can be explained by the minimum force experienced by the particle when the beam is focusing on the back surface. The focusing of beam on the front surface is dependent upon the particle size whereas beam focusing on back surface is independent of particle size which is why there is no change in the reduced z/R position for minima force, but there is small change in the reduced z/R position for maximum force as per increase in particle size for fixed NA. Table 6.5 shows the numerical values of trap stiffness at equilibrium point calculated by using linear fit of force curve near the focus shown by red and green curve in figure 6.13 (inset). It can be seen that there is no change in trap stiffness values on increasing particle size for both theories, but there is a significant change in stiffness as per the increase in NA from 1.3 to 1.4 for fixed average power. As per the increase in the particle size, we are getting good agreement between both the theories under CW excitation although there is a negligible decrease in the peak maxima of EMT as per increase in particle size for fixed NA shown in table 6.3.

For EMT figure 6.13 shows that with increase in the particle size and numerical aperture, the nature of hump is changing near the focus (shown in the inset), which is an indication of changing nature of force curve. In contrast, the increase in average power leads to a change in the magnitude of the force, not the nature of force curve for CW excitation because, in the case of CW excitation, force is directly proportional to the average power of trap beam in the absence of nonlinearity. These changes in the nature of force curve are occurring due to the scattering coefficient and BSC of the Gaussian beam profile, as can be seen from figure 6.6, 6.7, and 6.8.

Particle Size	$4\mu m$		$6\mu m$		$8\mu m$	
NA	GO-3D	EMT	GO-3D	EMT	GO-3D	EMT
1.3	0.9	0.91	0.9	0.86	0.9	0.83
1.4	0.97	0.93	0.96	0.88	0.96	0.85

Tab. 6.3.: Magnitude of force (at peak maxima; pN) for Gaussian beams under CW excitation at 1 mW average power for a GO 3D distribution and EMT. Here, GO-3D represents the geometric optics approximation for 3D distribution of light cones, and EMT represents the EMT.

6.5.2 Pulsed Excitation

Figure 6.14 shows axial force curves at 1 mW average power under pulsed excitation, where the solid and dashed lines correspond to the EMT and GO

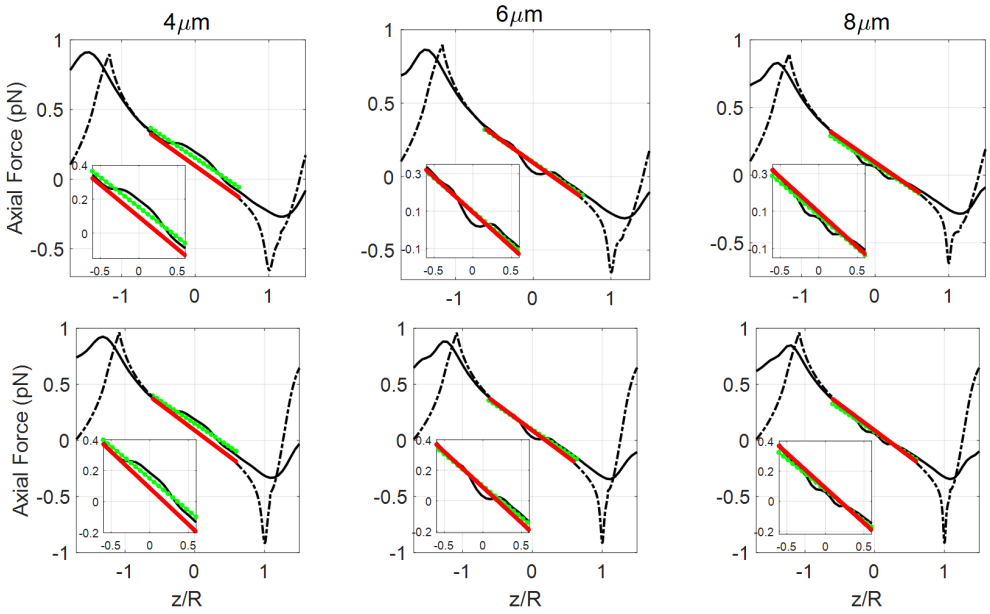

Fig. 6.13.: Plots of axial force top panel for NA=1.3 and bottom panel for NA=1.4 at 1 mW average power under CW excitation. Here, solid/dotted line corresponds to EMT/GO 3D distribution. Color: green/red curve corresponds to linear fit to EMT/GO 3D distribution.

Particle Size	$4\mu m$		$6\mu m$		$8\mu m$	
NA	GO-3D	EMT	GO-3D	EMT	GO-3D	EMT
1.3	-0.65	-0.27	-0.65	-0.28	-0.65	-0.28
1.4	-0.91	-0.33	-0.91	-0.34	-0.91	0.34

Tab. 6.4.: Magnitude of force (at peak minima; pN) for Gaussian beams under CW excitation at 1 mW average power for a GO 3D distribution and EMT. Here, GO-3D represents the geometric optics approximation for 3D distribution of light cones, and EMT represents the EMT.

Particle Size	$4\mu m$		$6\mu m$		$8\mu m$	
NA	GO-3D	EMT	GO-3D	EMT	GO-3D	EMT
1.3	0.38	0.35	0.38	0.35	0.37	0.35
1.4	0.47	0.41	0.47	0.41	0.47	0.41

Tab. 6.5.: The trap stiffness $\left(k_{stiffness}\left(\frac{pN}{\mu m}\right)\right)$ for Gaussian beams under CW excitation at 1 mW average power for a GO 3D distribution and EMT. Here, GO-3D represents the geometric optics approximation for 3D distribution of light cones, and EMT represents the EMT.

3D distribution, respectively. Red and green lines are linear fit corresponds to the GO 3D distribution and EMT, respectively. It can be seen that at very low

average power, under pulsed excitation, with increasing particle size, there is a significant change in a hump near the focus in the force curve, whereas no such effect observed under CW excitation. If we compare tables 6.3, 6.4, and 6.5 with table 6.6, 6.7, and 6.8 it can be seen that there is not much change in the peak maxima, peak minima and trap stiffness at low average power.

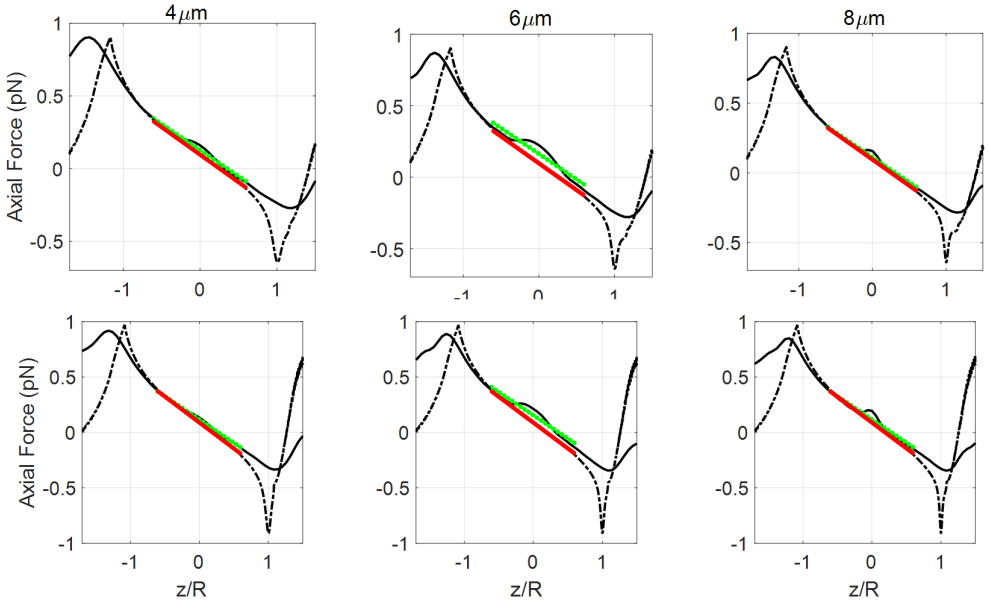

Fig. 6.14.: Plots of axial force top panel for NA=1.3 and bottom panel for NA=1.4 at 1 mW average power under pulsed excitation. Here, solid/dotted line corresponds to EMT/GO 3D distribution. Color: green/red curve corresponds to linear fit to EMT/GO 3D distribution.

Particle Size	$4\mu m$		$6\mu m$		$8\mu m$	
NA	GO-3D	EMT	GO-3D	EMT	GO-3D	EMT
1.3	0.9	0.9	0.9	0.87	0.9	0.83
1.4	0.97	0.92	0.97	0.89	0.97	0.85

Tab. 6.6.: Magnitude of force (at peak maxima; pN) for Gaussian beams under pulsed excitation at 1 mW average power for a GO 3D distribution and EMT. Here GO-3D represents the geometric optics approximation for 3D distribution of light cones, and EMT represents the EMT.

Figures 6.15 and 6.16 show the axial force curve at NA 1.3 and 1.4 respectively; where top panel (corresponds to 1 mW average power), middle panel (corresponds to 10 mW average power) and bottom panel (corresponds to 100 mW average power) under pulsed excitation; Solid/dotted line: EMT/GO 3D distribution at 1 mW average power under pulsed excitation. In EMT for a fixed average

Particle Size	$4\mu m$		$6\mu m$		$8\mu m$	
NA	GO-3D	EMT	GO-3D	EMT	GO-3D	EMT
1.3	-0.64	-0.027	-0.64	-0.28	-0.64	-0.28
1.4	-0.91	-0.33	-0.91	-0.34	-0.91	-0.34

Tab. 6.7.: Magnitude of force (at peak minima; pN) for Gaussian beams under pulsed excitation at 1 mW average power for a GO 3D distribution and EMT. Here GO-3D represents the geometric optics approximation for 3D distribution of light cones, and EMT represents the EMT.

Particle Size	$4\mu m$		$6\mu m$		$8\mu m$	
NA	GO-3D	EMT	GO-3D	EMT	GO-3D	EMT
1.3	0.38	0.36	0.38	0.36	0.37	0.36
1.4	0.47	0.41	0.47	0.41	0.47	0.42

Tab. 6.8.: Equilibrium position and trap stiffness $\left(k_{stiffness}\left(\frac{pN}{\mu m}\right)\right)$ for Gaussian beams under pulsed excitation at 1 mW average power for a GO 3D distribution and EMT. Here GO-3D represents the geometric optics approximation for 3D distribution of light cones, and EMT represents the EMT.

power and NA, an increase in particle size leads to a decrease in trap stiffness while increasing NA leads to an increase in the trap stiffness for fixed particle size and average power. Comparing NA of 1.3 and 1.4, it can be seen that trap stiffness is more for NA 1.4 as compared to NA 1.3 because increasing NA gives more confinement due to tight focusing condition can be seen from table 6.9. Nonlinearity dominates as per the increase in the average power, which results in the drastic change in the magnitude and the nature of the force curves near the focus. Quite interestingly, the total force exhibits oscillatory behavior near the focus, and that behavior increases with average power for fixed particle size, while the oscillatory behavior increases with increasing particle size for a fixed power. This oscillatory behavior is appearing due to the significant contribution of MSC. From figures 6.6 and 6.7, it can be seen that nonlinearity effects this oscillatory nature more near the focus. As we are going away from the focus, distortion in the oscillatory behavior is less, that is why near the focus, these spikes are appearing more as per increase in average power for fixed particle size and NA. For a fixed power, it is observed that NA 1.4 gives more oscillatory behavior as compared to NA 1.3. So, at high power, it is difficult to estimate force using EMT because of the nonlinear nature of the curve, but in the case of 3D GO distribution, there is an instant rise in the peak at z/R=1, which will not give a

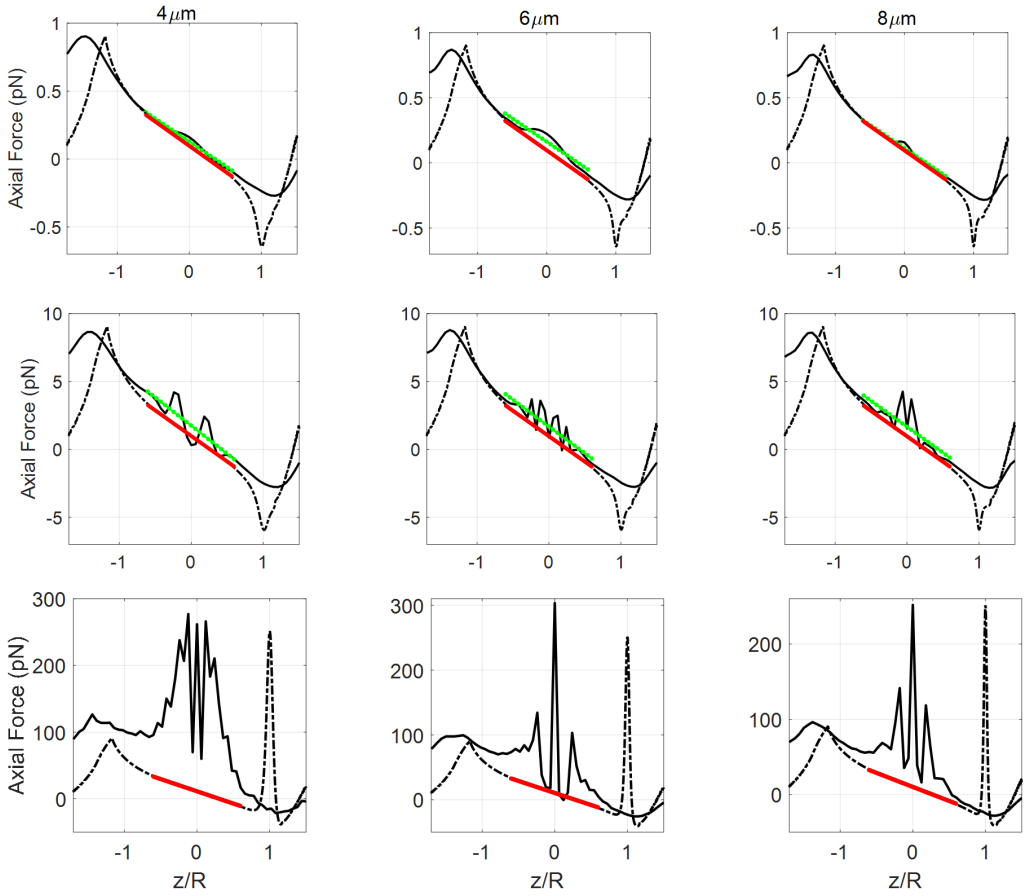

Fig. 6.15.: Plots of axial force for NA=1.3 at different average power (1 mW; top panel, 10 mW; middle panel, 100 mW; bottom panel) under pulsed excitation.

qualitative trap stiffness. Conclusively, we can say that in linear (CW excitation)

Particle Size		$4\mu m$		$6\mu m$		$8\mu m$	
NA	Power (mW)	GO-3D	EMT	GO-3D	EMT	GO-3D	EMT
1.3	1	0.38	0.36	0.38	0.36	0.37	0.36
	10	3.77	4.16	3.75	3.94	3.74	3.81
	100	36.78	—-	37.15	—-	37.24	—-
1.4	1	0.47	0.41	0.47	0.41	0.47	0.42
	10	4.69	4.87	4.66	4.56	4.65	4.44
	100	46.77	—-		—-	46.55	—-

Tab. 6.9.: Trap stiffness $\left(k_{stiffness}\left(\frac{pN}{\mu m}\right)\right)$ for Gaussian beams under pulsed excitation at different average power for a GO 3D distribution and EMT.

case, the EMT and 3D GO theories are well in agreement with each other. These theories are not able to get a quantitative force estimation at high average power

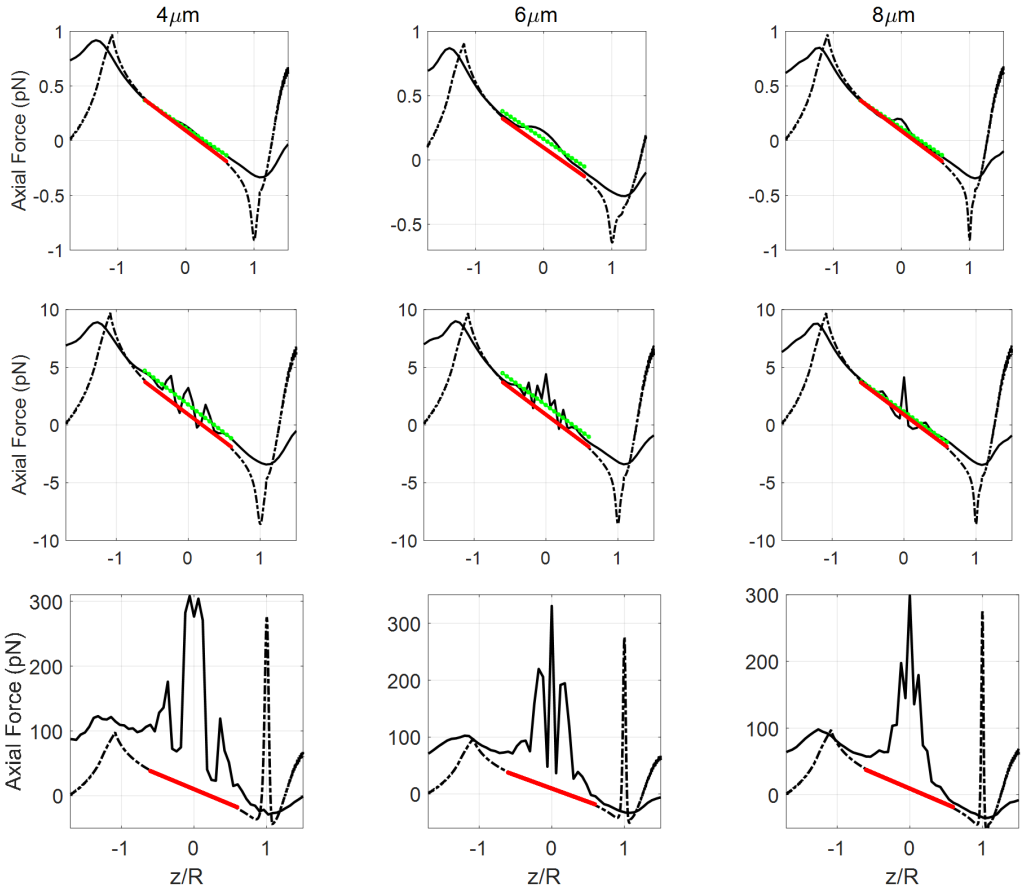

Fig. 6.16.: Plots of axial force for NA=1.4 at different average power (1 mW; top panel, 10 mW; middle panel, 100 mW; bottom panel) under pulsed excitation.

due to the significant contribution of OKE but could get a quantitative force estimation for low average power.

6.6 Comparison of GLMT and EMT in intermediate regime

EMT and GLMT are valid for all size limits, so here for the Mie regime, considered particle size is of the order of wavelength. For Mie regime 0.4 μm particle size force calculations converge for summation over 40 terms in both GLMT and EMT.

6.6.1 CW excitation

Figure 6.17a shows the force acting on 0.4 μm (radius of the particle) using both GLMT and EMT at 1 mW average power where black corresponds to the EMT and blue corresponds to the GLMT. From figure 6.17b, it can be seen that gradient and

scattering forces have similar behavior. There is no attraction; the only repulsion is present in GLMT theory. From here, it is apparent that the GLMT theory using localized approximation is not a valid theory for the Mie regime. However, EMT gives a relevant (attractive) force acting on the particle, which is why further analysis in the Mie regime is done using EMT.

Further analysis in the Mie regime for force calculations is done at 10 mW average power because for 4 μm particle size near the focus oscillations are appearing; however, in this case, no such oscillatory behavior is present for NA 1.3 and 1.4. Figure 6.18 shows the axial curve using EMT for NA 1.3 and 1.4 at 10 mW average power.

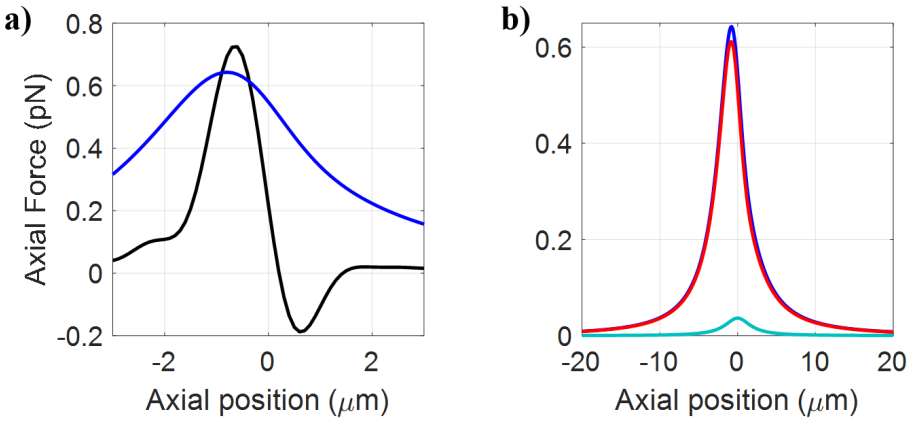

Fig. 6.17.: Plots of axial force for NA=1.3 at 1 mW average power for both GLMT and EMT.

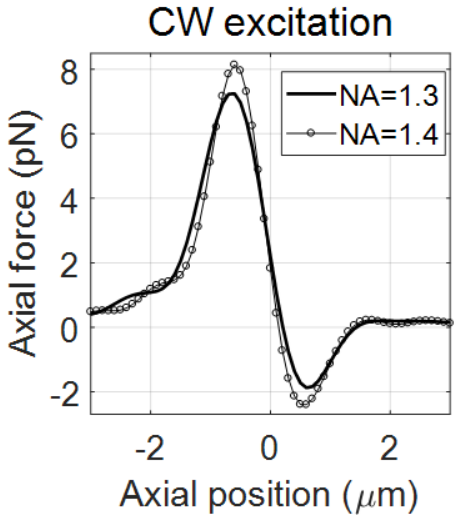

Fig. 6.18.: Plots of trapping force acting on the 0.4 μm particle at 10 mW average power under CW excitation for NA 1.3 and 1.4.

6.6.2 Pulsed Excitation

Figure 6.19 shows the trapping force curve for 0.4 μm particle size under pulsed excitation at 10 mW average power for fixed NA 1.3. It can be seen that at similar average power, there is a significant change in force curve for CW and pulsed excitation, and quantitatively it can be seen from table 6.10. From table 6.11, it

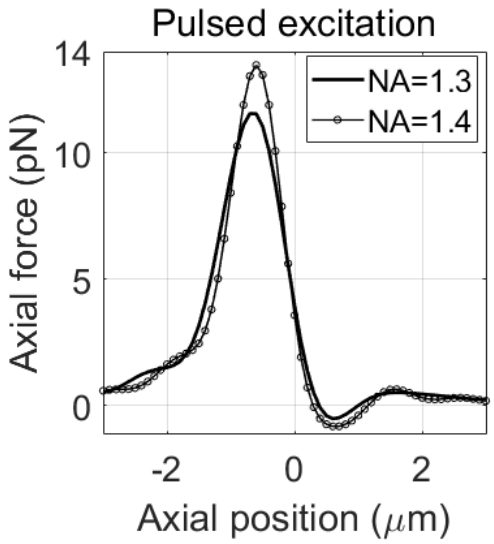

Fig. 6.19.: Plots of trapping force acting on the 0.4 μm particle at 10 mW average power under pulsed excitation for NA 1.3 and 1.4

NA	CW excitation	Pulsed excitation
1.3	7.25	11.55
1.4	8.14	13.47

Tab. 6.10.: Peak maxima of force for Gaussian beams under CW and pulsed excitation at 10 mW average power for EMT.

can be seen that for fixed NA and particle size, trapping efficiency of CW excitation is less as compared to pulsed excitation at similar average power. It implies that pulsed excitation gives better trapping as compared to CW excitation in the Mie regime or small-sized particles. Because for large-sized (micron-sized) particles, there is no impulsive effect of pulses; particle experiences the cumulative effect of pulses which is similar to CW excitation, that is why there is no change in trap stiffness.

Conclusively, GLMT, and EMT are not in good agreement for any regime. GLMT is not valid for GO limit because we are not getting any attractive force acting on the particle. In contrast, EMT gives a significant reliable force acting on the

NA	CW excitation	Pulsed excitation
1.3	10.83	14.94
1.4	13.85	19.84

Tab. 6.11.: Trap stiffness $\left(k_{stiffness}\left(\frac{pN}{\mu m}\right)\right)$ for Gaussian beams under CW and pulsed excitation at 10 mW average power for EMT.

particle, and including nonlinearity also gives a significant relevant result for trapping efficiency. We observed that at similar average power, pulsed excitation gives better trapping as compared to CW excitation.

The same model we have repeated to support our experimental results, which is discussed later in chapter 9, using pulse width as 526 fs and repetition rate as 80 MHz. Results are as follows:

We have used 1 μm sized polystyrene beads in our experiments. Since the particle size is approximately equal to the wavelength $(\lambda \approx a)$ of trapping beam, we have used EMT. Under this condition, EMT is a valid theory to calculate the force and potential acting on the particle. It is observed that the force and potential curves show a significant change in magnitudes under pulsed excitation, whereas no such effect is observed under CW excitation while ignoring or including OKE into account. However, the nature of force and potential curves remains the same for both CW and pulsed excitation. From this, we can conclude that including OKE into account plays an essential role under pulsed excitation as compared to CW excitation due to its high peak power, which can be seen from figure 6.20. From

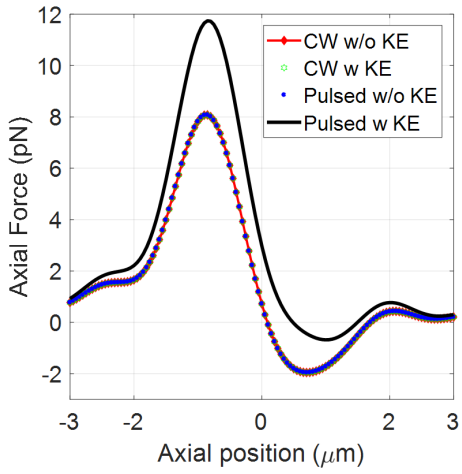

Fig. 6.20.: Plots of trapping force along axial direction on an 1 μm particle at 10 mW average power under CW and pulsed excitation with and without Kerr effect.

the above discussion, it is clear that only pulsed excitation shows a significant

change. Therefore, we have studied the power variation of force and potential curve, as shown in figure 6.21. It is obtained that absolute depth of potential well increases with increase in average power whereas escape potential (U_{abs} and U_{esc}; refer to chapter 3) becomes unbound at high average power.

The absolute well depth is increasing monotonically while the escape potential

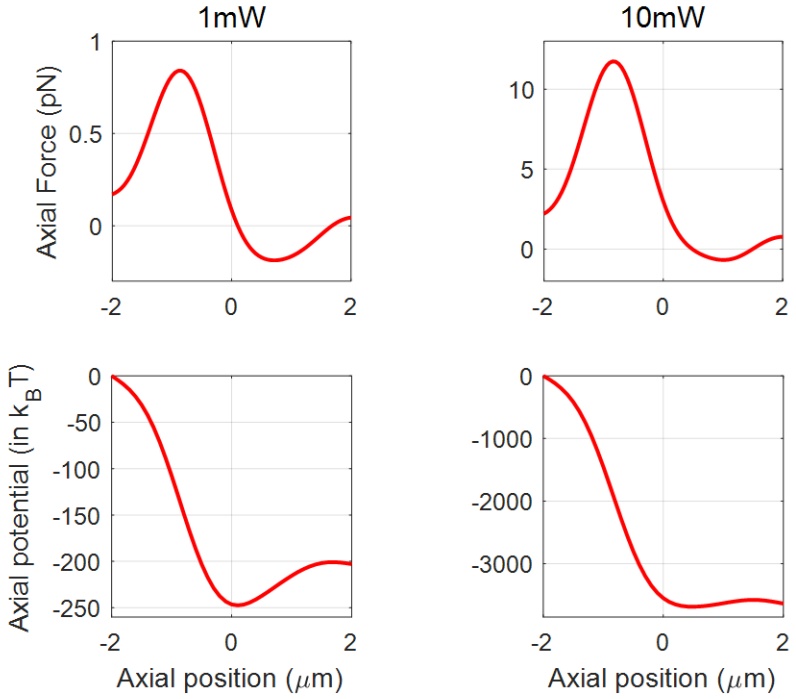

Fig. 6.21.: Plots of trapping force and potential on an 1 μm particle at 1 mW and 10 mW average power under pulsed excitation including Kerr effect respectively. Color: red correspond to force/potential.

passes through a maxima. The power corresponding to this maxima is the power where the trap is most stabilized under pulsed excitation (nature of curve is nonlinear). While in the case of CW excitation (nature of curve is linear, but U_{abs} increasing rapidly compared to U_{esc}), there are no such maxima at similar average power as can be seen in the figure 6.22. From this, we can see in the case of pulsed excitation, the optimal power for 1 μm polystyrene bead is found to be $\sim$ 22 mW average power.

6.7 Phase portrait

To study the dynamics of a single particle (of mass 4.4 $\times$ 10^{-15} Kg) moving in a 3D optical trap, we have shown phase portrait at 1 mW average power for both CW and pulsed excitation. It can be seen from figure 6.23; the particle is initially confined and then moved out with the continuous change in velocity

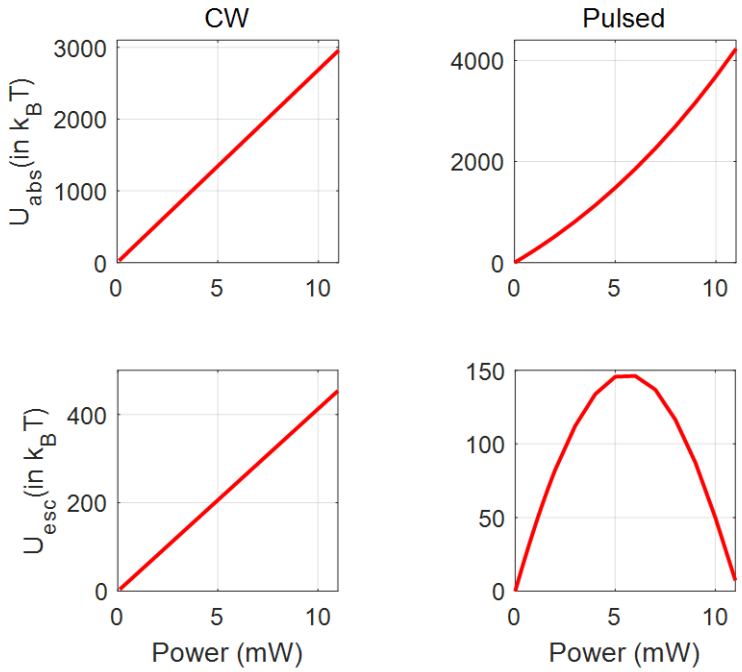

Fig. 6.22.: Plots of minimum potential (U_{abs}; top panel) and the escape potential (U_{esc}; bttom panel) with respect to average power under CW and pulsed excitation.

vector, which might be due to the accumulation of energy. For bounding a particle, the net energy of the system (E_{axial}) should be less than the potential energy barrier ($V_{1,axial}$) and the particle confinement region is delimited by two classical turning points (z_1 and z_2). The condition for confinement of the particle is $V_{0,axial} < E_{axial} < V_{1,axial}$. If $V_{1,axial} < E_{axial} < V_{2,axial}$ then particle can move only in one direction $z \to \infty$. If $E_{axial} > V_{2,axial}$ particle is free to move anywhere along $z \to \pm\infty$ as shown in figure 6.23a. This phase portrait can be correlated with the proposed model of particle motion inside the trap. Figures 6.23b and 6.23c represent the velocity vector field of a particle inside the trap for CW and pulsed excitation at 10 mW average power and the pattern of velocity vector field determines the time of confinement of a particle inside the trap. From the pattern, we observed that the time of confinement in CW excitation prolongs the pulsed excitation.

6.8 Conclusion

From the above discussion, we can say that the definition of light bending inside the medium that we have proposed is more appropriate than the existing one for calculating the force acting on the particle for high NA. As shown above, in the case of CW excitation, EMT matches with GO 3D distribution approximation and

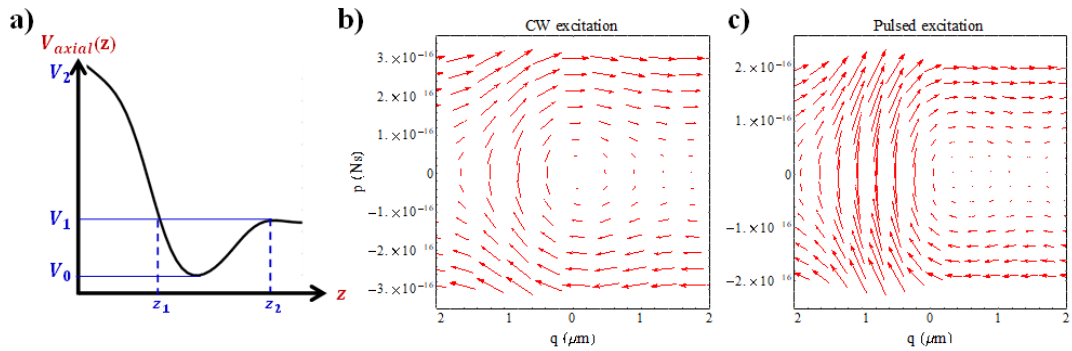

Fig. 6.23.: a) Schematic diagram for particle to be bound inside the trap and phase portrait for b) CW excitation and c) pulsed excitation at 10 mW average power.

gives a reliable prediction of the force acting on the particle, but fails to agree with dipole approximation. In literature, it is proposed that GLMT using localized approximation is a general theory, which holds for all particle sizes. This is in contrast with our findings; it is applicable only for small-sized particles as evident from the nature of the curves.

We have also found that under pulsed excitation case, EMT matches with Geometric optics theory at very low average power (where nonlinear effects are negligible). At high average power, both GO and dipole approximations stand in disagreement with EMT. EMT is reliable in the Mie regime for the force calculations in both CW and pulsed excitation and able to calculate power corresponding to the most stable trap compared with GLMT approximation. We can say that this theory gives a reliable result for Mie and GO regime under CW excitation whereas the Mie regime under pulsed excitation.

7 Force and potential on silver, hybrid, and hollow-core silver nanoparticles using dipole approximation

7.1 Introduction

In chapters 3 to 6, we have discussed that nonlinearity plays an important role in determining the trapping force/potential for dielectric particles. In this chapter, we are going to discuss the behavior of metallic nanoparticles, which are different from the dielectric. Initially, it was believed that the trapping of metallic particles was extremely difficult because metals are more reflecting and absorptive in nature [143–145]. Reflectivity causes a significant dominance of scattering force over gradient force, and absorptivity results in an additional force known as absorption force which is absent in the case of dielectric particles and is responsible for unwanted thermal effects. On top of this, trapping becomes more challenging when we go to the nanometre size because of the increased Brownian motion of the particles. The behavior of metallic particles towards light is markedly different from that of dielectric particles because of the presence of free electrons. These particles exhibit a unique phenomenon upon interaction with light that is hardly achievable in dielectric cases Therefore, metallic nanoparticles' properties are remarkably different from those of the bulk properties of the metals. For example, small metallic structures can sustain coherent electron oscillations known as Surface Plasmon Polaritons (SPP) [146, 147]. A metallic nanoparticle experiences an attractive or repulsive force which not only depends on the surrounding medium, but also depends on the wavelength of the trapping beam because the polarizability of metallic nanoparticles changes drastically by changing the wavelength of the trapping beam. Metallic nanoparticle shows resonance behavior around 400 nm wavelength. Also, for metallic particles, trapping depends upon the scattering cross-section because metallic particles are inclined to reflect, scatter and absorb more photons, which tends to destabilize the trap [143, 144, 148]. Earlier, it was believed that the trapping of metallic nanoparticles is impossible. Later in 1994, Block and co-workers showed that the trapping of metallic particles could be achieved due to their higher polarizability [97]. Under dipole approximation,

the surface plasmons are localized and experience the characteristic resonance phenomena. Since then, there have been various studies to quantify the trapping behavior depending upon the particle size [22, 71, 149] as well as considering the resonance conditions [150–154]. Here, we have theoretically investigated trapping behavior of metallic (silver) nanoparticles and study the effect of OKE (up to sixth order nonlinearity) under high repetition-rate femtosecond pulsed excitation for off-resonance wavelength (near IR), to explain the experimental observations under pulsed excitation. We have observed that with an increase in laser power, the escape potential initially disappears but subsequently reappears at higher laser power. Later, a comparative study of hybrid and hollow-core nanoparticles with conventional particles is done to examine how the performance is enhanced under both continuous-wave and pulsed excitation. We have observed that under similar conditions, the hybrid and hollow-core type nanoparticles experience more force than conventional nanoparticles. This has a potential advantage while doing bio-conjugated experiments that require high magnitudes of force. Also, the nature of force/potential can be controlled from repulsive to attractive by taking advantage of OKE depending on the material properties (such as nonlinear RI and the proportionality) of the core-shell radius. Certain particle sizes that could be stably trapped under CW excitation were found to be untrappable under pulsed excitation and vice -versa. Hence, according to the specific requirement, one should be careful while choosing the proportionality of a core-shell radius depending on the average power, numerical aperture, and other relevant laser parameters. Considering the novelty of this work, we envision the far-reaching application of controlled optical manipulation through tuning optical nonlinearity.

7.2 Mathematical formulation

The mathematical expressions for dipole approximation are already discussed, but for metallic nanoparticles, the way of calculating polarizability is different. The permittivity and the corresponding polarizability of metallic nanoparticles are described using the inter-band corrected Drude-Lorentz model [155, 156]. Apart from the scattering and gradient forces that act on dielectric particles, in the case of metallic particles, there is an additional contribution from the absorption forces along the axial direction that plays a major role in determining the stability of the trap, and absorption force mathematically can be written as [155]:

$$F_{axial,absorption}\left(z; r=0\right) = \frac{4k\pi n^{w} a^{3}}{c} Im\left[\alpha_0\right] \frac{2P_{peak/avg}}{\pi\omega_0^2\left(1+4Z^2\right)} \tag{7.1}$$

Here $\alpha' = \frac{4}{3}\pi a^3 \times 3\left(\frac{n^{p/s^2} - n^{w^2}}{n^{p/s^2} + 2n^{w^2}}\right) = V \times 3\alpha_0$ is polarizability and $\alpha = 3\alpha_0$ is polarizability per unit volume, hereafter polarizablility for polystyrene and silver are represented as α^p and α^s respectively. The refractive index (RI) of silver is expressed as $n^s = n_0^s + i\kappa_0^s$; n_0^s is linear real part of RI and κ_0^s is linear imaginary part which is directly proportional to the absorptivity. In the case of dielectric nanoparticles, the imaginary part does not contribute significantly because absorption is negligible whereas it cannot be neglected for silver nanoparticles. For silver nanoparticles RI can be calculated as: $n_0^s = \sqrt{\frac{\epsilon_1}{2} + \frac{\sqrt{\epsilon_1^2 + \epsilon_2^2}}{2}}$, $k_0^s = \frac{\epsilon_2}{2n_0^p}$, σ_0^s is the absorptivity of the particle $\sigma_0^s = \frac{4\pi\kappa_0^s}{\lambda}$; $\epsilon_1 = Re\left[\epsilon\right]$, $\epsilon_2 = Im\left[\epsilon\right]$ and $\epsilon = \varepsilon_\infty - \frac{\omega_p^2}{\omega^2 + i\gamma_c\omega}$ according to the corrected Drude-Lorentz model [123]. In addition to the linear RI, the role of nonlinear effects is investigated by incorporating nonlinear refractive indices. The total RI can be calculated from the given expression:

$$n^w = n_0^w + n_2^w \times I \tag{7.2}$$

$$n^p = n_0^p + n_2^p \times I \tag{7.3}$$

$$n^s = n_0^s + n_2^s \times I + n_4^s \times I^2 + n_6^s \times I^3 + i\left(k_0^s + k_2^s \times I + k_4^s \times I^2 + k_6^s \times I^3\right) \tag{7.4}$$

where, n_0^p , n_2^p and n_0^w , n_2^w are the linear and nonlinear refractive index for polystyrene and water, respectively, however, in this chapter, we have considered only CW excitation for polystyrene (*i.e.* $n^p \sim n_0^p$). Since the nonlinear RI of water is very small, can be neglected as discussed in chapter 3 (*i.e.* $n^w \sim n_0^w$). For silver, n_0^s and k_0^s are the linear RI (real and imaginary parts) whereas n_2^s , n_4^s , n_6^s , k_2^s , k_4^s , and k_6^s are the nonlinear RI (the second, fourth, and sixth order real and imaginary part). Using this relation, polarizability can be decomposed into real and imaginary parts as given below:

$$\begin{aligned}\alpha_0^s = &\frac{\left(n_R^{s^2} - n_I^{s^2} - n^{w^2}\right)\left(n_R^{s^2} - n_I^{s^2} + 2n^{w^2}\right) + 4n_R^{s^2}n_I^{s^2}}{\left(n_R^{s^2} - n_I^{s^2} + 2n^{w^2}\right)^2 + 4n_R^{s^2}n_I^{s^2}} \\ &+ i\frac{6n_R^s n_I^s n^{w^2}}{\left(n_R^{s^2} - n_I^{s^2} + 2n^{w^2}\right)^2 + 4n_R^{s^2}n_I^{s^2}}\end{aligned} \tag{7.5}$$

where, $n_R^s = n_0^s + n_2^s \times I\left(r,z\right) + n_4^s \times I^2\left(r,z\right) + n_6^s \times I^3\left(r,z\right)$, and $n_I^s = k_0^s + k_2^s \times I\left(r,z\right) + k_4^s \times I^2\left(r,z\right) + k_6^s \times I^3\left(r,z\right)$. $I_{peak/avg}\left(r,z\right)$ is the intensity of the focused

Gaussian beam, which can be described as [39, 94]:

$$I_{peak/avg}\left(r; z=0\right) = \left(\frac{2P_{peak/avg}}{\pi\omega_0^2}\right) e^{-2R^2} \tag{7.6}$$

$$I_{peak/avg}\left(z; r=0\right) = \left(\frac{2P_{peak/avg}}{\pi\omega_0^2}\right) \frac{1}{1+\left(2Z\right)^2} \tag{7.7}$$

The total force acting on the particle in the case of dielectric and metallic particles can be written as:

$$\begin{aligned} F_{total,dielectric,axial}\left(z; r=0\right) = F_{axial,grad}\left(z; r=0\right) \\ + F_{axial,scatt}\left(z; r=0\right) \end{aligned} \tag{7.8}$$

$$F_{total,dielectric,radial}\left(z; r=0\right) = F_{radial,gradient}\left(r; z=0\right) \tag{7.9}$$

The total force acting along axial direction for metallic particles is:

$$\begin{aligned} F_{total,metallic}\left(z; r=0\right) = F_{gradient}\left(z; r=0\right) \\ + F_{scattering}\left(z; r=0\right) \\ + F_{absorption}\left(z; r=0\right) \end{aligned} \tag{7.10}$$

The total force acting along radial direction for metallic particles is:

$$F_{total,metallic}\left(r; z=0\right) = F_{gradient}\left(r; z=0\right) \tag{7.11}$$

Table 2.1 lists the important parameters which are used in the calculations. The values for NA and average power under CW and pulsed excitation are equal to 1.4 and 100 mW, respectively, unless mentioned otherwise.

7.3 Comparison between dielectric and metallic nanoparticles

Figures 7.1 and 7.2 show the force/potential curves along radial and axial directions for 10 nm and 30 nm polystyrene and silver nanoparticles under CW excitation. Here, red/green/blue/black curves correspond to total/gradient/scattering/absorption force/potential, respectively. Total force/potential is symmetric about the axis in the case of radial direction because only gradient force contributes. However, they are asymmetric along axial direction due to significant contributions from scattering and absorption forces.

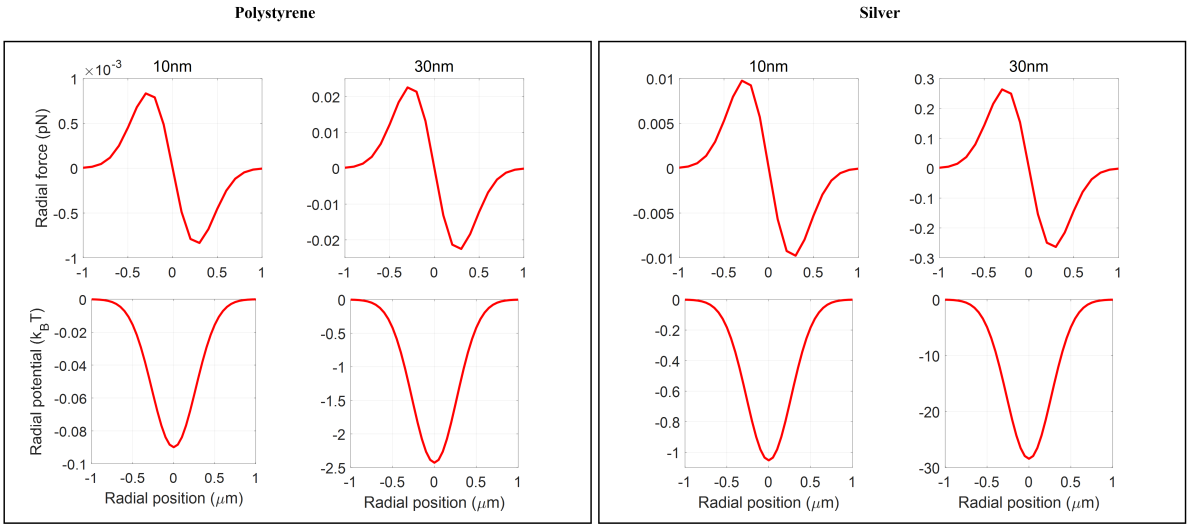

Fig. 7.1.: Plots of trapping force and potential along radial direction for both polystyrene and silver under CW excitation.

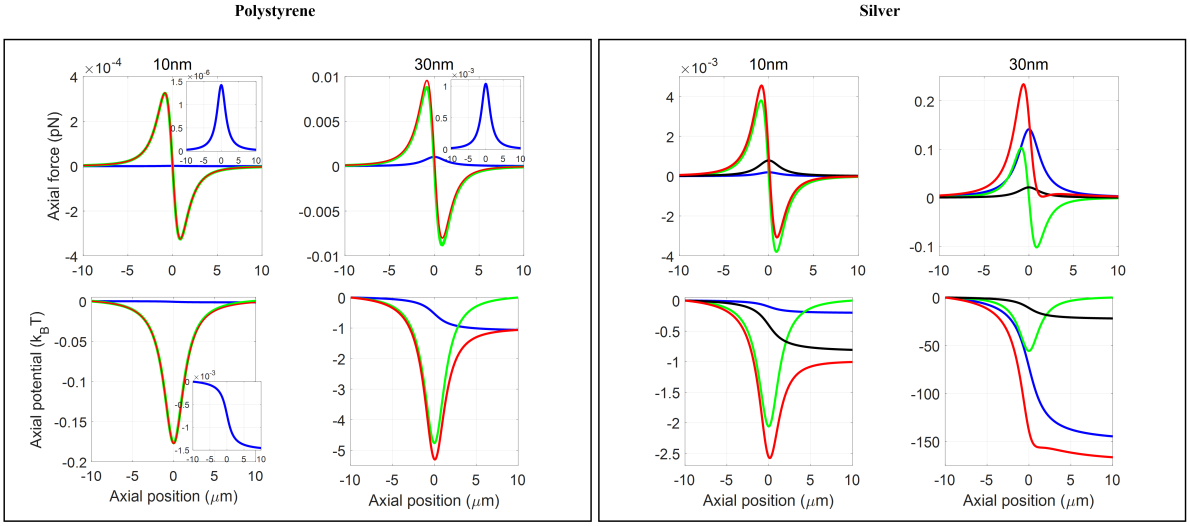

Fig. 7.2.: Plots of trapping force and potential along axial direction for both polystyrene and silver under CW excitation, and zoomed-in plot shows the contribution of scattering force/potential to the total force/potential.

From tables 7.1 and 7.2, it is apparent that the magnitude of force maxima is higher along the radial direction than the axial direction for very small particles (for example 10 nm), but with increase in particle size, the axial force increases rapidly and exceeds the radial force maxima for larger particles (for example 40 nm). The escape potential is high in magnitude for silver nanoparticles than polystyrene nanoparticles. In the radial direction, the absolute potential rises quickly towards higher magnitudes with increasing particle sizes because only gradient force contributes, which is symmetric about the axis. In contrast to this, the potential becomes unbound along the axial direction beyond a certain size for

a fixed average power because absorption and scattering forces dominate over gradient force, which results in destabilizing the trap. The enhancement factor for different sized particles is constant along the radial direction as only gradient force is present. The effect of increasing particle size gets canceled while taking the ratio for fixed particle size because polarizability is directly proportional to the volume of the particle. However, it increases consistently along the axial direction because along the axial direction, polystyrene experiences only gradient and scattering forces while silver experiences gradient, scattering, and absorption forces. From the mathematical expressions of the gradient, scattering, and absorption force, it can be seen that the gradient and absorption forces are proportional to a^3 while scattering force is proportional to a^6. So, increasing the particle size decreases the contribution of the absorption force to the total force. The high magnitude of the imaginary part results in an enhanced absorption force, which is absent in the case of polystyrene. Therefore, the enhancement factor of total force increases rapidly with an increase in the particle size along the axial direction but remains the same along the radial direction. This enhancement in force is due to the higher polarizability of silver particles as compared to polystyrene particles, as shown in figure 7.3a. The plot shows the nature of polarizability as a function of wavelength. The peak in the polarizability of silver nanoparticles (highlighted by the blue rectangle) corresponds to the surface plasmon resonance phenomenon which is absent in the case of dielectric particles.

The zoomed-in inset in figure 7.3a indicates the higher magnitude of real part of

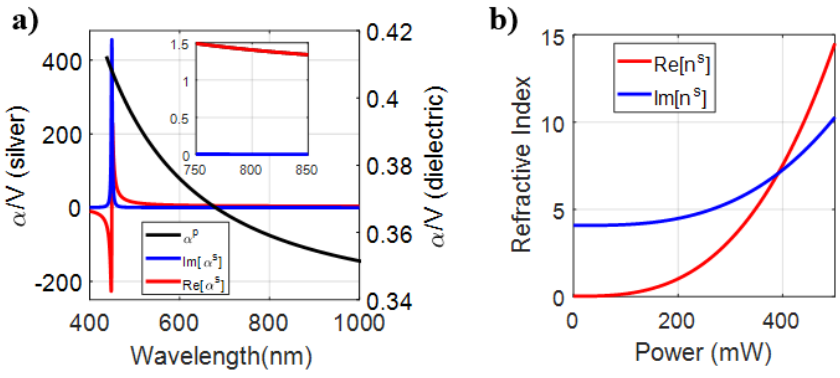

Fig. 7.3.: Plots of a) polarizability per unit volume against wavelength for both polystyrene and silver particles under CW excitation, and b) real and imaginary RI against average power at geometric focus for silver nanoparticles.

polarizability, even at off-resonant condition which suggests trapping is possible

PS(nm)	$F_{max}(pN)$			$F_{min}(pN)$			$U_{esc}(k_BT)$	
	Silver	Polystyrene	Ratio	Silver	Polystyrene	Ratio	Silver	Polystyrene
10	0.0098	0.0008	11.7038	-0.0098	-0.0008	11.7050	1.0528	0.0899
20	0.0781	0.0067	11.7030	-0.0781	-0.0067	11.7046	8.4220	0.7192
30	0.2635	0.0225	11.7039	-0.2635	-0.0225	11.7055	28.4244	2.4273
40	0.6246	0.0534	11.7037	-0.6246	-0.0534	11.7048	67.3762	5.7537

Tab. 7.1.: Comparison of maxima and minima of radial force along with escape potential for both polystyrene and silver nanoparticles under CW excitation.

PS(nm)	$F_{max}(pN)$			$F_{min}(pN)$			$U_{esc}(k_BT)$	
	Silver	Polystyrene	Ratio	Silver	Polystyrene	Ratio	Silver	Polystyrene
10	0.0046	0.0003	13.9467	-0.0031	-0.0003	9.4936	1.5717	0.1757
20	0.0449	0.0027	16.8079	-0.017	-0.0024	7.2027	7.5871	1.3650
30	0.2342	0.0096	24.4734	0.0022	-0.0080	-0.2753	-	4.2406
40	0.9627	0.0252	38.1570	-	-0.0166	-	-	8.3876

Tab. 7.2.: Comparison of maxima and minima of axial forces along with escape potential for both polystyrene and silver nanoparticles under CW excitation.

due to increased gradient forces.

Figure 7.3b shows the variation of the real and imaginary part of RI with

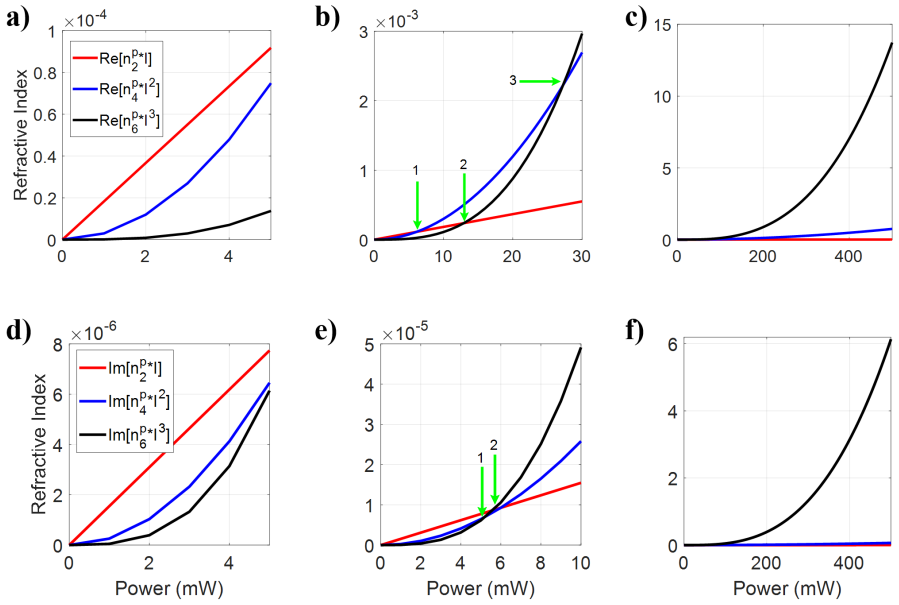

Fig. 7.4.: Plots of RI against average power at geometric force for a-c) real, and d-f) imaginary part of RI for individual higher (second, fourth, and sixth) order refractive index contribution.

average power. It can be seen that at low average power, the imaginary part of the RI dominates over the real part, however with an increase in power, this is

PS(nm)	$F_{max}(pN)$			$F_{min}(pN)$			$U_{esc}(k_BT)$		
	10 nm	20 nm	30 nm	10 nm	20 nm	30 nm	10 nm	20 nm	30 nm
CW	0.0098	0.0781	0.2635	-0.0098	-0.0781	-0.2630	1.0528	8.4220	28.4244
2nd	0.0098	0.0781	0.2635	-0.0098	-0.0781	-0.2635	1.0528	8.4220	28.4244
Up to 4th	0.0098	0.0781	0.2635	-0.0098	-0.0781	-0.2635	1.0528	8.4220	28.4244
Up to 6th	0.0098	0.0781	0.2635	-0.0098	-0.0781	-0.2635	1.0528	8.4220	28.4244

Tab. 7.3.: Comparison of maxima and minima of radial force along with U_{esc} for silver nanoparticles under both CW and pulsed excitation.

reversed.

Figure 7.4 represents the individual contribution of nonlinear RI terms where figures 7.4a-c show the real part and figures 7.4d-f show imaginary part contribution to the total RI. At low average power, the contribution from the linear RI exceeds that of the second, fourth, and sixth orders. At higher powers, the contribution from higher-order terms exceeds that of the lower order terms in both real and imaginary parts, as indicated by the green arrows showing the cross-over points. Hereafter, all the simulations are done for silver nanoparticles exclusively.

7.4 Conventional nanoparticles

7.4.1 Along radial direction: CW and pulsed excitation

Figures 7.5 and 7.6 illustrate the trapping force/potential curves along the radial direction for different particle sizes. There is no change in the magnitude and the nature of the force/potential curves while including and excluding OKE (even higher-order), which is quantitatively emphasized by table 7.3. It is because only gradient force contributes to the total force through the real part of the polarizability, which does not increase significantly with the inclusion of nonlinear terms at low average power. However, with the increase in particle size, there is an increase in the magnitudes of maxima and minima of the force curves and the corresponding U_{esc} also increases.

7.4.2 Along axial direction: CW and pulsed excitation

Figure 7.7 illustrates the total trapping force/potential curves along axial direction for different particle sizes. It can be seen that for fixed particle size, there is no significant difference in the magnitude and nature of force/potential curve under pulsed excitation compared with CW excitation when only second-order

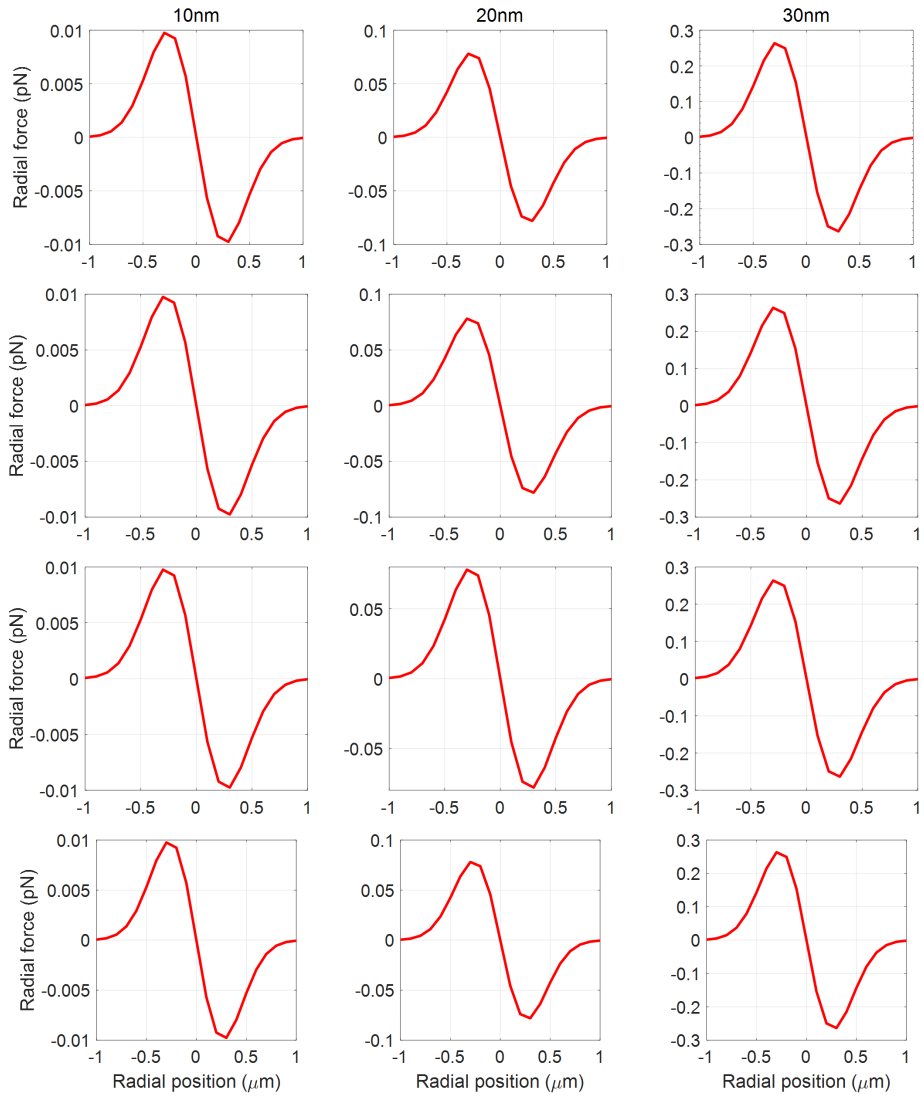

Fig. 7.5.: Plots of trapping force along radial direction for silver nanoparticles. First row corresponds to CW excitation, subsequent rows correspond to higher order nonlinearity included under pulsed excitation (second row: second order, third row: up to fourth order, and forth row: up to sixth order nonlinearity).

nonlinearity is included. However, the change is significant when higher-order nonlinear terms contribute. This trend in the nature of force curves remains the same with increasing particle size, but there is a significant change in the magnitude. In previous theoretical work on dielectric particles, we defined the absolute depth of axial trapping potential as *absolute potential* (U_{abs}) and height of the axial trapping potential barrier (along beam propagation direction) as *escape potential* (U_{esc}) and identified as the relevant parameter to be quantified while considering the stability of the trap under pulsed excitation.

The quantitative change can be seen from the potential curves in figure 7.7d

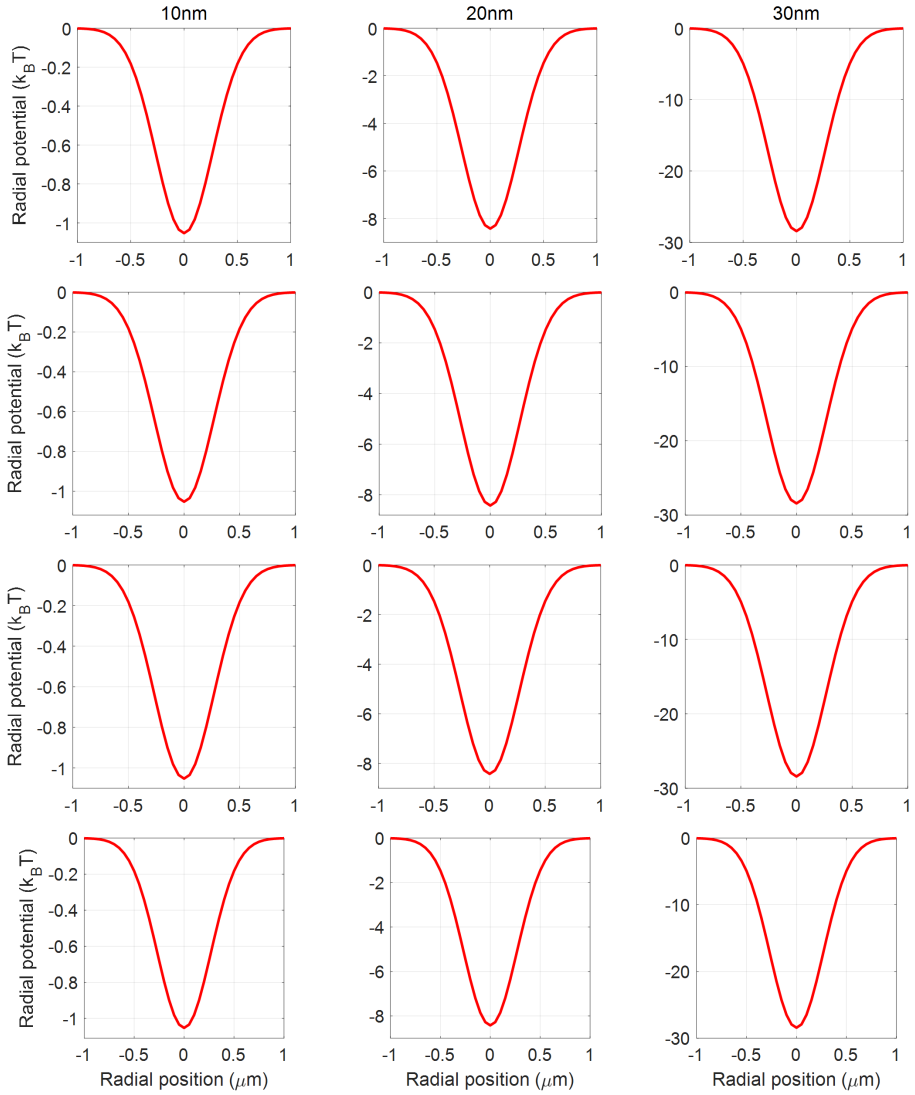

Fig. 7.6.: Plots of trapping potential along radial direction for silver nanoparticles. First row corresponds to CW excitation, subsequent rows correspond to higher order nonlinearity included under pulsed excitation (second row: second order, third row: up to fourth order, and forth row: up to sixth order nonlinearity).

where U_{abs} is shown as a longer double-sided arrow and U_{esc} is shown as a smaller double-sided arrow. The increase in the particle size initially increases escape potential, but eventually potential becomes unbound, and no stable trapping can be achieved for a fixed average power for 30 nm particle size. There is a slight deviation in the nature of curve while including second-order nonlinear RI, whereas there is a significant change while including fourth and sixth order nonlinearity. The contribution of each force component to the total force is shown in figures 7.8 and 7.9.

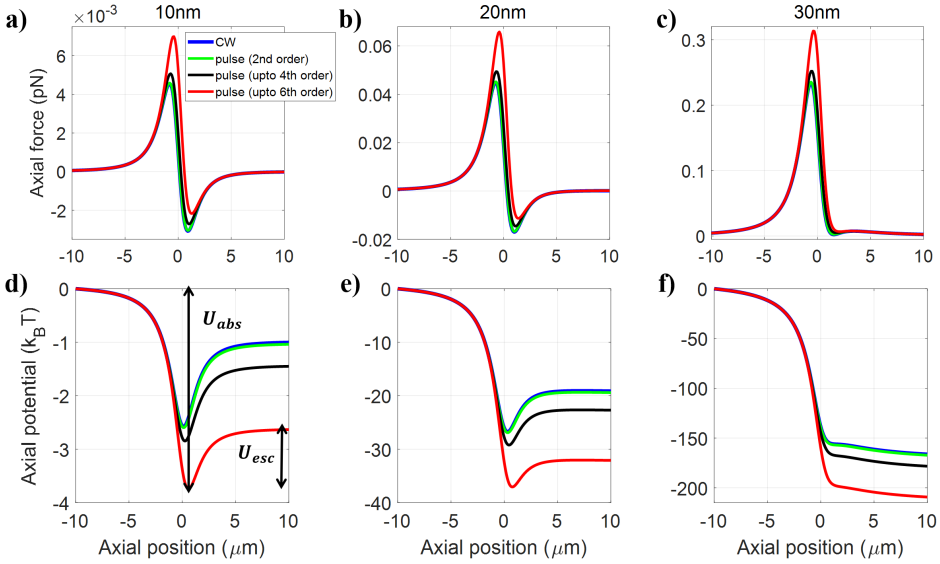

Fig. 7.7.: Plots of trapping force (a-c) and potential (d-f) along axial direction for different particles sizes under both CW and pulsed excitation.

Figures 7.8 and 7.9 show the trapping force/potential curves along axial direction for different particle sizes, where red/green/blue/black curves correspond to total/gradient/scattering/absorption force, respectively. Under CW excitation, in the case of the small-sized particle, the absorption force is dominating over scattering force. With an increase in particle size, both forces increase significantly, but scattering force increases more rapidly as compared with the absorption force. Eventually, scattering force dominates over both gradient and absorption forces, thereby destabilizing the trap. Under pulsed excitation, the inclusion of only second-order nonlinearity shows no change in both the magnitude and nature of force/potential curves for a small-sized particle. With the increase in the particle size, there is a small change in magnitudes, which can be seen from table 7.3. However, including nonlinearity up to fourth-order significantly contribute, which results in changing the magnitude as well as the nature of force curves in which the absorption force shows significant enhancement. Because the absorption force is directly proportional to the imaginary part of the polarizability and nonlinearity contributes significantly to the imaginary part more at low average power compared with high average power, which is shown in figure 7.13.

Further inclusion of the sixth order nonlinearity increases the absorption force. It dominates over gradient force, which results in destabilizing the trap for small-sized particles at low average power, and the degree of destabilizing effect increases with an increase in the particle size. Eventually, there is no stable trap for a higher sized particle for a fixed average power. Table 7.3 confirms this

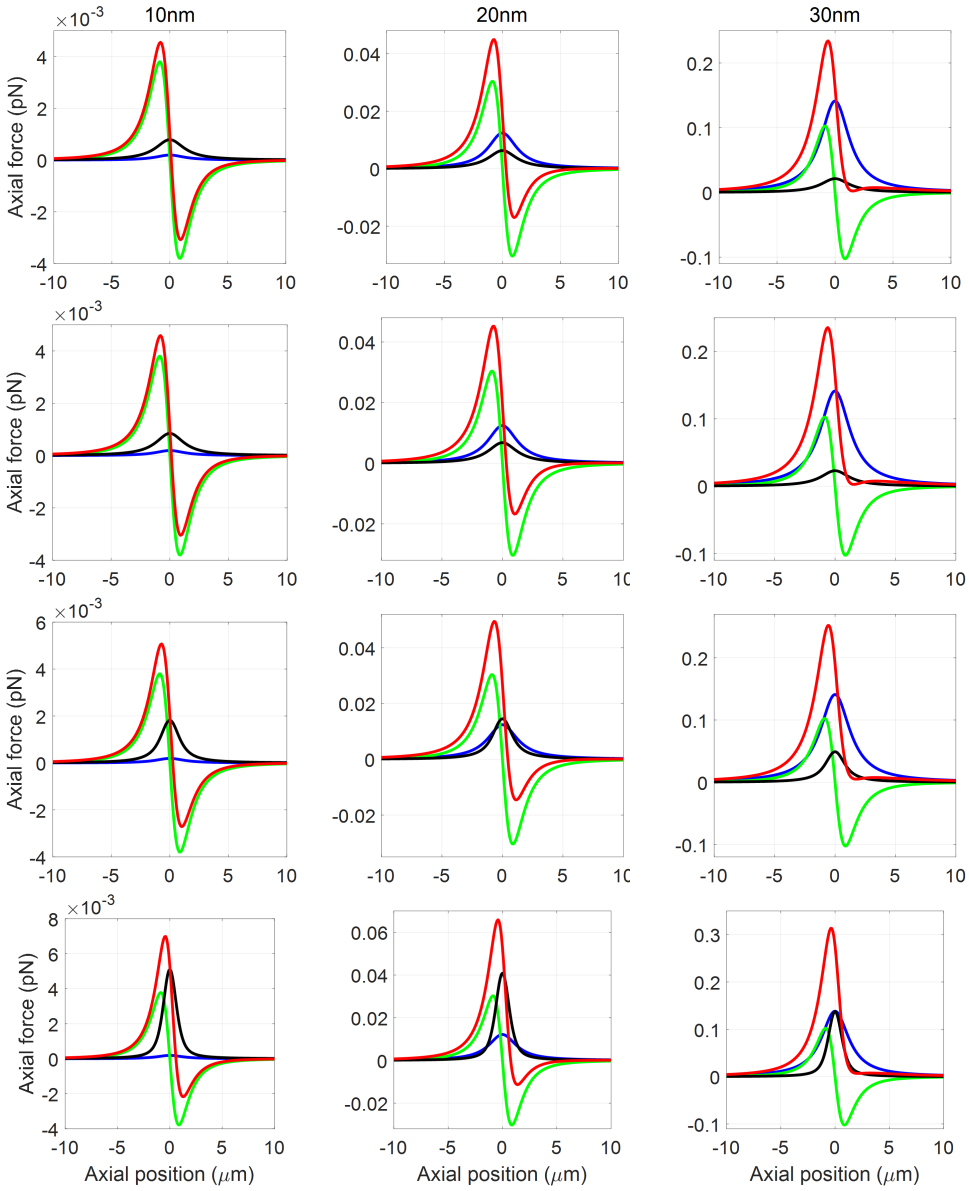

Fig. 7.8.: Plots of trapping force along axial direction for silver nanoparticles. First row corresponds to CW excitation, subsequent rows corresponds to higher order nonlinearity included under pulsed excitation (second row: second order, third row: up to fourth order, and forth row: up to sixth order nonlinearity).

behavior through the escape potential values that decrease with the inclusion of higher-order terms which signify the destabilization of the trap for fixed particle size. The increase in the particle size initially increases the escape potential, but eventually, potential becomes unbound, and no stable trapping can be achieved for a fixed average power. It can be observed that the absolute potential increases monotonically with increasing particle size, however, escape potential passes through maxima which correspond to an optimal particle size that can be stably

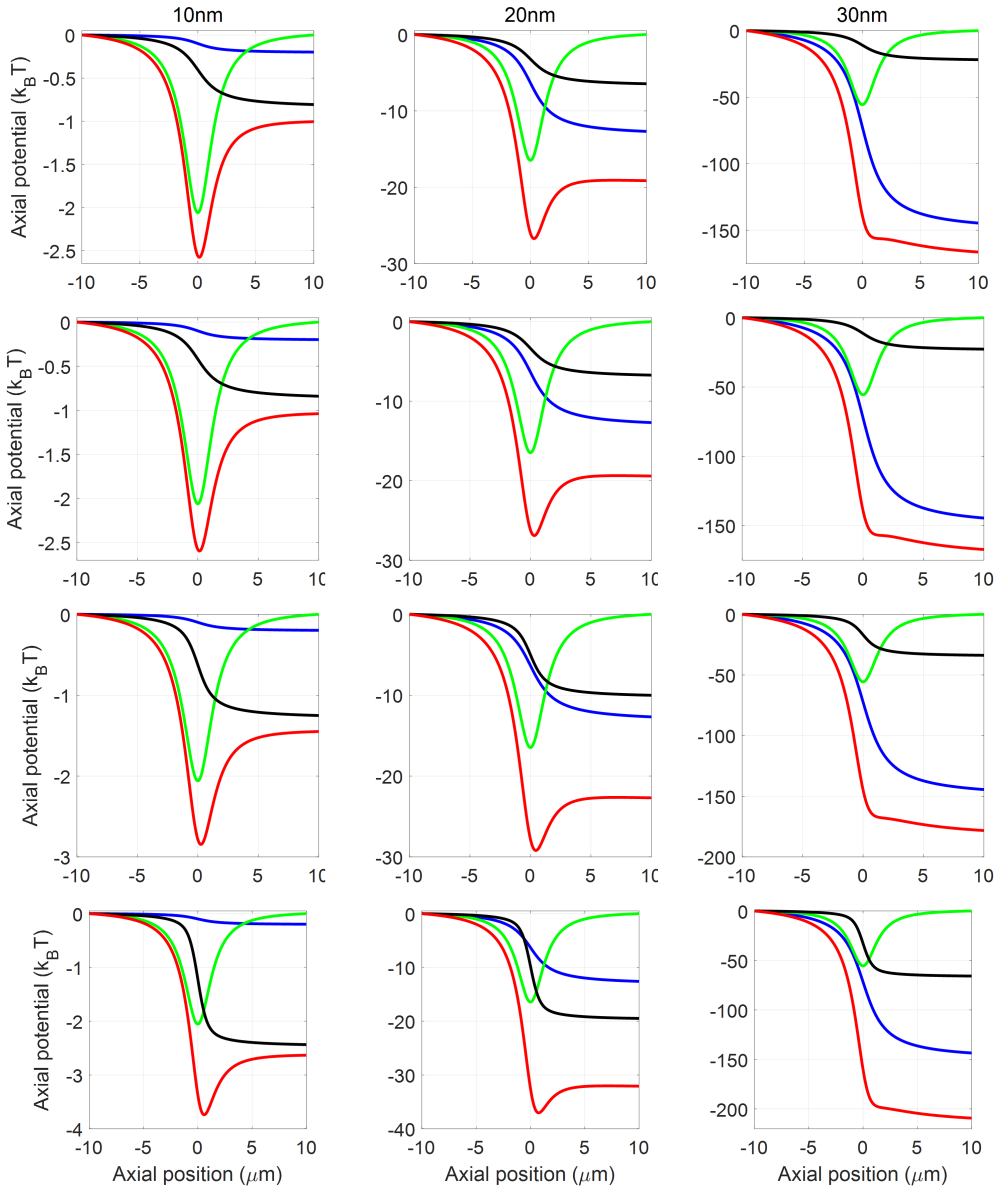

Fig. 7.9.: Plots of trapping potential along radial direction for silver nanoparticles. First row corresponds to CW excitation, subsequent rows corresponds to higher order nonlinearity included under pulsed excitation (second row: second order, third row: up to fourth order, and forth row: up to sixth order nonlinearity).

trapped for a fixed average power. There is a slight deviation in the nature of curve while including second-order nonlinear refractive index, whereas there is a significant change while including fourth and sixth order nonlinearity. For CW excitation and including second-order nonlinearity, can trap particle having radius till 27 nm while fourth and sixth order can trap up to 26 nm and 25 nm at 100 mW average power, respectively as shown in figure 7.10.

Figures 7.11 and 7.12 show the trapping force/potential curves for different

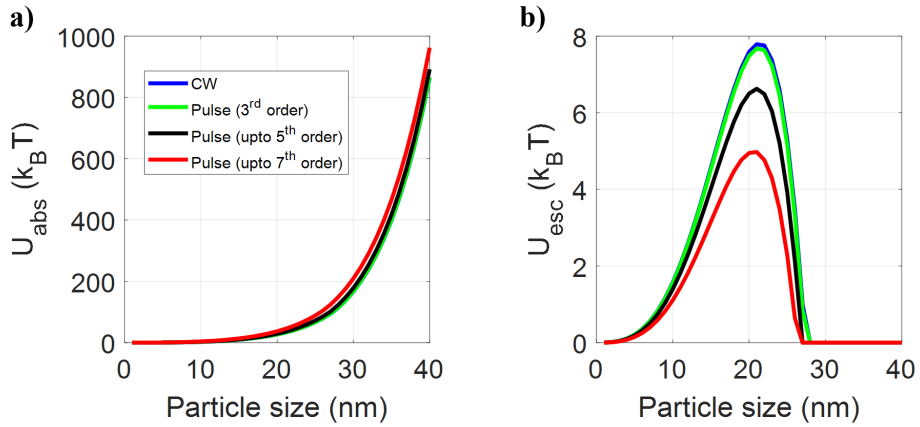

Fig. 7.10.: Plots of a) U_{abs} and b) U_{esc} against particle size under pulsed excitation.

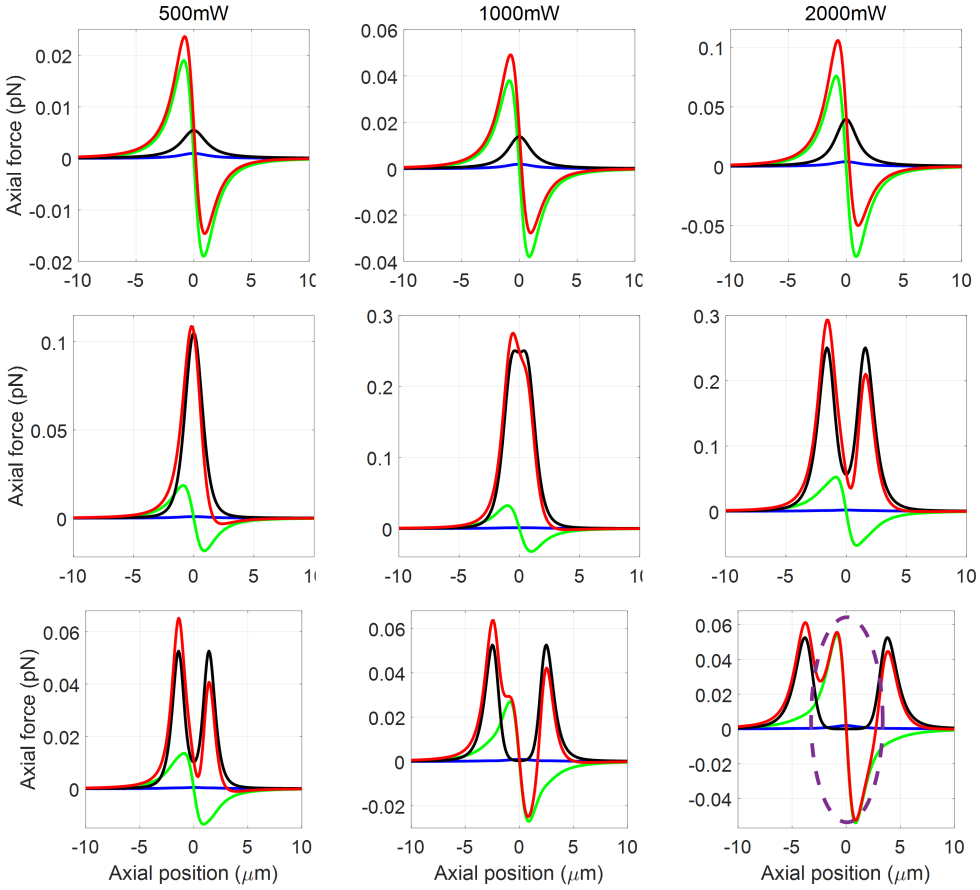

Fig. 7.11.: Plots of trapping force along axial direction for 10 nm silver nanoparticles at different average power under pulsed excitation including higher order nonlinearity (first row: second order, second row: up to fourth order, and third row: up to sixth order).

average power under pulsed excitation including second, fourth, and sixth-order nonlinearity for 10 nm particle size. Including second-order nonlinearity changes the magnitude of force/potential, but the nature of force curves remains the same

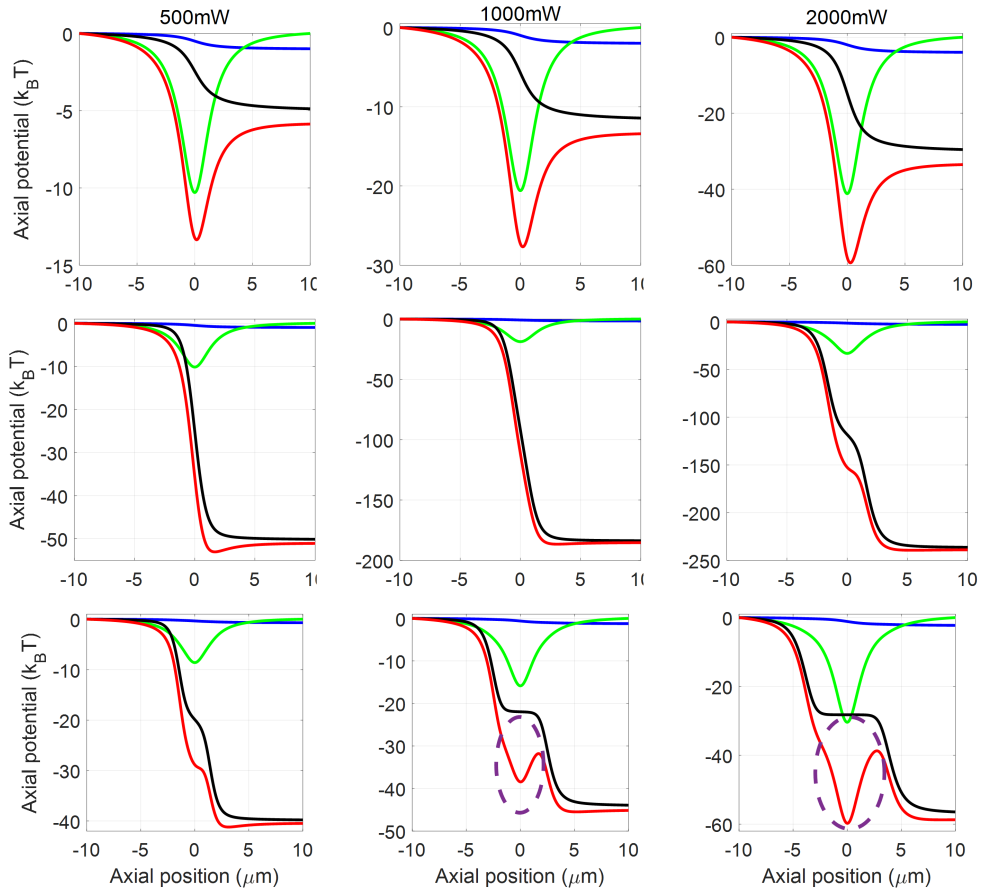

Fig. 7.12.: Plots of trapping potential along axial direction for 10 nm silver nanoparticle at different average power under pulsed excitation including higher order nonlinearity (first row: second order, second row: up to fourth order, and third row: up to sixth order).

with an increase in average power. Interestingly, the inclusion of fourth-order nonlinearity along with second-order gives a significant enhancement in absorption force at similar average power, which results in destabilizing the trap. Further increase in power splits the absorption force. Consequently, the total force curve also splits. Including up to sixth order nonlinearity, split the absorption force curve at low average power compared with that up to fourth-order and a further increase in average power recreates a steeper potential well, which can stably trap the nanoparticles. In other words, increasing power first stabilizes the trap, reaches to a maxima and then destabilizes the trap but further increase in average power again stabilizes the trap which is highlighted by purple color circle. From this behavior, we can predict that the subsequent increase in power would follow the same trend of stabilizing and destabilizing the trap. Consequently, there are two average powers for having a stable trap. Thus, the overall behavior of the nature of the total force curve is dictated by the absorption force after inclusion

of higher-order (up to sixth order) nonlinearity.

At high average power, the absorption force curve is seen to split, which in turn splits the total force curve. This splitting may be explained through the behavior of the imaginary part of polarizability, which is a function of the strength of the applied electric field and refractive indices of the nanoparticles and medium. A part by part analysis of the polarizability function is done to get an insight into what causes the splitting. Figure 7.13 shows the variation of the imaginary

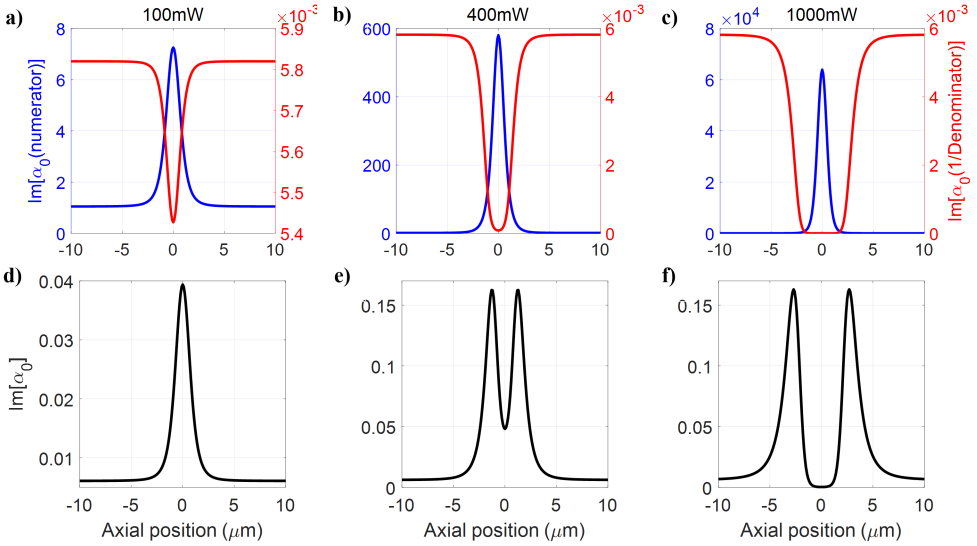

Fig. 7.13.: Plots of imaginary part of numerator and one over denominator of α_0 (a-c) and total imaginary part (d-f) of α_0 at 100 mW (a, d), 400 mW (b, e) and 1000 mW (c, f) average power.

part of polarizability as a function of the particle's axial position at different average power, where blue and red curves correspond to the numerator, and one over a denominator of the imaginary part of α_0, and black corresponds to the total imaginary part of α_0. Figures 7.13a-c show separate plots of the numerator and one over a denominator of the imaginary part of polarizability, as shown in equation 7.5. At low average power, both the curves have similar broadening, but with an increase in power, the one over denominator broadens more and, at the same time, increases in magnitude. The product of these two terms results in the splitting of polarizability function as shown in figure 7.13d-e. Thus, at high average power, the overall behavior of the nature of the total force curve is dictated by the absorption force under pulsed excitation. A more rigorous analysis is performed by varying power in a stepwise manner as shown in figure 7.14 where, red/green/blue/black curves correspond to total/gradient/scattering/absorption force/potential, respectively. From figure 7.14b, it can be observed that at low

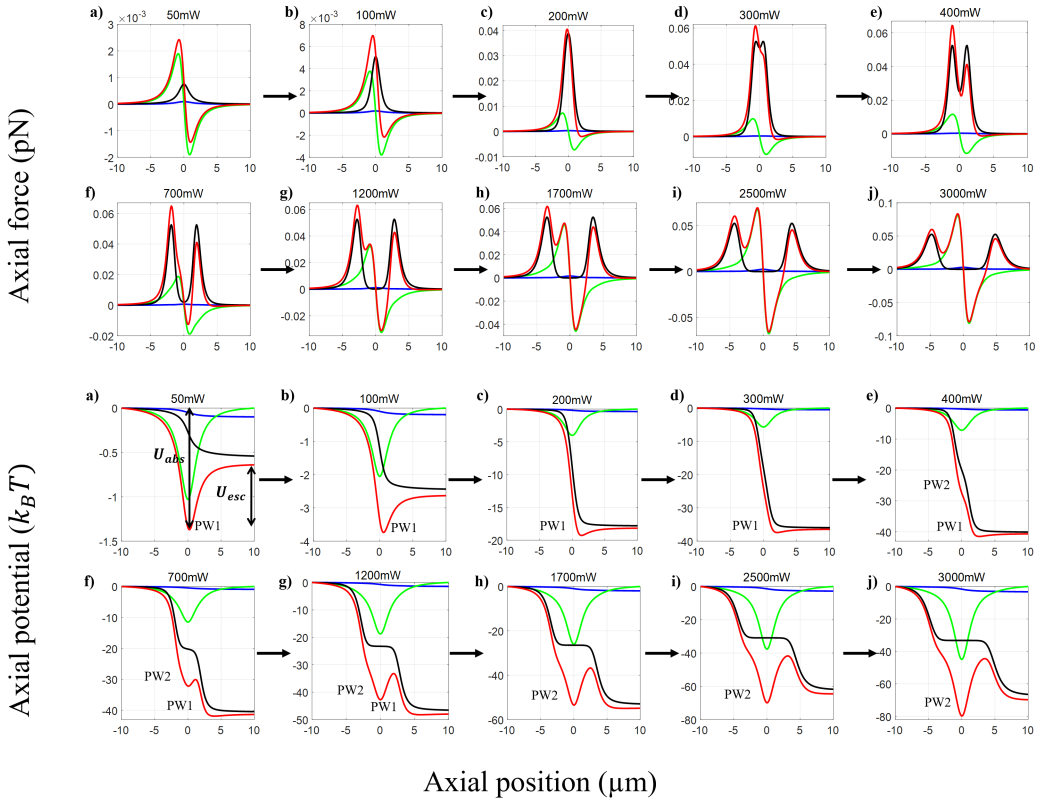

Fig. 7.14.: Plots of trapping force and potential along axial direction for 10 nm silver nanoparticle at different average power under pulsed excitation (including up to 6^{th} order nonlinearity).

average power, only one potential well (PW1) exists which stabilizes with increase in average power, but $\sim$ 400 mW average power another well (PW2) gets created. Further increase in average power stabilizes the PW2, whereas destabilizes the PW1, and at high average power, PW1 disappears while PW2 remains.

Clear evidence of this behavior shown in figure 7.15, which shows the plot of escape potential against average power for different NA, where blue/green/black curve corresponds to NA 1.2/1.3/1.4, respectively. It can be seen that initially, it increases with an increase in average power, then reaches a maximum. Further increase in power decreases the escape potential. In addition to this, it can also be observed that when escape potential decreases, at the same time, another well gets created, and the escape potential for this second well increase with average power. Quite interestingly, there is a region where the first escape potential destabilizes, and the second escape potential tries to stabilize at the same time, which is highlighted by the red rectangle. The optimal power corresponding to PW1 for different NA equal to 1.2, 1.3, and 1.4 are $\sim$ 160 mW, $\sim$ 150 mW, and $\sim$ 140 mW, respectively. With decreasing NA, the optimal power increases for

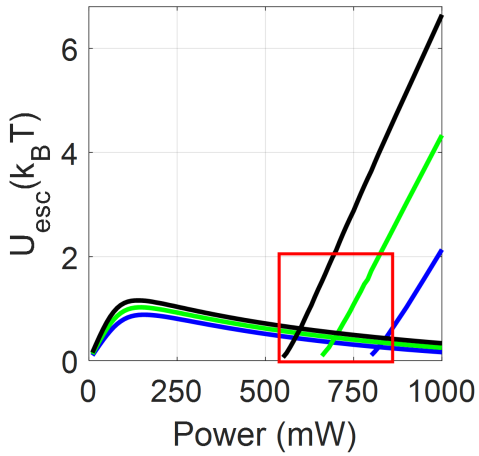

Fig. 7.15.: Plots of U_{esc} against average power for different NA for 10 nm silver nanoparticle under pulsed excitation (including nonlinearity up to 6th order). The red box indicates a region where PW1 destabilizes but PW2 stabilizes.

PW1, and PW2 shifts to lower average power. No such effect is seen under CW excitation at similar average power.

The metallic nanoparticles are susceptible to heating effects, and the temperature rise of metallic particles is highly dependent on the particle size and wavelength of the trapping beam [157, 158]. Such thermal effects are more prominent near the resonance at ∼449 nm for silver (figure 7.10a) corresponding to absorption maximum; so, we deliberately chose the wavelength 800 nm which is away from the resonance to minimize the heating effects [123]. The significant temperature rise of silver nanoparticles can destabilize the trap due to the increase in thermal Brownian motion or even change the surface properties of the trapped particles. However, the probability of changing surface properties is more prominent. If the particle is stuck on the glass surface or if we use non-spherical particles, both of which we avoided here. Also, an advantage of using (femtosecond) pulsed excitation is that the short duration of the pulse ensures that heat accumulation is less due to a continuous dissipation of heat to the surrounding medium during the dead-time between successive pulses, thereby, reducing thermal-induced melting and fragmentation [159].

The nonlinear trap splitting of the potential well was experimentally demonstrated for gold nanoparticles, and it was observed that the splitting of the optical trap occurs around 80 mW average power [157]. However, silver nanoparticles are less thermal efficient than gold nanoparticles because absorption cross-section is higher for gold than for silver nanoparticles [158] for which trap splitting is achieved around 400 mW average power which is significantly higher than the

power required for gold nanoparticles. Thus, it is apparent that trap splitting is directly related to the absorption cross-section. Consequently, dielectric nanoparticles are not likely to exhibit similar trap splitting.
Later, we have extended our work for hybrid and hollow-core nanoparticles, and it is observed that the optical trap is always stable along the radial direction as gradient force is the only contributing force. While along the axial direction, the potential well is anharmonic due to contributions from scattering and absorption forces. Hence, we have restricted all the discussion in this paper to axial forces which determine the stability of the optical trap.

7.5 Comparison of hybrid and conventional nanoparticles

7.5.1 CW excitation

To quantify the advantage of using hybrid core-shell particles over the conventional *i.e.* purely metallic or dielectric nanoparticles, we did a comparison of the force/potential experienced by both the types of particles. The comparison of force/potential of conventional dielectric (polystyrene) with metallic-dielectric (silver-polystyrene) nanoparticles and conventional silver with dielectric-metallic (polystyrene-silver) nanoparticle shown in figures 7.16a-d and figures 7.16e-h, respectively. Figure 7.16a shows the force/potential of pure polystyrene nanoparticles having a radius of 10 nm compared with a silver core having a radius of 5 nm embedded within a polystyrene shell having a thickness of 5 nm (size composition corresponding to core-shell particles denoted as core-shell (5 nm-10 nm) radius throughout the paper). The silver-polystyrene hybrid particle experiences considerably enhanced forces than the conventional polystyrene particles, and corresponding U_{abs} and U_{esc} potentials are also higher for the hybrid particles (shown in figure 7.16c). Thus, by integrating a silver core within a polystyrene particle, the forces acting on it can be significantly enhanced due to the high polarizability of the metallic component of the hybrid particle. Therefore, by accurately controlling the core and shell radius, we can control the force acting on the trapped particle according to our requirement. Figure 7.16b shows force/potential for 20 nm polystyrene compared with varying thickness of silver-polystyrene particle: 10 nm-20 nm and 15 nm- 20 nm. The force acting on the particle increases with an increasing radius of the silver core, which can be seen from figure 7.16a-b. This can also avoid the problem of heat damage caused while using high laser powers

for high force experiments. The choice of outer surface also matters, especially for bio-conjugated samples where we require materials that are bio-compatible while not compromising with the trapping efficiency. Silver nanoparticles have high biological applications due to its anti-microbial and anti-cancer properties. Comparison for 10 nm– 20 nm and 15 nm- 20 nm polystyrene-silver core-shell particles with 10 nm and 20 nm conventional nanoparticles respectively shows that there is only a slight enhancement in the force/potential as the force on conventional silver nanoparticles sphere is already high enough.

On the other hand, 15 nm- 20 nm particles feel highly enhanced forces than 20 nm silver nanoparticle, although, the potential becomes unbound due to enhanced scattering and absorption forces. Thus, we must be careful while choosing the outer material, the thickness of the outer shell, and the inner core according to the specific requirements of our experiment.

Similarly, along the radial direction, the force/potential experienced is both enhanced as well as diminished depending upon the choice of size/composition of the hybrid particle. As already mentioned, the axial stability of the trap is what ultimately dictates the efficiency of the trap, and the use of hybrid particles increases the axial forces, which improve the trapping efficiency. While along the radial direction, the force may be increased/decreased depending upon the choice of size/composition of hybrid particles. The trap is always stable along the radial direction; the reduction in magnitude force is a minor drawback and, the change in the magnitude of force may be used for fine-tuning the overall force experienced.

7.5.2 Pulsed excitation

Under pulsed excitation, the comparison of force/potential of conventional dielectric (polystyrene) with metallic-dielectric (silver-polystyrene) and conventional silver with dielectric-metallic (polystyrene-silver) nanoparticles are shown in figures 7.17a-d and figures 7.17e-h, respectively. Figures 7.17a-b correspond to the axial force/potential under pulsed excitation and for different size ratios of silver-polystyrene nanoparticles. The forces are enhanced similar to CW excitation; however, under pulsed excitation, the enhancement is more pronounced and can be seen from the figures 7.17c-d. But we have to be very careful since both materials have high nonlinearity, the contribution of both can give a better or worse result depending upon their relative composition and size. Figures 7.17e-h indicates that polystyrene-silver with 5 nm-10 nm and 10 nm-20 nm size composition shows a significant enhancement in force; however, 15 nm-20

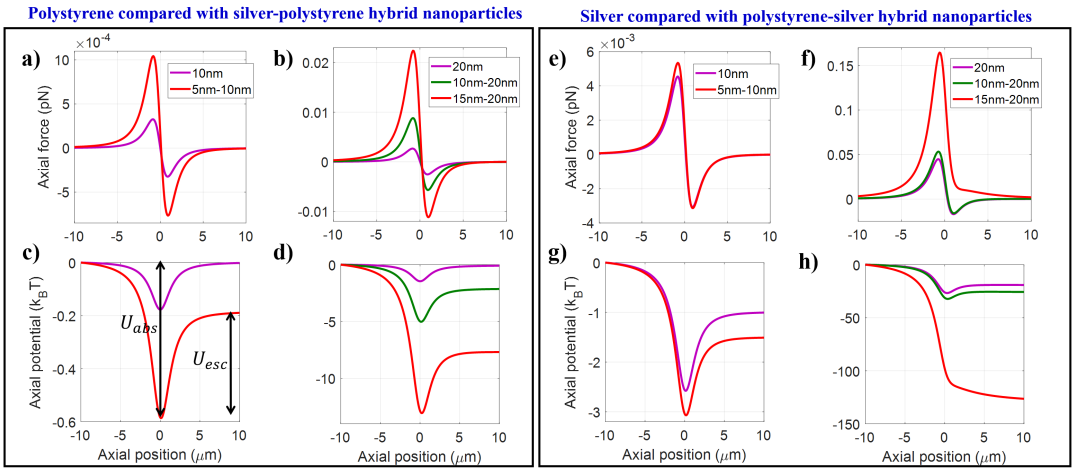

Fig. 7.16.: Plots of trapping force/potential along axial direction for conventional (polystyrene and silver) and hybrid (silver-polystyrene and polystyrene-silver) nanoparticles at 100 mW average power under CW excitation for fixed NA=1.4.

nm shows splitting nature due to the splitting of absorption force. This is because, after a certain size of core particles, plasmonic effects from silver particles dominates. So, the material composition has to be chosen in such a manner that absorption should be minimized. Thus, under pulsed excitation, the choice of shell thickness is crucial and must be decided with caution. Under pulsed excitation, the comparison of radial force/potential, the trend is similar to the case of CW excitation; the only difference is in the magnitude of force/potential which is more in the case of pulsed excitation.

In previous theoretical work on dielectric and metallic particles, we have identified that escape potential is a more relevant parameter to quantify the stability of the trap under pulsed excitation. Figure 7.18 shows the plot of escape potential against particle size at 100 mW average power under CW excitation for fixed NA equal to 1.4. Silver particles having a radius of more than 27 nm cannot be trapped due to the dominance of scattering and absorption forces. However, polystyrene particles can be trapped up to 40 nm and beyond this limit, which we cannot make any comment on trapping of particle since dipole approximation is not valid anymore.

7.6 Hybrid nanoparticles

To generalize these phenomena for hybrid nanoparticles as well, we have rigorously studied the variation in core and shell particle size with different NA.

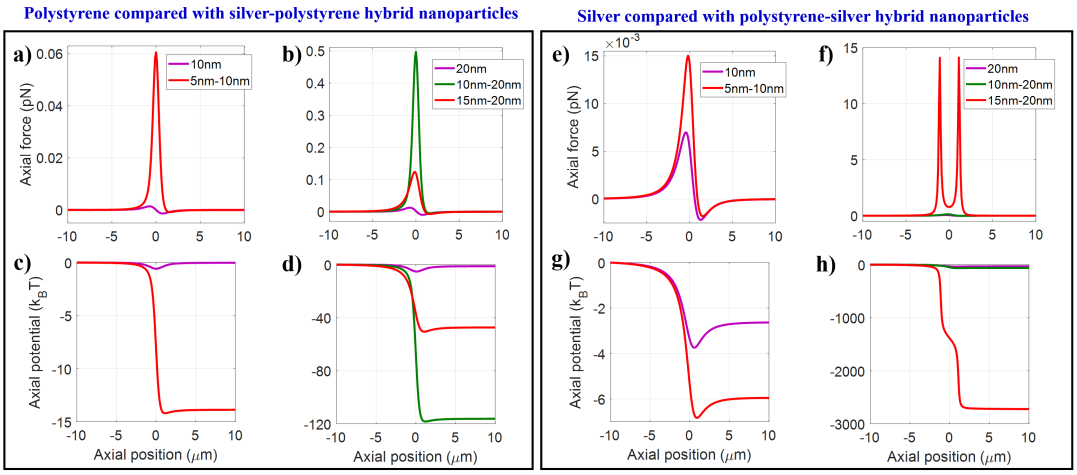

Fig. 7.17.: Plots of trapping force/potential along axial direction for conventional (polystyrene and silver) and hybrid (silver-polystyrene and polystyrene-silver) nanoparticles at 100 mW average power under pulsed excitation for fixed NA=1.4.

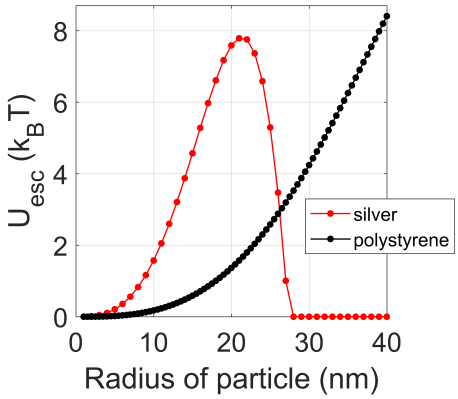

Fig. 7.18.: Plots of escape potential against particle size at 100 mW average power under pulsed excitation for fixed NA 1.4.

7.6.1 CW excitation

Figures 7.19 and 7.20 show the variation of escape potential for silver-polystyrene nanoparticles at 100 mW average power under CW excitation for different NA by fixing shell radius but varying core radius and vice-versa. We observe that if we are fixing shell/core (metallic/polystyrene) radius and varying the core/shell (dielectric/metallic) radius, the radius of the core of particle that can be trapped is less than 27 nm. This is because above a threshold, the absorption and scattering forces dominate over the gradient force, which results in destabilizing the trap. Adding a dielectric coating over the core does not appear to give any advantage in terms of improvement in the range of particle size that can be trapped. But it has an advantage in terms of trap stability which can be seen by comparing figure

7.18 with figures 7.19 & 7.20. For example, escape potential for conventional 20 nm polystyrene nanoparticles is $< 2k_BT$, but we can get escape potential $> 2k_BT$ for hybrid nanoparticles under similar conditions according to figure 7.19a, which is a clear advantage of using hybrid nanoparticles over conventional nanoparticles for stable trapping. Hence, depending on the requirement, choosing an accurate combination of core and shell size can help us to give stable trapping.

Further, we have shown similar analysis for polystyrene-silver nanoparticles

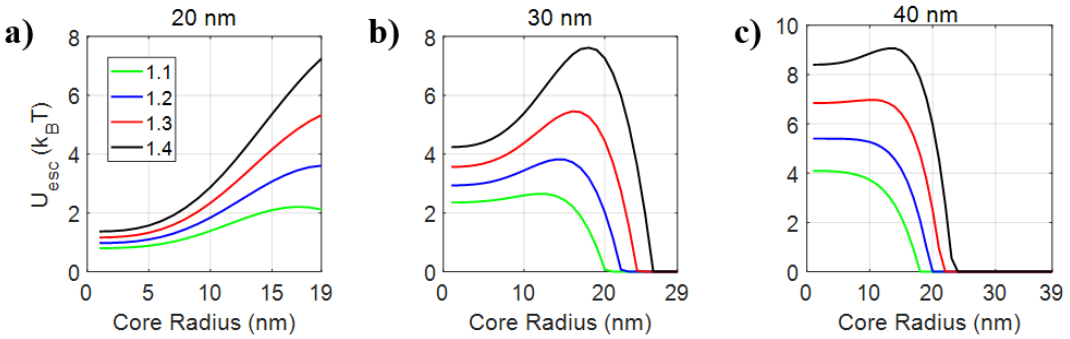

Fig. 7.19.: Plots of escape potential against core radius by fixing shell radius a) 20 nm, b) 30 nm, and c) 40 nm for silver-polystyrene nanoparticles under CW excitation at 100 mW average power.

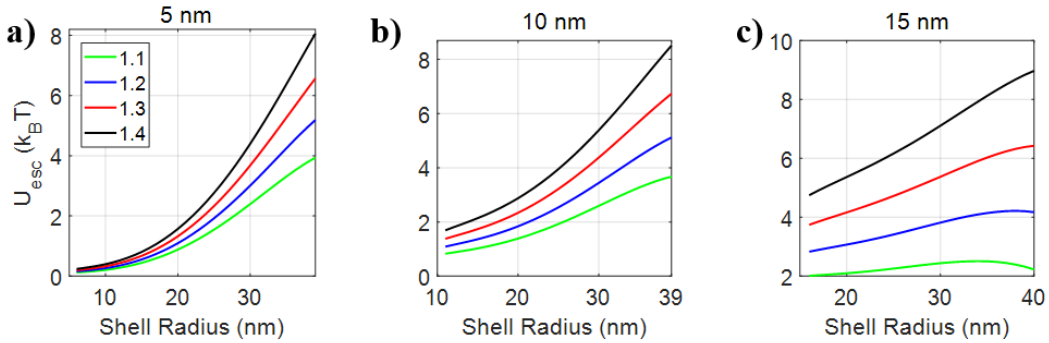

Fig. 7.20.: Plots of escape potential against shell radius by fixing core radius a) 5 nm, b) 10 nm, and c) 15 nm for silver-polystyrene nanoparticles under CW excitation at 100 mW average power.

by varying core radius for a fixed shell radius at 100 mW average power under CW excitation for different NA. From figure 7.21, it can be observed that for getting a stable trap, if we fix the shell radius to be 20 nm then the polystyrene core can be varied till 14 nm, 13 nm, 12 nm, 11 nm for NA=1.1, 1.2, 1.3, 1.4, respectively. For 20 nm shell, the value of U_{esc} decreases with an increase in the radius of the polystyrene core. This is because, with the increase in the core

size, the effect of absorption and scattering forces becomes prominent, where the absorption force gets enhanced faster than the scattering force, and the resulting destabilization can be seen from figures 7.21d-e. Quite interestingly, we have observed that for 19 nm-20 nm (polystyrene-silver) particle size, gradient force shows repulsive nature. Hence, the overall force acting on the particle is also repulsive in nature. With decreasing shell thickness, the polarizability due to the shell layer also decreases, and after a certain limit, i.e., $n_s^2 - n_w^2 < 0$, the sign of real part of polarizability changes. Hence gradient force shows a repulsive nature, as shown in figure 7.21f. Further, figures 7.21b-c show the variation of escape potential with varying core radius when we fixed the shell radius to be 30 nm and 40 nm. No stable trapping is observed, which is similar to the case of conventional particles because of increased scattering and absorption forces for bigger sized particle. For example, when the core radius is 5 nm, and shell radius is either 30 nm or 40 nm, we can observe three distinct causes for the destabilization of the trap as we increase the size of core: initially, the scattering force dominates over both gradient and absorption force. With the further increase, absorption exceeds scattering force and at 28 nm-30 nm particle size, in addition to this, the gradient force shows reversal nature of force due to negative polarizability as discussed above and shown in figures 7.21g-i.

Later, we fixed the polystyrene core-radius and varied the metallic shell radius and observed that for core radius of 5 nm, we could trap the particle with shell radius till 22 nm, 23 nm, 25 nm, 27 nm, corresponding to NA=1.1, 1.2, 1.3, 1.4 as shown in figure 7.22. In this case, initially, for a small-sized hybrid particle, gradient force dominated over both scattering and absorption force (figure 7.22d), resulting in stable trapping but further increase in particle size or shell radius results in destabilizing of the trap (figures 7.22e-f). When the core radius is fixed to be 10 nm, and shell thickness is less than 4 nm, the absorption force dominates over scattering and gradient forces, and gradient force shows reverse behavior because polarizability of the shell layer is less than the surrounding medium. Consequently, the total force acting on the particle results in destabilizing the trap (figure 7.22g). A further increase in shell thickness results in a more stabilized trap due to a fine balance between all the three forces (figure 7.22h). However, if the shell thickness is more than 20 nm, the trap gets destabilized due to the dominance of scattering force over both gradient and absorption force (figure 7.22i). Thus, there is only a size range in which particles can be stably trapped. If the particle size is less than this region, then the absorption force is responsible

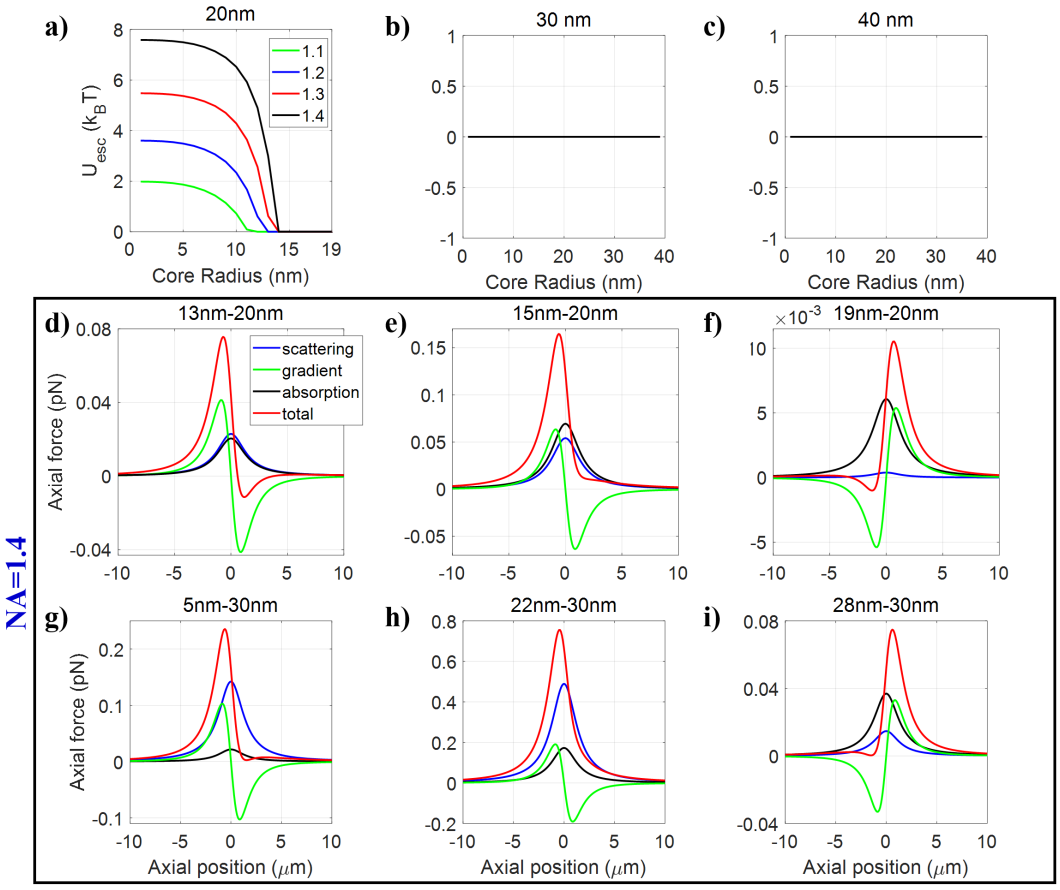

Fig. 7.21.: Plots of escape potential against core radius by fixing shell radius a) 20 nm, b) 30 nm, and c) 40 nm for polystyrene-silver nanoparticles under CW excitation at 100 mW average power. The plots of trapping force/potential along axial direction for d) 13 nm-20 nm, e) 15 nm-20 nm, f) 19 nm-20 nm, g) 5 nm-30 nm, h) 22 nm-30 nm, and i) 28 nm-30 nm polystyrene-silver nanoparticles under CW excitation at 100 mW average power for fixed NA 1.4.

for destabilizing. Beyond this size range, scattering force is responsible for destabilizing the trap. However, when we increase the core radius to 15 nm, no stable trapping is achieved for any particle size due to the combined effect of both scattering and absorption forces.

7.6.2 Pulsed excitation

Figure 7.23 shows the variation of escape potential by fixing shell radius and varying core radius for silver-polystyrene nanoparticles under pulsed excitation. Figures 7.23a-c show the variation of core radius at three different fixed shell radius 20 nm, 30 nm, and 40 nm at 100 mW average power. Under pulsed excitation, nonlinearity contributes significantly, leading to significant enhancement in scattering and absorption forces than the case of CW excitation. The

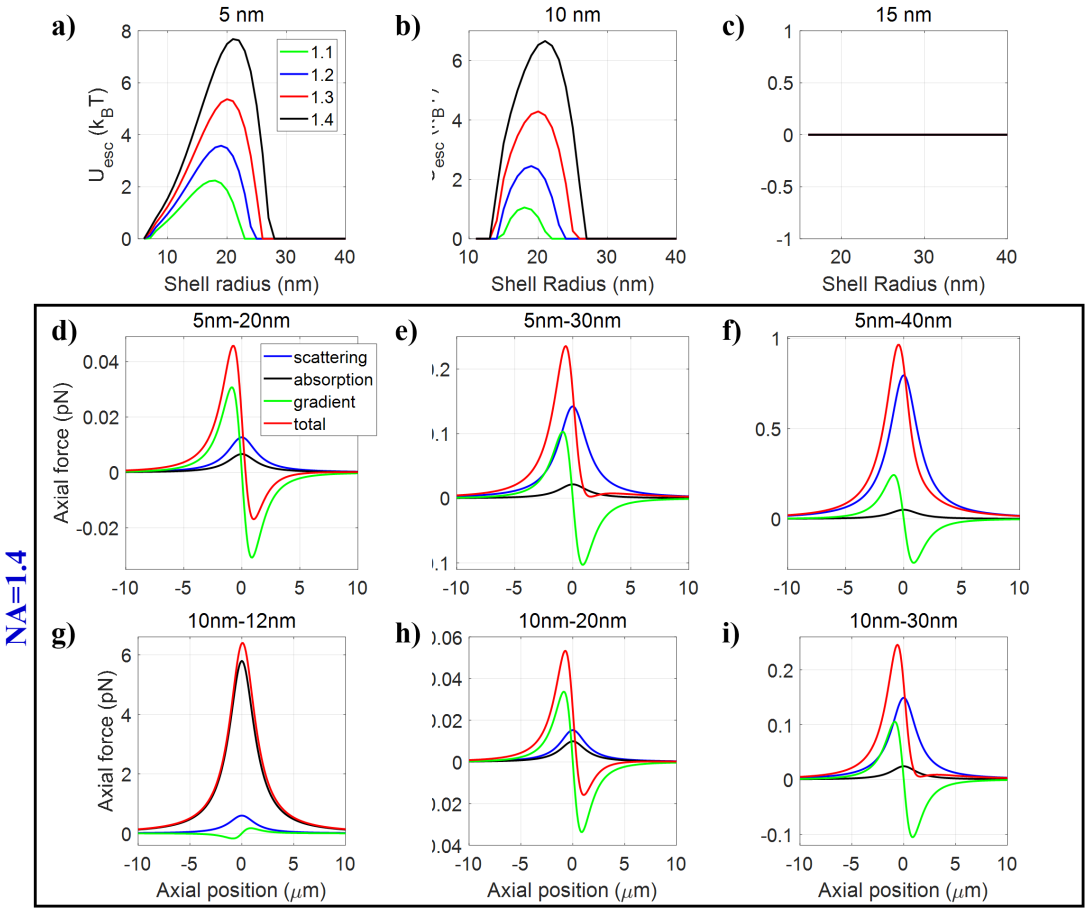

Fig. 7.22.: Plots of escape potential against shell radius by fixing core radius a) 5 nm, b) 10 nm, and c) 15 nm for polystyrene-silver nanoparticles under CW excitation at 100 mW average power. The plots of trapping force/potential along axial direction for d) 5 nm-20 nm, e) 5 nm-30 nm, f) 5 nm-40 nm, g) 10 nm-12 nm, h) 10 nm-20 nm, and i) 10 nm-30 nm polystyrene-silver nanoparticles under CW excitation at 100 mW average power for fixed NA 1.4.

destabilization is worse for bigger sized particles. For instance, 20 nm-40 nm (silver-polystyrene) particle can be trapped under CW excitation, but not under pulsed excitation for fixed NA=1.4. On the other hand, for small-sized particles, pulsed excitation can trap more stably than CW excitation. For example, 5 nm – 30 nm (silver -polystyrene) particle has $U_{esc} \sim 4k_BT$ under CW excitation, but under pulsed excitation, $U_{esc} \sim 7k_BT$ which is a clear evidence that pulsed excitation is advantageous over CW excitation for smaller sized particles but the disadvantage for bigger size particles under certain conditions. Later, we also studied the variation of average power by fixing the shell radius as 20 nm and varying the core radius because OKE is strongly dependent on the average power. For smaller core (silver) particles, we have observed that at high average powers (300 mW or 500 mW), there is an appearance of a second potential well in

addition to the one already present. Such behavior was not observed in the case of dielectric particles, and we have traced the origin of this phenomenon which is due to the splitting observed in the absorption force and the imaginary part of the polarizability. This splitting behavior may be attributed to the plasmonic and heating effects that are absent in the case of dielectric particles which results in an initial decrease in U_{esc} with increasing core radius followed by subsequent increase shown in figure 7.23d-f.

Figure 7.24 shows the variation of escape potential by fixing the core radius and

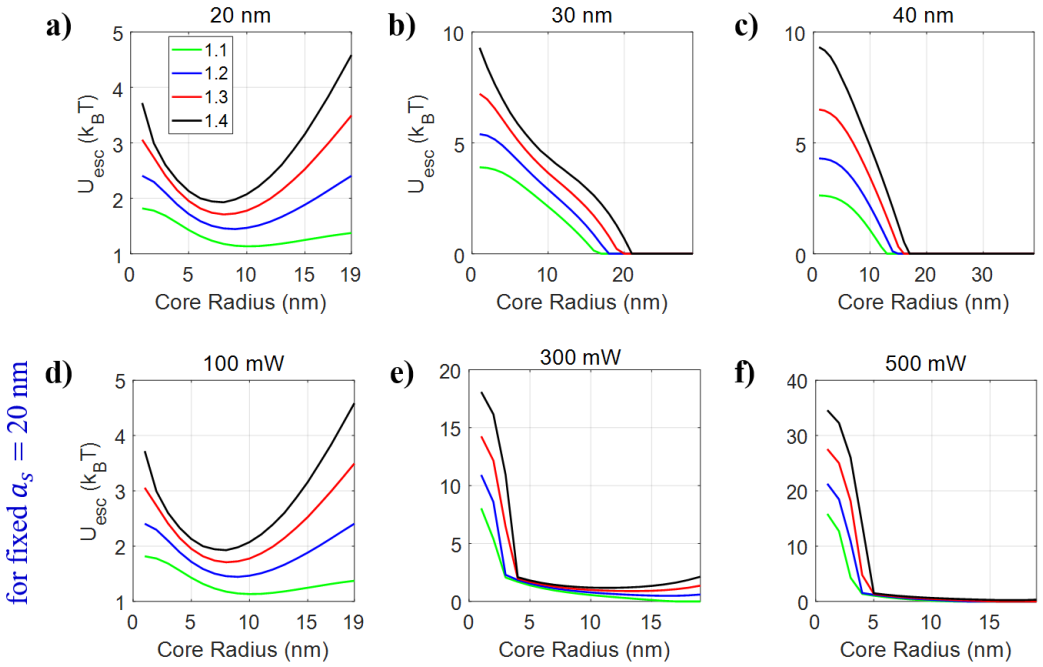

Fig. 7.23.: Plots of escape potential against core radius by fixing shell radius a) 20 nm, b) 30 nm, and c) 40 nm at 100 mW average power, and d) 100 mW, e) 300 mW, and f) 500 mW for fixed shell radius 20 nm for silver-polystyrene nanoparticles under pulsed excitation.

varying shell radius for silver-polystyrene nanoparticles under pulsed excitation. Figures 7.24a-c show the escape potential against variation of shell radius at three different fixed core radius 5 nm, 10 nm, and 15 nm at 100 mW average power. Under pulsed excitation, the escape potential first increases with increasing overall particle size along the axial direction, followed by a maximum and then decreases. Whereas, under CW excitation, the escape potential continuously increases with increasing overall particle size when the core radius is 5 nm. Comparing the plots in figure 7.24, we can see that the maxima in the curve become less defined on increasing the size of silver core from 5 nm to 15 nm. This is because of the nonlinear contribution is dependent on the size proportionality of

core-shell. With increasing contribution from metallic, the magnitude of escape potential diminishes rapidly. As seen in figure 7.20, in the linear case, there is a no well-defined maximum for silver-polystyrene nanoparticle, which means that within the domain of CW excitation, the corresponding size for optimal trapping is much higher, for a fixed average power. The inclusion of non-linearity brings a shift in the peak for the case of polystyrene, which indicates that even smaller particles can be trapped with better trapping efficiency. So, it can be concluded that for a fixed power, nonlinear contributions must be included to predict the optimal size for stable trapping correctly. This is particularly important for particles having high nonlinear refractive indices like polystyrene and silver. The appearance of maxima can be explained by considering the fact that for a small size, the contribution of scattering and absorption force is comparatively less. However, it does start contributing as particle size increases, first stabilizing the trap and then destabilizing as size increases further. A peak in the curve marks this change from stabilizing to destabilizing behavior. This discussion only holds when the core radius is smaller in size, so that polystyrene effects dominate over silver because the outer layer is polystyrene. However, with increasing core radius, the effect of silver also contributes significantly. After a threshold particle size limit, it dominates over polystyrene, and the trap becomes unbound. Another feature observed is that including non-linearity leads to a strong dependency on the average power for achieving stable trapping. Under pulsed excitation, there is a shift of maxima towards smaller particle size, indicating that by increasing the power, it is possible to trap even smaller particles. However, under CW excitation, unlike pulsed excitation, there is no shift in peaks (w. r. t to particle size) with a change in power because power is linearly dependent.

Figure 7.25 shows the variation of escape potential by fixing shell radius and

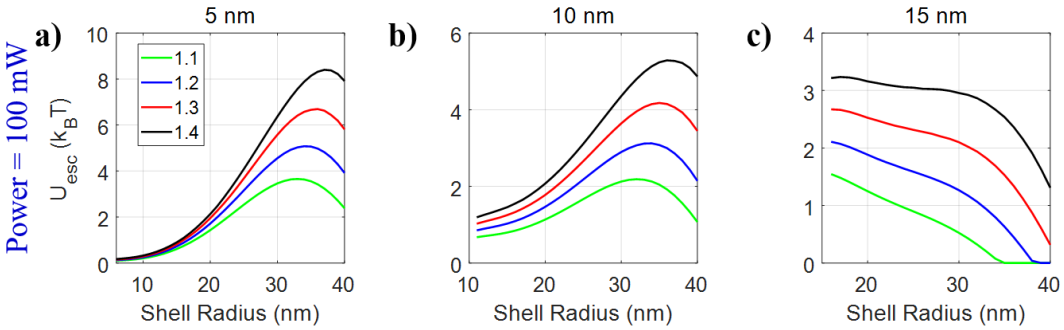

Fig. 7.24.: Plots of escape potential against shell radius by fixing core radius a) 5 nm, b) 10 nm, and c) 15 nm at 100 mW average power for silver-polystyrene nanoparticles under pulsed excitation.

varying core radius for polystyrene-silver nanoparticles under pulsed excitation. Figures 7.25a-c show the variation of core radius at three different fixed shell radius 20 nm, 30 nm, and 40 nm. It is evident that if shell material is silver, then overall particle size more than 27 nm cannot be trapped, as discussed above. Figures 7.25d-f show the trapping force along the axial direction and for 10 nm-20 nm particle size, where the absorption force dominates over the gradient and scattering force. The resultant force shows confinement along the axial direction — further increasing core radius results in splitting the absorption force curve and which regains confinement again. In other words, we can say that with increasing core radius, the optical trap first stabilizes and then becomes unbound, and after a certain particle size, it again stabilizes. An interesting point here is that force acting on the particle for 19 nm-20 nm is repulsive under CW excitation while it is attractive under pulsed excitation under similar conditions. This means that 19 nm-20 nm particle cannot be trapped under CW excitation, but it can be trapped under pulsed excitation due to the significant contribution of nonlinear effects. Since the OKE is strongly dependent on the average power. We further explore the effect of average power on trapping efficiency, as shown in figure 7.25g-i, and observe that for smaller size particles, increasing power destabilizes the trap. However, the bigger sized particles, which cannot be trapped at low average power, can be trapped at high average power. For example, 18 nm-20 nm particle cannot be trapped at 100 mW average power but can be trapped at 500 mW average power, in contrast, 10 nm-20 nm particles can be trapped at 100 mW average power but cannot be trapped at 500 mW average power. So, depending on the particle size, we should judiciously choose the average power to get stable trapping under certain conditions.

Figure 7.26 shows the variation of escape potential by fixing the core radius and varying shell radius for polystyrene-silver nanoparticles under pulsed excitation. Figures 7.26a-c show the variation of shell radius at three different fixed core radius 5 nm, 10 nm, and 15 nm at 100 mW average power. If the core (metallic) radius is more than 15 nm, no stable trapping is observed, as discussed in figure 7.22 under CW excitation. The trend of the curve similar to CW excitation but increasing average power narrow down the region of stable trapping in terms of particle size, as shown in figure 7.26d-f. This is because with increasing power, the contribution of nonlinear refractive index increases more than the linear refractive index, which elevates the absorption and scattering force. So, for small-sized particles, the absorption force significantly increases, which is responsible for

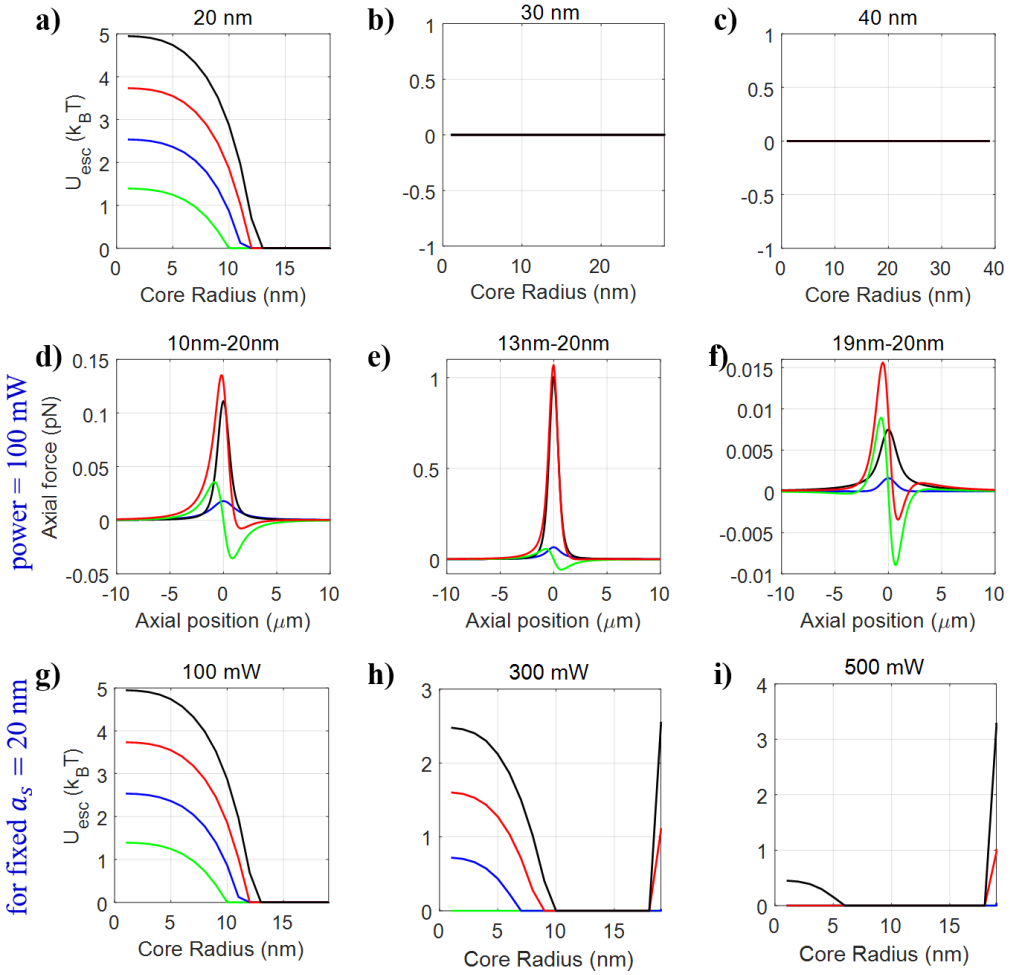

Fig. 7.25.: Plots of escape potential against core radius by fixing shell radius a) 20 nm, b) 30 nm, and c) 40 nm for polystyrene-silver nanoparticles under pulsed excitation at 100 mW average power. The plots of trapping force/potential along axial direction for d) 10 nm-20 nm, e) 13 nm-20 nm, and f) 19 nm-20 nm for polystyrene-silver nanoparticles under pulsed excitation at 100 mW average power for fixed NA 1.4. The plots of escape potential against core radius by fixing shell radius 20 nm g) 100 mW, h) 300 mW, and i) 500 mW average power for polystyrene-silver nanoparticles under pulsed excitation.

destabilizing the optical trap, and for bigger sized particles, the rapidly increasing scattering force is responsible for destabilizing the trap. While in between both cases, there is a region where scattering, gradient, and absorption forces balance each other in such a way that stable trapping can be obtained.

7.7 Hollow-core nanoparticles

Figure 7.27 shows the trapping force/potential along axial direction for conventional (silver) and hollow-core silver nanoparticles at 100 mW average power for

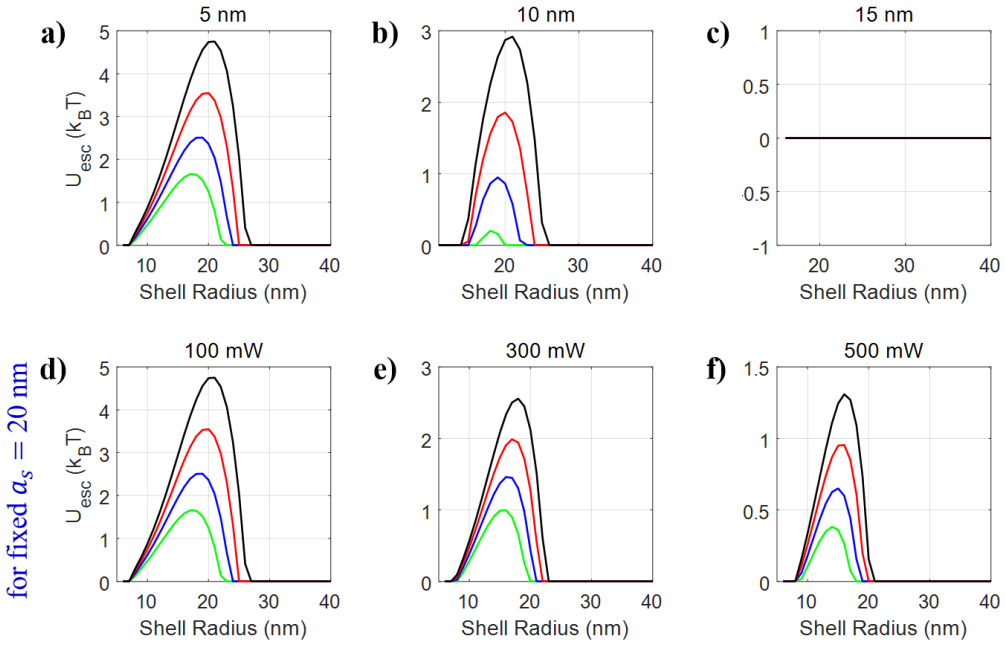

Fig. 7.26.: Plots of escape potential against shell radius by fixing core radius a) 5 nm, b) 10 nm, and c) 15 nm at 100 mW average power, and d) 100 mW, e) 300 mW, and f) 500 mW for fixed core radius 5 nm for silver-polystyrene nanoparticles under pulsed excitation.

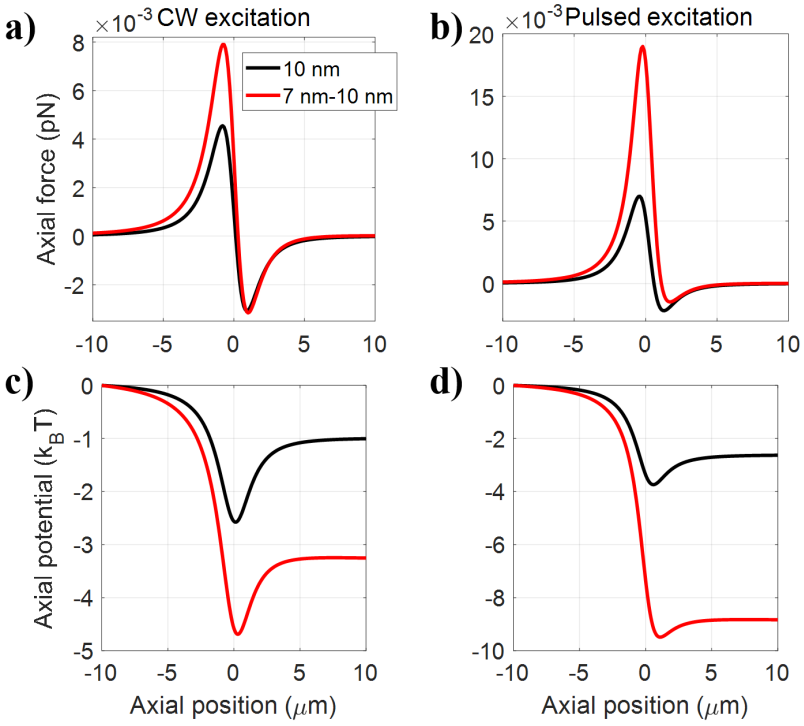

Fig. 7.27.: Plots of of trapping force/potential along axial direction for conventional (silver) and hollow-core silver nanoparticles at 100 mW average power for fixed NA=1.4.

fixed NA 1.4 under both CW and pulsed excitation. On comparison of force/potential for 10 nm silver nanoparticle with 7 nm -10 nm (air-silver) hollow nanoparticles, we have observed that hollow-core nanoparticles show significant enhancement in force than conventional nanoparticles. This enhancement is further intensified under pulsed excitation.

7.8 Conclusion

We have shown the trapping behavior of silver nanoparticles and studied the effect of OKE under high repetition-rate femtosecond pulsed excitation. Most significantly, we have observed the initial disappearance of trapping potential well along the axial direction with an increase in laser power but subsequent reappearance at higher laser power. This work shows how one can harness OKE to fine-tune the stability of an optical trap and thereby have controlled optical manipulation. On comparing CW and pulsed excitation, certain particle sizes that could be stably trapped under CW excitation were found to be untrappable under pulsed excitation due to disproportionate enhancement in destabilizing forces. Also, after studying the diverse trapping behavior of conventional, hybrid, and hollow-core nanoparticles, it can be concluded that hybrid and hollow-core nanoparticles are advantageous over conventional nanoparticles. Mainly, it has a significant advantage while doing bio-conjugated experiments which require a high magnitude of the force. The hybrid and hollow particles offer a wide range of new possibilities and flexibility due to their tunable properties. These novel materials need further attention and rigorous characterization to optimize their performance. In terms of application, while core-shell particles offer limited storage capacity but more stability and vice-versa for hollow-core nanoparticles. Hence, according to the requirement, one should be careful while choosing the proportionality of core and shell radius depending on the average power, NA, the nonlinear refractive index of the material, etc.

Part B: Experiment

Experimental techniques 8

8.1 LASER system used

Experimental work shown in this thesis is done using a diode-pumped, Mode-locked Ti: Sapphire Laser (Vitesse 2W; Coherent Inc. USA.). This is a solid-state femtosecond oscillator having a repetition rate of 80 MHz, central wavelength 800 nm, average power $\sim$ 150 mW, bandwidth >10 nm, and polarization $> 200:1$; horizontal polarization. This can be operated in both CW and pulsed excitation mode.

8.2 Characterization of LASER pulses

Before using any LASER system for experimental quantification, we require precise characterization of the energy of each pulse or average power, beam size, beam shape, the spectrum of the laser pulse, wavelength, pulse width, repetition rate, etc. This is because depending upon the environmental conditions; properties change slowly.

8.2.1 Measurement of average power

To measure the average power, we have used power meter (PM30; Coherent Inc. USA.), which integrates for a long time for a range of wavelength ranging from 250 nm to 1100 nm, which has a thermopile sensor. The minimum resolution for measuring power is 2 mW, and the maximum it can measure is 30 W.

8.2.2 Measurement of beam shape and size

To determine the shape and size of the laser beam, we have used a beam profiling camera (LBP2-HR-VIS2, Newport Inc, USA). The measured diameter of the laser beam is ~ 5.2 mm. From figure 8.1, it can be seen that the beam shape is distorted before the pinhole as compared to after pinhole. Therefore, we used a mode cleanup setup where we have used a 50 μm pinhole diameter and 150 mm lens to focus onto the pinhole, and another lens of the same focal length is used to collimate the beam (other possible combination shown in table 8.1), which is also known as spatial filter. After beam cleanup, we remove the diffraction ring using an aperture and couple the beam into the optical tweezer setup.

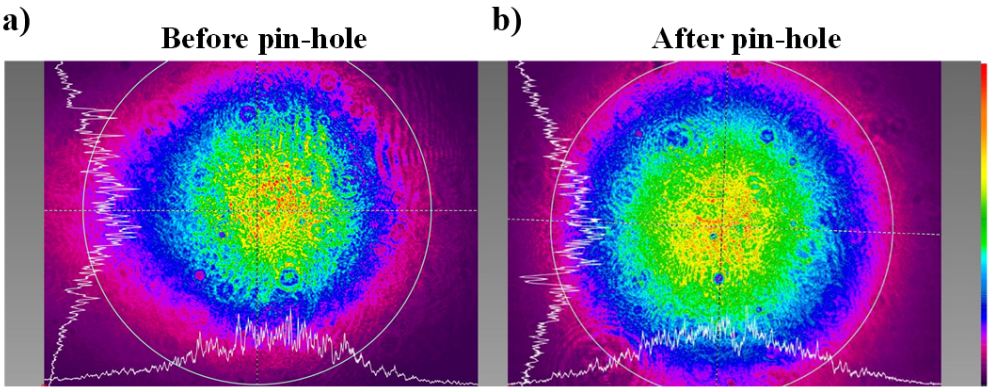

Fig. 8.1.: Beam profile of the laser system a) before, and b) after the mode cleanup setup.

D (μm)	$P_{input}(mW)$	f (mm)	$P_{output}(mW)$	Diffraction Ring
100	~125	50	~123	No
	~ 115	75	~ 113	No
	~105	100	~104	No
50	~ 115	50	~ 114	No
	~ 114	75	~ 112	Yes (distorted spot)
	~ 105	100	~ 102	Yes (distorted spot)
	~115	150	~99	Perfect ring

Tab. 8.1.: Calibration table for mode cleanup setup.

8.2.3 Measurement of central wavelength

The beam spectrum is measured by a spectrometer (HR4000CG-UV-NIR, Ocean Optics Inc., UK), and the spectrum is shown in figure 8.2, where black dots represent the experimental data and the red curve is Gaussian fit. Here, a slight asymmetry in the laser spectrum can be seen. FWHM corresponding to the spectrum is ~29 nm, and the central wavelength is ~800 nm (800.53 nm).

8.2.4 Measurement of pulse width

The transform-limited pulse width can be calculated using $\Delta\nu\Delta t = 0.414 \Leftrightarrow -\frac{c}{\lambda^2}\Delta\lambda\Delta t = 0.414$; where $\Delta\lambda$ is FWHM corresponding to the laser spectrum as shown in figure 8.2 which is ~29 nm. The calculated transform-limited pulse width using the laser spectrum is ~32 fs.

There are several methods to calculate pulse width but all are limited by resolution.

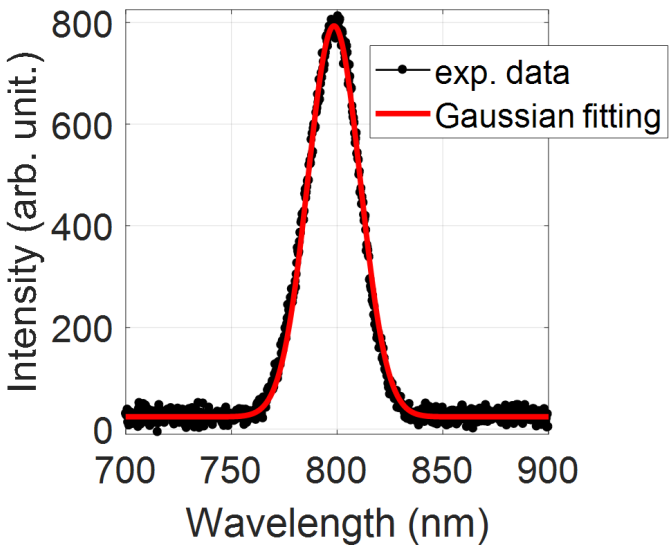

Fig. 8.2.: Laser spectrum.

8.2.4.1. Electronic method

The photodiode can be used to detect the temporal profile of laser pulses. Within photodiode, there are different types of detectors: PIN (intrinsic semiconductor sandwiched between p-doped and n-doped semiconductors) and high-speed MSM (intrinsic semiconductor sandwiched between metal; metal-semiconductor-metal) photodetectors, etc. These detectors require a finite time to clean up the depletion layer. Therefore, PIN and MSM can measure the pulse width >100 ps and > 10 ps, respectively. This method is still in use for measuring the pulse width of the CW mode-locked argon LASER and Nd-YAG oscillator[160].

The streak camera can be used to characterize shorter pulses. In a streak camera, the light beam is passed through a slit, and an image is formed onto the photocathode of a streak tube. The optical pulses vary slightly in time and space. They have different intensity when they arrive at photocathode of streak tube and convert into electrons (same as PMT) depending upon their intensities. Afterward, they pass through a pair of accelerating electrodes where optical pulses bombard against a phosphor screen, and a high voltage is applied to sweep electrodes at a time-synchronized to the incident light. This initializes a high-speed sweep in which electron sweep from top to bottom. The optical pulses shift slightly in time and deflect at a different angle along the vertical direction and enter to a microchannel plate (MCP). Finally, the image can be read easily by a standard CCD camera. However, this method is limited by the electronic resolution. Thus, the pulse width, which can be measured, is >100 fs.

8.2.4.2. Optical method

To measure the pulse width <100 fs, we have to use optical methods, which can be categorized into two parts [160]: non-collinear and collinear autocorrelation. In the autocorrelation technique, we have measured pulse width in the time domain using photodetectors (photodiode and PMT), but photodetector's rise and fall times are approximately 1 ns which is a very slow response compared to our measurement time. The important point here is that photodetectors should have a band gap greater than the photon energy. So, the output voltage (V_{output}) we have measured is the time integral of pulse intensity *i.e.* pulse energy which can be expressed as:

$$V_{output} \propto \int_{-\infty}^{\infty} |E(t)|^2 dt \tag{8.1}$$

here, E(t) is the electromagnetic field.

Non-collinear autocorrelation

Intensity autocorrelation

In this autocorrelation technique, laser pulses focus non-collinearly onto the BBO crystal through a plano-convex lens. A schematic diagram for noncollinear auto-correlation setup is shown in figure 8.3. In this, we have used a 50:50 beam splitter and the delay stage having a precision of 0.1 μm. A 100 mm plano-convex lens is used to focus the laser beam onto 200 μm thick BBO crystal. The resulting SHG signal is detected using photodiode and PMT. The crucial point in this technique is that SHG phase-matching conditions should satisfy which suppress the background signal. However, a constant background signal is observed, which can be further minimized by using an iris just before the detector. So, the output signal observed is background free.

Mathematical formulation

Laser pulse electric field can be written as:

$$E(t) = E_0 e^{j(\omega_0 t - \phi(t))} \tag{8.2}$$

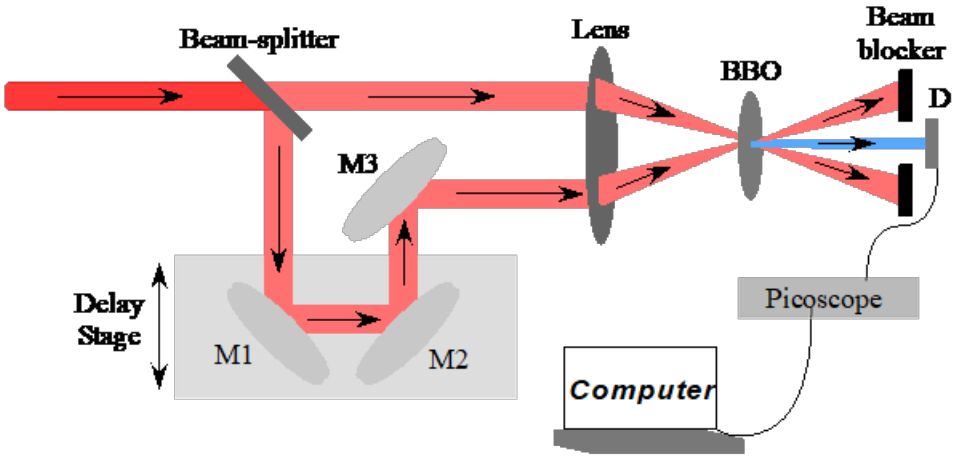

Fig. 8.3.: Schematic diagram for non-collinear autocorrelation set-up.

Here, E_0 represents the amplitude and $\phi(t)$ represents the phase shift. In the non-collinear autocorrealtion technique, a SHG signal appears, so the corresponding electric field can be written as:

$$E_{SHG}(t) = E(t)\,E(t-\tau) \tag{8.3}$$

here, τ is the delay between the two pulses. The autocorelation intensity measured by the detector can be expresssed as:

$$I_{AC}(\tau) = V_{SHG}(\tau) \propto \int_{-\infty}^{\infty} |E_{SHG}(t)|^2 dt = \int_{-\infty}^{\infty} |E(t)\,E(t-\tau)|^2 dt \tag{8.4}$$

$$I_{AC}(\tau) \propto \int_{-\infty}^{\infty} I(t)\,I(t-\tau)\,dt \tag{8.5}$$

At $\tau = 0$, pulses are perfectly overlapping, and the intensity is maximum. To measure the pulse width, we have fitted the output signal with Gaussian. The laser pulse intensity mathematically can be written as:

$$I(t) = I_0 e^{-2\left(\frac{\sqrt{ln2}t}{\tau_p^{FWHM}}\right)} \tag{8.6}$$

here, t is the real time and τ_p^{FWHM} is the actual pulse width. The measured autocorrelation signal can be written as:

$$I_{AC}(\tau) = I_0 e^{-2\left(\frac{\sqrt{ln2}\tau}{\tau_A^{FWHM}}\right)} \tag{8.7}$$

here, τ is delay time and τ_A^{FWHM} is the measured pulse width. The actual pulse width and measured pulse width differ by a factor of$\sqrt{2}$, which can be expressed as: $\tau_A^{FWHM} = \sqrt{2}\tau_p^{FWHM}$ according to Wiener-Khinchin theorem. This factor is different for different beam profiles.

Experimental pulse width measurement

The figure 8.4 shows the experimental data for non-collinear autocorrelation (black curve) and fitted with a Gaussian fit (red curve) for both horizontal and vertical polarization of the laser beam. The minimum delay between the two data points is 1 μm, which is equivalent to 6.67 fs in the time domain. When the laser beam is vertically polarized (figure 8.4b), the overlap of the laser beam at the focal plane onto BBO is better (side by side) than the horizontal polarization (figure 8.4a) which results in the higher intensity of SHG signal in vertical polarization than horizontal polarization. The measured pulse widths are $\sim 146\pm$ 0.5 fs and $\sim 154\pm$ 0.7 fs corresponding to horizontal and vertical polarization respectively. This deviation in the pulse width is due to the overlapping of pulses at the focal plane. Depending upon certain conditions, non-collinear autocorrelation has few

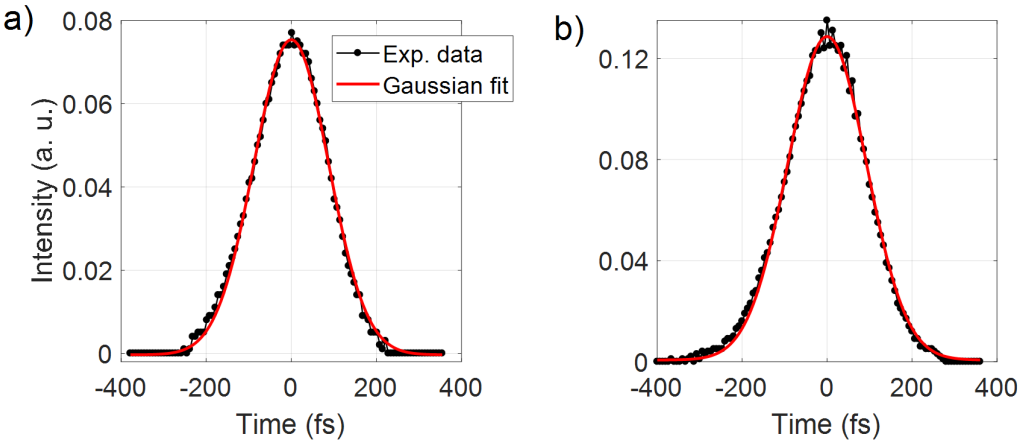

Fig. 8.4.: Plots of non-collinear autocorrelation trace when laser is a) horizontally polarized, and b)vertically polarized.

pros and cons:

- To measure the actual pulse width, we have to pre-assume the type of the pulse (Gaussian, Lorentz, sech etc.) so that we can calculate the pulse width from the autocorrelation trace.
- The autocorrelation trace is symmetric about the axis, so $I_{AC}(-\tau) = I_{AC}(\tau)$.

- If the pulse width of the laser pulses is < 50 fs, then very thin crystal should be used, so that phase matching bandwidth is enough to accommodate the information about pulses.
- This technique does not provide any information about pulse phase and chirping. It gives only the pulse width (envelope) information.
- Intensity autocorrelation can not give complete information about the pulse intensity profile such as chirping, coherence time etc.

Collinear autocorrelation

In this autocorrelation technique, laser pulses are recombining at the same straight-line path and focused onto pin-hole/ BBO/ sample depending on the type of autocorrelation, as shown in figure 8.5. We have used two 50:50 beam splitter. Among them, one is used to split the beam into two parts, and another is used to recombine them. A 100 mm plano-convex lens is used to focus the laser beam onto 200 μm thick BBO, and then the SHG signal is detected using photodiode/PMT. Collinear auto-correlation is further characterized into three different categories:

1. First-order autocorrelation
2. Second-order autocorrelation
3. Third order autocorrelation

In this thesis, we will rigorously explain the first-order and second-order autocorrelation, which we have performed experimentally. Third-order autocorrelation can be done using third-harmonic generation or through the Kerr experiment, which we did not do experimentally.

First order autocorrelation

Field autocorrelation

In the field autocorrelation technique, a pin-hole is used instead of BBO. Field autocorrelation is the first-order autocorrelation, also known as linear autocorrelation. The principle behind this technique is based upon the Mach-Zehnder interferometer.

Mathematical formulation

The measured field autocorrelation intensity can be written as:

$$I_{FA} \propto \int_{-\infty}^{\infty} |E(t) + E(t-\tau)|^2 dt \tag{8.8}$$

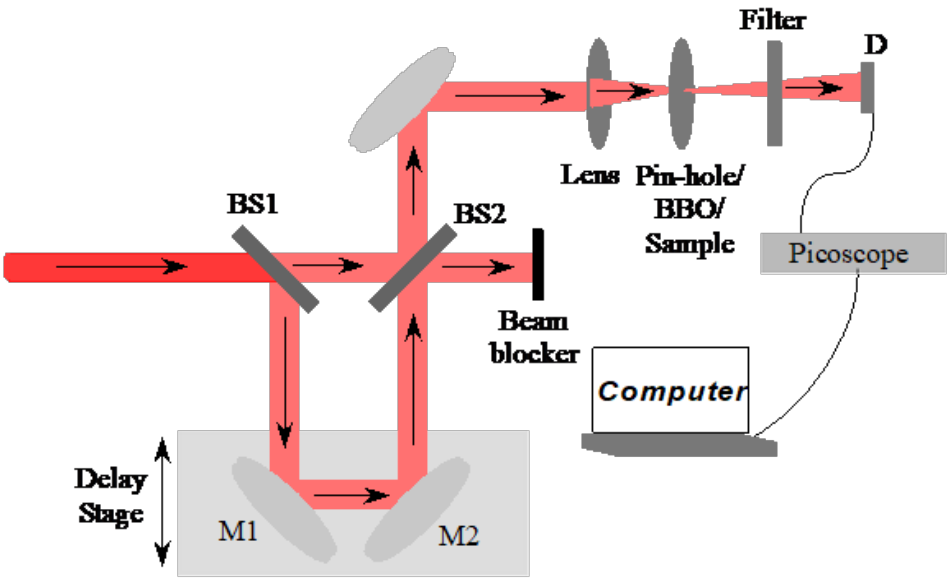

Fig. 8.5.: Schematic diagram for collinear autocorrelation set-up.

$$I_{FA} \propto \int_{-\infty}^{\infty} \left(|E(t)|^2 + |E(t-\tau)|^2 + E^*(t)\, E(t-\tau) + E(t)\, E^*(t-\tau) \right) dt \quad (8.9)$$

$$I_{FA} \propto 2\int_{-\infty}^{\infty} I(t)\, dt + 2Re \int_{-\infty}^{\infty} E(t)\, E(t-\tau)\, dt = 2\int_{-\infty}^{\infty} I(t)\, dt + 2G_1(\tau) \quad (8.10)$$

In the above equation, the first term corresponds to the pulse energy and the the second term corresponds to the first order autocorrelation function. The measured pulse width and the actual pulse width are related as $\tau_{FA}^{FWHM} = \sqrt{2}\tau_p^{FWHM}$. This method also does not reveal any information about the phase of the pulse.

Experimental pulse width measurement

The field autocorrelation trace is shown in figure 8.6. The pulse width is determined using the upper envelope, and lower envelope fitting is ~ 39.39 fs and ~ 39.37 fs, respectively. As field autocorrelation has no information about the chirping, so this pulse width is equivalent to the coherence time of the laser pulse.
Coherence time: Coherence time is the time during which two simultaneously propagating pulses are in phase. However, depicting the actual pulse width using this method is difficult if the pulses are chirped.

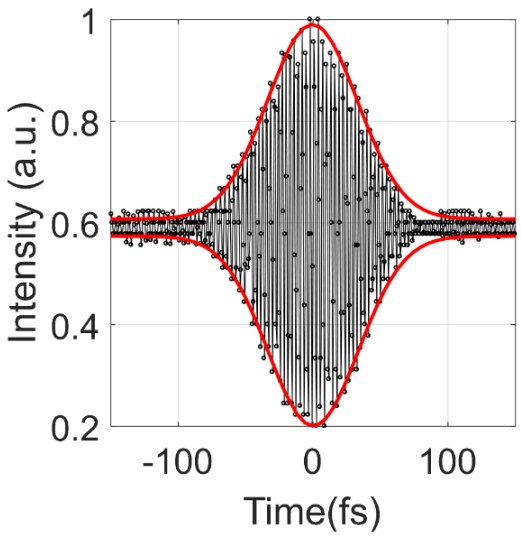

Fig. 8.6.: Plot of collinear first order, field autocorrelation trace.

Second-order autocorrelation

Unlike the field autocorrelation, second-order autocorrelation gives the information about chirping and phase of the laser pulse. In general, the higher-order correlation functions are generated by multi-photon processes. Second-order autocorrelation can be done using two different methods, which are two-photon absorption and SHG. In the two-photon absorption method, the detector should be excited at a wavelength less than its band gap cut-off. The measured second-order correlation function mathematically can be written as:

$$I_{SHG/TPF}(\tau) \propto \int_{-\infty}^{\infty} \left[\left(E(t) + E(t-\tau) \right)^2 \right]^2 dt \tag{8.11}$$

BBO autocorrelation

We have done SHG autocorrelation using a BBO having a thickness of 200 μm.

Mathematical formulation

The measured field autocorrelation intensity can be written as:

$$\begin{aligned} I_{SHG}(\tau) \propto & \int_{-\infty}^{\infty} \left[2I^2(t)\right] dt \\ & + \int_{-\infty}^{\infty} \left[4I(t) I(t-\tau)\right] dt \\ & + \int_{-\infty}^{\infty} \left[4E(t) E(t-\tau) \left[I(t) + I(t-\tau)\right] cos\left[\omega\tau + \phi(t) - \phi(t-\tau)\right]\right] dt \\ & + \int_{-\infty}^{\infty} \left[2I(t) I(t-\tau) cos\left[2\left(\omega\tau + \phi(t) - \phi(t-\tau)\right)\right]\right] dt \end{aligned} \tag{8.12}$$

For $\tau = 0$, when both pulses are perfectly overlapping, known as coherent superposition, the measured intensity becomes:

$$\begin{aligned} I_{SHG}(\tau = 0) &\propto \int_{-\infty}^{\infty} \left[2I^2(t) + 4I^2(t) + 8I^2(t) + 2I^2(t)\right] dt \\ &= 16 \int_{-\infty}^{\infty} \left[I^2(t)\right] dt \end{aligned} \tag{8.13}$$

Whereas, for $\tau = \infty$, when both pulses are far apart, measured intensity becomes:

$$I_{SHG}(\tau = \infty) \propto 2 \int_{-\infty}^{\infty} \left[I^2(t)\right] dt \tag{8.14}$$

The above expression implies that the same ratio (2:16 or 1:8) of the intensity should be observed in the autocorrelation trace i.e., when pulses are far apart, and the delay between pulses is zero. In the above equation 8.12, the first term corresponds to the background signal, the second term corresponds to the intensity autocorrelation, the third term corresponds to the coherence time oscillation with frequency ω, and the fourth term corresponds to the coherence time oscillation with frequency 2ω. This method gives information about the phase and chirping of the laser pulses.

Experimental pulse width measurement

The SHG autocorrelation trace is shown in figure 8.7. The obtained pulse width is $\sim 274.58 \pm 0.93$ fs, fitted with a Gaussian distribution. Coherence time for an upper and lower envelope for TPF is ~ 56.76 fs and ~ 60.18 fs, respectively, using BBO. It can be observed that the background signal to the peak of the upper fringe envelope signal ratio is approximately 1:8.

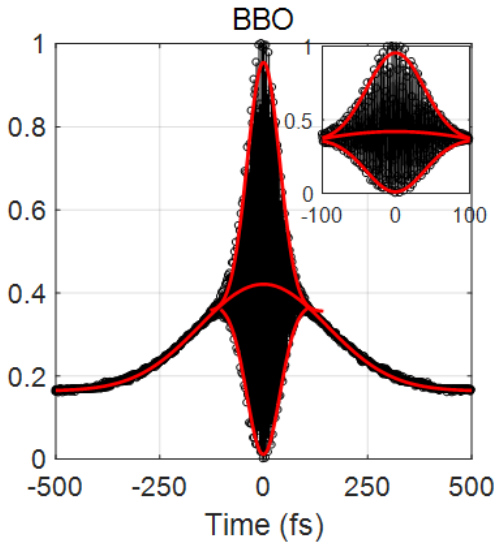

Fig. 8.7.: Plot of collinear second order SHG autocorrelation trace.

TPF autocorrelation

TPF autocorrelation is similar to SHG autocorrelation because it is also a two-photon process. To check whether TPF and SHG autocorrelation methods yield the same results, we have performed the free-space measurement of the pulse width using both SHG and TPF autocorrelation. TPF autocorrelation is done using Rhodamine 6G, in which sample (rhodamine 6G dissolve in water) is placed at the focal plane in 1 mm quartz cuvette placed instead of BBO. The obtained pulse width is $\sim 298.97\pm$ 2.51 fs. This small deviation in the pulse width as compared to BBO is due to chirping by the wall of the cuvette.

8.3 Experimental technique

We have built a table-top optical tweezer set up from scratch, which is designed solely by us. It is a versatile setup which can be used in:

- wide-field detection mode using camera (with CMOS or EMCCD detector): we can detect both
  - bright-field images to record transmitted images under white-light illumination.
  - dark-field images to record both TPF and backscattered signals.
- point detection mode using photo-multiplier tubes (PMTs): we can simultaneously detect both TPF and backscattered signal

A detailed discussion is given below.
We have used commercial laser in both continuous-wave (CW) and high repetition-rate (80 MHz) femtosecond pulsed excitation mode for trapping.

8.3.1 Wide field microscopy using CMOS camera

The experimental set up for the home built table-top optical tweezer is shown in figure 8.8. A linearly polarized laser beam from a Ti-Sapphire oscillator is centered at $\sim$ 800 nm and 80 MHz repetition rate with a Gaussian beam profile. A 50 μm diameter pin-hole is used to clean-up the spatial mode of the Gaussian beam profile, and laser power is controlled by using a combination half-wave plate and polarizer. The oscillator beam has a diameter of $\sim$4.8 - 5.2 mm. To fill the back aperture of the objective, it is expanded to $\sim$ 10 mm using a beam expander setup (a combination of the convex and concave lens). We use a dichroic beam-splitter (FF670-SDi01-25$\times$ 36, Semrock Inc, New York) to route the beam to an oil immersion objective (UPlanFLN100X UIS2, OLYMPUS Inc, Japan) with NA=1.3 which focuses the beam onto the sample plane, and the sample holder is kept at XYZ translational stage (PT3, Thorlab Inc).
The TPF signal is collected using a 680 nm short-pass filter (FF01-680/SP-25, Semrock Inc, New York), and the backscattered signal is collected using a 770 nm long-pass filter (FF01-776/LP-25, Semrock Inc, New York). Bright field signal is collected using 460$\pm$ 10 nm bandpass filter for coated particles (to block TPF signal from dye) and 680 nm short-pass filter for uncoated particles respectively.

The height of the focal plane from the glass substrate is $\sim$50 μm, and the thickness of the glass substrate is $\sim$100 μm, and the interaction between the particles and glass substrate is negligible.
All the data are collected at room temperature (295 K). The dark-field TPF and backscattered signals are captured by a CMOS camera (DCC1645C, Thorlabs Inc, USA).

8.3.1.1. Mapping trapping plane to CMOS camera

Figure 8.9 shows the schematic for imaging the focal plane onto the CMOS camera plane. When the particle is trapped, the projection of the radial profile is projecting onto the CMOS plane. If a particle moves axially, the signal intensity fluctuates, but if the particle moves radially then average intensity remains approximately the same, however, fluctuations increase with time along both radial and axial directions, and the radial fluctuations can be seen through the

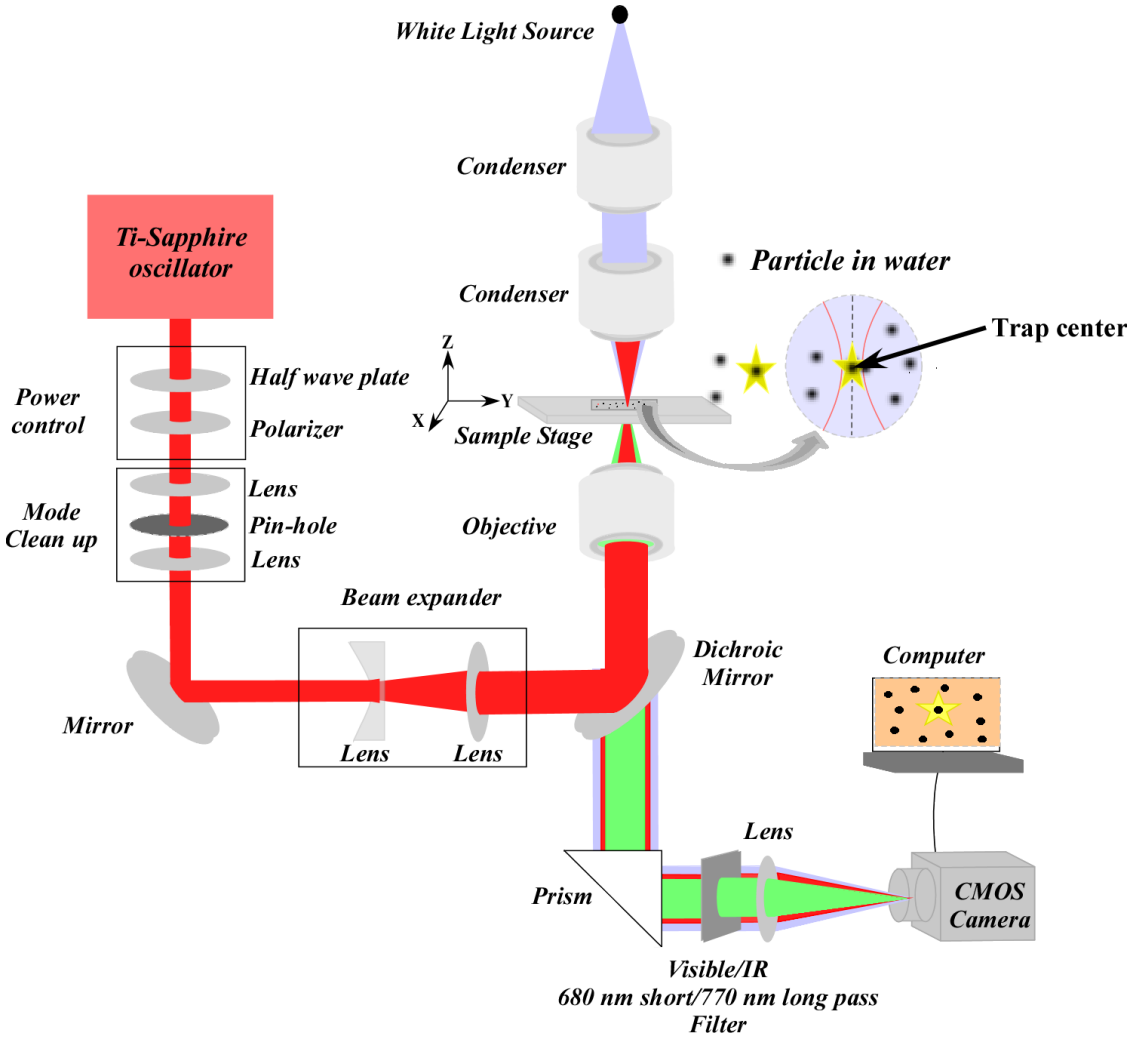

Fig. 8.8.: A schematic diagram for experimental set-up of a home built optical tweezer for wide field microscopy.

video microscopy whereas axial fluctuations can be analyzed by integrating over the radial projection for a fixed time interval.

For the study of the dynamics of the particle, we should be more careful about the focal plane of CMOS camera because if we are imaging any other plane instead of the focal plane, then the signal might be distorted.

8.3.1.2. Demonstration of stable trapping using video microscopy

With our home-built optical tweezer set-up, we demonstrated stable optical trapping of fluorophore-coated and uncoated particles. Figure 8.10 shows the snapshots taken from the bright-field video as the particle is gradually dragged towards the trap and from the dark-field video when it is trapped. Here, the blue circle represents the position of the particle, and the arrow represents the direction in which the particle is dragged towards the trap center.

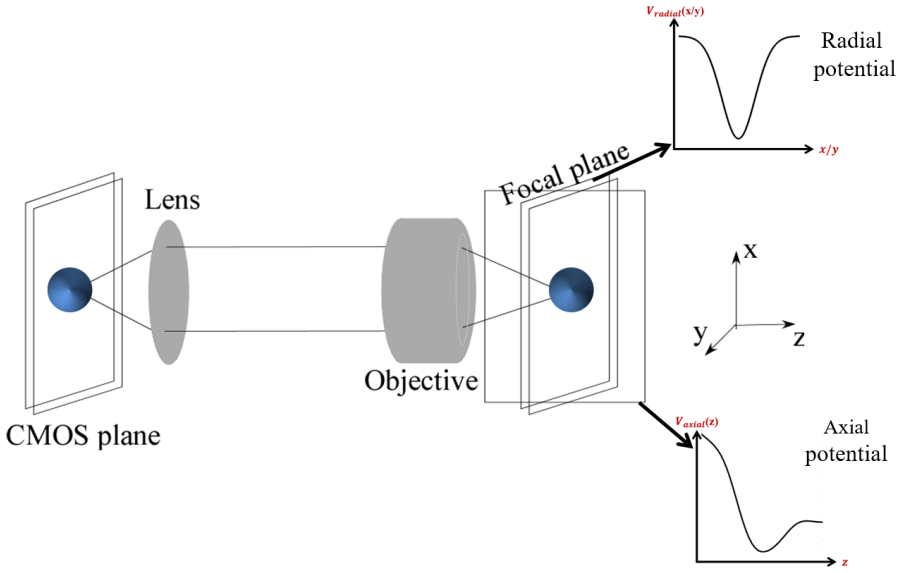

Fig. 8.9.: Schematic diagram for imaging the focal plane onto a CMOS camera plane.

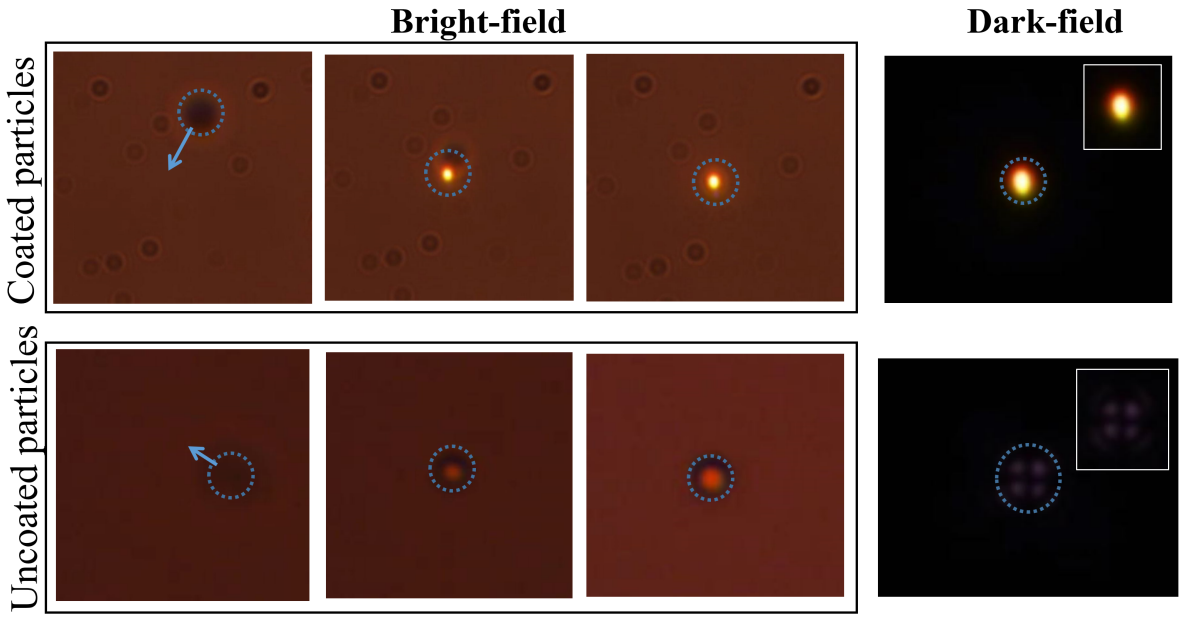

Fig. 8.10.: Snapshots capturing events of optical trapping in different modes of detection for 1 μm polystyrene bead (diameter), and size of the image is $\sim 170 \times 190$ pixels.

8.3.2 Point detection using PMTs

Figure 8.11 shows the modified home-build optical tweezer for the simultaneous detection of TPF and backscattered signals for polystyrene micron and nanometer-sized particles. We have performed experiments without confocality as well as

with confocality, and all the data are collected using PMTs. Simultaneous data for both the channels (TPF and backscattered) are collected using a picoscope (PicoScope 3405D, Pico Technologies, Vigven Tech Mark Pvt Ltd.) at 400 μs and 400 ns time intervals. In TPF channel we have used 680 nm short-pass filter since our emission is near 575 nm, and for the backscattered signal we have used 770 nm long-pass filter.

While performing the experiment using point detection mode with confocality,

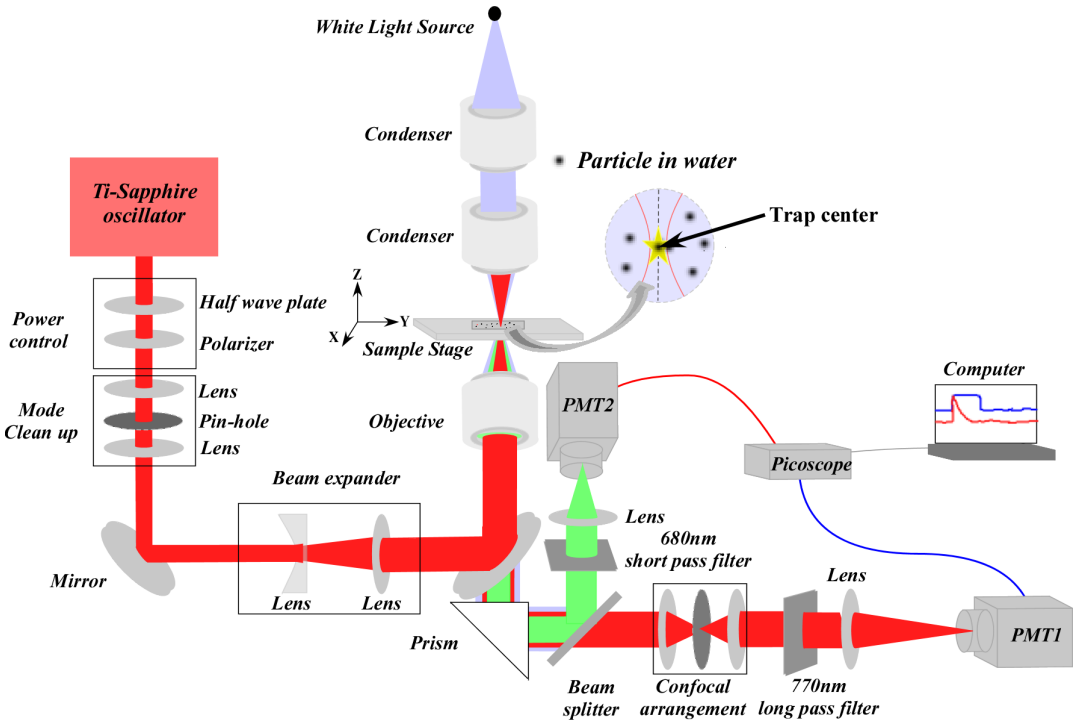

Fig. 8.11.: Schematic of home-built optical tweezer set-up using point detection mode.

first, we need to do calibration of the system.

8.3.2.1. PMTs Calibration

For the TPF detection channel, we are using visible range PMT and for backscattered detection channel near IR. The near IR spectrum range PMT (PMM02, Thorlabs Inc, USA) is more sensitive as compared to the visible spectrum range PMT (PMM01). To calibrate the PMTs for visible, we have measured the Rhodamine 6G TPF signal, and for near IR, we have measured the backscattered signal from the glass slide at a different gain. The corresponding gain curve is shown in figure 8.12. For collecting the data, we have kept gain 0.7 for both near IR (PMM02, Thorlabs Inc, USA) and visible (PMM01, Thorlabs Inc, USA) spectrum range PMT respectively.

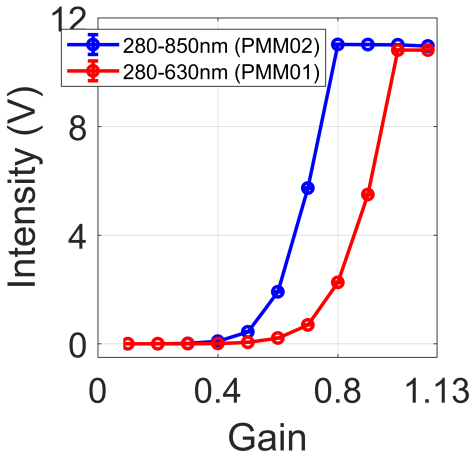

Fig. 8.12.: Plot of the photo-multiplier tubes (PMTs) gain curve for near IR and visible range.

8.3.2.2. Calibration of confocal arrangement

The confocal arrangement is used to enhance the signal to noise ratio because when the signal is detected from an optical path, a lot of backscattered signals also contributes to it, which suppress the original signal. Here, in an optical tweezer, this effect is prominent in backscattered than TPF detection because the TPF signal is obtained only at the focal plane. Therefore, to reduce the out of focus background backscattered signal, we are using a confocal arrangement. A spatial pinhole of 200 μm aperture is used at the confocal plane of the lens (Plano-convex lens of 10 cm focal length) onto a translational stage of minimum step size 10 μm. First, the backscattered signal focus onto the pinhole and then an another lens of the same focal length is used to collimate the beam. Subsequently, it is focused onto the photo-multiplier tube. To optimize the accurate position for pinhole, the backscattered signal from a glass cover-slip is obtained by placing pinhole at different positions, as shown in figure 8.13. Eventually, the pinhole is fixed at the position corresponding to the maximum signal.
Figures 8.14a, 8.14b, and 8.14c show the backscattered profile from glass cover-slip without confocal arrangement, with the confocal arrangement, and trapped particle profile with the confocal arrangement at PMT position taken by beam profiling camera respectively. After confocal arrangement, all the backscattered signal is minimized for the trapped particle at PMT position.

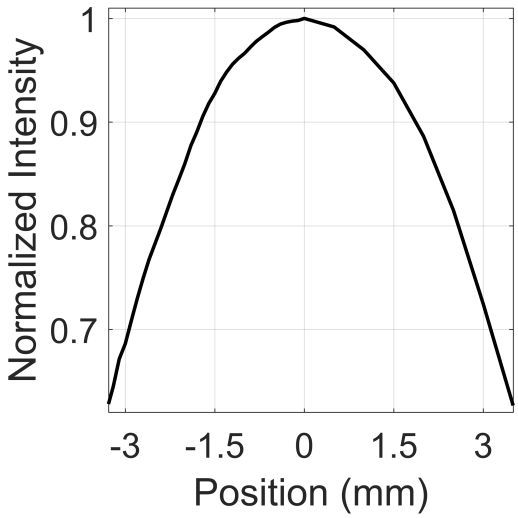

Fig. 8.13.: Plot of the backscattered signal from glass cover-slip against the pin-hole position.

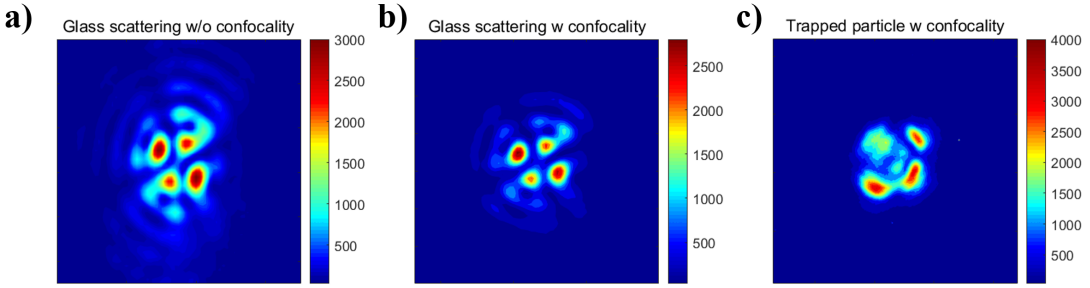

Fig. 8.14.: Plots of the backscattered signal from a) glass cover-slip without confocality, b) glass cover-slip with confocality, and c) trapped particle with confocality.

Power measurement at sample position

To determine the average power at the sample position, we have measured the laser power just before the beam expander (figures 8.8 and 8.11), then kept long focal length lens at the position of objective instead of objective and measured the average power by putting adjustable iris. The iris is kept the same as the back-aperture of the objective and then took 85 percent of the measured average power because transmission from the objective is 85 percent. We have plotted the average power before the beam expander against the average power measured at the sample position and determined the slope, which is 0.47. All the average laser power reported in this thesis for experimental analysis is calculated by measuring the laser power before the beam expander, and 0.47 of that power is assumed at the sample stage.

Pulse Width measurement at the sample position of optical tweezer

Since it is very difficult to calculate the exact pulse width at the sample position using second harmonic generation (SHG) autocorrelation, so we have used the TPF signal from Rhodamine 6G to measure the pulse width [160] which is ∼526±5.61 fs. The corresponding signal is shown in figure 8.15; where black curve corresponds to the experimental data and the red curve to the fitted Gaussian distribution.

We have estimated the pulse width using the following theoretical formulation [160, 161]:

$$\tau_{out} = \tau_{in}\sqrt{1 + 7.7\left(\frac{D^2}{\tau_{in}^4}\right)} \tag{8.15}$$

Here, τ_{in} is input pulse width measured on the table using BBO and TPF, and D is the product of group velocity dispersion (GVD) and propagation length. We have used GVD for SF-10 glass that is $\sim 159.2\, fs^2/mm$ at ~ 800 nm [161] and the propagation length is ~ 45 mm (length of the objective). The calculated pulse width for TPF autocorrelation in free space using this equation is $\sim 306.27\pm$ 2.33 fs. If the laser pulse is chirped with a significant amount, SHG and TPF autocorrelation traces give the pulse width and coherence time of the chirped pulse. The coherence time for the upper and lower envelope in case of TPF (at the sample stage) is ~ 56.76 fs and ~ 60.18 fs; in the case of BBO and TPF (on the table; before the objective), ~ 63.21 fs & ~ 64.91 fs and $\sim 60.55\pm$ 6.91 fs & 58.07± 3.03 fs respectively. The coherence time for TPF and BBO autocorrelation is almost comparable, whereas pulse width shows a significant difference, which might be due to the photo-bleaching occurring in TPF. Although theoretically estimated and the measured pulse width is not matching in literature, it is well known that when it passes through SF-10 objective (Olympus objective), the pulse width can increase dramatically [162]; therefore, in theoretical simulations, ~ 526 fs pulse width is used.

8.4 Sample preparation

The fluorescence emission spectrum is recorded using a steady-state fluorimeter (RF-6000, Shimadzu) by exciting the sample at 535 nm, and the fluorescence excitation spectrum is recorded by fixing the emission at 575 nm; the spectra are shown in figure 8.16. For trapping, we have used both fluorophores coated (F8819: 1 μm; F8800:100 nm, Thermo Fisher Scientific, USA) and uncoated

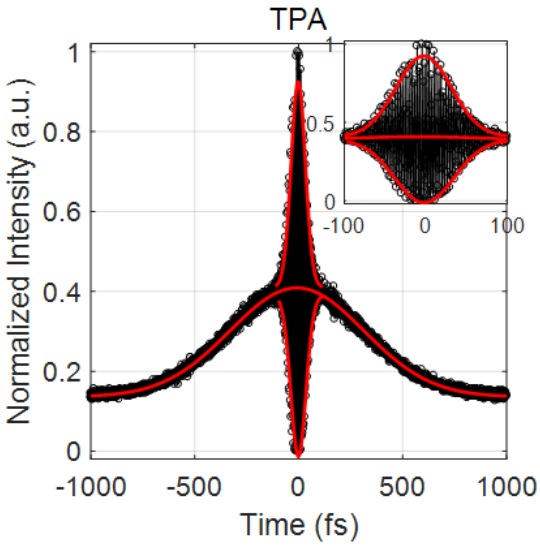

Fig. 8.15.: Plot of TPF autocorrelation trace for pulse width measurement at the sample position.

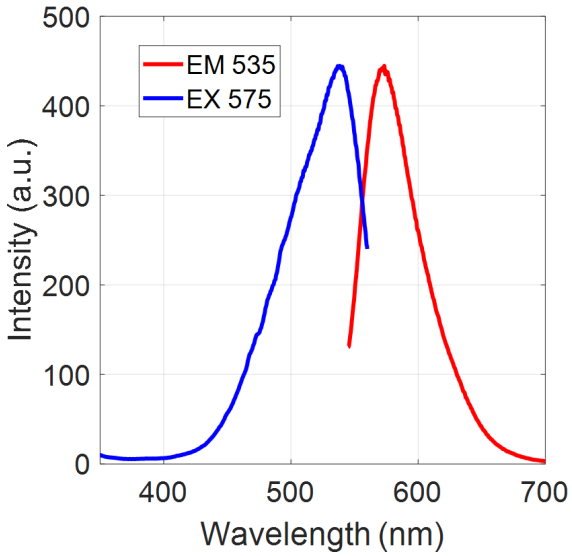

Fig. 8.16.: Plot of fluorescence excitation spectrum (shown in blue) recorded at 575 nm emission wavelength and fluorescence emission spectrum (shown in red) recorded at 535 nm excitation wavelength.

(C37274, Thermo Fisher Scientific, USA) polystyrene beads of 1μm in diameter suspended in water. To prevent the occurrence of the hydrodynamics reaction as well as aggregation between the particles and the environment, the sample is prepared in ultra-pure water by diluting it to 1:8000 ratio (v:v), followed by sonicated for $\sim$3 hours, and then kept onto a glass cover-slip with a substrate thickness of 100 μm.

8.5 Data analysis

8.5.1 Autocorrelation

For autocorrelation data collection, we have written Lab-VIEW code to synchronize translation stage and picoscope. The delay is converted into time as follows: Minimum step size is 0.1 μm and considering twice the delay at each point because of the retro-reflector, the minimum delay is: $\frac{2\times10^{-7}}{3\times10^{8}} \approx 0.67fs$.
After collecting data, FWHM calculations are determined using Origin and Matlab (Mathwork).

8.5.2 Wide field microscopy

The dark-field TPF signal are taken at 15 frames per second (fps) and the backscattered signal at 15 and 25 fps while the bright field images are collected at 100 fps in cropped mode.
From wide-field video microscopy, we have analyzed the trapping data by measuring the TPF/backscattered intensity of a region-of-interest of every frame over time by extracting each frame using the open-source 'Physics Tracker' software [163]. Contour plots of images are plotted by extracting counts from each pixel of the image after converting it into the gray-scale to the color-coded images, and data processing/fitting are done in Matlab (Mathworks).

8.5.3 Point detection mode

Simultaneous detection of dark-field TPF and backscattered signals are collected using a picoscope (PicoScope 3405D, Pico Technologies, Vigven Tech Mark Pvt Ltd.) at 400 μs and 400 ns time intervals. Origin and Matlab (Mathworks) software are used for data processing and fitting.

Optical Trapping of 1μm dielectric particles

9

9.1 Introduction

In earlier chapters, theoretically, we have shown that at lower power levels, the trap becomes progressively more stable upon increasing the power. However, as nonlinearity sets in, the trapping potential along axial direction becomes more asymmetric, and above a critical power level, it becomes completely unbound. In spite of these stimulating experimental [68, 74, 77, 81, 82] and theoretical endeavor (chapter 3 to 7), till date there has been no theoretical development to include OKE for particles having diameter comparable with laser wavelength ($d \approx \lambda$) and no experimental demonstration to map the nonlinear force/potential, both of which we present here in this chapter. Using a theory to include OKE developed within the framework of EMT [141] combined with analysis from time traces of TPF signal (for fluorophore coated particles) and of backscattered signal (for both coated and uncoated particles) in detail video microscopy of optical trapping of micron-sized polystyrene particles, we show how to map the nonlinear potential as the particles execute orchestrated excursion under the influence of nonlinear optical force created by a train of femtosecond laser pulses. In this chapter, we present the very first attempt in building a bridge between nonlinear optical phenomena and optical trapping.

9.2 Probing dynamics through wide field microscopy

9.2.1 TPF signal analysis

9.2.1.1. TPF signal profile

Figure 9.1 shows that a TPF image of a single particle confined in an optical trap where figures 9.1a and 9.1b show the image and 2D intensity distribution of TPF signal. Figure 9.1c shows the normalized 1D intensity distribution for pixel average over the region of interest (ROI; rectangular region in figure 9.1a), where black dots correspond to the experimental data, and the red line is a Gaussian fit. The center of the rectangular region (~ 15 pixel) chosen in Tracker software to analyze TPF data.

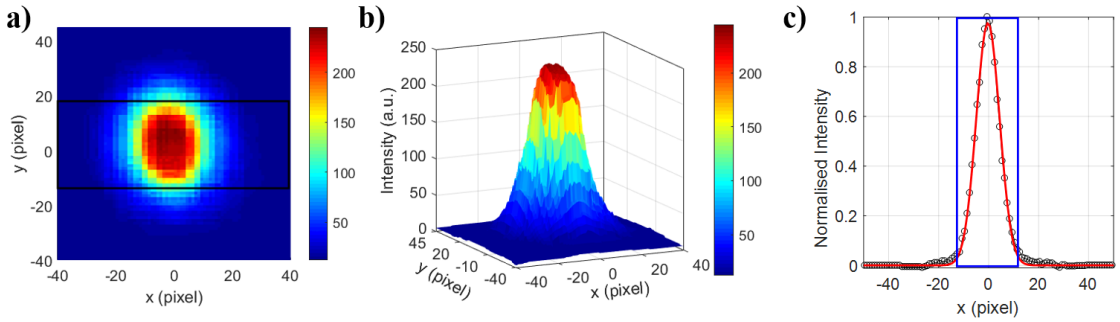

Fig. 9.1.: Plots of TPF profile of single particle inside the optical trap a) image b) 2D intensity distribution and c) normalized 1D intensity distribution.

9.2.1.2. Stuck particles

To study the effect of photo-bleaching, one drop of the diluted sample (~ 400 μL) is put onto cover-slip following putting it in the air (free space) to evaporate the water. Consequently, the particles get stuck on the surface of the cover-slip. Afterward, cover-slip is put on the sample stage, and one of the particles is brought in the focal plane manually, and the TPF signal is captured over time. The normalized TPF signal decays over time fits into a double exponential:

$$ae^{-\frac{t}{\tau_1}} + be^{-\frac{t}{\tau_2}} \tag{9.1}$$

by using the constraint $a + b = 1$. Figure 9.2 shows the TPF signal for the dry sample at 5.17 mW and 9.40 mW average power; here, the black curve corresponds to the experimental data, and the red curve corresponds to the exponential fit. It is observed that the TPF signals have no fluctuations over time, and photo-bleaching decay is smooth. Tables 9.1 and 9.2 show 10 sets of data fitting parameters at these two average powers. For a dry sample, the average time constants are random, as there is always some error associated while bringing the particle in the focal plane. Another important factor that could be possible is that the coating of particles is a statistical probability, thence, all the particles are not uniformly coated. Due to the occurrence of photo-bleaching, the overall/average time constant decreases while intensity increases with increasing average power (as shown in table 9.3). The data cannot be collected at high average power because the particle starts melting or ablating [164].

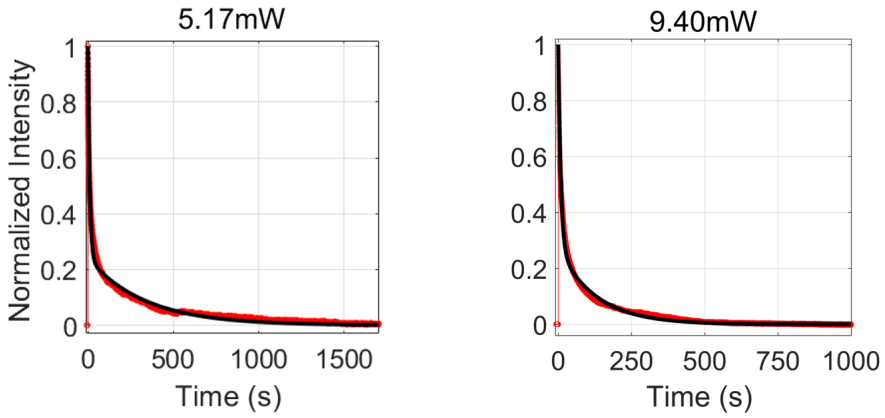

Fig. 9.2.: Plots of TPF signal analysis over time for stuck particle under pulsed excitation.

Peak Intensity (a. u.)	a	τ_1 (s)	b	τ_2 (s)	τ_{avg} (s)	R^2
209.76	0.30	324.6	0.71	16.37	107.30	0.99
287.30	0.24	332.2	0.76	9.95	87.42	0.97
298.40	0.24	374.6	0.76	10.25	95.87	0.97
256.27	0.31	307.6	0.70	15.24	104.30	0.98
277.80	0.28	337.4	0.73	14.76	103.49	0.96
232.10	0.26	411.7	0.74	15.35	118.04	0.96
233.30	0.30	326.5	0.70	10.63	104.13	0.97
291.18	0.26	370	0.74	10.57	105.46	0.96

Tab. 9.1.: Fitting parameters for the TPF signal collected for a single stuck particle after normalization for 5.17 mW average power.

9.2.1.3. Trapped single particle dynamics

When the particle is dragged to the trap center, there is an immediate rise in the TPF signal followed by decay over time due to photo-bleaching as shown in figure 9.3 for different average powers; here black dots represent the experimental data, and the red curve represents the fitted curve using equation 9.1. It can be observed that at high average power, the TPF signal shows more fluctuations as compared to low average power because when a laser beam is incident on a fluid sample containing the polystyrene particles, the local temperature around the particle will change. The temperature distribution follows the Gaussian distribution of the incident laser beam, and due to the inhomogeneous distribution of temperature [165], the surface tension non-uniformly varies, which results in exerting a net force on the particles that lead to a change in MSD of the particle. If the temperature profile is uniform, the particle would not have

Peak Intensity (a. u.)	a	τ_1 (s)	b	τ_2 (s)	τ_{avg} (s)	R^2
436.04	0.27	128.8	0.73	8.55	41.33	0.99
375.91	0.27	167.6	0.73	8.83	52.25	0.98
364.17	0.31	152.2	0.69	8.34	52.73	0.99
405.14	0.21	199	0.78	8.55	49.52	0.94
465.25	0.25	161.1	0.74	6.09	45.52	0.98
449.33	0.26	159.6	0.74	8.05	47.21	0.98
392.54	0.25	154.5	0.75	9.27	45.68	0.98
433.20	0.30	153.4	0.70	6.68	50.48	0.98
498.94	0.33	116.9	0.67	4.45	42.01	0.98
394.69	0.28	140.9	0.72	8.33	45.52	0.99

Tab. 9.2.: Fitting parameters for the TPF signal collected for a single particle after normalization for 9.40 mW average power.

Power (mW)	Peak Intensity (a. u.)	$\tau_{avg}(s)$
5.17	255.67 ± 37.37	105.61 ± 10.58
9.40	421.52 ± 42.46	47.22 ± 3.97

Tab. 9.3.: Average fitting parameters for 10 set of data for TPF signal collected for a single particle after normalization at different average power.

experienced any net force due to zero surface tension gradient, which results in no change in MSD. The temperature of the local environment rises with increasing power, and the particles experience more thermal kicks in order to conserve the momentum. When the particles are stuck on the surface, they do not experience any thermal kicks due to the absence of the surrounding medium. Therefore, the TPF signal does not fluctuate in the case of the dry sample, while in the solution phase, the particles experience thermal kicks and signal fluctuate more with increasing average power. Tables 9.4, 9.5, 9.6, 9.7, and 9.8 show 10 sets of data fitting parameters for different average powers. The average time constants are comparable for all these data sets at a particular average power because the particle is dragged in an optical trap. However, for the dry sample, they are not comparable as the particle is forcefully brought within the focal plane. Table 9.9 shows that the average time constant of all these data sets, and it decreases while intensity increases with increasing average power.

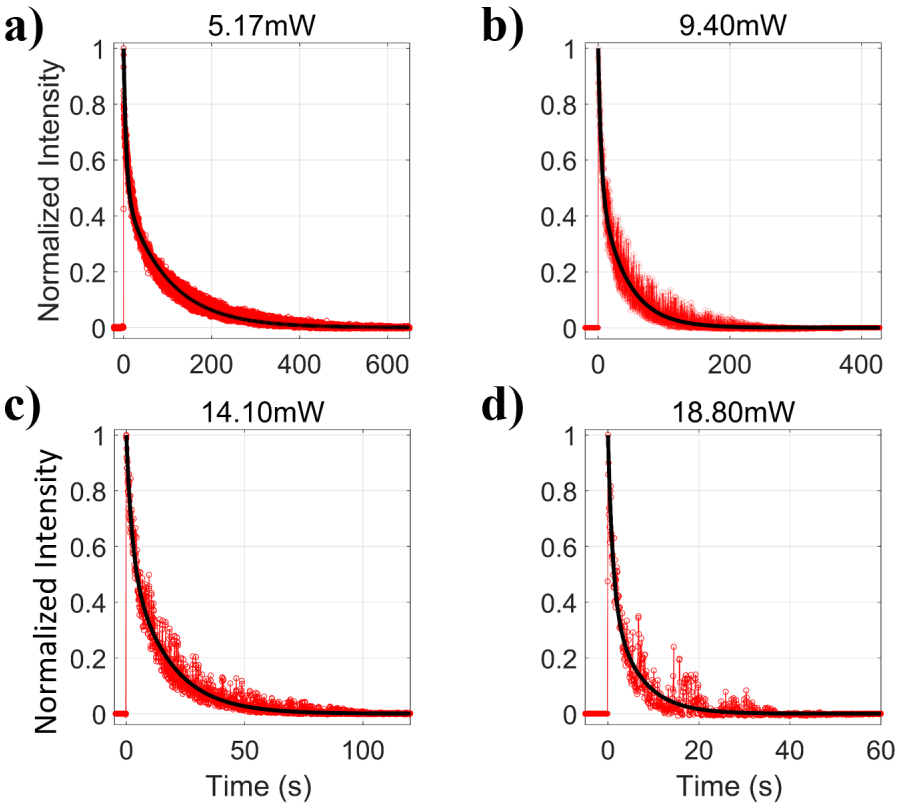

Fig. 9.3.: Plots of TPF signal from a trapped particle at different average powers under pulsed excitation.

Peak Intensity (a. u.)	a	τ_1 (s)	b	τ_2 (s)	τ_{avg} (s)	R^2
141.59	0.48	97.88	0.52	6.32	50.55	0.98
145.22	0.47	96.8	0.53	5.42	48.85	0.97
139.57	0.49	97.04	0.51	6.52	50.75	0.99
141.56	0.55	82.24	0.45	8.03	48.44	0.99
139.82	0.40	112.2	0.60	11.95	51.88	0.98
144.58	0.48	99.59	0.52	10.24	53.46	0.99
146.87	0.50	92.47	0.50	8.85	50.93	0.99
123.77	0.49	106	0.51	11.78	58.44	0.98
123.10	0.50	105.7	0.50	11.73	58.36	0.99
148.41	0.51	91.68	0.49	8.88	51.02	0.99

Tab. 9.4.: Fitting parameters of the TPF signal collected for a single particle after normalization at 5.17 mW average power.

Peak Intensity (a. u.)	a	τ_1 (s)	b	τ_2 (s)	τ_{avg} (s)	R^2
174.08	0.53	39.92	0.47	4.31	23.25	0.97
170.92	0.51	40.07	0.49	4.51	22.73	0.96
182.81	0.53	36.15	0.47	4.95	21.52	0.98
199.13	0.5	34.74	0.5	2.84	18.87	0.93
184.58	0.5	36.96	0.5	4.37	20.77	0.95
173.7	0.51	35.92	0.49	4.13	20.29	0.98
220.63	0.41	37.03	0.59	5.24	18.3	0.96
175.92	0.71	23.17	0.29	2.1	17.05	0.96
235.65	0.51	30	0.49	3.54	16.94	0.96
218.1	0.48	29.57	0.52	3.94	16.14	0.94

Tab. 9.5.: Fitting parameters of the TPF signal collected for a single particle after normalization at 9.40 mW average power.

Peak Intensity (a. u.)	a	τ_1 (s)	b	τ_2 (s)	τ_{avg} (s)	R^2
249.16	0.57	16.3	0.43	2.37	10.35	0.97
256.75	0.56	15.59	0.44	2.34	9.80	0.98
261.17	0.54	15.95	0.46	2.47	9.73	0.97
261.58	0.48	16.97	0.52	2.66	9.52	0.95
251.56	0.39	21.87	0.61	3.57	10.71	0.93
271.45	0.51	16.65	0.49	2.5	9.66	0.97
265.47	0.46	18.12	0.54	2.95	9.87	0.96
291.18	0.49	14.73	0.51	2.43	8.45	0.96
288.02	0.51	14.33	0.49	2.66	8.60	0.98
280.11	0.31	19.34	0.69	3.46	8.39	0.96

Tab. 9.6.: Fitting parameters of the TPF signal collected for a single particle after normalization at 14.10 mW average power.

9.2.1.4. Trapped multiple particles dynamics

Figure 9.4 shows the different or possible TPF signals for different trapping events. From figure 9.4a, it can be seen that when the particle is dragged towards the optical trap, there is a sudden rise in the signal, and then the signal immediately drops down to the baseline. There are two possibilities: ablation due to high peak power and unwanted species (dust particle/impurity) present in the sample

Peak Intensity (a. u.)	a	τ_1 (s)	b	τ_2 (s)	τ_{avg} (s)	R^2
322.46	0.66	4.52	0.34	0.5	3.15	0.98
322.46	0.42	6.16	0.58	1.06	3.22	0.93
334.82	0.63	4.79	0.37	0.4	3.18	0.96
321.07	0.67	4.71	0.33	0.56	3.35	0.98
334.52	0.61	4.91	0.39	0.58	3.23	0.97
358.46	0.58	4.71	0.42	0.36	2.9	0.95
322.45	0.74	4.04	0.26	0.18	3.02	0.95
359.22	0.65	4.24	0.35	0.34	2.88	0.98
332	0.61	4.31	0.39	0.52	2.82	0.97
327.07	0.5	5.34	0.5	0.86	3.1	0.97

Tab. 9.7.: Fitting parameters of the TPF signal collected for a single particle after normalization at 18.80 mW average power.

Peak Intensity (a. u.)	a	τ_1 (s)	b	τ_2 (s)	τ_{avg} (s)	R^2
358.08	0.66	4.52	0.34	0.5	3.15	0.98
380.32	0.42	6.16	0.58	1.06	3.22	0.93
413.33	0.63	4.79	0.37	0.4	3.18	0.96
361.42	0.67	4.71	0.33	0.56	3.35	0.98
384.63	0.61	4.91	0.39	0.58	3.23	0.97
395.45	0.58	4.71	0.42	0.36	2.9	0.95
406.98	0.74	4.04	0.26	0.18	3.02	0.95
379.21	0.65	4.24	0.35	0.34	2.88	0.98
341.48	0.61	4.31	0.39	0.52	2.82	0.97
387.05	0.5	5.34	0.5	0.86	3.1	0.97

Tab. 9.8.: Fitting parameters of the TPF signal collected for a single particle after normalization at 23.50 mW average power.

that collide with trapped particles inelastically and take particle out from the trap forcefully. Figure 9.4b shows the TPF signal, which represents that initially, one particle is dragged towards the trap center and then another particle, which can be traced by an immediate rise in the TPF signal. It is difficult to get the information about the particles whether the first particle is still confined or not. On the basis of rising in the TPF signal, it can be depicted that only one particle stays back. Since the height of the TPF signal approximately equals to the height

Power (mW)	Peak Intensity (a. u.)	$\tau_{avg}(s)$
5.17	139.45 ± 8.93	52.30 ± 3.52
9.40	193.55 ± 23.41	19.6 ± 2.50
14.10	267.65 ± 14.70	9.51 ± 0.79
18.80	333.45 ± 14.34	3.09 ± 0.17
23.50	380.79 ± 22.24	2.98 ± 0.24

Tab. 9.9.: Average fitting parameters of the TPF signal collected for a single particle after normalization at different average power.

of the TPF signal when the first particle is dragged and gets photo-bleached. So, the second particle stays back, but due to the non-uniform distribution of dye on top of the particle surface, it fluoresces more as compared to the first signal or possibility of the presence of both particles, but we cannot distinguish between them. A similar trend is observed in figure 9.4c where it is very difficult to say that whether the second particle is dragged into the optical trap or TPF signal gets enhanced by the existing particle due to the non-uniform coating at the surface. Figure 9.4d shows the multiple particle phenomena, however, getting information about the individual particle dynamics is very difficult. The particle gets photo-bleached, and the TPF signal decays while the particle is still trapped, and it is difficult to distinguish the multiple particle phenomena by the TPF signal alone. Thus, the analyzing trapping by TPF signal is not a good way to give concrete evidence for particle dynamics, so analysis by backscattered signal would be a better way.

9.2.2 Backscattered signal analysis

9.2.2.1. Backscattered profile

Figure 9.5 shows spatial backscattered snapshots of a particle confined in an optical trap where Figures 9.5a-b show the image and 2D intensity distribution of the backscattered signal. The region of interest (ROI; rectangular region of figure 9.5a) is chosen to take an average over pixel for normalized 1D intensity distribution, as shown in figure 9.5c; where black dots correspond to the experimental data and red line curve represents the Gaussian fit for each lobe. The center of the rectangular region (~ 15 pixel) chosen in Tracker software to analyze backscattered data.

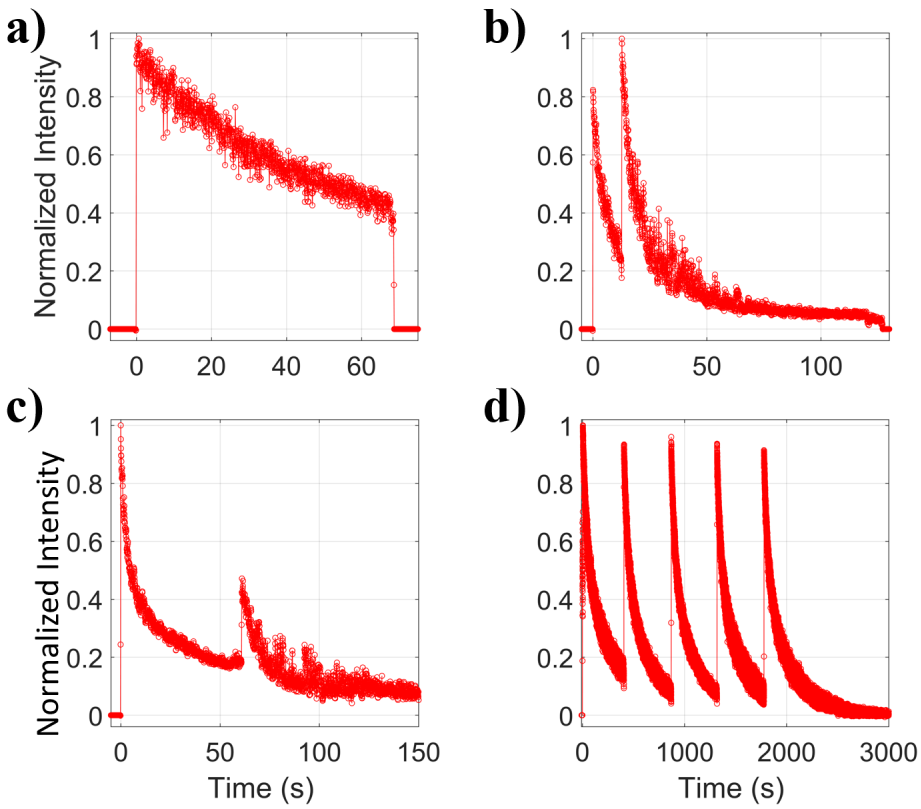

Fig. 9.4.: Plots of TPF signal from multiple or aggregated trapped particles at 18.80 mW average power.

The backscattered patterns are shown in figure 9.6, and it is observed that

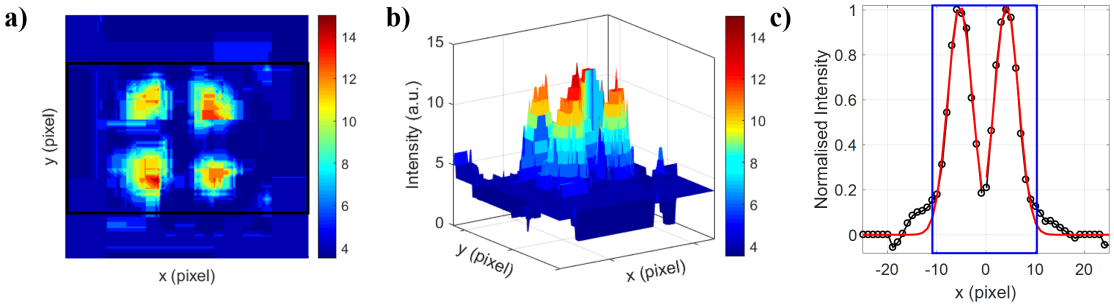

Fig. 9.5.: Plots of backscattered signal of the single particle inside the optical trap a) image b) 2D intensity distribution and c) normalized 1D intensity distribution (over the rectangular regime shown in a).

the pattern contains a quadrupole mode. When light interacts with a particle, multipolar modes are induced due to the interaction of electromagnetic field (asymmetric distribution of charge), which can be written as infinite series of spherical harmonics functions of electromagnetic scattering field. Depending on

the particle size and wavelength of the laser beam, the scattering pattern from the particle is dominated by different modes, so that it is different [134, 166, 167]. The occurrence of electric quadrupole moment [168] inside the dielectric particle is due to the dominance of quadrupole over a dipole and other modes, which occurs due to the simultaneous coherent excitation of the dipole and quadrupole moments. This phenomena can be observed in near field imaging, however, we are doing far field imaging for our experiments. So, this imaged quadrupole pattern arises in focused field depending on the orientation of the induced dipole with respect to the field polarization. In our case, incident laser beam is s-polarized, which is tightly focused with high NA objective onto the dielectric medium. The reflected light is collected through the same objective, which contains both s- and p- polarization components. The reflected light then passes through the dichroic mirror (FF670-SDi01-25x36, Semrock Inc, New York), which only transmit $\sim 2\%$ of the p-polarized light and block the s-polarized light for 800 nm wavelength. Therefore, the measured light is p-polarized, which corresponds to the pattern as shown in figure 3.20 in the reference [169]. The percentage of signal extracted determines the resolution of scattering pattern, where 1-2 % signal extraction leads to quadrupole scattering pattern as shown in figures 9.6a-b, 10 % signal leads to merging of lobes which results in a distorted pattern (figure 9.6c), and more than 10 % signal results in merging of all the four lobes that give rise to a circle along with diffraction rings (figure 9.6d). This is because when beamsplitter is used instead of dichroic mirror, both s- and p-polarized light will transmit and a pattern similar to figure 3.19 in the reference [169] is observed due to induced dipole with respect to the field polarization .

9.2.2.2. Backscattered signal analysis for coated particles

A sharp rise in the backscattered signal represents that the particle is trapped, and the height of the backscattered signal helps in determining the number of particles that have been trapped. So, first, we have rigorously studied the single-particle dynamics using backscattered signal. The backscattered signal is collected at different average power, and it is found that the trapping/confinement time of the particles changes with average power (table 9.10). Figure 9.7 represents the backscattered data of CW and pulsed excitation for coated particles, where black/blue curves correspond to CW/pulsed excitation at different average power. For pulsed excitation, the backscattered signal shows a sharp rise followed by a plateau region, afterward signal decays gradually, whereas under CW excitation

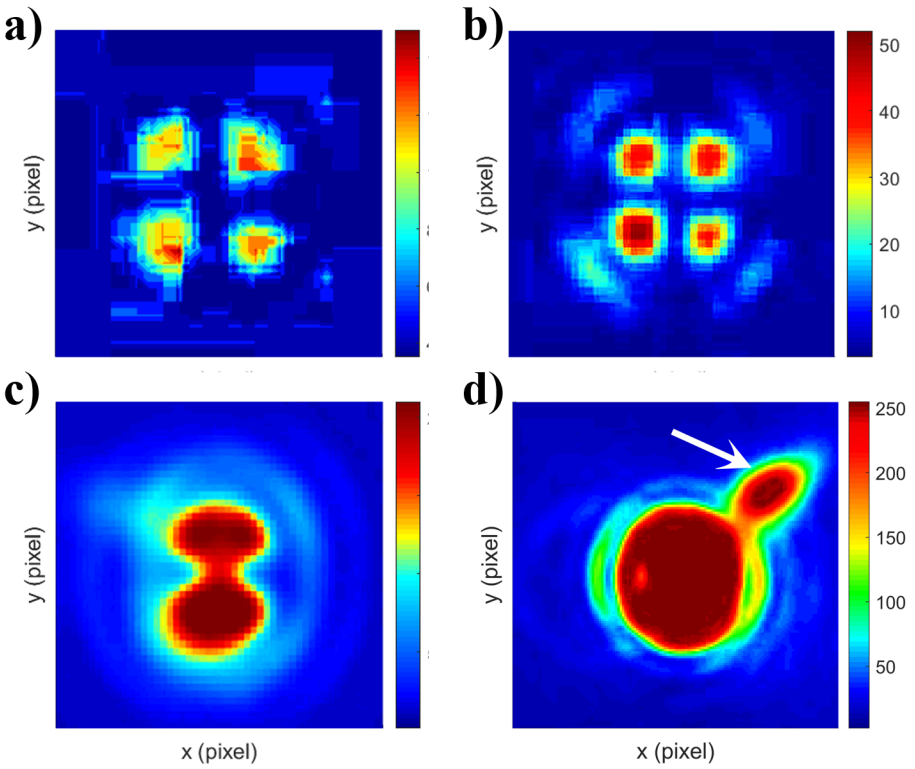

Fig. 9.6.: Plots of scattering pattern when a) single particle is inside the trap, b) two particles are inside the trap, c) single particle is present with approximately 10 percent of the total backscattered signal collected and d) single particle is present for approximately 30 percent of the backscattered signal collected. In (d) white arrow shows the diffraction pattern (image imperfection)

Power (mW)	Confinement time (s)
5.17	> 2300
9.40	786 ± 81.56
14.10	240 ± 10.52
18.80	103 ± 6.72
23.50	76.2 ± 3.52
28.20	57.49 ± 4.29
32.90	9.12 ± 1.41

Tab. 9.10.: List of confinement or trapping time of a single coated particles inside an optical trap at different average power under pulsed excitation.

backscattered signal gives just a plateau in the pulsed excitation time domain. Under pulsed excitation, the time range of the plateau region is decreasing with increasing average power, as shown in figure 9.8. It has been observed that

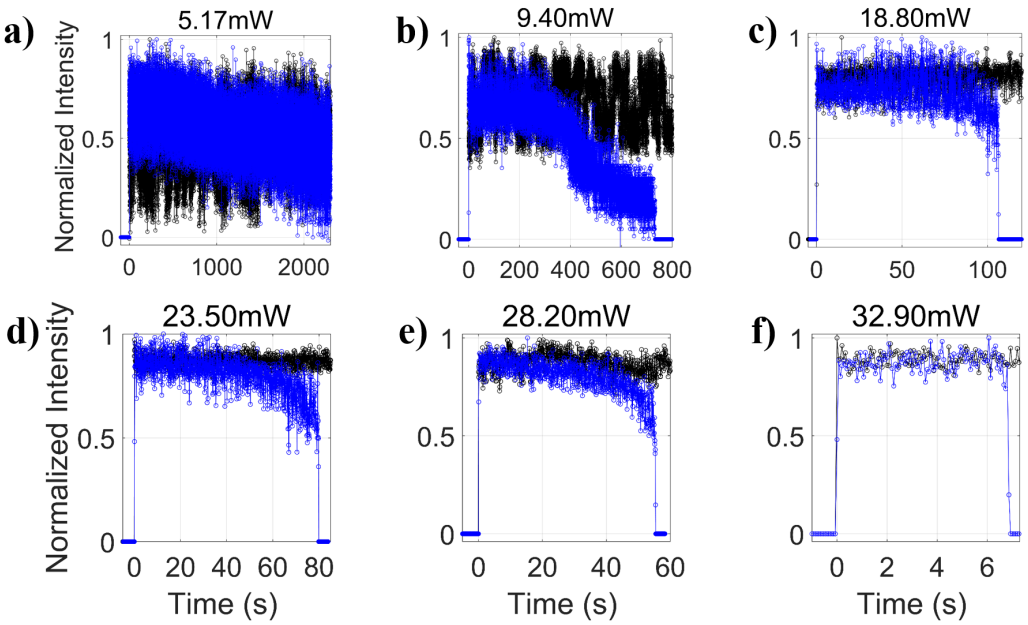

Fig. 9.7.: Plots of normalized backscattered signal of single particle over time under both CW and pulsed excitation at different average power.

fluctuations in the signal increase with time along both radial and axial directions owing to the asymmetric trap. Till now, it was assumed that the optical trapping potential is harmonic, but we have studied theoretically (in chapters 3 to 8) and experimentally that the trap potential is asymmetric, henceforth, the overall signal is decaying.

Table 9.10 shows the confinement time of a single particle within the optical trap for coated particles at the different average power. Here, the confinement time of the particle strongly dependent upon the asymmetricity of an optical trap, which is indirectly proportional to the average power of the trapping beam. So, it can be seen that confinement time for coated particles decreases with an increase in the average power as the asymmetricity of the trap is increasing, and the barrier to well depth height is decreasing.

Proposed model for single particle dynamics

In figure 9.9, we proposed a model for the behavior of a single particle in water confined by asymmetric potential. Here, the first row (figures 9.9a-c) is the experimental backscattered signal in different trapping time windows. Second and third rows are hypothetical models depicting asymmetric potential along the axial direction and 2D representation of optical trapping along radial as well as axial directions, respectively. Figures 9.9a, 9.9d, and 9.9g represent the

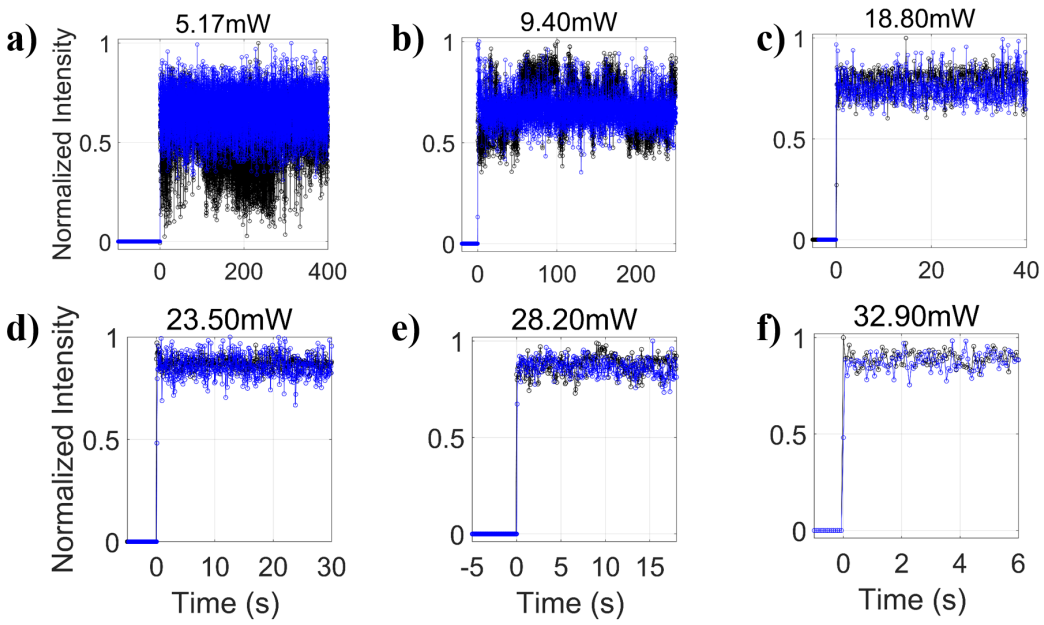

Fig. 9.8.: Plots of plateau region of normalized backscattered signal of single particle over time under both CW and pulsed excitation at different average power.

particle dragging; figures 9.9b, 9.9e and 9.9h show behavior of particle in initial time of trapping (when particle is trying to equilibrate inside the trap and starts fluctuating along radial and axial directions due to thermal kicks) as shown by green arrow in figure 9.9h. Afterward, the particle fluctuates slowly, and then fluctuations become faster due to the asymmetric nature of trap and particle experiences thermal kicks from the environment. Thus, at this point of discussion, we conjecture that the particle gets ejected from the trap following a particular trajectory shown in figure 9.9f as analyzed from the change in the backscattered signal pattern. The 2D representation of this ejection process is shown in figure 9.9i. To visualize the particle's motion inside the optical trap, we further analyze the backscattered signal from each lobe shown in figure 9.10a. It is observed that the intensity of the signal from each of these four lobes varies differently with time (figure 9.10b-e) compared with the overall intensity integrated over all the four lobes (figure 9.10f). At different time windows, the intensity of any two lobes may vary in a correlated or anti-correlated or un-correlated fashion (figure 9.10g-i). From this, we can say that while being trapped, the particle may have (harmonic) motion along with all possible radial directions inside the optical trap (figure 9.11a). To simplify the discussion, we have considered only the motion1 (M1) and motion2 (M2) and the phenomena exhibiting by these two motions can further replicate on the other motions. When the particle moves along M1, there is an intensity correlation between lobe 1 and lobe 4, but the other two (lobe

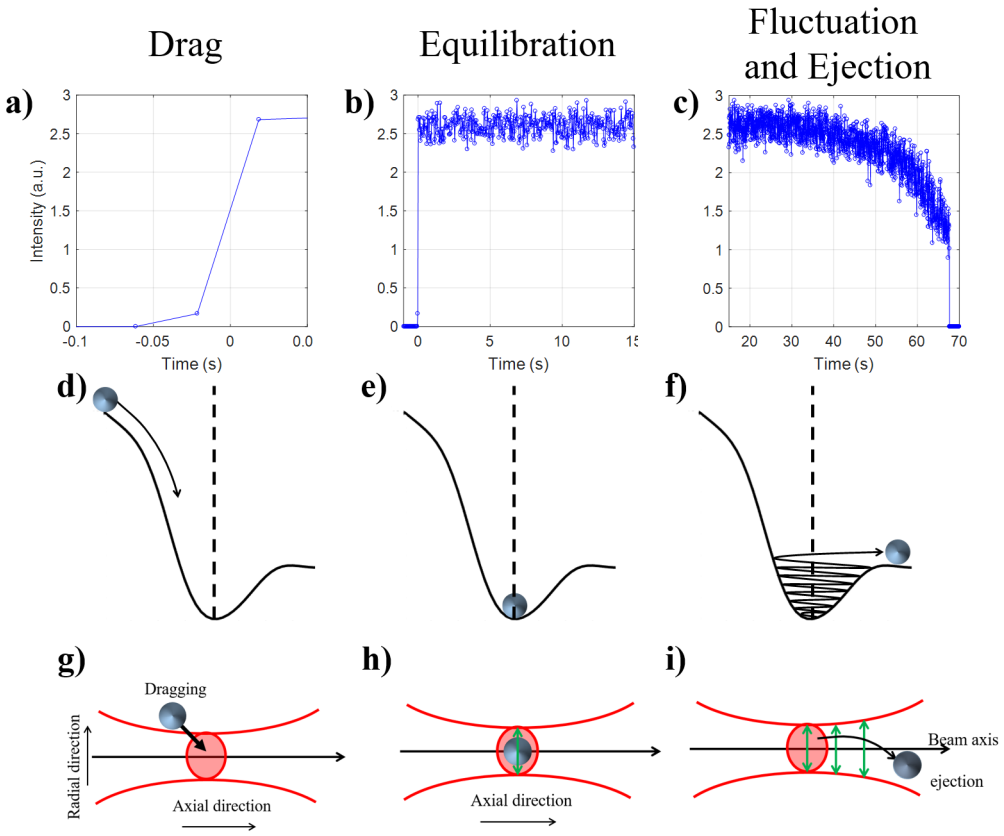

Fig. 9.9.: Top pannel: Plots of time traces of backscattered signal depicting significant sequential steps under pulsed excitation at 18.80 mW average power. Middle panel: A proposed model for trapping dynamics along axial direction depicting the sequential event. Bottom panel: A proposed model for 2D representation of trapping dynamics along axial and radial direction depicting the sequential event.

2 and lobe 3) lobes may or may not be correlated, as shown in figure 9.11b. A similar intensity correlation between lobe 1 and lobe 2 can be defined when the particle is along M2, as shown in figure 9.11c. The random motion comprises of four/three/two/one or no correlation among the lobes is shown in figures 9.10c-e.

9.2.2.3. Backscattered signal analysis for uncoated particles

The backscattered signals shown in figure 9.12 for single-particle confinement at different average power under pulsed excitation, where black/blue curves correspond to CW/pulsed excitation. It is observed that the trapping/confinement time changes with average power as shown in table 9.11.

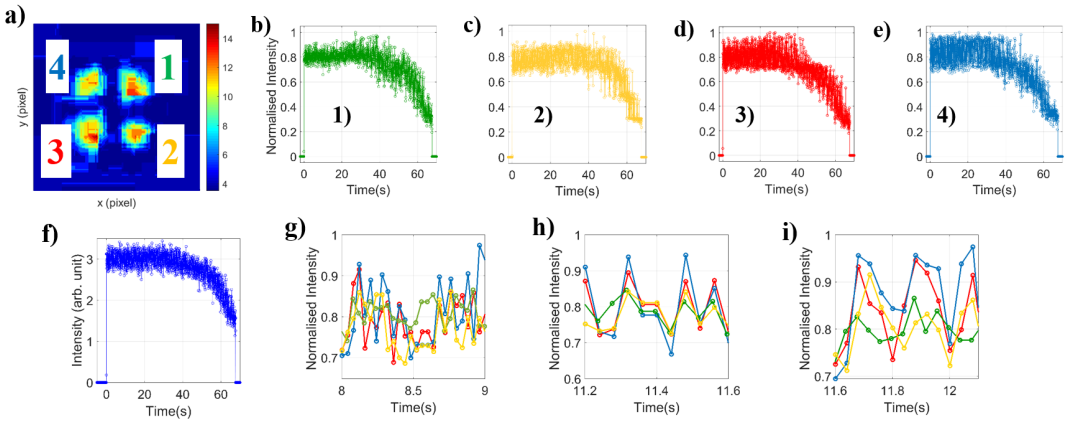

Fig. 9.10.: Image of backscattered from an optically trapped particle. b-e) Time traces of intensity of individual lobes of the scatter pattern (shown in figure a) and f) time trace of the integrated intensity of all four lobes (shown in figure a). g-i) zoomed-in time traces the intensity of individual lobes.

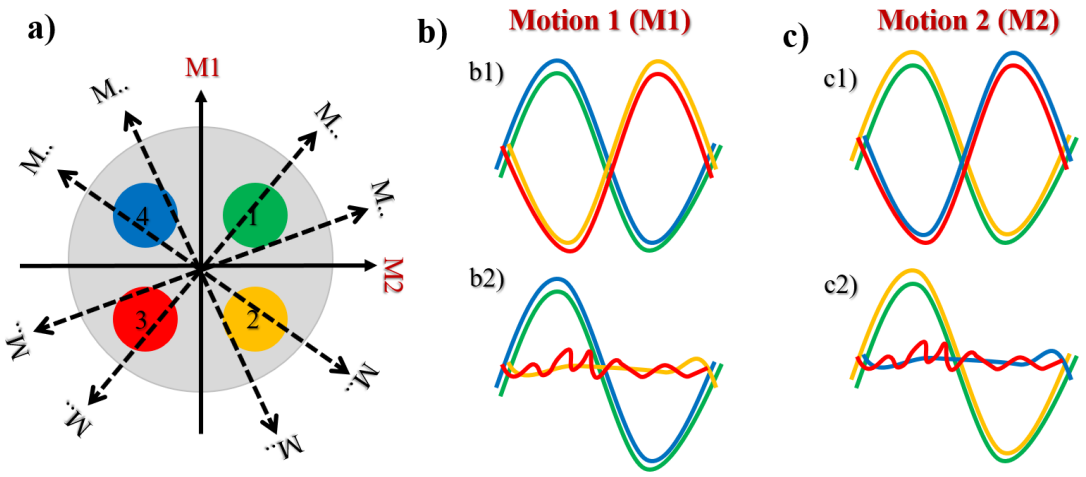

Fig. 9.11.: The schematic diagram for a single particle motion inside an asymmetric optical trap.

In the comparison of coated and uncoated particles, it can be seen that they behave similarly under CW excitation but differently under pulsed excitation. The most significant effect which can be observed under pulsed excitation is that confinement time for coated particles is less than the uncoated particles. This is because when the light is incident on a coated particle, the dye molecule absorbs, and the particle gets more heat accumulation than the uncoated particle. Thus, fluctuations are more in the case of coated particles than an uncoated particle, which results in decreasing the confinement time for coated particles under similar conditions. Since we did not observe any change in CW excitation,

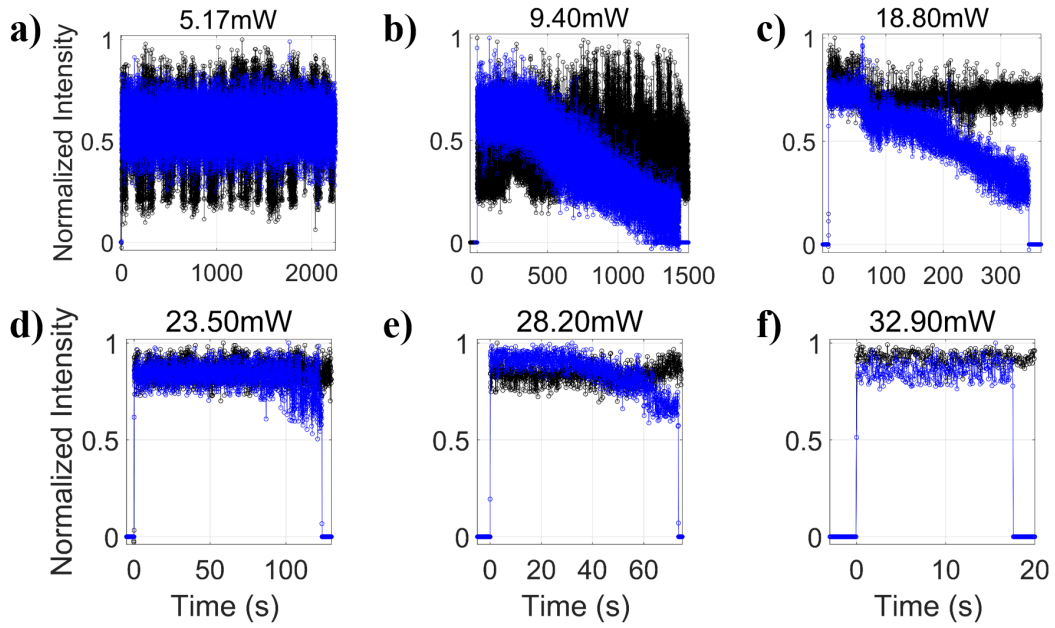

Fig. 9.12.: Plots of backscattered signal of uncoated single particle for normalized backscattered signal over time under pulsed and CW excitation at different average power.

Power (mW)	Confinement time (s)
5.17	> 2700
9.40	≈ 1413.93
14.10	765 ± 88.70
18.80	317 ± 22.7
23.50	128.0 ± 7.45
28.20	78.03 ± 5.29
32.90	16.9 ± 1.89

Tab. 9.11.: List of confinement or trapping time of a single uncoated particle inside an optical trap at different average power under pulsed excitation.

we discuss single and multiple particle dynamics inside the optical trap under pulsed excitation only.

Trap stiffness

The optical trap can be characterized in terms of the potential well by monitoring the displacement of trapped particles through the bright field transmitted images. The trap stiffness is calculated by using the following relation $k_{stiffness} = \frac{k_B T}{x^2}$; here x corresponds to MSD. To understand the detailed dynamics of a single

particle, trap stiffness calculations have been done at 5.14 mW average power under pulsed excitation, and signal has been collected at 100 fps in cropped mode. All the calculations have done for initial 36000-42000 frames when the particle is dragged within the focal volume. To calculate the trap stiffness, the exposure time plays an important role, as shown in figure 9.13, where red, blue, and black trap stiffness corresponds to the x-axis, y-axis, and radial direction respectively. At 100 fps, maximum exposure time is 10 ms, but the sensor requires a few μs (dead time) to relax; therefore, maximum exposure time can be given as 9.94 ms. The trap stiffness shows a sigmoidal curve with increasing exposure time. So, for getting accurate trap stiffness, we have to capture the dynamics with relevant exposure time because the MSD decreases with increasing exposure time by averaging over the particle's positions. For further analysis, we have chosen

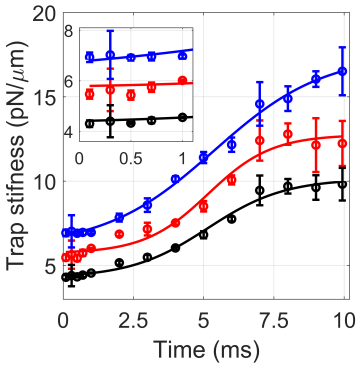

Fig. 9.13.: Plot of trap stiffness against exposure time of uncoated particle at 5.17 mW average power under pulsed excitation.

100 μs exposure time for capturing the fast dynamics of the particle by comparing the trap stiffness of CW and pulsed excitations at two different average power, as shown in table 9.12. It can be seen that the trap stiffness increases significantly with increasing average power and also depends upon the nature of the potential. As per the above discussion, pulsed excitation shows a stable trap at low average power as compared to higher while increasing power stabilizes the trap stiffnesses corresponding to the low power domain in the case of CW excitation. At low (5.17 mW) average power, CW and pulsed excitations show stable trapping implying approximately equal trap stiffness. However, CW excitation shows stable trapping at high average power as compared to pulsed excitation, which reveals that the particle is more stably confined in CW excitation. Therefore the motion of the particle is bounded within the limit, and average distance (moved by the particle) is less as compared to pulse excitation. If the MSD is less, then trap stiffness is more as shown in table 9.12. A slight change in trap stiffness along x- and y-axis

which might be due to asymmetry in the beam profile or slope/tilt in the sample stage.

Figures 9.14a and 9.14d show the trajectory of a single particle, figures 9.14b and

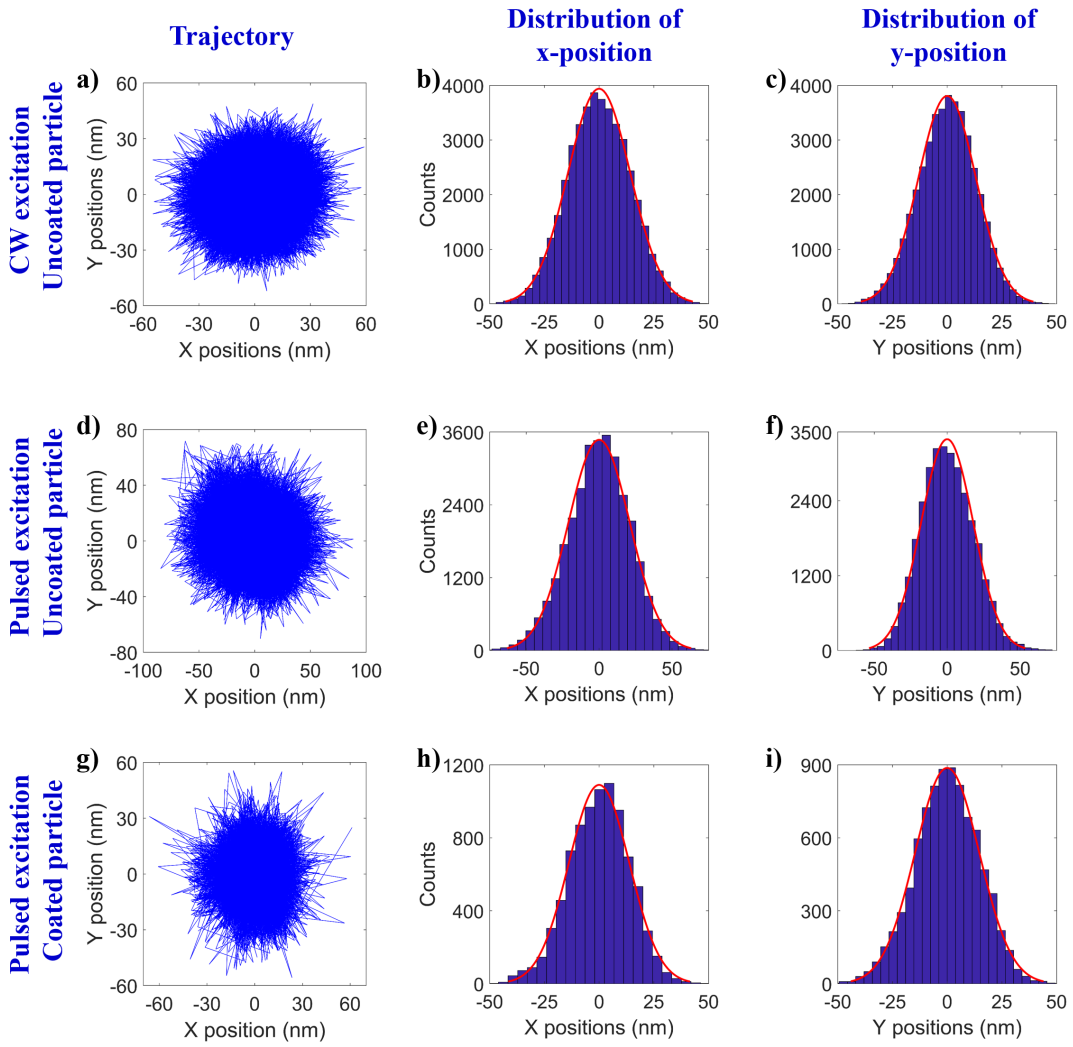

Fig. 9.14.: Plots of a) trajectory of a single uncoated particle, distribution along the b) x-axis and c) y-axis under CW excitation; d) trajectory of single uncoated particle; distribution of along the e) x-axis, and f) y-axis under pulsed excitation; g) trajectory of a single coated particle; distribution of coated particle along the h) x-axis, and i) y-axis under pulsed excitation at 18.80 mW average power respectively.

9.14c and 9.14e and 9.14f show the position distribution of particle along x- and y-axis where blue color corresponds to the experimental data and the red color is fitted to a normal distribution. Figure 8.2b shows the asymmetry in the radial beam profile, which results in an asymmetry in the trap stiffness values along the x- and y-axis. However, pulsed excitation shows more asymmetric as compared to CW excitation, because under pulsed excitation, nonlinear effects also contribute

which results in an increase in asymmetry along the radial direction.

Figures 9.14g-i show the trajectories and position distributions along the x-

Power (mW)	5.17 mW			18.80 mW		
$k_{stiffness}(pN/\mu m)$	k_x	k_y	k_r	k_x	k_y	k_r
CW excitation	5.59 ± 0.13	6.30 ± 0.05	4.18 ± 0.06	20.90 ± 1.55	25.95 ± 1.81	16.27 ± 1.12
Pulsed excitation	5.47 ± 0.18	6.93 ± 0.19	4.30 ± 0.13	9.01 ± 0.45	12.38 ± 0.31	7.28 ± 0.28

Tab. 9.12.: Trap stiffness ($k_{stiffness}$) for uncoated particles at different average power under CW and pulsed excitations.

and y-axis of the coated particle inside the optical trap. The total number of frames for a coated particle is less than an uncoated particle at similar average power. In the case of coated particles, the dye layer absorbs energy, which down-converts into heat, increasing the temperature of the local environment, which results in an increased thermal fluctuation of the trapped particles. However, the slow frame rate may not be able to capture the individual steps, which may create a false impression that the MSD is decreased (and hence the trap stiffness is increased) for coated particles. The trap stiffness k_x, k_y and k_r for coated particle are $21.91 \pm 3.26\ pN/\mu m$, $20.04 \pm 2.59\ pN/\mu m$ and $14.43 \pm 0.24\ pN/\mu m$ respectively, at 18.80 mW average power. A significant difference in the numerical values of trap stiffness (calculated for overall confinement time) for coated and uncoated particles is observed. Therefore, better temporal resolution is needed for measurements involving coated particles.

Quite interestingly, under pulsed excitation, the trap is more stable at low average power while increasing power stabilize the trap under CW excitation, as shown in figure 9.15. To estimate how the trap stiffness changes as the particle leave the trap, we measure trap stiffness from MSD over 20 sec time window (keeping 100 μs exposure time); this is shown in figure 9.15d (along with an exponential fit). Under pulsed excitation, the harmonic approximation is valid when the trapped particle is at the bottom of the potential well. As the particle leaves the trap, it experiences the more asymmetric part of the well, which is characterized by a lower trap stiffness due to a progressive change in curvature of the well.

9.2.2.4. Two particles dynamics

Figure 9.16 shows the backscattered signal pattern for two particles, where the first row corresponds to a contour plot captured by the CMOS camera when two particles are present inside the optical trap. It is noticeable that this pattern is changing over time, which can be inferred from the video microscopy. The second

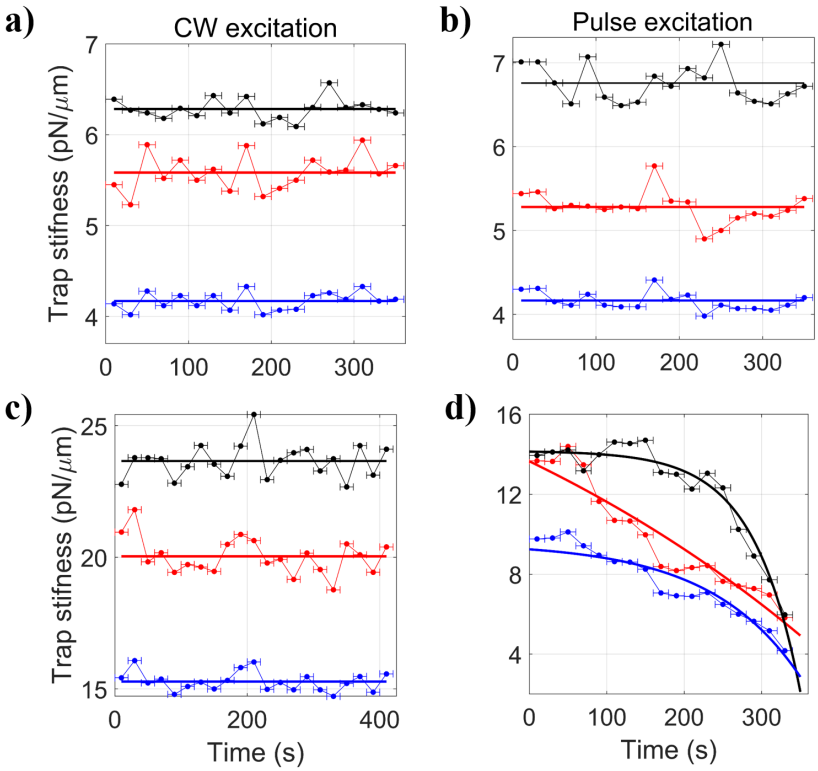

Fig. 9.15.: Plots of the evolution of trap stiffness evaluated at every 20 sec interval at 5.17 mW average power under a) CW and b) pulsed excitations and at 18.80 mW average power under c) CW and d) pulsed excitation. Color: Red/Blue/Black curves correspond to the trap stiffness along x-axis/y-axis/radial direction respectively.

row is a radial (top) view of the particle inside the optical trap with respect to the reference particle P1. The third row shows a hypothetical 3D representation of two particles inside the trap. The fourth row shows the different configurations of the two confined particles inside the asymmetric well. The first column represents the backscattered signal pattern in which one particle is residing in the trap, after that, the second particle is superimposing on the first, and this will make all the four lobes equally intense along with first-order diffraction ring. After superimposing on the first particle, the particle relaxes in all directions due to its internal and collisional degrees of freedom. The intensity of lobes will determine the overlapping region of two particles. This statement is confirmed by the proposed schema in the second, third, and fourth row. Figure 9.17a shows an overall backscattered signal for two particles confined in an optical trap where the trapping of the second particle gives an immediate rise in the signal. Figure 9.17b show the dragging of the second particle where one particle is already confined in the trap. For confining the second particle inside the trap, the residing particle

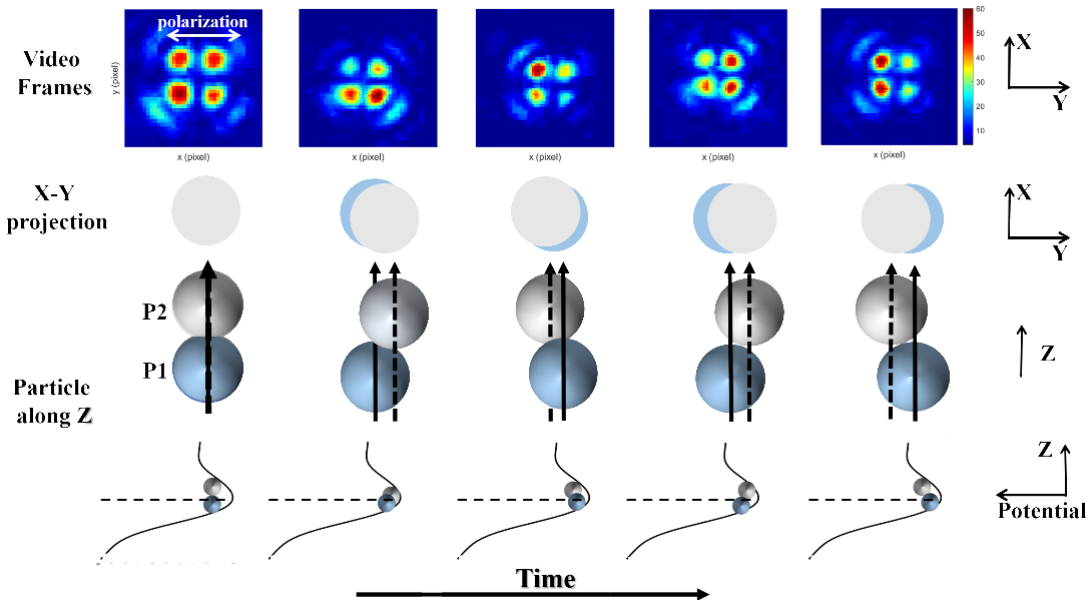

Fig. 9.16.: Plots of two-particle backscattered signal images (pattern) changing over time, where vertical solid and dotted arrow represents the particle axis of P1 and P2 particles respectively, and horizontal dotted arrow represent the z_0 under pulsed excitation at 18.80 mW average power. The first row is the scattering pattern captured while two-particle are trapped within the focal volume. The second row represents a hypothesis that represents the X-Y projection of trapped particles. The third row shows the axial alignment of these particles inside the focal volume. The fourth row represents the alignment of these particles inside the potential well.

has to shift its position inside the optical trap. Afterward, it can adjust itself in many possible configurations, as shown in figure 9.16. It is unlikely, both particles can go out from the trap due to the collisional degree of freedom, or the residing particle can go out from the trap and dragged particle stays there due to an elastic collision and vice versa. Figure 9.18 shows that the two particles backscattered

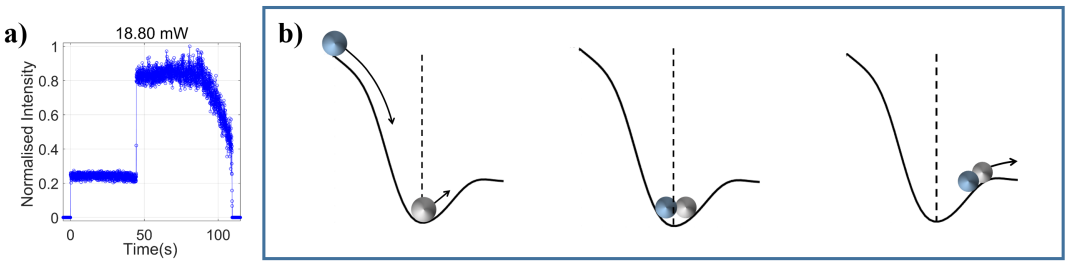

Fig. 9.17.: The plot of the backscattered signal (integrated for all four lobes) during trapping of two particles under pulsed excitation; a) at 18.80 mW, b) a proposed model when the second particle is dragged inside the focal volume while one particle is already confined within the focal volume.

signal at different average power, and it can be seen that confinement time for particles inside the trap decreases with increasing average power. This is strongly dependent upon the barrier to well depth height of the potential well, which decreases with the average power within this limit; consequently, there is a decrease in the residing time inside the trap. For similar average power, the

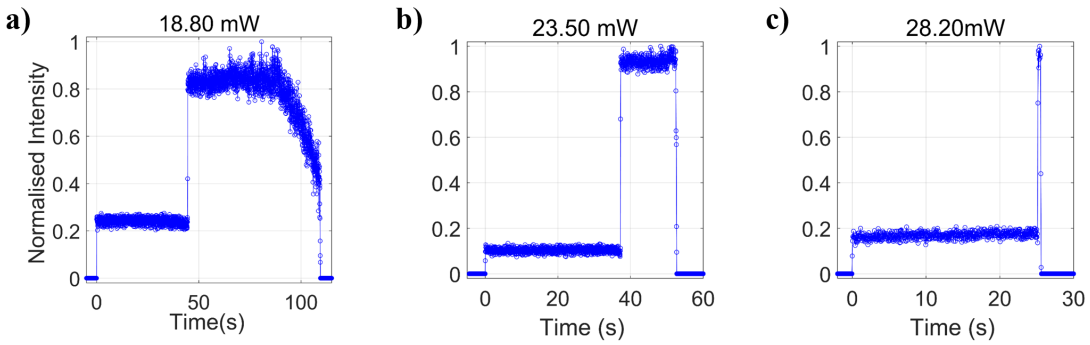

Fig. 9.18.: Plots of backscattered signal (integrated for all four lobes) during trapping of two particles under pulsed excitation; a) at 18.80 mW, b) at 23.50 mW, and c) at 28.20 mW average powers.

arrival time of dragging the second particle within the focal volume also matters. For example, if the second particle is dragged when the first particle is about to leave the trap, the existing particle needs tiny momentum to escape from the trap, henceforth, when the second particle is dragged within the focal volume, the first particle gets a momentum kick and escapes the trap due to collision with the first particle and the second particle stays back as shown in figure 9.19a. If the second particle comes earlier, then the confinement time of the second particle will depend on the barrier to well depth height. If the barrier to well depth height is higher than the required well depth height to stay two particles inside the trap, then these particles will stay for longer, as shown in figure 9.18. If escape potential is not enough to sustain two particles, then the second particle is dragged or trapped inside the optical trap and tries to stabilize. However, due to inelastic collisions with the residing particle and the surrounding molecules, the particle crosses the barrier of the asymmetric potential, resulting in both particles leaving the trap, as shown in figure 9.19b. But there might be a possibility that instead of two particles, only one will cross the barrier and another stays back as shown in figure 9.19c.

The dynamics of two particles inside the trap involve a collision between the particles and surrounding molecules. To understand the dynamics, we analyze the backscattered signal, as shown in figure 9.20a (image), and figures 9.20b

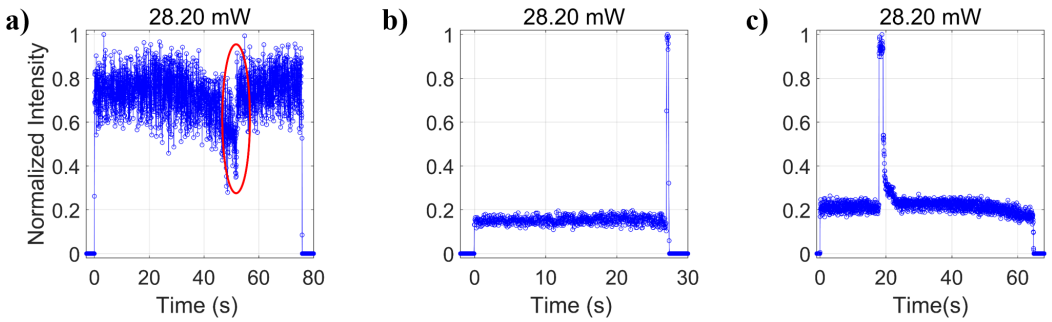

Fig. 9.19.: Plots of backscattered signal (integrated over all four lobes) during trapping of two particles under pulsed excitation a) the Second particle is dragged when the first particle is about to leave so due to the collision, one is retained and other leaves the trap, b) the second particle is dragged when particle is settled at equilibrium position and start leaving the trap but after collision both went out and c) the second particle is dragged after first, because of small escape potential, two-particle cannot stay together, so one is ejected at 28.20 mW average power.

to 9.20e show the individual time trace signal of all the four lobes marked in the figure 9.20a. It can be observed that all four lobes have different decay for the signal of the second particle. Decay signal of lobes 1 and 3 looks similar showing oscillatory nature, and that of lobes 2 and 4 looks similar, which reveals that there is some correlation between the lobes. Figure 9.20f shows the total backscattered signal (integrated over all four lobes), and the decay observed in this case is similar to that of lobes 2 and 4. This is because lobes 1 and 3 are anti-correlated to each other, which results in the canceling of their contribution to the total backscattered signal. This correlation behavior of the two sets of the lobes is further illustrated by zoomed time traced windows shown in figures 9.20g-j, where figure 9.20g shows the time window for lobes 1 and 3 which are anti-correlated while figure 9.20h shows that lobes 2 and 4 does not correlate with the same time window. However, in subsequent time windows, the lobes 1, 3 and lobes 2, 4 become anti-correlated to each other, as shown in figures 9.20i-j. Thus, it is observed that decay in lobes 1 and 3 are anti-correlated, while lobes 2 and 4 have a random correlation in different time windows of trapping time. Similarly, when we analyze the complete signal in small steps of duration, either lobes 1, 2 are correlated, or both are anti-correlated with the lobe 3 or all four, three or just two could be correlated. In the case of multiple particles, the collisional degree of freedom is more, and the force experienced by the individual particles might be different due to the temperature gradient. Therefore, the occurrence of a collision between the particles might be inelastic or elastic, depending on the cumulative

energy gained by each particle. Accordingly, the trajectory of the particle gets changed. Eventually, both particles leave the trap. One of the particles, which is away from the potential minimum, exhibits large amplitude motion while being trapped, modulating the intensity of the individual lobes of the backscattered pattern. Just like the single particle, the motion of two particles can give rise to correlated/anti-correlated/un-correlated intensity fluctuations between the lobe-pairs.

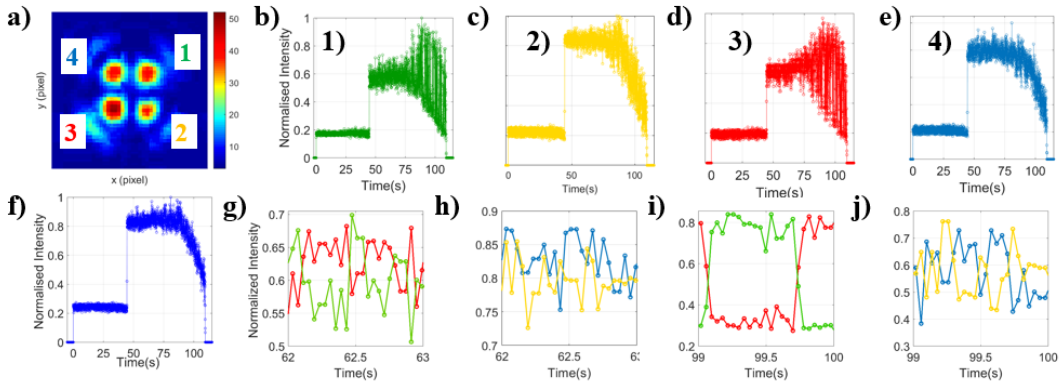

Fig. 9.20.: a) Image of backscattered from an optically trapped two particles at 18.8mW average power under pulsed excitation. b-e) Time traces of intensity of individual lobe of the scatter pattern (shown in figure a) and f) time trace of the integrated intensity of all four lobes (shown in figure a). Time traces for g) time window where lobes 1 & 3 are anti-correlated, h) same time window of g where lobes 2 & 4 do not correlate; i) another time window where lobes 1 & 3 are anti-correlated; j) lobes 2 & 4 are anti-correlated, but both do not correlate. Color: blue/green/yellow/red/light blue corresponds to the backscattered all four lobes/ lobe1/lobe2/lobe3/lobe4 respectively.

9.2.2.5. Multiple particles dynamics

Figure 9.21a shows the backscattered signal (integrated over four lobes) for multiple particles trapping at 18.80 mW average power under pulsed excitation. We observed that more than two particles could not stay inside the optical trap due to asymmetric potential boundary conditions created by a trapping beam due to certain limitations on escape potential. These conditions are different for different average power, such as at high average power, only one particle can stay, as discussed above. The circles in figure 9.21a represent a kink (signal decreasing followed by immediate rise) in the backscattered signal, which can be explained by the corresponding proposed model shown in figure 9.21b. The proposed model shows that the incoming particle collides with the two existing

particles and eject one of them. Eventually, both particles go out from the trap, which results in an immediate drop in the backscattered signal. However, in general, the incoming particle collides with existing particles that will result in the ejection of any one/two/all particle(s) depending on the elastic or inelastic collision between particles and the average power of trapping beam. As average power increases, asymmetricity also increases; hence, escape potential height decreases, so higher the average power lesser will be the probability of finding particle(s) in the trap. For example, another possible case can be seen in figure 9.21c, which shows the backscattered (integrated over all four lobes) signal for multiple particles trapping at 28.20 mW average power under pulsed excitation. This backscattered signal can be well explained by the proposed model, as shown in figure 9.21d. The model shows that initially, one particle is dragged, which results in a rise in the signal, but after some time, another particle is dragged, interestingly due to collision, second dragged particle is kicked out from the trap. Later the third particle is dragged while the second dragged particle is in an equilibrium position. When the third particle interacts with any of the existing two particles, it starts collision with either one of them or both the particles, for getting stable trapping, but due to limited focal volume, both the particles go out from the trap. Therefore, the corresponding scattering signal is dropped immediately.

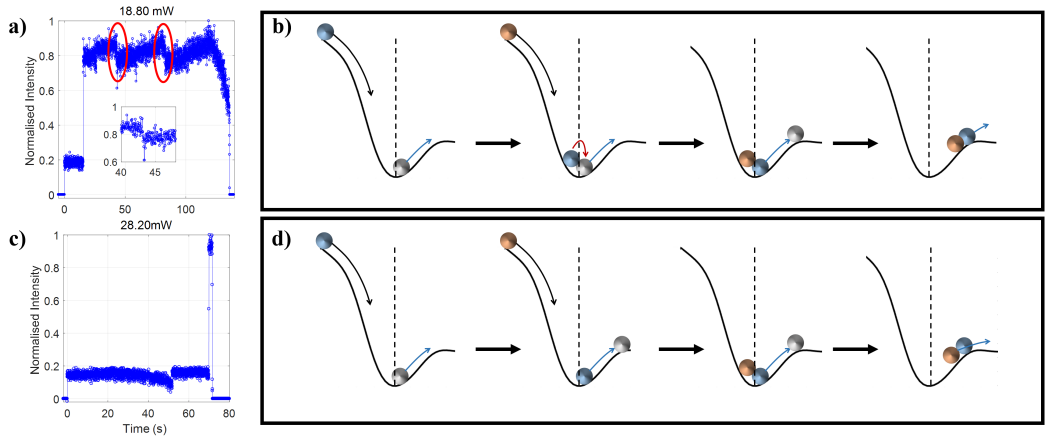

Fig. 9.21.: Dynamics of trapping of multiple particles under pulsed excitation: a) backscattered (integrated over all four lobes) at 18.80 mW average power, b) proposed model corresponding to a; c) backscattered signal (integrated for all four lobes) at 28.20 mW average power; d) proposed model corresponding to c.

9.3 Probing dynamics through simultaneous detection of TPF and backscattered signals

Earlier, we have discussed the dynamics of 1 μm coated and uncoated polystyrene particles using wide-field microscopy. It is observed that to get the complete information about particle dynamics, the TPF signal alone is inadequate since the particle gets photo-bleached while trapping. So, it is difficult to predict whether the particle is still confined or not. When the second particle is dragged into the optical trap, either the first particle is already photo-bleached or started getting bleached. Therefore, it is very difficult to get information from the height of the TPF signal. To get the complete information about two-particle dynamics by TPF detection alone is difficult since we are not able to get any information about a single particle from the TPF signal alone. Sometimes, it is quite possible that instead of the particle, some other impurity or dust particle has been trapped, which significantly increases the backscattered signal. In this case, the TPF signal can act as a trigger to identify whether the particle is trapped or any unwanted impurity. Also, using wide-field microscopy, the overall motion of the particle can be broken down into four major events: 1) drag, 2) equilibration, 3) (thermal) fluctuation and 4) ejection, where the first and the last steps are not well time-resolved (limited by frames per second (fps) of the video recording). To confirm the dynamics of a single particle, we have repeated the same experiment using PMTs to time-resolve the faster dynamics. We observe the rise (due to drag), followed by a quick decay of the backscattered signal, which was not captured by the camera. Since a confocal aperture was used, this decay may be attributed to some fast movement of the particle along axial direction; so, we call this motion adjustment.

9.3.1 Optimization of plane for stable trapping

To analyze the dynamics of the single trapped particle, first, we require the optimization of the focal plane for trapping the particle. Figure 9.22 shows the schematic diagram for different planes and corresponding backscattered and TPF signals at 18.80 mW average power under pulsed excitation shown in figure 9.23; where blue and red curves correspond to backscattered and TPF signals respectively. Here, we consider plane 0 as a reference in which backscattered signal from the glass substrate is maximum. Since we are using a manual translation stage of minimum precision $\sim$ 10 μm, the exact gap between one

plane and another is $\sim$ 10 μm. The fraction of light backscattered from the glass substrate reduces as the beam focus moves inside the sample. Therefore, an increase in transmitted light results in a decrease in the peak intensity of the backscattered signal (as well as TPF signal, most likely due to increased photo-bleaching) when the particle is dragged within the optical trap. This movement of beam focus within the sample also reduces the interfacial interactions of the microsphere with the glass substrate, and stable trapping is observed (confinement time increases for a single particle). Table 9.13 lists all the parameters such as confinement time, backscattered/TPF signal peak intensity, and the average lifetime of TPF signal for different planes. The optical trap stabilizes after a certain limit if the beam focus moves further inside the sample. Wherefore, the optical trap first stabilizes then destabilizes as beam focus moves inside the sample. Thus, we have determined that stable trapping occurs in plane 4 because confinement time for a single particle inside the asymmetric potential well is more. This optimization holds for different average powers as well. Conclusively, to get stable trapping, beam focus should be inside the sample of the order of few tens of micrometers from the glass surface. Quantitatively, it should be $\sim$ 50 μm above the glass cover-slip plane. Hereafter all the analysis are done for plane 4.

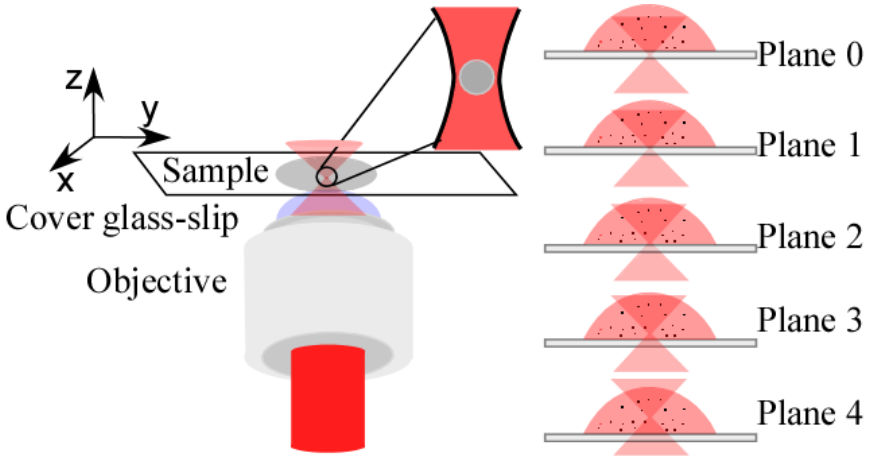

Fig. 9.22.: The schematic diagram for trapping the single particle in a different plane.

9.3.2 Moving-averaging analysis of backscattered and TPF signals for single particle confinement

Figure 9.24 shows the backscattered and TPF signals at 18.80 mW average power under pulsed excitation, where figure 9.24a shows the raw data and figures 9.24b-c show the 50-pt, 100-pt, and 150-pt moving-averaging of raw data. The

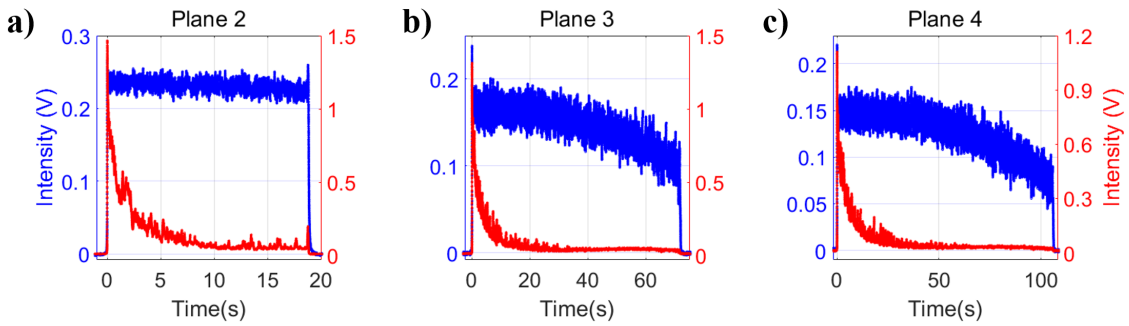

Fig. 9.23.: Plots of 50-pt moving-averaging of raw data for backscattered and TPF signals for single particle against real-time a) plane 2, b) plane 3, and c) plane 4 at 18.80 mW average power under pulsed excitation.

Plane	Confinement time (s)	Maxima of backscattered signal (a. u.)	τ_{avg} of two exponential (s)	τ_{avg} of three exponential (s)	Maxima of TPF signal (a. u.)
2	22.35 ±5.47	0.40 ±0.04	0.83 ±0.09	0.99 ±0.09	1.93 ±0.04
3	65.20 ±3.40	0.38 ±0.04	1.43 ±0.21	1.58 ±0.23	1.68 ±0.07
4	102.47 ±23.91	0.33 ±0.04	3.09 ±1.15	3.13 ±0.86	1.29 ±0.19

Tab. 9.13.: For different plane : confinement time, average lifetime, maximum of backscattered and TPF signals at 18.80 mW average power under pulsed excitation.

moving-averaging method is used to get information from noisy data. Tables 9.14 and 9.15 show the average lifetime of TPF signal at different average power under pulsed excitation. The particle gets photo-bleached faster with an increase in average power, thence, average lifetime decreases. A similar trend is observed for 50-pt, 100-pt, and 150-pt moving-averaging of raw data. However, at fixed average power, the average lifetime of the TPF signal increases with an increase in the number of raw data points for moving-averaging. Inevitably, an increasing number of data points for moving-averaging results in losing the information about the system. The same trend is observed for three exponential fittings. The fitting equation for two and three exponentials are:

$$Ae^{-\frac{t}{\tau_1}} + Be^{-\frac{t}{\tau_2}} + const \tag{9.2}$$

$$Ae^{-\frac{t}{\tau_1}} + Be^{-\frac{t}{\tau_2}} + Ce^{-\frac{t}{\tau_3}} + const \tag{9.3}$$

by using constraint for two exponential is $A+B+const = 1$, and three exponential is $A + B + C + const = 1$. Thus, all the plots shown for 50-pt moving-averaging,

and analysis is done for raw data.

Power (mW)	Two exponential (τ_{avg}): Average lifetime (s)			
	Raw data	50-pt mov-avg	100-pt mov-avg	150-pt mov-avg
9.40	9.95 ± 4.22	13.45 ± 5.68	14.61 ± 6.23	15.36 ± 6.59
14.10	5.62 ± 1.56	7.33 ± 1.67	8.28 ± 1.92	9.05 ± 2.07
18.80	3.09 ± 1.15	3.97 ± 1.51	4.50 ± 1.64	4.85 ± 1.87
23.50	1.17 ± 0.06	1.66 ± 0.14	1.92 ± 0.21	2.08 ± 0.21
28.20	0.76 ± 0.04	1.08 ± 0.05	1.24 ± 0.05	1.32 ± 0.04
31.96	0.42 ± 0.05	0.64 ± 0.09	0.80 ± 0.19	0.88 ± 0.22

Tab. 9.14.: Average lifetime of TPF signal at different average power for raw data, 50-pt, 100-pt, and 150-pt moving-averaging (mov-avg) of raw data using two exponential fitting.

Power (mW)	Three exponential (τ_{avg}): Average lifetime (s)			
	Raw data	50-pt mov-avg	100-pt mov-avg	150-pt mov-avg
9.40	11.61 ± 4.66	14.75 ± 5.83	15.60 ± 6.26	16.22 ± 6.59
14.10	7.27 ± 1.02	8.66 ± 1.18	9.64 ± 1.25	10.30 ± 1.27
18.80	3.13 ± 0.86	4.38 ± 1.69	4.86 ± 2.04	5.17 ± 2.21
23.50	1.27 ± 0.05	1.74 ± 0.06	1.96 ± 0.08	2.09 ± 0.08
28.20	0.83 ± 0.04	1.20 ± 0.13	1.38 ± 0.16	1.47 ± 0.13
31.96	0.56 ± 0.13	0.81 ± 0.19	0.95 ± 0.21	0.97 ± 0.20

Tab. 9.15.: Average lifetime of TPF signal at different average power for raw data using three exponential fitting.

Power (mW)	Two exponential (τ_{avg} (s))				
	A	τ_1	B	τ_2	Const
9.40	0.40 ± 0.07	23.13 ± 7.95	0.59 ± 0.08	0.39 ± 0.25	0.014 ± 0.016
14.10	0.42 ± 0.08	13.29 ± 3.28	0.56 ± 0.08	0.07 ± 0.038	0.017 ± 0.0037
18.80	0.45 ± 0.03	6.70 ± 2.75	0.53 ± 0.03	0.06 ± 0.056	0.018 ± 0.0029
23.50	0.41 ± 0.03	2.74 ± 0.27	0.57 ± 0.03	0.022 ± 0.009	0.019 ± 0.0039
28.20	0.43 ± 0.02	1.71 ± 0.17	0.55 ± 0.02	0.016 ± 0.004	0.019 ± 0.0030
31.96	0.39 ± 0.02	1.02 ± 0.17	0.57 ± 0.03	0.014 ± 0.003	0.038 ± 0.016

Tab. 9.16.: Fitting parameters for TPF signal at different average power for raw data using two exponential fitting.

Power (mW)	Three exponential ($\tau_{avg}(s)$)						
	A	τ_1	B	τ_2	C	τ_3	Const
9.40	0.23 ± 0.09	41.09 ± 9.91	0.35 ± 0.06	5.62 ± 2.13	0.41 ± 0.04	0.0256 ± 0.0154	0.0084 ± 0.0122
14.10	0.28 ± 0.05	22.28 ± 4.68	0.28 ± 0.04	3.94 ± 1.39	0.43 ± 0.02	0.0204 ± 0.0060	0.0114 ± 0.0011
18.80	0.26 ± 0.06	9.72 ± 2.26	0.31 ± 0.06	1.89 ± 0.61	0.42 ± 0.04	0.0153 ± 0.0066	0.0139 ± 0.0027
23.50	0.26 ± 0.09	4.20 ± 0.76	0.27 ± 0.08	0.78 ± 0.44	0.46 ± 0.03	0.0093 ± 0.0028	0.0162 ± 0.0017
28.20	0.22 ± 0.07	2.89 ± 0.66	0.29 ± 0.07	0.68 ± 0.27	0.47 ± 0.04	0.0088 ± 0.0023	0.0161 ± 0.0019
31.96	0.28 ± 0.07	1.85 ± 0.69	0.24 ± 0.06	0.30 ± 0.17	0.47 ± 0.06	0.0076 ± 0.0021	0.0160 ± 0.0193

Tab. 9.17.: Fitting parameters for TPF signal at different average power for raw data using three exponential fitting.

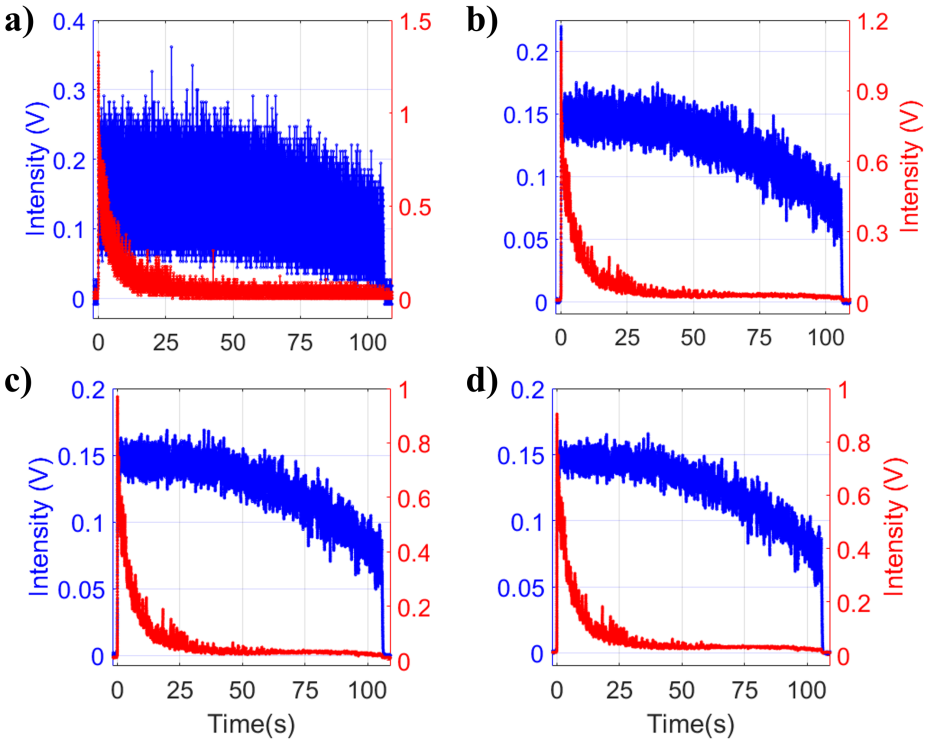

Fig. 9.24.: Plots of backscattered and TPF signals for single-particle against real-time a) raw data, b) 50-point moving-averaging, c) 100-point moving-averaging, and d) 150-point moving-averaging of raw data at 18.80 mW average power under pulsed excitation. Color: blue and red correspond to backscattered and TPF signals, respectively.

9.3.3 Backscattered and TPF signal analysis for single particle dynamics

When the particle is dragged to the optical trap, an immediate rise is obtained in both TPF and backscattered signals, followed by a decay. This decay is a continuous process in the TPF signal due to photo-bleaching of dye molecule on the surface of the trapped particle, whereas in backscattered signal decays

followed by a plateau in which the first particle tries to adjust itself at the bottom of the potential well or equilibrium position. In the TPF signal, sudden rise followed by the decay contains drag and adjustment time information of the trapped particle along with the rising and decaying time of fluorescent dye molecule surrounded at the surface of the trapped particle. The deconvolution of drag and rising, adjustment, and decaying time signals is very difficult because we do not have enough information about the dye molecules surrounded on the surface of the particle. However, after a certain time when the particle gets photo-bleached, a residual fluorescence signal is present. Although the residual fluorescence signal is very less and difficult to get information from raw data, it stays until the particle is confined within the optical trap. The information of the residual signal can be gathered by moving-averaging of raw data, and it is observed that residual signal increases with an increase in average power quantitatively, as can be seen from tables 9.16 and 9.17. Since the particle gets photo-bleached during trapping, it is difficult to get information whether the particle is still in the trap or went out from the trap from the height of the TPF signal after a certain time, as shown in figure 9.25. TPF signal decays very fast due to photo-bleaching; consequently, determining the dynamics of the trapped particle through the TPF signal alone is very difficult. Therefore, simultaneous detection of backscattered and TPF signals is necessary to assess the dynamics of the trapped particle. Hereafter, all the analysis under pulsed excitation has been done through simultaneous detection for backscattered and TPF signals, to determine the dynamics of a single particle. Figure 9.25a shows the TPF signal for a single trapped particle against real-time. Figure 9.25b showed the maxima

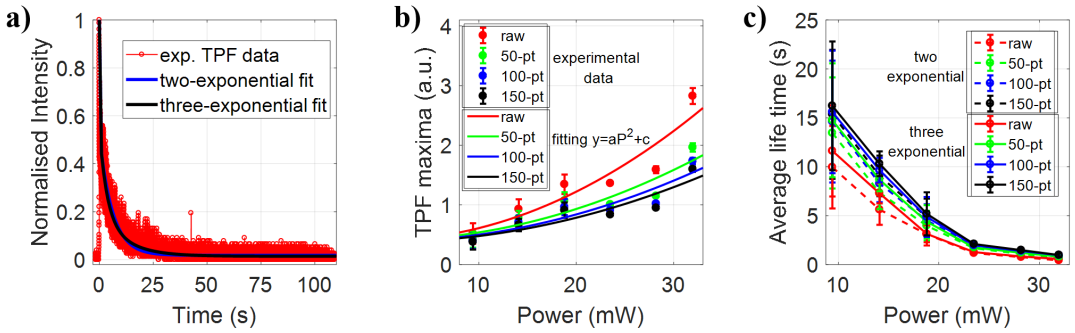

Fig. 9.25.: Plots of a) TPF signal over time for single-particle under pulsed excitation, b) maximum value of TPF signal when the particle is dragged to the optical trap against average power, and c) average fluorescence lifetime against average power for trapped particle.

of the TPF signal against average power when the particle dragged within the

optical trap. It can be observed that TPF maxima increase with an increase in average power. The fitting slopes 0.00204, 0.00131, 0.00113, and 0.001025 correspond to raw data, 50-pt, 100-pt, and 150-pt moving-averaging of raw data, respectively. Noticeably, deviation in the slope also increases with an increase in the number of raw data points for moving-averaging. Figure 9.25c shows the average lifetime (overall time constant) of the TPF signal for both two and three exponential fits against average power. The overall time constant decreases while intensity increases with an increase in average power as the maximum intensity of the TPF signal is proportional to average power. Consequently, the process of photo-bleaching in TPF occurs faster at high average power, which results in decreasing the overall time constant and increasing the peak intensity. For fixed average power, the overall time constant for the TPF signal increases while intensity maxima decrease with the increase in the number of raw data points for moving-averaging. Thus, an increasing number of data points for the moving-averaging results in losing the original information about the system can be seen from figures 9.25b and 9.25c.

Figures 9.26 shows the confinement of a single particle, confined by an asym-

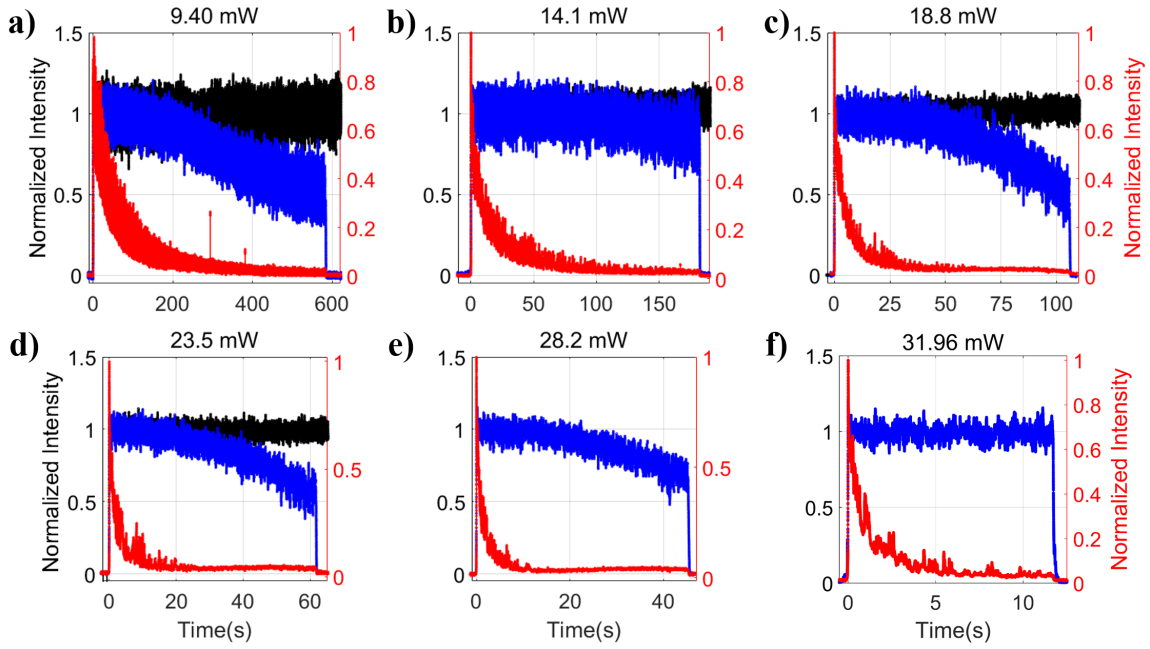

Fig. 9.26.: Plots of 50-point moving-averaging of raw data for backscattered (under both CW and pulsed excitation) and TPF (under pulsed excitation) signals for single-particle against real-time a) 9.40 mW, b) 14.10 mW, c) 18.80 mW, d) 23.50 mW, e) 28.20 mW, and f) 31.96 mW average power.

metric potential well at different average power under both CW and pulsed excitation. Under CW excitation, we are limited by the average output power;

hence, data is shown till 23.50 mW average power. Under CW excitation, the only backscattered signal is determined, whereas both backscattered and TPF signals are obtained under pulsed excitation because nonlinear effects are prominent. With increasing average power, confinement time for particle decreases, and eventually trap becomes unbound at high average power. Therefore, the particle cannot be trapped. At low (5.14 mW) average power, particle stays for more than half an hour under both CW and pulsed excitation, quantitatively listed in table 9.18. The confinement time of the single-particle strongly depends upon the average power and wavelength of the trapping beam. With an increase in the average power, asymmetricity of the optical trap increases due to the dominance of scattering force over gradient force under pulsed excitation. The asymmetricity of the potential well is more under pulsed excitation than CW excitation. Because under CW excitation, the nonlinear effect does not contribute significantly due to less average power. Therefore, increasing average power leads to a monotonic increase in both absolute potential and escape potential. The wavelength of the trapping beam also plays an important role, whether the wavelength we are using is resonant or non-resonant. In the case of resonant, thermal effects are prominent under CW excitation as well. Since we are working in the non-resonant scenario, no thermal effects are observed under CW excitation, whereas, under pulsed excitation, TPF is observed. Consequently, thermal effects are observed due to the accumulation of kinetic energy over time. Thus, no such behavior is observed under CW excitation. Hereafter, all the analysis done under pulsed excitation only.

Figure 9.27a shows the drag, figure 9.27b shows the adjustment of the particle

Power (mW)	Confinement time (s)
4.70	> 1560 min
9.40	558.14 ± 28.96
14.10	169.13 ± 25.95
18.80	102.47 ± 23.91
23.50	57.96 ± 3.75
28.20	42.87 ± 5.98
31.96	7.15 ± 2.51

Tab. 9.18.: The confinement time for single particle under pulsed excitation at different average power.

at the bottom of the potential well, figure 9.27c shows the confinement time, and

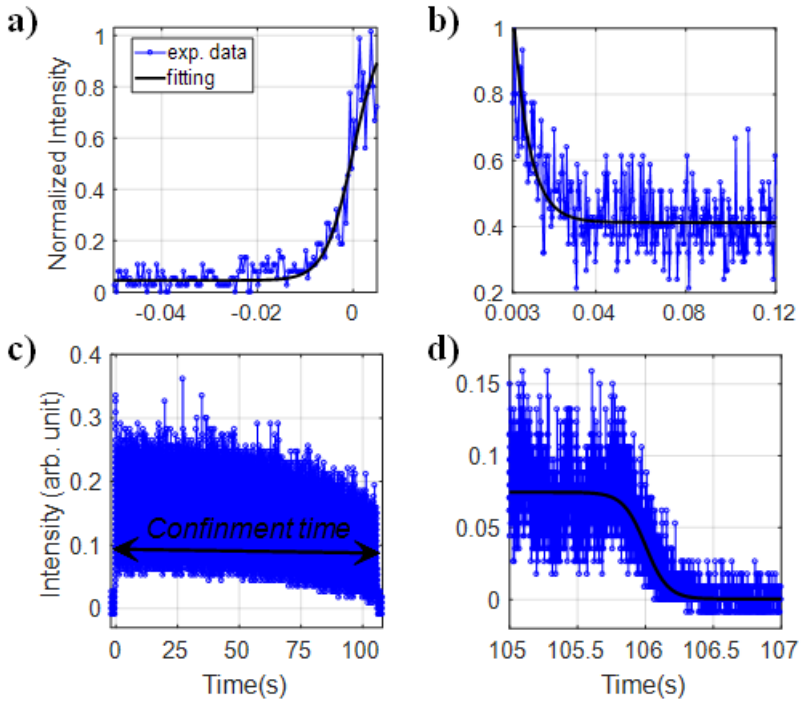

Fig. 9.27.: Plots of the backscattered signal of a single particle confined in an asymmetric potential well a) drag, b) adjustment, c) confinement time, and d) ejection of a single particle under pulsed excitation at 18.80 mW average power.

figure 9.27d shows the ejection of a single particle inside the potential well at 18.80 mW average power under pulsed excitation. A similar feature is observed under CW excitation as well, but it is difficult to get information about ejection dynamics because under CW excitation particle is quite stable.

Note: The drag and adjustment dynamics of the single-particle are collected at both 400 ns and 400 μs time intervals, whereas the ejection dynamics is at 400 μs time interval only because adjustment dynamics for CW excitation is not apparent at 400 μs time interval. Both 400 μs and 400 ns time interval data follows a similar trend, and quantitatively all the values listed in the tables 9.19, 9.20, 9.21, 9.22, 9.23, and 9.24. Ejection dynamics also capture at 400 ns time interval but at 9.40 mW average power where particle confinement time is around 600 s. So, the capturing ejection dynamics at 400 ns time interval is difficult because the transfer rate of data collection is limited. At low average power, getting information about drag, adjustment, and ejection dynamics from the raw data is difficult because of the signal to noise ratio increases when average power decreases. So, all data shown in plots are from 9.40 mW onward.

9.3.3.1. Drag dynamics

The drag time of a single particle decreases with an increase in average power under both CW and pulsed excitation because drag time is proportional to the steepness of the potential well. Since steepness increases with average power, particle takes less time in drag at high average power. The noticeable point here is that drag time varies nonlinearly with average power under both CW and pulsed excitation. However, nonlinearity is more under pulsed excitation than CW excitation, as shown in figure 9.28.

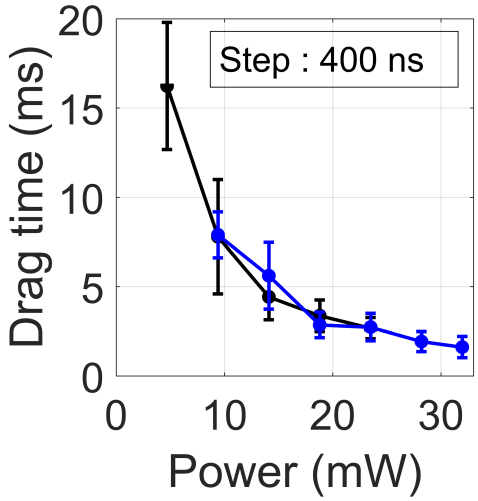

Fig. 9.28.: Plot of drag time against average power under both CW and pulsed excitation.

Power (mW)	Pulsed excitation (s)	CW excitation (s)
4.70	—-	0.0162 ± 0.0036
9.40	0.0079 ± 0.0013	0.0078 ± 0.0032
14.10	0.0056 ± 0.0019	0.0044 ± 0.0013
18.80	0.0029 ± 0.0007	0.0034 ± 0.0009
23.50	0.0027 ± 0.0008	0.0027 ± 0.0006
28.20	0.0019 ± 0.0006	—-
31.96	0.0016 ± 0.0006	—-

Tab. 9.19.: The drag time for single-particle under both CW and pulsed excitation at different average power at 400 ns time interval.

Power (mW)	Pulsed excitation (s)
4.70	—-
9.40	—-
14.10	0.0053 ± 0.0019
18.80	0.0038 ± 0.0024
23.50	0.0024 ± 0.0010
28.20	0.0020 ± 0.0006
31.96	0.0017 ± 0.0005

Tab. 9.20.: The drag time for single-particle under pulsed excitation at different average power at 400 μs time interval.

9.3.3.2. Adjustment dynamics

The adjustment time of a single particle depends on both steepness and equilibrium position of the potential well. Since increasing average power increases U_{abs} and shifts the equilibrium position towards the positive axial direction, which results in decreasing the adjustment time, thence, at high average power, particle adjusts itself with a faster rate as shown in figure 9.29. To determine the adjustment time from the TPF signal corresponds to the backscattered signal, we fit the TPF signal to three exponential and observed that time constants are of the order of a few tens of seconds, second, and millisecond respectively (tables 9.17). From the backscattered signal, we observed that adjustment dynamics happen in the millisecond time scale, so we can say that the millisecond component of the TPF signal contains adjustment dynamics information. But the millisecond component of TPF and backscattered signals are not matching because the TPF signal contains information of both photo-bleaching and adjustment dynamics, and deconvolution of these two signals is difficult, so getting information about adjustment dynamics from TPF signal is arduous.

Comparison of drag and adjustment dynamics

On comparison of drag and adjustment time, it can be observed that with an increase in average power, drag time decreases with a faster rate than the adjustment time. At low average power, drag time is more than the adjustment time; however, at high average power, the adjustment time is more than the drag time. Because the dragging of the particle only depends on the steepness of the potential well, which is directly related to average power, but adjustment time

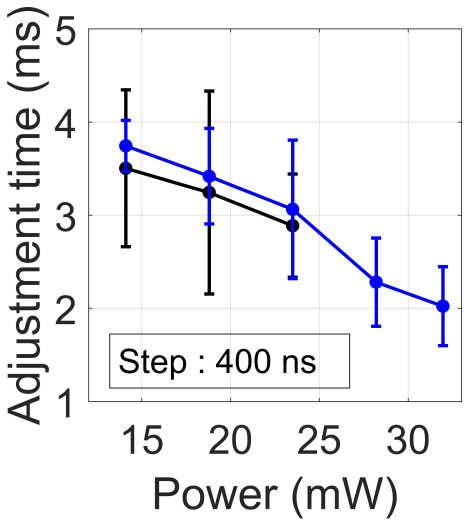

Fig. 9.29.: Plot of adjustment time against average power under both CW and pulsed excitation.

Power (mW)	Pulsed excitation (s)	CW excitation (s)
4.70	—-	—-
9.40	—-	0.0021 ± 0.0009
14.10	0.0037 ± 0.0003	0.0035 ± 0.0008
18.80	0.0034 ± 0.0005	0.0032 ± 0.0011
23.50	0.0031 ± 0.0007	0.0029 ± 0.0006
28.20	0.0023 ± 0.0005	—-
31.96	0.0020 ± 0.0004	—-

Tab. 9.21.: The adjustment time for single-particle under both CW and pulsed excitation at different average power at 400 ns time interval.

Power (mW)	Pulsed excitation (s)
4.70	—-
9.40	—-
14.10	0.0056 ± 0.0016
18.80	0.0051 ± 0.0015
23.50	0.0046 ± 0.0013
28.20	0.0044 ± 0.0009
31.96	0.0035 ± 0.0008

Tab. 9.22.: The adjustment time for single-particle under pulsed excitation at different average power at 400 μs time interval.

depends on both steepness and equilibrium position of the potential well. The increase in average power results in shifting the equilibrium position towards positive axial direction due to the significant contribution of the scattering force. Wherefore, the contribution of steepness in adjustment time proportionally varies with drag time, but shifting in the equilibrium position results in increasing overall time constant for adjustment time. Thus, at low average power drag time is more than the adjustment time and at high average power, the case is reversed.

Justification of adjustment dynamics due to particle alone

To verify the decay, which we have observed just after the immediate rise is only particle effect, not due to the amount of light collected through the objective. We have performed the experiment by changing the surrounding medium. We have done a comparative study for two different types of medium: water and water-glycerol mixture (75:25; water: glycerol). The obtained drag and adjustment times for water-glycerol medium are $\sim$28.08 ms and $\sim$10.26 ms, whereas, for water medium, $\sim$3.82 ms and $\sim$5.07 ms at 18.80 mW average power under pulsed excitation. The drag and adjustment time of the trapped particle inside the water-glycerol medium should be longer than that of the water medium because it is denser medium.

Another point to be noticed is that at similar average power, in the water-glycerol mixture, drag time is more than the adjustment time, whereas, for water medium, the case is reversed. This is because the relative refractive index (which is a crucial quantity that dictates the optimal power for a stable optical trap) is different for both water and water-glycerol mixture. Corresponding optimal power is higher for the water-glycerol mixture. Thus, the drag and adjustment dynamics of a trapped particle in the water at high average power is similar to the dynamics observed at low average power in the water-glycerol mixture. For example, the trend of the drag and adjustment time we observed at $\sim$18.80 mW average power for water-glycerol mixture should be similar to the trend we observed at $\sim$4 mW average power for water medium. As shown in figures 9.28 and 9.29, at low average power, drag time is more than adjustment time, and the case is reversed at high average power. Consequently, drag time is more for the water-glycerol mixture than adjustment time at 18.80 mW average power.

From this discussion, it is apparent that the decay we obtained in the backscattered

signal just after the immediate rise is due to trapped particle adjustment at the equilibrium position and not due to instrumental data collection.

9.3.3.3. Peak intensity of the backscattered signal

The peak intensity of the backscattered signal just after drag varies linearly with average power under both CW and pulsed excitation, as shown in figure 9.30. At low average power, peak intensity corresponding to CW excitation is more than pulsed excitation; however, the case is reversed at high average power. Because at high average power, nonlinear effect contributes significantly under pulsed excitation, and it can be predicted that a further increase in average power results in nonlinearly varying the peak intensity.

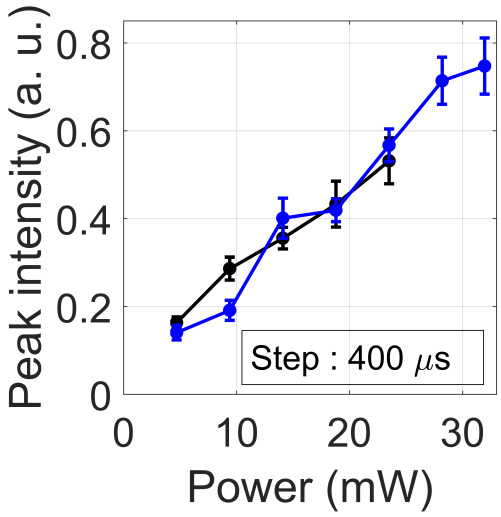

Fig. 9.30.: The plot of peak intensity of the backscattered signal against average power under both CW and pulsed excitation.

9.3.3.4. Confinement time

Figure 9.31 shows that with increasing average power, the confinement time of a single coated particle is decreasing as the asymmetricity of the trap increases while U_{esc} decreases; quantitatively listed in table 9.18.

9.3.3.5. Ejection time

Figure 9.32 shows the ejection time against average power, and it is observed that an increase in average power results in a decrease in the ejection time because, asymmetricity of the potential well increases along the axial direction, quantitatively listed in tables 9.23, and 9.24. The slope of U_{esc} becomes flatten along

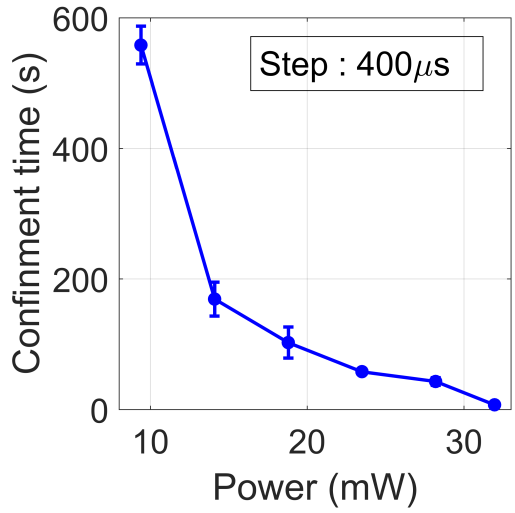

Fig. 9.31.: Plot of confinement/trapping time of a single particle against average power under both CW and pulsed excitation.

the axial direction with increasing average power, which results in decreasing the ejection time because the ejection of the particle is always along the axial direction.

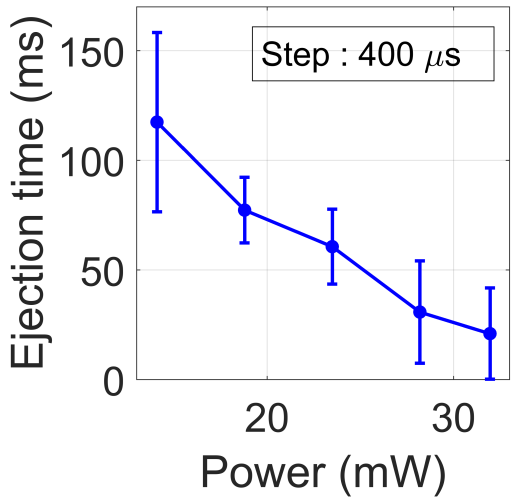

Fig. 9.32.: Plot of ejection time of a single-particle against average power under pulsed excitation.

9.3.3.6. Mapping of confinement time with potential height

As per the above discussion, the confinement time of the coated single-particle decreases, as shown in figure 9.31, because it is strongly dependent on the asymmetricity of the optical trap which is indirectly proportional to the average power of trapping beam. In figures 9.33, we have shown one to one mapping of potential

Power (mW)	Pulsed excitation (s)
4.70	—-
9.40	—-
14.10	0.1174 ± 0.0409
18.80	0.0772 ± 0.0150
23.50	0.0606 ± 0.0171
28.20	0.0308 ± 0.0234
31.96	0.0209 ± 0.0208

Tab. 9.23.: The ejection time for single-particle under pulsed excitation at different average power at 400 ns time interval.

Power (mW)	Pulsed excitation (s)
4.70	—-
9.40	0.1647 ± 0.0227
14.10	0.0829 ± 0.0402
18.80	0.0768 ± 0.0111
23.50	0.0702 ± 0.0243
28.20	0.0544 ± 0.0127
31.96	0.0170 ± 0.0131

Tab. 9.24.: The ejection time for single-particle under pulsed excitation at different average power at 400 μs time interval.

by using $e^{-U/k_BT} \propto \frac{1}{t_{confinement}}$. From the theoretical results, it is apparent that increasing power first increases the confinement time then decreases. Therefore, at low average power (5.14 mW), particle confinement time is long enough that (> 1 hour) even before capturing the ejection dynamics, another particle is dragged into the potential well. Also, the theoretical plots of U_{esc} against average power indicate a mismatch between the theoretical and experimental results, which could be because we did not incorporate the hydrodynamic effects (for example, a change in convection current, etc). The stable maxima are obtained theoretically at ∼20 mW average power when only OKE is incorporated while incorporating nonlinear thermal effects along with OKE results in a shift in stable maxima from ∼20 mW to ∼9 mW. However, experimentally, it is observed at ∼5 mW average power. A detail discussion on thermal nonlinear effect is given in appendix F.

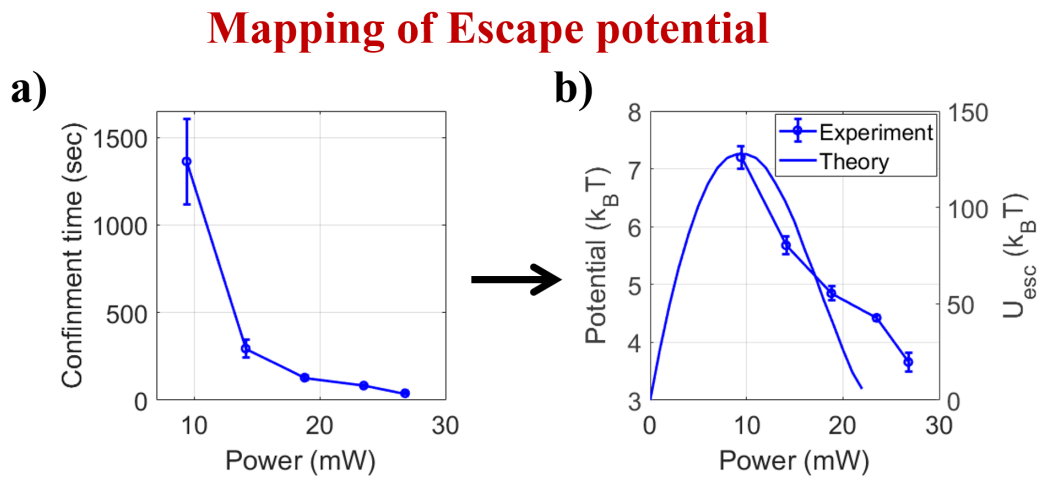

Fig. 9.33.: a) The plots of confinement time vs average power for uncoated particles, and b) plots of potential/escape potential vs time for uncoated particles. The measured pulsed width while performing the experiment using PMT pulse widths is $\sim 460\ fs$ for uncoated particles.

9.3.4 Proposed model for single particle dynamics

From the above discussion, it can be inferred that when the particle is dragged towards the focal volume, it tries to adjust itself at the equilibrium position, followed by stabilizing the particle. The particle starts accumulating energy, which conserves the momentum through thermal fluctuations, and eventually, particle leaves the trap. Accordingly, figures 9.34a to 9.34e show all five steps for motion of a single particle under pulsed excitation. A similar feature is observed under CW excitation as well, but it is difficult to get information about (thermal) fluctuation and ejection dynamics because under CW excitation particle is quite stable within the observation window. Accordingly, figures 9.34f to 9.34j show the schematic of the proposed model depicting the highly skewed potential along the axial direction and 2D representation of optical trapping along both radial and axial directions, respectively. Initially, the particle is dragged towards the focal volume due to a steep (three-dimensional) gradient potential, which is minimum at the geometric focus; subsequently, the particle moves forward due to (axial) scattering force, adjusting itself to the global potential minimum which is slightly ahead of the focus. In conclusion, the trapping dynamics can be described in five sequential steps: 1) drag, 2) adjustment, 3) equilibration, 4) (thermal) fluctuation, and 5) ejection. Theoretically, it can be seen through one to one mapping with the phase space trajectory by the change in the magnitude of velocity vectors of the single-particle, as shown in figure 6.23.

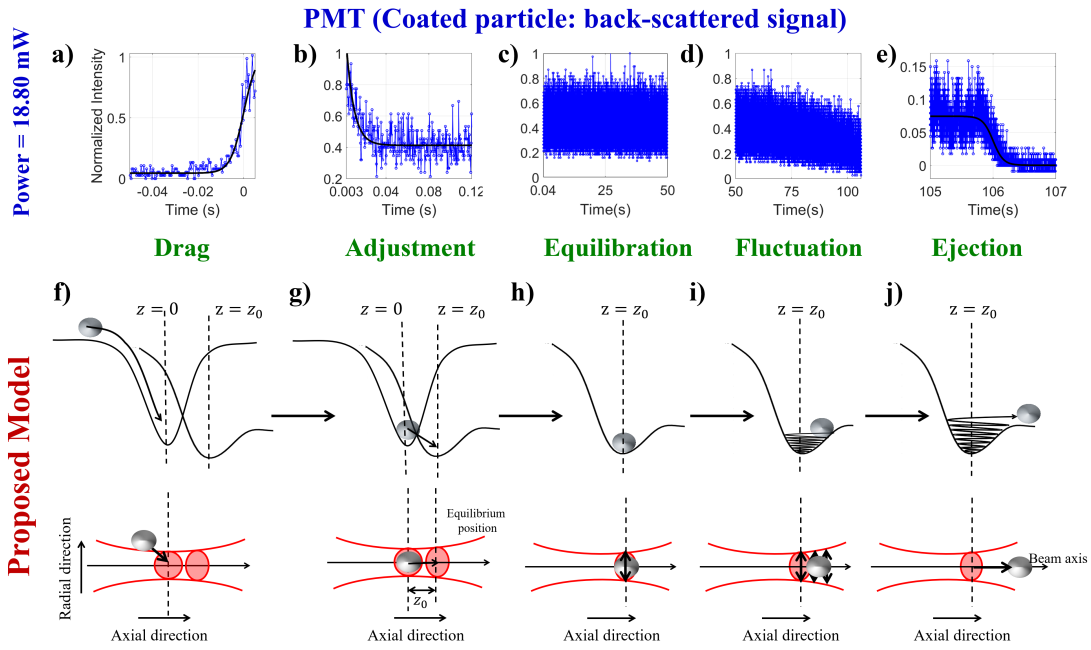

Fig. 9.34.: a) to e): Plots of the backscattered of a single particle during optical trapping under pulsed excitation at 18.80 mW average power depicting sequential steps. Color: blue curve corresponds to raw data, and black correspond to sigmoidal fit (drag and ejection) or exponential (adjustment) fit raw data. Bottom panel: f) to j) A proposed model for trapping dynamics along axial and radial directions depicting the sequential event. Note the global maxima $z = z_0$ is shifted from geometric focus (z = 0).

9.3.5 Backscattered and TPF signal analysis for two particles dynamics

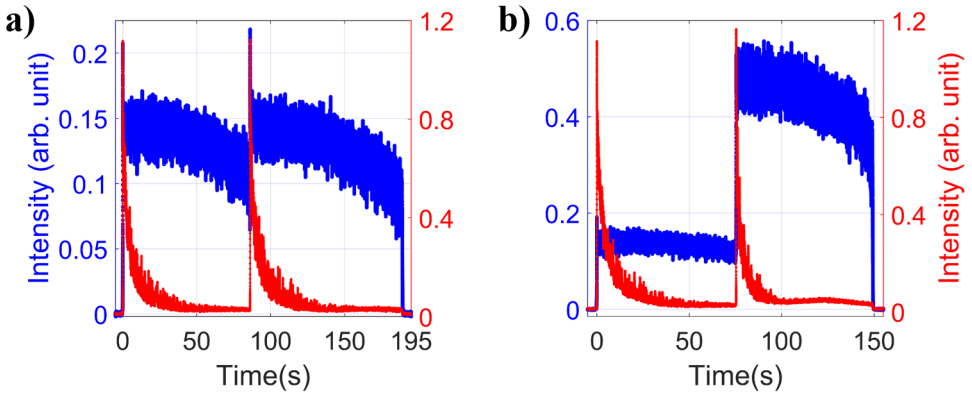

Fig. 9.35.: Plots of backscattered and TPF signals for two particles dynamics at 18.80 mW average power under pulsed excitation.

The backscattered signal in figure 9.35a reveals that initially, a particle is dragged inside the optical trap, and sometimes later, the second particle is dragged, which

are also marked by a concomitant rise in TPF signal. Figure 9.35b shows another set of data for two particles. The height of the TPF signal alone is inadequate to give information about the second particle because the first particle gets photo-bleached while trapping, whereas the height of the backscattered signal changes significantly, which reveals the confinement of the second particle inside the optical trap along with the first particle. The critical point here is that the height of the TPF signal is same for both the cases. In figure 9.35a, first particle went out from the trap because the moment the second particle is dragged, the first particle has accumulated enough energy to cross the barrier. Therefore, a small momentum kick can throw particle out from the trap, and that momentum kick provided by the second particle when it is dragged. As a result, the first particle leaves the trap. In figure 9.35b, the first particle does not accumulate enough energy when the second particle is dragged. Also, the collision of the second particle with the first particle can not provide enough energy to cross the barrier; consequently, both particles stay back in an optical trap. Whether both particles are confined in the trap or the first particle leaves the trap depends on the amount of energy accumulated by the first particle until the second particle is dragged, and the energy required to cross the barrier is different for different average power. TPF signals look similar for both the cases, but processes are different, which can be analyzed through the backscattered signal. Thus, both signals have a significant contribution to revealing the complete particles dynamics.

Figure 9.36 shows the simultaneous detection of backscattered and TPF signals

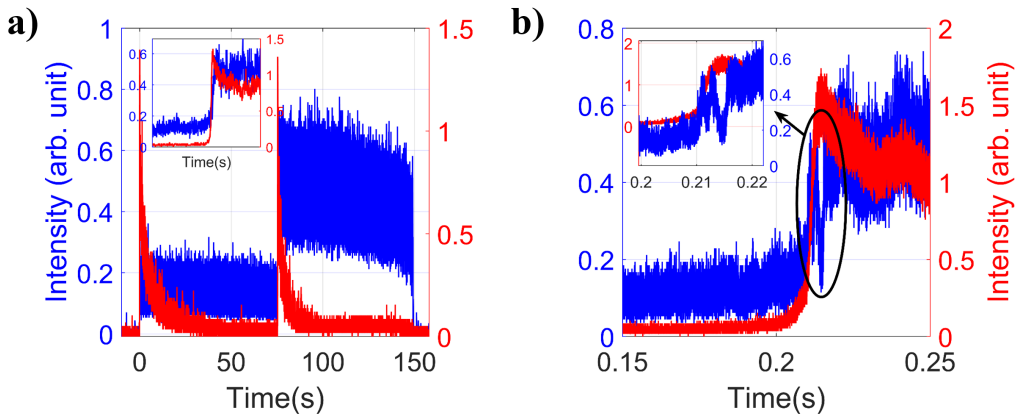

Fig. 9.36.: Plots of backscattered and TPF signals for second particle dragging, data collected at a) 400 μs, and b) 400 ns time intervals at 18.80 mW average power under pulsed excitation.

for two particles confined in an optical trap under pulsed excitation at 18.80 mW average power at 400 μs (figures 9.36a) and 400 ns (figures 9.36b) time

interval. The zoomed plot in figure 9.36a shows the drag of the second particle, and drag shows a smooth rise for both backscattered and TPF signals. Figure 9.36b shows the drag of the second particle for another set of data collected at 400 ns time interval. The rise of the backscattered signal is oscillatory. However, these oscillations can be observed in 400 ns time interval data, but not in 400 μs interval data, whereas TPF rise is smooth in both the cases since the first particle gets photo-bleached. This oscillatory nature of rising is coming due to the interference between the backscattered signal of the trapped particle and dragged particle.

9.4 Probing dynamics through simultaneous detection of backscattered signal and video microscopy

Later, we demonstrate the modulation of optical trap using trap stiffness and immobilization dynamics of the 1 μm uncoated polystyrene particle by simultaneous detection of video microscopy and backscattered signal detection.

9.4.1 Single particle dynamics

Figure 9.37 shows the single uncoated particle dynamics when the particle is confined within a nonlinear optical trap at 14.10 mW average power under pulsed excitation. For clear visualization, the data is plotted with 10-point moving averaging of raw data. However, all the data analysis has been done for raw data. A similar trend is observed that trapping occurs in five sequential steps, as discussed above for coated particles. The drag, adjustment, and ejection time corresponding to the signal are shown in figure 9.37a are 11.8 ms, 4.68 ms, and 5.57 ms, respectively. Figure 9.37b shows the corresponding transmitted wide-field microscopy images of drag, adjustment, and ejection dynamics. Figures 9.37c-d show the position distribution along x- and y-axis, and figure 9.37e shows trajectory of a single particle when it is confined within optical trap corresponding to backscattered signal shown in figure 9.37a. Figures 9.37f-g show the x and y position of the confined particle against time and the trap stiffness k_x, k_y and k_r for the confined particle are $\sim$ 40.17 $pN/\mu m$, $\sim$ 29.41 $pN/\mu m$ and $\sim$ 23.73 $pN/\mu m$ respectively. The difference in trap stiffness along x- and y-axis, which might

be due to asymmetry in the beam profile or slight slope/tilt in the sample stage. Moreover, under pulsed excitation, nonlinear effects also contribute significantly to this power level. Figure 9.37h shows the trap stiffness measurement over 20 sec time window to estimate the particle dynamics when the particle leaves the trap, where the circle represents the experimental data, and the solid line represents the exponential fit. It is observed that as the particle moves out from the trap, it experiences more and more asymmetry along the axial direction, which results in increasing the amplitude of motion along the radial direction. Hence, the trap stiffness decreases. Under pulsed excitation, the harmonic approximation is valid when the particle is at the equilibrium position. When particle leaves the trap, it experiences the more asymmetric part of the well, which is characterized by a lower trap stiffness due to a progressive change in curvature of the well. A similar

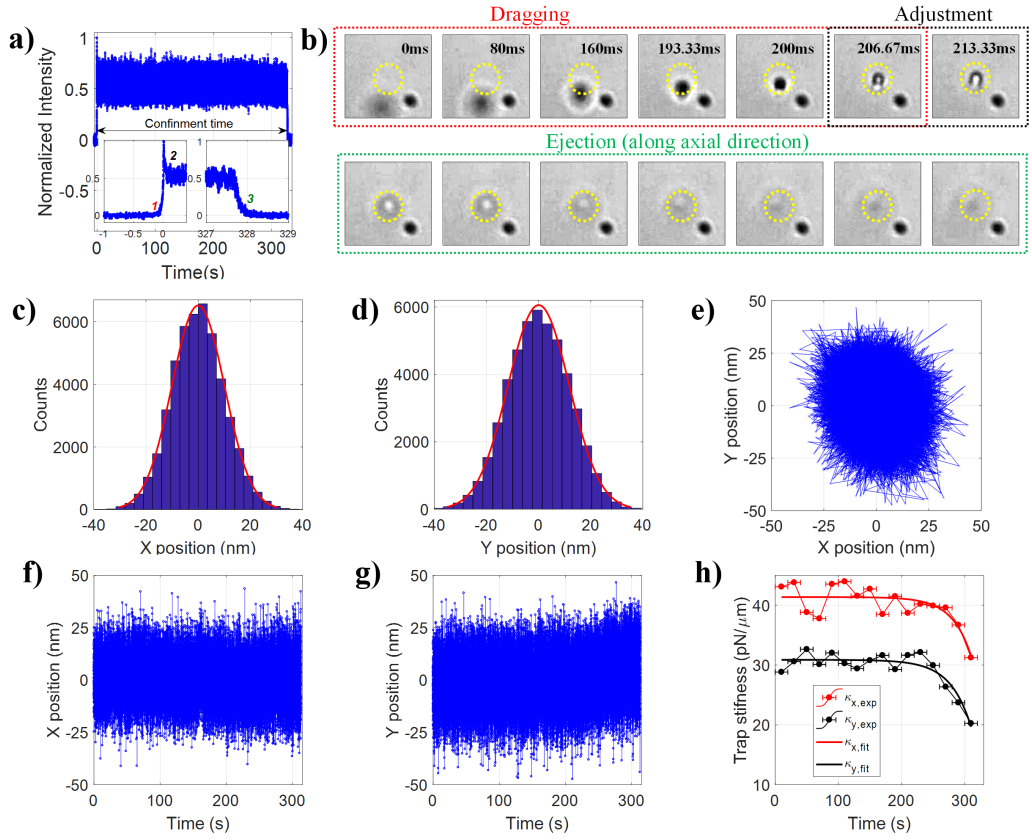

Fig. 9.37.: a) The plot of the backscattered signal, b) corresponding transmitted wide-field microscopy images of the particle to map drag, adjustment, and ejection; the plots of position distribution along c) x-axis, d) y-axis, e) xy trajectory; the plots of the variation of f) x-position against time, g) y-position against time, and h) evolution of trap stiffness evaluated at every 20 sec time interval at 14.10 mW average power under pulsed excitation for a single confined particle within nonlinear optical trap.

trend is observed for uncoated particles as coated particles for confinement, drag, adjustment, ejection, and trap stiffness changes at different average power, as shown in figure 9.38a-e. In figure 9.38f, we have also shown the trap stiffness against average power, and it can be seen that as power increases trap stiffness increases, however, at low average power trap stiffness along x-axis and y-axis is approximately equal, but the deviation between the trap stiffness increases with increase in average power due to significant contribution of nonlinear effects and asymmetry in radial beam profile. Also, the trap stiffness measurement over a small time window (as shown in figure 9.37h) decays with a faster rate as average power increases because escape potential is decreasing, so the curvature of the potential changes rapidly.

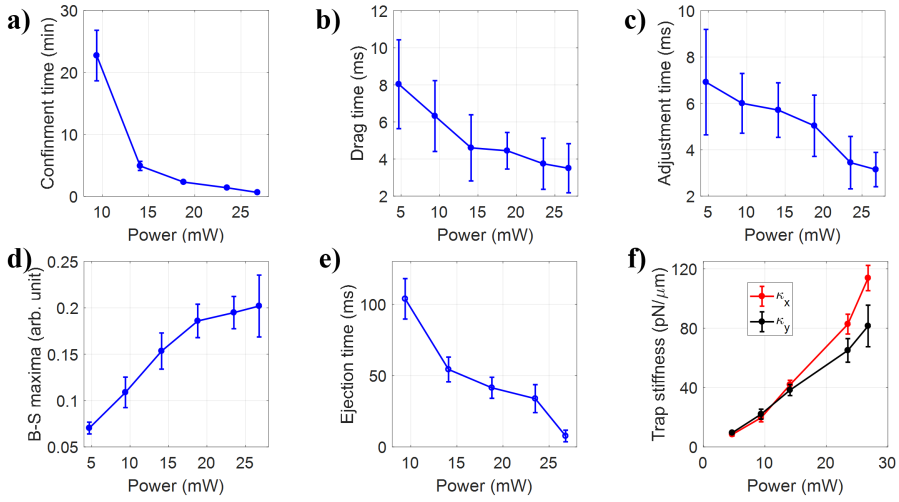

Fig. 9.38.: The plots of a) confinement time, b) drag time, c) adjustment time, d) maxima of backscattered signal, e) ejection time, and f) trap stiffness against average power for a single confined particle within nonlinear optical trap under pulsed excitation.

9.4.2 Two particles dynamics

Figure 9.39a shows the backscattered signal (from point detection) for two particles confined in the optical trap at 14.10 mW average power. The sudden rise in the backscattered signal (marked by 3) indicates the drag of the second particle. The notable point here is that this rise is not followed by any decay in the signal (that we called adjustment in the above discussion). This is because the shift in the equilibrium position is significant for the first particle, but when second particle is dragged, the optical trap is already modulated by the first particle, so further modulation effects are not evident because the observed signal is an integrated signal for both the trapped particles. Eventually, both particles

leave the trap (marked as 4 in figure 9.39a), but this is one of the cases, there is also a possibility that one particle leaves the trap earlier and one stays back. Figure 9.39b shows the corresponding transmitted images of drag of second/latter

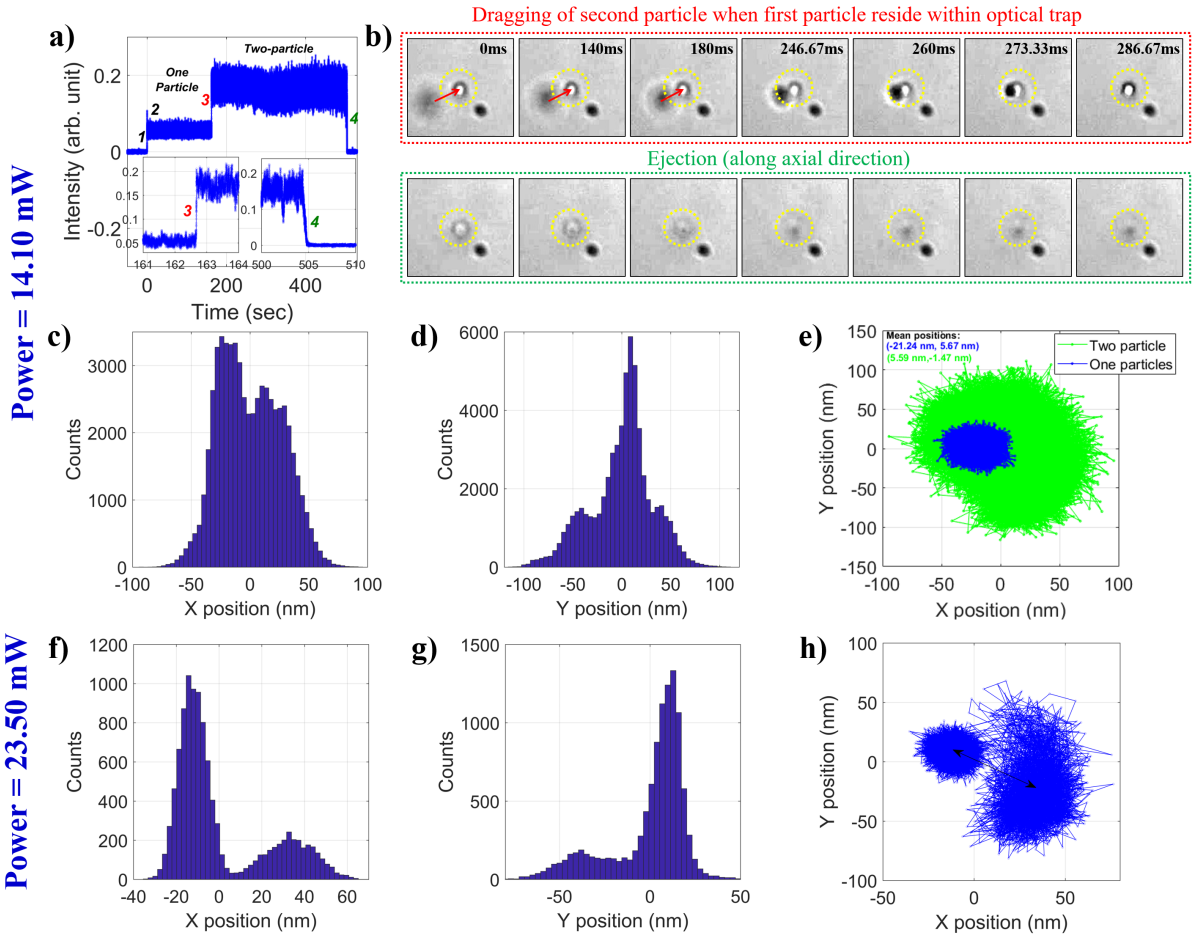

Fig. 9.39.: a) The plot of the backscattered signal for two particles, b) corresponding transmitted wide-field microscopy images of the particles to map drag of latter particle when the first particle is residing inside the nonlinear optical trap and ejection of both the particles; the plots of position distribution along c) x-axis, d) y-axis, e) xy trajectory at 14.10 mW average power; and f) x-axis, g) y-axis, h) xy trajectory at 23.50 mW average power under pulsed excitation for confinement of two-particle within the nonlinear optical trap.

particle and ejection of both the particles along the axial direction. Figures 9.39c-d show the distribution of particle position along x- and y-axis, and figure 9.39e shows the trajectory of particles inside the nonlinear optical trap at 14.10 mW average power; here blue color represents the trajectory of a single particle, and green color represents the trajectory when two particles are confined within the optical trap. A shift in the mean position of the particle's trajectories is obtained from one to two particles confinement within the optical trap, from $x = -21.24$

nm, $y = 5.67\ nm$ to $x = 5.59\ nm$, $y = -1.47\ nm$, respectively. However, when two particles are present within the optical trap, fluctuations in the particle position increase rapidly due to the collisional degree of freedom. Since particle adjusts itself along the axial direction, the deconvolution of both particle trajectory individually is complicated. In addition, the position distribution along x- and y-axis are merged in such a way that it is difficult to deconvolute them, can be seen from the figures 9.39c to 9.39e. This might be because the overall number of frames is more since the particle stays ∼505 sec, so accordingly, the number of frames is ∼75750. Hence, a clear distribution can not be seen along both the x- and y-axis. However, a clear shift in the particle's position distribution and trajectories can be seen from figures 9.39f-h, because at 23.50 mW average power where particle confinement time ∼84 sec, and asymmetry is more at high average power so that shift can be detectable easily. Accordingly, we can see two clear distribution along both x- and y-axis, and shift in the trajectory of the particles as shown by the double-sided black arrow in figure 9.39h. Afterward, we

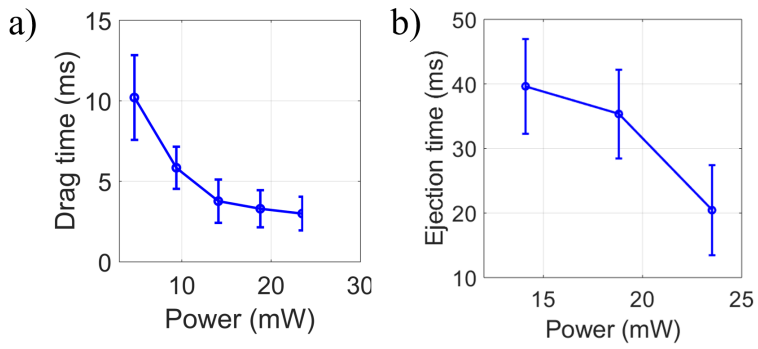

Fig. 9.40.: a) The plots of latter particle a) drag, and b) ejection time in two particles dynamics against average power under pulsed excitation.

have also studied the drag time of second/latter particle and ejection time (when both particles eject together) against average power, as shown in figures 9.40a-b. It can be seen that drag time for the second particle decreases with increasing average power because of the steepness of the potential increases significantly. Similarly, ejection time also decreases with increasing average power because asymmetry is more, so trap becomes smoothen towards ejection direction. The notable point here is that at low average power, particle confinement time is so long that detecting dynamics for the second particle is a bit difficult because sample aggregates over time; hence, the local field modulates itself. At very high average power, the escape potential is not enough to confine two particles. Consequently, when the second particle is dragged, both particles leave the trap

immediately. Moreover, the drag time for the second particle is different from the first particle drag time because the second particle experiences a modulated optical potential due to the presence of the first particle.

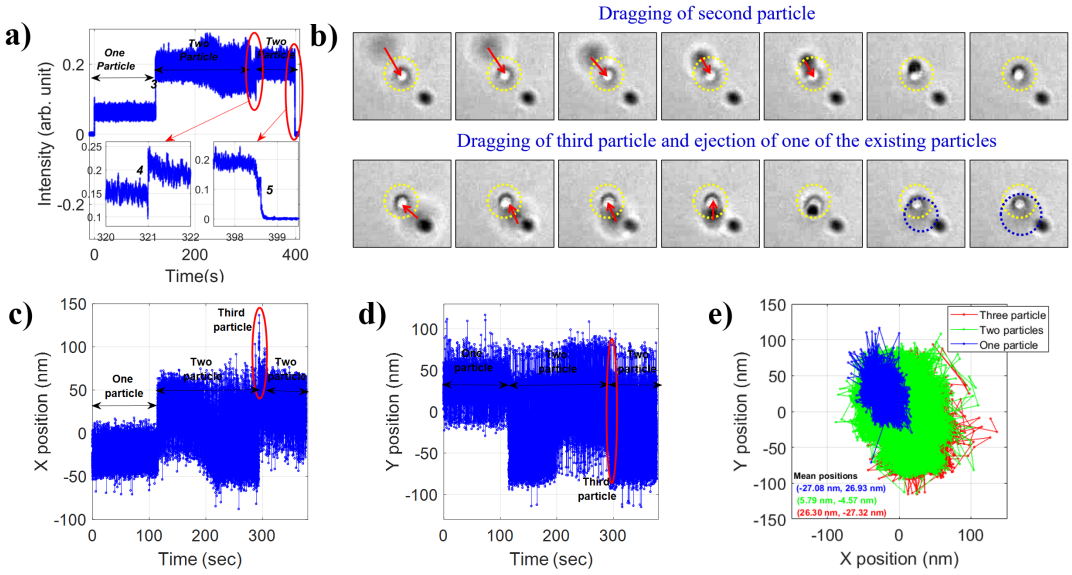

Fig. 9.41.: a) The plot of the backscattered signal for multiple (more than two) particles, b) corresponding transmitted wide-field microscopy images of the particles to map drag of second and third particle when first and among one of two particles is residing inside the nonlinear optical trap respectively. The plots of particle position along c) x-axis, d) y-axis against time, and e) xy trajectory of confined particles within the nonlinear optical trap at 14.10 mW under pulsed excitation.

9.4.3 Multiple particles dynamics

Figure 9.41a shows the backscattered signal (from point detection) of more than two particles trapping inside a nonlinear optical trap at 14.10 mW average power. A sudden rise of the signal indicates the drag of the third particle (marked by 4), as shown in the zoomed window of the first red circle of figure 9.41a. The decay in the signal followed by a sudden rise indicates the ejection of one of the residing particles, not the adjustment. Depending on the particle size, wavelength of trapping beam, and NA, more than two particles can not stay together inside the optical trap because of the limitations of the focal volume. The zoomed window of the second red circle shows the ejection of both the particles (marked by 5). The corresponding transmitted wide-field microscopy images are shown in figure 9.41b. Here, the yellow dotted circle represents the trap center, and the red arrow shows the drag direction of the second and third particles. From these images, it is very clear that when the third particle is dragged, one of the exiting particles

has to leave the trap, which is marked by the blue circle, and the particle is not seen with a clear vision because ejection is along the axial direction. Figures 9.41c and 9.41d show the plots of x- and y-position of the particles against time, and a shift in the mean position of the particles (a diagonal shift most likely, although this shift can be in any direction) is observed when second or third particles are dragged within the focal volume. The red circle marks the drag of the third and ejection of one of the existing particles. Figure 9.41e shows the trajectories of the particles here, blue represents the trajectory of a single particle, green represents the trajectory after the drag of the second particle, and red represents the trajectory after the drag of third particle and ejection of the existing one. The shift in the mean positions of the particle trajectories are also mentioned. Similar behavior is observed at different average power as well.

9.5 Conclusion

We have observed from the experimental evidence that the TPF signal alone is inadequate to get information about particle dynamics as particle gets photobleached while trapping. From the height of the TPF signal, it is difficult to predict whether the particle is still trapped or not. Since we are not able to get information about particle dynamics from the TPF signal, getting information about second particle dynamics is even more difficult.

To get the complete information about particle dynamics, the backscattered signal is the appropriate quantity because it is present as long as the particle is confined within the optical trap. The height of the backscattered signal increases significantly when another particle is trapped, which helps to detect the dynamics of two particles. When a single particle is trapped, firstly, it tries to stabilize at the equilibrium position, then accumulate energy over time and emit in the non-radiative form to conserve the momentum. This non-radiative energy results in increasing the thermal fluctuations of the particle along both radial and axial directions over time. Due to an increase in the thermal fluctuations, the particle crosses the escape potential and leaves the trap. We proposed a hypothetical model accordingly which gives direct evidence of mapping the nonlinear nature of optical trapping potential along with a detailed theory of trapping including optical Kerr effect independent of particle size under pulsed excitation.

To the best of our knowledge, it is the first time the direct experimental mapping of the nonlinear nature of optical trapping potential under pulsed excitation, including optical Kerr effect independent of particle-size with a detailed theory of

trapping has been performed. Most experimental groups rely on the TPF signal to detect and analyze the trapped particle dynamics, but we have shown that the TPF signal alone is not adequate since it gets photo-bleached while trapping. Therefore, backscattered data is more appropriate to get information about the particle dynamics as the signal stays throughout the particle confinement. Thus, through the simultaneous detection of both the signals, we can study the detailed dynamics of a trapped particle. From the study, we have observed that the trapping occurs in five sequential steps: drag, adjustment, equilibration, fluctuation, and ejection. We have proposed a model by integrating all these processes which may apply to various kinds of the system such as the hard-sphere, lipids, etc. Also, we have rigorously analyzed the effect of nonlinearity on each of these processes by changing the average power for a trapped particle and shown a direct mapping with theoretical results. Considering the wide range of practical applications of optical tweezer, we envision the far-reaching application of tuning trapping force/potential by harnessing optical nonlinearity.

Optical Trapping of 100 nm dielectric nanoparticles

10

10.1 Introduction

We now extend our dynamical study from μm (as discussed in chapter 9) to nm particles. In this chapter, experimentally, we have explored the dynamics of nanoparticles by TPF signal detection using CMOS camera and simultaneous detection of TPF and backscattered signals for 100 nm polystyrene nanoparticles. We also discuss methods of analysis of the signal and show how moving-averaging of the raw data can help in extracting a tiny signal embedded within a huge noise floor, however, at the expense of losing valuable information on particle trapping dynamics.

10.2 Result and discussion

10.2.1 TPF analysis

We explored the dynamics of 100 nm polystyrene beads using high repetition-rate Ti-Sapphire oscillator pulsed laser with gaussian beam profile. The data for both linearly polarized (LP) and circularly polarized (CP) light at 50 mW average power is shown in figure 10.1. We have collected TPF signal for a particle while it is trapped and how TPF decays with time. The signal is collected using a CMOS camera and the counts are extracted by using the software Tracker (Open Source Physics).

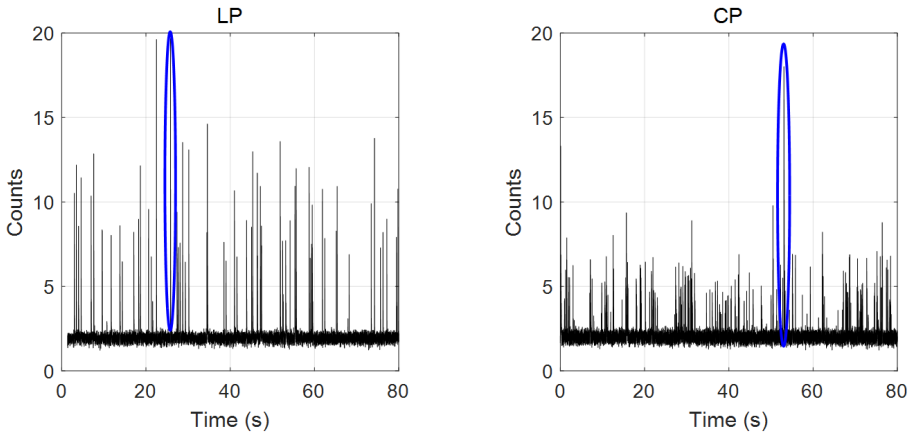

Fig. 10.1.: Plots show the TPF signal counts versus time for Linearly Polarized (LP) and Circularly Polarized (CP) light for a concentrated solution.

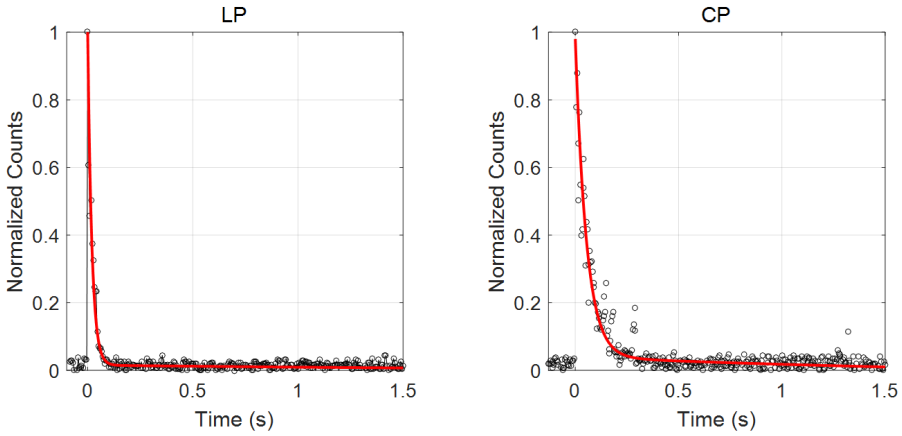

Fig. 10.2.: Plots show fitted curves for the TPF signal counts (normalised counts versus time) for a single particle (marked in blue in figure 10.1) for Linearly Polarized (LP) and Circularly Polarized (CP) light.

Polarization	a	τ_1	b	τ_2	τ_{avg}	R^2
Linear	0.03	3.83	0.97	0.02	0.12	0.97
Circular	0.07	2.07	0.93	0.05	0.19	0.93

Tab. 10.1.: Fitting parameters for the TPF signal collected for a single particle after normalization.

We are exploring the dynamics of 100 nm polystyrene beads using high repetition-rate Ti-Sapphire oscillator pulsed laser with a gaussian beam profile. The data for both linearly polarized (LP) and circularly polarized (CP) light at 50 mW average power is shown in figure 10.1. We have collected the TPF signal for a particle while it is trapped and how TPF decays with time. The signal is collected using a CMOS camera, and the counts are extracted by using the software Tracker (Open Source Physics).

$$f = a * exp\left(-\frac{x}{\tau_1}\right) + b * exp\left(-\frac{x}{\tau_2}\right) \tag{10.1}$$

where, we are following the criteria, $a + b = 1$. From table 10.1 it can be seen that the lifetime is changing with the change in polarization of light. It can also be observed from figure 10.2 that the average lifetime of TPF differs by orders of magnitude for different polarization. The possible reason for decaying the TPF signal over time could be the particle getting photo-bleached.

Here, average life is calculated as:

$$\tau_{avg} = \frac{a * \tau_1 + b * \tau_2}{a + b} \tag{10.2}$$

In conclusion, we can say that the CMOS camera is not a sensitive detector as the TPF signal alone can not provide a detailed dynamics of single particles. The detection of the backscattered signal using the CMOS camera for 100 nm polystyrene bead is very difficult since the amount of backscattered signal is very less. So, it is very hard to tell about the stability of the trap. Therefore, we have to do simultaneous detection of TPF and backscattered signals to gather information about particle dynamics by using more sensitive detectors like PMTs.

10.2.2 Simultaneous detection of TPF and backscattered signals

Figure 10.3 shows backscattered and TPF signal for a single 100 nm polystyrene particle suspended in water at 9.40 mW (figure 10.3a) and 28.2 mW (figure 10.3b) average power respectively where blue curves correspond to the backscattered and red curves correspond to the TPF signal. The data collected at 400 μs time interval.

Figures 10.3c and 10.3d show the 100-point moving averaging of the raw data in figures 10.3a and 10.3b respectively. From the amplitude of both signals and the nature of the TPF signal at this power, it appears that most likely, a single particle is trapped. It can be seen that in raw data, both backscattered and TPF signals are not distinguishable at different average power, but after moving-averaging (over 100 data points), it is very clear in 9.40 mW average power (figure 10.3c). However, at 28.2 mW average power trapping signal is not very clear even after moving-averaging (marked within a circle in figure 10.3d) since at high average laser power background noise ratio is also increased significantly. It is clearly observed that the TPF signal rapidly decays over time due to photo-bleaching, and the backscattered signal persists as long as the particle is trapped. However, the TPF signal is useful to distinguish whether a (TPF) particle is trapped instead of a dust particle, which may also contribute to the backscattered signal. Therefore, simultaneous detection of both types of signals is necessary to track the particle's motion.

Figure 10.4 shows backscattered and TPF signal for a sample after prolonged (more than 3 hours) exposure when trapping of clusters (*i.e.* aggregates of 100 nm polystyrene particles suspended in water) were observed at 9.40 mW average power. Figures 10.4b shows the 100 point moving-averaging of raw data in figure 10.4a. It can be seen that after moving averaging data shows a smooth rise in

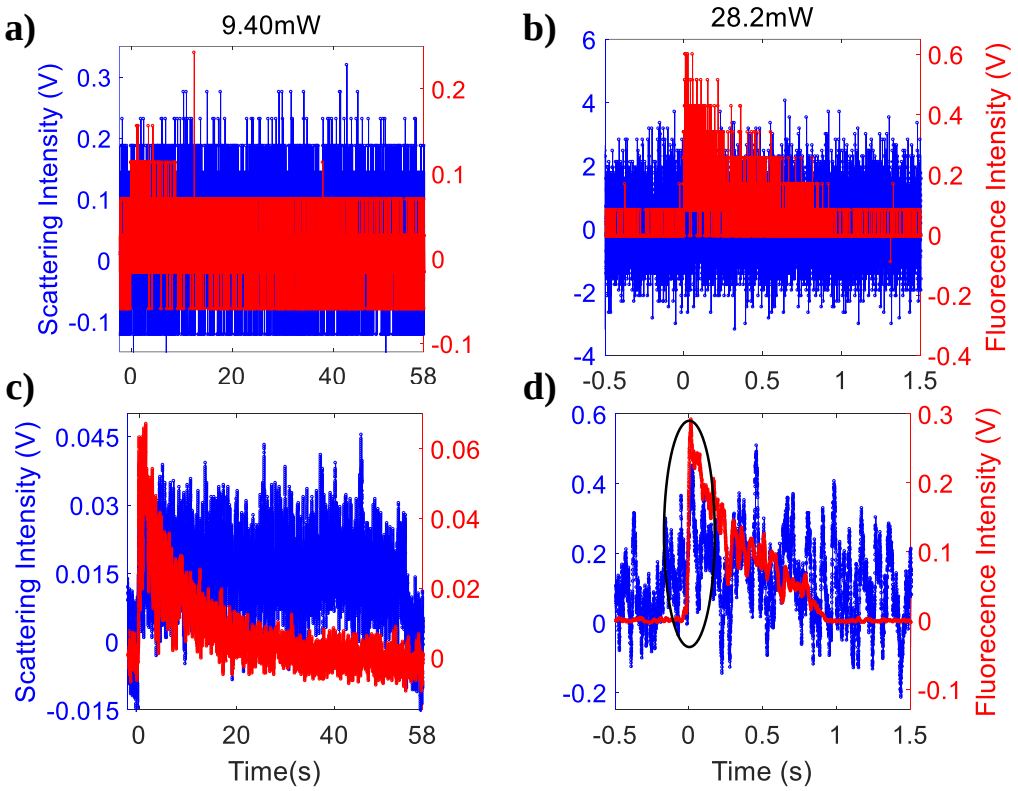

Fig. 10.3.: Plots of TPF and backscattered signals from a trapped single 100 nm fluorescent particle suspended in water at 9.40 mW (a & c) and 28.20 mW (b & d) average power respectively; top panel (a & b) corresponds to raw data and bottom panel (c & d) corresponds to the 100-point moving averaging of the raw data.

both backscattered and TPF signal. In figure 10.4a zoomed-in, the plot shows a sudden rise in signal followed by immediate fall, which may be due to PMT response or early time signal captured when the particle is adjusting inside the potential well. However, if we increase the number of data points more and more for moving averaging, then this early 'rise followed by fall' feature is lost by smoothing the data, and it becomes more difficult to get significant information about the particle's dynamics inside the potential well.

The rise part of the signal was fitted with a Sigmoidal (Boltzmann fit):

$$f = A_2 + \frac{A_1 - A_2}{1 + e^{\frac{t-t_0}{dt}}} \tag{10.3}$$

Figures 10.4c and 10.4d show the sigmoidal fit to the rise part backscattered data corresponds to figures 10.4a and 10.4b. In all these plots, the baseline is corrected according to A_1 and time zero is chosen corresponds to t_0 .

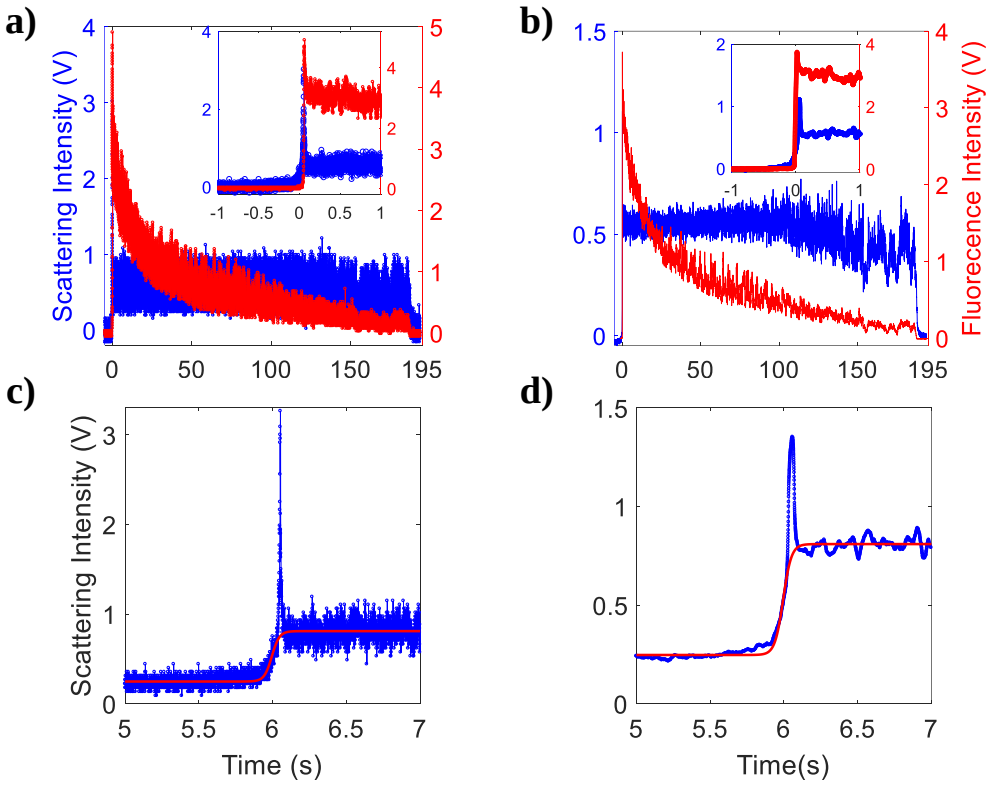

Fig. 10.4.: Plots of trapping signal for a cluster of 100 nm particle suspended in water at 9.40 mW average power a) raw data of TPF and backscattered signals; b) 100 point moving-averaging of raw data shown in figure a; c) sigmoidal fitting for backscattered data shown in figure a; b) sigmoidal fitting for 100 point moving-averaging of backscattered data shown in figure b.

Table 10.2 shows the sigmoidal fitting parameters for increasing the number of data points in moving-averaging. It can be observed that as we increase the number of data points, the fitting becomes better and smoother, but the rising time also increases monotonically; consequently, we lose information about the dragging of the particle inside the focal volume. We note that the time zero (t_0) remain the same, but A_1 and A_2 parameters decrease and increase respectively. This is because, as the number of data points for moving averaging increases, it becomes smoother and tries to maximize signal-to-noise ratio, which results in a decrease in background noise (or equivalently the baseline, A_1). However, this also increases the window of averaging, allowing the inclusion of the data points of the spike (corresponding to the adjustment dynamics), which results in a simultaneous increase in maximum (or equivalently A_2).

Figure 10.5 shows the FFT analysis of simultaneously detected signal for a cluster of particles at 9.40 mW average power, where red, blue, black, gray,

N	A_1	A_2	t_0	dt	R^2
Raw data	0.247	0.809	5.99	0.027	0.914
100	0.247	0.809	5.99	0.028	0.99
200	0.245	0.809	5.99	0.033	0.994
300	0.244	0.809	5.99	0.041	0.996
400	0.242	0.81	5.99	0.051	0.997
500	0.24	0.811	5.99	0.06	0.998
600	0.238	0.812	5.99	0.069	0.998
700	0.237	0.813	5.99	0.078	0.999
800	0.236	0.814	5.99	0.086	0.999
900	0.234	0.815	5.99	0.095	0.999
1000	0.233	0.817	5.99	0.103	0.999

Tab. 10.2.: The sigmoidal fitting parameter for increasing number of data points in moving averaging; N : number of data points chosen for moving averaging.

green curves correspond to TPF, backscattered, fitted curve, residual, FFT signals respectively. Figure 10.5a shows the decay of the TPF signal with time where the red curve corresponds to the raw data, and the black curve corresponds to the two exponential fits of the same. Figure 10.5b shows the residual signal obtained by subtracting the fitted curve from raw data. Figure 10.5c shows the FFT of the residual signal, and it can be observed that there are three frequencies (around 50 Hz, 150 Hz, and 250 Hz) as numbered (1, 2 and 3) in the zoomed inset. Figures 10.5d, 10.5e, and 10.5f are obtained in similar manner for 100-point moving averaging of TPF signal. Figures 10.5g, 10.5h, and 10.5i are obtained by following the same procedure for raw data of backscattered signal. It can be observed that the same frequencies are also observed, as shown in zoomed inset figure 10.5i. Figure 10.5j, 10.5k, and 10.5l are obtained in the similar manner for 100-point moving averaging of backscattered signal. The FFT after moving-averaging does not contain any unique frequency which implies that moving-averaging of signal leads to a loss in the information about the particle's dynamics. This behavior is evident from the figures 10.6a, 10.6b, & 10.6c and figure 10.6d, 10.6e, & 10.6f for both TPF and backscattered signals respectively, which shows 5-point, 20-point and 45-point moving averaging of the backscattered signal at 9.40 mW average power. It can be seen that loss in the information about particle dynamics increases as the number of points in moving averaging increases for both TPF and

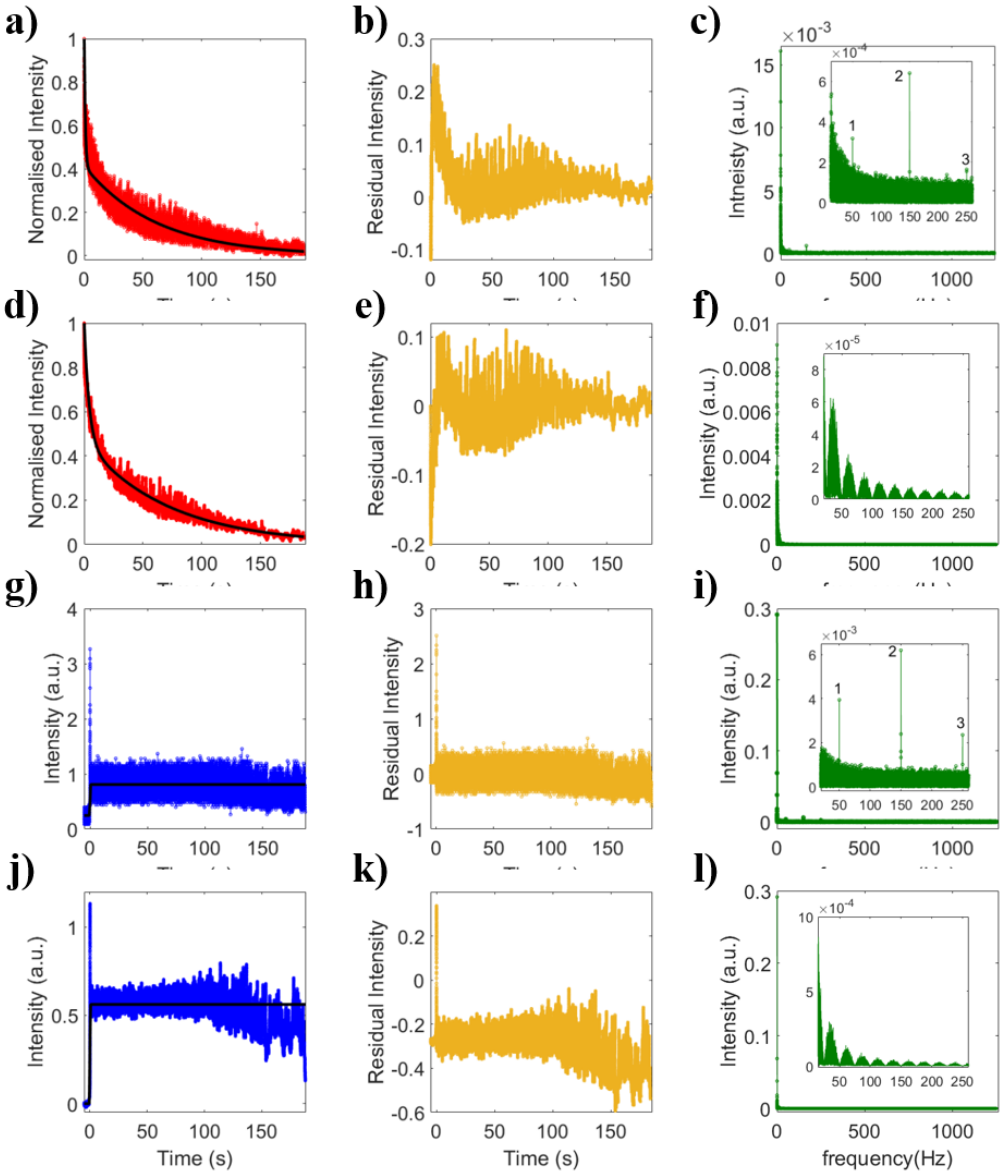

Fig. 10.5.: Plots of trapping signal for a cluster of 100 nm particle suspended in water at 9.40 mW average power; first row (a-c) corresponds to TPF signal; second row (d-f) corresponds to 100 points moving-averaging of TPF signal; third row (g-i) corresponds to backscattered signal; fourth row (j-l) corresponds to the 100 points moving-averaging of horizontal middle panel; however left panel (a, d, g, & j) corresponds to the raw data; vertical middle panel (b, e, h, & k) corresponds to the residual intensity obtained by subtracting fitted curve from raw data; right panel (c, f, i, & l) corresponds to FFT of residual signal.

backscattered signals. For 5-point moving-averaging, all the three frequencies are present, whereas 20-point moving-averaging shows two frequencies, 45-point moving-averaging shows one frequency, and 100-point moving-averaging shows no frequency. Starting from raw data, as the number of averaging points increases

(5-point, 20-point, 45-point, and 100-point), the frequency bandwidth decreases from 1250 Hz to 500 Hz, 125 Hz, 55.55 Hz, and 25 Hz, respectively. However, the trap stiffness could not be calculated as the number of particles in a cluster (and, hence, the mass of the cluster) cannot be accurately determined from both backscattered and TPF signals.

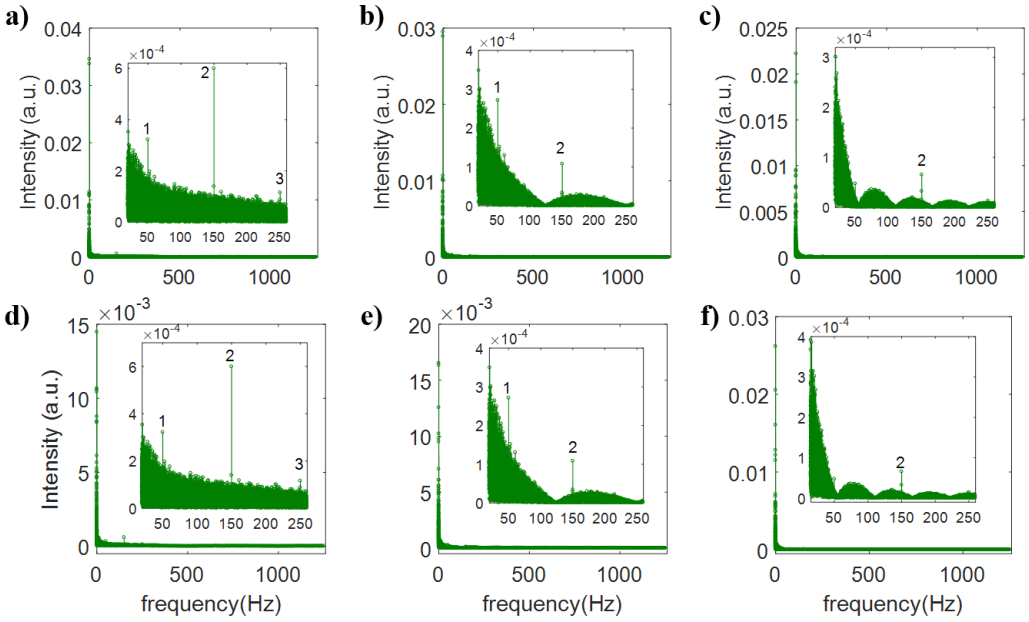

Fig. 10.6.: Plots of TPF and backscattered signals for a cluster of 100nm particle suspended in water at 9.40 mW average power; top panel (a-c) corresponds to the TPF signal, and bottom panel (d-f) corresponds to the backscattered signal, where left panel (a & d) corresponds to 5-point moving-averaging, middle panel (b & e) corresponds to 20-point moving-averaging, and right panel (c & f) corresponds to 45-point moving averaging.

10.3 Conclusion

We have demonstrated simultaneous detection of the signal to capture optical trapping dynamics of 100 nm polystyrene beads under high repetition rate femtosecond pulsed excitation and discussed the analysis of data emphasizing the usefulness and drawback of moving averaging method. From the FFT analysis signal, it can be concluded that the number of points for moving-averaging should be chosen judiciously in such a way that our signal should be smoothed enough to extract the information about the particle trapping dynamics but not at the expense of losing it.

Conclusion and future direction

11

We have shown that under high-repetition-rate ultrafast pulsed excitation, the optical Kerr effect plays a notable role in modulating the efficiency of optical trapping of both dielectric and metallic particles. Also, we have identified that the relevant parameter to quantify the trapping efficiency is escape potential along the direction of propagation and not the absolute depth of the potential. We have estimated the optimal average powers that lead to the most stable trap, which is extremely important in direct trapping of any arbitrarily sized particles. We have optimized the average power and particle size by fixing the other parameters in numerical simulations for micron to nanometer-sized particles using different theories such as dipole approximation, GO approximation, GLMT (using localized approximation), and EMT.

For large-sized particles, we have used GO approximation in which first, we have explored the role of OKE under pulsed excitation for the existing model (2D distribution of rays). However, we have found that the appropriate way to calculate the accurate force acting on the particle is to consider the rays as a light cone. Thus, we have systematically developed a general methodology for theoretically estimating optical force/potential in the GO limit using the 3D distribution of light cones for flat-top and Gaussian beam profiles, which circumvents the limitations of earlier theoretical formulation of using the 2D distribution of light rays for plane-wave excitation. Also, we compared our general methodology with EMT and found a good agreement than the existing model. Most importantly, we have shown that in GO approximation, the force acting on the particle is dependent on the particle size which was earlier believed to be independent of the particle size.

Next, we have addressed the issue of why high-repetition-rate ultrafast pulsed excitation is advantageous over CW excitation. Earlier, it was believed that pulsed excitation is advantageous for the trapping of nanometer-sized particles, as particle size decreases Brownian motion increases, so, to compensate random motion, we need very steep well to confine the particles. Apart from this, we have also shown that by taking advantage of OKE under pulsed excitation, we can trap the particles which have RI less than the surrounding medium, and also hollow-core type particles which cannot be trapped under CW excitation. We have determined that under CW excitation, particles having RI less than

surrounding medium and hollow-core type particles show the repulsive nature of force, whereas attractive nature of force under pulsed excitation at similar conditions. Thus, it can be observed that there is a certain regime of RI where CW excitation is unable to trap while pulsed excitation can trap the particles under similar conditions. The case is reversed when the RI of the particle is greater than the surrounding medium. If the particle has RI much higher than the surrounding medium, it cannot be trapped under both CW and pulsed excitation because scattering force dominates over gradient force and results in destabilizing the trap. Therefore, both CW and pulsed excitations have their advantages and disadvantages depending upon the RI of the particle and surrounding medium. Similarly, for metamaterials, RI regimes exist corresponding to the different nature of force/potential curves. In comparison with dielectric particles, the range of RI is the same for metamaterial particles under CW excitation but different under pulsed excitation for all regimes.

We have shown the trapping behavior of silver nanoparticles and studied the effect of the optical Kerr effect under high repetition-rate femtosecond pulsed excitation. The estimated forces on the small metal nanoparticles are larger than that of polystyrene nanoparticles of the same dimension. Most significantly, we observed the splitting of potential well into two wells along the axial direction where an increase in average power first potential well appear and then disappear. However, at high average power, a second well gets created while the first potential well disappears. This is useful to study long-range interaction between the nanoparticles since at least two particles can be trapped at two wells. No such effect was observed in the case of CW excitation in the case of dielectric particles. Experimentally, we have explored the dynamics of 100 nm and 1 μm polystyrene bead under both CW and pulsed excitation using wide-field microscopy as well as point detection mode.

We have observed experimentally that the TPF signal alone is inadequate to get information about particle dynamics as the particle gets photo-bleached while being trapped. To get the complete information about particle dynamics backscattered signal is the appropriate measure because it is present until the particle is confined within the optical trap. The height of the backscattered signal increases significantly when another particle is trapped, which helps to detect the dynamics of two particles. From the experimental results, it is evident that trapping of the particle occurs in three steps: dragging, stabilizing, and ejection. Since we are limited by fps of the camera while using the wide-field microscopy,

we have repeated the same experiment using point mode detection and observed that the trapping of the particle occurs in four steps rather than three steps. While experimenting using wide-field microscopy, we are not able to capture the adjustment dynamics. Consequently, the point detection method gives us rigorous information about the particle dynamics than wide-field microscopy, and four steps are as follows: dragging, adjusting, stabilizing, and ejection. Thus, when a single particle is dragged, first, it tries to adjust at the equilibrium position and stabilizes at the bottom of the potential well then accumulates energy over time. Laser-induced heating results in increasing the thermal fluctuations of the particle along both radial and axial directions over time. Due to an increase in the thermal fluctuations, the particle crosses the escape potential and leaves the trap. According to the experimental evidence, we have proposed a hypothetical model of mapping the nonlinear nature of optical trapping potential along with a detailed theory of trapping, including optical Kerr effect independent of particle size under pulsed excitation. Also, we have discussed the analysis of data emphasizing the usefulness and drawback of moving averaging method. From the signal analysis, it can be concluded that the number of points for moving-averaging should be chosen judiciously in such a way that our signal should be smoothed enough to extract the information about the particle trapping dynamics, but not at the expense of losing it. Considering the wide-ranging practical applications of optical tweezer, we envision the far-reaching application of tuning trapping force/potential by harnessing optical nonlinearity.

Our theoretical studies suggest that particles having RI less than the surrounding medium, as well as hollow-core type particles cannot be trapped under CW excitation, but it can be trapped under pulsed excitation utilizing the OKE. For a coherent understanding, the theoretical inference should correlate with the experimental observations. So, in the future, we will try to demonstrate it experimentally and map with theoretical studies using EMT. Till now, for 100 nm polystyrene particles, only preliminary work has been done. First, we would like to do a rigorous analysis of the experimental data for both these particles using the EMCCD camera in wide-field microscopy and point detection mode. We wish to explore the effect of OKE under pulsed excitation in the Maxwell Stress Tensor method. For core-shell particles, so far, we have explored the dipole approximation and GLMT approximation, so we would like to explore it using EMT, which applies to all sized particles. As of now, there has no theoretical calculation for core-shell particle under GO approximation; we would like to

solve this challenging problem for a general 3D light cone method.

In metallic particles, we have investigated the behavior of silver nanoparticles in an optical trap. Our next aim is to study the same for gold nanoparticles (400 nm and 10-20 nm nanosphere) both theoretically and experimentally. Since the nonlinear refractive index of gold is reported to be higher, we anticipate a better trapping efficiency for these particles and that the splitting of the potential well would occur at lower average power than that was observed in the case of silver particles. Also, we would include heating effects into consideration, as gold nanoparticles are more photothermally efficient. The effect of inter-band transition near resonance excitation will be a formidable task to understand.

Appendix A: Electric field for Gaussian beam

A

To write the electric field for any wave we have to use Maxwell's equations. Maxwell's equations for free space can be written as [170, 171]:

$$\bigtriangledown.E = 0 \tag{A.1}$$

$$\nabla \times E = -\frac{dB}{dt} \tag{A.2}$$

$$\bigtriangledown.B = 0 \tag{A.3}$$

$$\nabla \times B = \mu_0 \epsilon_0 \frac{dE}{dt} \tag{A.4}$$

In order to write the wave equation we have to solve Maxwell equation with vector identity:

$$\nabla \times (\nabla \times E) = \nabla (\nabla.E) - \nabla^2 E = \nabla \times \left(-\frac{dB}{dt}\right) = -\frac{d}{dt}(\nabla \times B) = -\mu_0 \epsilon_0 \frac{d^2 E}{dt^2} \tag{A.5}$$

Similarly, we can solve for the magnetic field:

$$\nabla^2 B(r,t) - \frac{1}{c^2}\frac{d^2 B(r,t)}{dt^2} = \nabla^2 E(r,t) - \frac{1}{c^2}\frac{d^2 E(r,t)}{dt^2} = \nabla^2 u(r,t) - \frac{1}{c^2}\frac{d^2 u(r,t)}{dt^2} = 0 \tag{A.6}$$

Using variable separable method we can consider $u(r,t) = u_1(r)\, u_2(t)$:

$$u_2(t)\, \nabla^2 u_1(r) - \frac{1}{c^2} u_1(r) \frac{d^2 u(t)}{dt^2} \Longleftrightarrow \frac{\nabla^2 u_1(r)}{u_1(r)} = \frac{1}{c^2 u_2(t)} \frac{d^2 u(t)}{dt^2} \tag{A.7}$$

From the above equation, it can be seen that left hand side expression is a function of radial part whereas right hand function is function of time only consequently both are independent and can be applied to any general case by equating with a separation constant and the constant $-k^2$ is chosen for convenience in the resulting solutions.

$$\frac{\nabla^2 u_1(r)}{u_1(r)} = \frac{1}{c^2 u_2(t)} \frac{d^2 u(t)}{dt^2} = -k^2 \tag{A.8}$$

$$\frac{\nabla^2 u_1(r)}{u_1(r)} = -k^2 \Longleftrightarrow \nabla^2 u_1(r) + k^2 u_1(r) = 0 \tag{A.9}$$

$$\frac{1}{c^2 u_2(t)} \frac{d^2 u_2(t)}{dt^2} = -k^2 \Longleftrightarrow \frac{d^2 u_2(t)}{dt^2} + k^2 c^2 u_2(t) = 0 \tag{A.10}$$

This equation is also known as Helmholtz equation. Here, the electric field is taken to be a complex function which is given by $E(x,y,z) = \psi(x,y,z)\, e^{-ikz}$ and equation becomes:

$$\left(\frac{\partial^2 \psi}{\partial x^2} + \frac{\partial^2 \psi}{\partial y^2} - 2ik\frac{\partial \psi}{\partial z}\right) e^{-ikz} = 0 \tag{A.11}$$

Now we apply paraxial approximation and assume that the solution of wave equation has cylindrical symmetry and hence can be rewritten in (r, ϕ, z) coordinates instead of (x, y, z) :

$$\frac{1}{r}\frac{\partial}{\partial r}\left(r\frac{\partial \psi}{\partial r}\right) - 2ik\frac{\partial \psi}{\partial z} = 0 \tag{A.12}$$

Using hit and trial method the solution of the wave equation is:

$$\psi = Ae^{-i\left(P(z) + \frac{kr^2}{2q(z)}\right)} \tag{A.13}$$

but this solution is valid for Gaussian beam TEM_{00} mode only. Using this equation becomes:

$$\frac{k^2}{q^2(z)}\left(\frac{dq(z)}{dz} - 1\right) r^2 - 2k\left(\frac{dP(z)}{dz} + i\frac{1}{q(z)}\right) = 0 \tag{A.14}$$

by equating the coefficient on both side

$$\frac{dq(z)}{dz} = 1 \tag{A.15}$$

$$\frac{dP(z)}{dz} = -i\frac{1}{q(z)} \tag{A.16}$$

solution of these equations is used to write the electric field:

$$E(x,y,z) = E_0 \frac{\omega_0}{\omega(z)} e^{-\frac{x^2+y^2}{\omega(z)^2}} e^{-i\frac{kr^2}{2R(z)}} e^{-ikz} e^{i\phi(z)} \tag{A.17}$$

In the above expression $E_0 \frac{\omega_0}{\omega(z)} e^{-\frac{x^2+y^2}{\omega(z)^2}}$ is known as propagation amplitude factor; where $\omega(z) = \omega_0\sqrt{1 + \left(\frac{z}{z_R}\right)^2}$ and z_R is Rayleigh length, $e^{-i\frac{kr^2}{2R(z)}}$ is longitudinal

phase factor, e^{-ikz} is wave propagation factor and $e^{i\phi(z)}$ corresponds to the phase shift of wave to spherical wave front. Using this, force can be written as:

$$F = \alpha \left(\frac{1}{2} \nabla \left(\left(E_0 \frac{\omega_0}{\omega\left(z\right)} \right)^2 e^{-\frac{2\left(x^2+y^2\right)}{\omega(z)^2}} \right) \right) \tag{A.18}$$

Appendix B: Calculation of polarizability

B

When a dielectric slab is placed inside a uniform electric field E, positive charge displace along the direction of electric field and negative charge opposite to the direction of field. Thus polarization P gets induced along the direction of electric field whose direction is taken from negative to positive by convention

$$P = D - \epsilon_0 E = \epsilon_0 (\epsilon_r - 1) E \tag{B.1}$$

Here, $E_{tot} = E + E_{int}$; E is applied field and E_{int} is a local field. In order to calculate the local field, an infinitesimally small spherical cavity of radius r is considered. The cavity is so small that the polarization vector P is not affected by it.
According to Gauss law [170]:

$$\int E.nds = \frac{q}{\epsilon_0} = \frac{\sigma.area}{\epsilon_0} \Longleftrightarrow dE_{int} = \frac{\sigma.area}{4\pi r^2 \epsilon_0} \tag{B.2}$$

Here $r.\hat{n} = rsin\theta$ and $area = 2\pi rsin\theta.rd\theta cos\theta$; $cos\theta$ factor arises because direction of area and unit vector are pointing at angle θ . The surface charge densities equal to | P| ≡ P and $\sigma = -P.\hat{n} = -Pcos\theta$.

$$dE_{int} = \int_0^{\pi} \frac{|P|cos\theta.2\pi rsin\theta.rd\theta cos\theta}{4\pi r^2 \epsilon_0} = \frac{|P|}{3\epsilon_0} \tag{B.3}$$

which implies

$$E_{tot} = E + \frac{|P|}{3\epsilon_0} \tag{B.4}$$

$$P = Np = N\alpha_e E_{tot} \Longleftrightarrow P = N\alpha \left(E + \frac{P}{3\epsilon_0}\right) \Longleftrightarrow P\left(1 - \frac{N\alpha_e P}{3\epsilon_0}\right) = N\alpha_e E \tag{B.5}$$

here p is dipole moment per atom and N is the number density (number of atoms or molecules per unit volume) [170]. After substituting this:

$$\epsilon_0 (\epsilon_r - 1) E \left(1 - \frac{N\alpha_e P}{3\epsilon_0}\right) = N\alpha E \Longleftrightarrow \alpha_e = \frac{3\epsilon_0}{N}\left(\frac{\epsilon_r - 1}{\epsilon_r + 2}\right) \tag{B.6}$$

This holds true when the surrounding medium considered as vacuum but if the outside medium have different permittivity (medium) the above expression

should be modified by replacing $\epsilon_r = \frac{\epsilon_1}{\epsilon_2}$; where ϵ_1 is permittivity of dielectric particle and ϵ_2 is permittivity of medium. Electronic polarizability can be written in terms of RI by using $\epsilon = n^2$:

$$\alpha_e = \frac{3\epsilon_0}{N}\left(\frac{m^2-1}{m^2+2}\right) \tag{B.7}$$

here, m is relative RI. This is known as Clausius-Mossotti relation [172]. In the field of the laser, the gradient force on an induced dipole is:

$$F_{gradient} = 4\pi\epsilon_0 a^3 n_m^2 \left(\frac{m^2-1}{m^2+2}\right)\left(\frac{1}{2}\nabla\left(\frac{2}{n_m\epsilon_0 c}I\left(r\right)\right)\right) = \frac{2\pi n_w a^3}{c}\left(\frac{m^2-1}{m^2+2}\right)\nabla I\left(r\right) \tag{B.8}$$

Appendix C: BSC for GLMT

C

The general expressions are derived from Maxwell's equation and the validity of approximation is verified by the same. The BSC mentioned here are applicable only for symmetric Gaussian beam which can be written in different ways using different approximation. In order to calculate the BSC, position of the object matters either it lies on on-axis (beam axis and particle axis coincide) or off axis (beam axis and particle axis are not coinciding). There are two BSC: $g^m_{n,\,TM}$ and $g^m_{n,\,TE}$, here one corresponds to transverse magnetic (TM) and another corresponds to transverse electric (TE) wave component which can be expressed as [109]:

$$g^m_{n,TM} = \frac{(2n+1)^2}{2\pi^2 n\,(n+1)\,C^{pw}_n}\frac{(n-|m|)!}{(n+|m|)!} \int_0^{\pi}\int_0^{2\pi}\int_0^{\infty}\frac{E_r\,(r,\theta,\phi)}{E_0} r\psi^{(1)}_n\,(kr)\,P^{|m|}_n\,(cos\theta)\,e^{-im\phi} sin\theta d\theta d\phi d\,(kr) \tag{C.1}$$

$$g^m_{n,TE} = \frac{(2n+1)^2}{2\pi^2 n\,(n+1)\,C^{pw}_n}\frac{(n-|m|)!}{(n+|m|)!} \int_0^{\pi}\int_0^{2\pi}\int_0^{\infty}\frac{H_r\,(r,\theta,\phi)}{H_0} r\psi^{(1)}_n\,(kr)\,P^{|m|}_n\,(cos\theta)\,e^{-im\phi} sin\theta d\theta d\phi d\,(kr) \tag{C.2}$$

For on-axis scattering calculations, $g^m_{n,\,TM}$ and $g^m_{n,\,TE}$ reduce to g_n and $z_0 = 0$ if beam axis and particle axis are coinciding. This can be calculated using three different methods [107]:

Rigorous Method

This is the most general way to calculate the BSC without any numerical approximation for on-axis paraxial approximation [107]:

$$g_n = \frac{2n+1}{(-1)^n\,i^{n-1}\pi n\,(n+1)} \int_0^{\pi}\int_0^{\infty} iQe^{-iQ\frac{r^2 Sin^2\theta}{\omega_0^2}+ikz_0-ikrcos\theta} kr\psi^1_n\,(kr)\,P^1_n\,(cos\theta)\,sin^2\theta d\theta d\,(kr) \tag{C.3}$$

Here, $Q = \frac{1}{i+\frac{2}{l}(z-z_0)}$; where $l = k\omega_0^2$ is spreading length, ω_0 is beam spot size, and k is propagation vector. This method is time consuming, it takes more than an hour to calculate one coefficient.

Finite Series Method

Finite series make expressions simpler and these expressions also called as rigorous expression because they are mathematically equivalent to the Quadrature when light beam incident description satisfies the Maxwell's equations. It was observed that this method is faster than the quadrature method. BSC in this case depend upon the value of n either it is odd or even and corresponding expressions are [107]:

$$g_{2n+1} = iQe^{ikz_0} \sum_{j=0}^{n} \frac{n!\Gamma\left(n+j+\frac{3}{2}\right)}{j!\,(n-j)!\Gamma\left(n+\frac{3}{2}\right)} \left(-4iQs^2\right)^j \tag{C.4}$$

$$g_{2n+2} = \frac{1}{k} e^{ikz_0} \sum_{j=0}^{p} \frac{n!\Gamma\left(n+j+\frac{3}{2}\right)}{j!\,(n-j)!\Gamma\left(n+\frac{5}{2}\right)} \left(A - \frac{jB}{iQ}\right) \left(-4iQs^2\right)^j \tag{C.5}$$

Here, $A = kiQ + k\frac{2}{kl\left(i-\frac{2z}{l}\right)^2} - \frac{2}{l}\varepsilon_L\,(iQ)^2$ and $B = -k\frac{2iQ}{kl\left(i-\frac{2z}{l}\right)^2}$; here $s = \frac{1}{k\omega_0} = \frac{\omega_0}{l}$. When modified light beam incident on the particle in case for quadrature method we have to change only quadrature integral while in finite series method we have to all the analytical work from the beginning and significant program modifications are required when the beam description is modified. In short, this is not a general theory which is applicable for all type of incident beams.

Localized approximation

By taking the advantage of principle of localization of Van de Hulst a localized approximation was developed which reduces computation time a lot and corresponding expression is [107]:

$$g_n = i\frac{1}{i+2\frac{z-z_0}{k*\omega_0^2}} exp\left[-i\frac{1}{i+2\frac{z-z_0}{k*\omega_0^2}}\left(\frac{\left(\frac{n+1/2}{2\pi}\right)\lambda}{\omega_0}\right)^2\right] * exp\left[ikz_0\right] \tag{C.6}$$

Here n is the order term of Bessel functions and spherical harmonics which can vary from 1 to ∞ .

Appendix D: Methods for incorporating OKE

D

There are two methods to incorporate OKE into account, one is considering nonlinearity susceptibility, and another is a nonlinear RI, which is rigorously discussed below:

Method 1

In literature, two methods exist to incorporate the nonlinearity into account. Since we know $p = \alpha.E$; here α is polarizability and **E** is applied an electric field. Here, we have discussed both the methods and proved that at the end both are same [173]:

$$p\left(r,t\right) = \frac{\alpha_e\left(r,t\right)}{1-\iota\frac{\alpha_e(r,t)k^3}{6\pi\epsilon_0}}\left|E\left(r,t\right)\right| \tag{D.1}$$

$$\alpha = \frac{\alpha_e\left(r,t\right)}{1-\iota\frac{\alpha_e(r,t)k^3}{6\pi\epsilon_0}} = \frac{\alpha_e\left(r,t\right)+\iota\left(\frac{\alpha_e(r,t)^2k^3}{6\pi\epsilon_0}\right)}{1+\left(\frac{\alpha_e(r,t)k^3}{6\pi\epsilon_0}\right)^2} \tag{D.2}$$

$$\alpha_e\left(r,t\right) = 4\pi\epsilon_0 a^3\left(\frac{\chi_1+\chi_3\left|E\left(r,t\right)\right|^2}{\chi_1+\chi_3\left|E\left(r,t\right)\right|^2+3}\right) \tag{D.3}$$

$$\alpha = \frac{4\pi\epsilon_0 a^3\left(\frac{\chi_1+\chi_3|E(r,t)|^2}{\chi_1+\chi_3|E(r,t)|^2+3}\right)+i\left(\frac{16\pi^2\epsilon_0^2a^6k^3}{6\pi\epsilon_0}\left(\frac{\chi_1+\chi_3|E(r,t)|^2}{\chi_1+\chi_3|E(r,t)|^2+3}\right)^2\right)}{1+\frac{16\pi^2\epsilon_0^2a^6k^3}{36\pi^2\epsilon_0^2}\left(\frac{\chi_1+\chi_3|E(r,t)|^2}{\chi_1+\chi_3|E(r,t)|^2+3}\right)^2} \tag{D.4}$$

$$Re\left[\alpha\right] = \frac{4\pi\epsilon_0 a^3\left(\frac{\chi_1+\chi_3|E(r,t)|^2}{\chi_1+\chi_3|E(r,t)|^2+3}\right)}{1+\frac{4a^6k^3}{9}\left(\frac{\chi_1+\chi_3|E(r,t)|^2}{\chi_1+\chi_3|E(r,t)|^2+3}\right)^2} \tag{D.5}$$

$$Im\left[\alpha\right] = \frac{\frac{8\pi\epsilon_0a^6k^3}{3}\left(\frac{\chi_1+\chi_3|E(r,t)|^2}{\chi_1+\chi_3|E(r,t)|^2+3}\right)^2}{1+\frac{4a^6k^3}{9}\left(\frac{\chi_1+\chi_3|E(r,t)|^2}{\chi_1+\chi_3|E(r,t)|^2+3}\right)^2} \tag{D.6}$$

After using Taylor expansion and neglecting higher order terms:

$$Re\left[\alpha\right] = \frac{4\pi\epsilon_0a^3\epsilon\frac{\chi_1}{\chi_1+3}\left(\frac{1+3\chi_3|E(r,t)|^2}{\chi_1(\chi_1+3)}\right)}{1+\frac{4a^6k^3}{9}\left(\frac{\chi_1}{\chi_1+3}\right)^2\left(1+\frac{6\chi_3}{\chi_1(\chi_1+3)}|E\left(r,t\right)|^2\right)} \tag{D.7}$$

$$Re\left[\alpha\right]=4\pi\epsilon_0 a^3\frac{\chi_1}{\chi_1+3}-\frac{16\pi\epsilon_0 a^9k^3\chi_1^3}{9\left(\chi_1+3\right)^3}+\left(\frac{12\pi\epsilon_0 a^3\chi_1}{\chi_1\left(\chi_1+3\right)^2}-\frac{16\pi\epsilon_0 k^3\chi_1^3a^9}{\chi_1\left(\chi_1+3\right)^4}\right)\chi_3|E\left(r,t\right)|^2 \tag{D.8}$$

here, $\chi_1=\frac{\epsilon_p}{\epsilon_w}-1=\frac{n_p^2}{n_w^2}-1=m^2-1$; m is the ratio of particle RI to medium (water). Above equation can be rewritten as:

$$\begin{aligned}Re\left[\alpha\right]&=4\pi\epsilon_0 a^3\left(\frac{m^2-1}{m^2+2}\right)\left(1-\frac{4k^3a^6}{9}\left(\frac{m^2-1}{m^2+2}\right)^2\right)\\&+\frac{12\pi\epsilon_0 a^3}{\left(m^2+2\right)^2}\left(1-\frac{4k^3a^6}{3}\left(\frac{m^2-1}{m^2+2}\right)^2\right)\chi_3|E\left(r,t\right)|^2\end{aligned} \tag{D.9}$$

In the above expression $\frac{4a^6k^3}{3}\left(\frac{m^2-1}{m^2+2}\right)^2$ is very small compare to 1 so, it can be neglected from the above expression for simplicity.

$$Re\left[\alpha\right]=4\pi\epsilon_0 a^3\left(\frac{m^2-1}{m^2+2}\right)+\frac{12\pi\epsilon_0 a^3}{\left(m^2+2\right)^2}\chi_3|E\left(r,t\right)|^2 \tag{D.10}$$

Here first highlighted part is a linear part and the second part of the above expression is due to nonlinear effects. Similarly, we can solve the imaginary part of the α :

$$\begin{aligned}Im\left[\alpha\right]&=\frac{8\pi\epsilon_0 a^6k^3}{3}\left(\frac{m^2-1}{m^2+2}\right)^2\left(1-\frac{4a^6k^3}{9}\left(\frac{m^2-1}{m^2+2}\right)^2\right)\\&+\left(\frac{8\pi\epsilon_0 a^6k^3n_w}{3}\left(6-\frac{16a^6k^3}{3}\left(\frac{m^2-1}{m^2+2}\right)^2\right)\times\frac{m^2-1}{\left(m^2+2\right)^3}\right)\chi_3|E\left(r,t\right)|^2\end{aligned} \tag{D.11}$$

In the above expression $\frac{4a^6k^3}{9}\left(\frac{m^2-1}{m^2+2}\right)^2$ and $\frac{192a^6k^3}{27}\left(\frac{m^2-1}{m^2+2}\right)^2$ factors are very less compared to 1. Consequently, they does not contribute significantly, can be neglected. So, above expression can be rewritten as:

$$Im\left[\alpha\right]=\frac{8\pi\epsilon_0 a^6k^3}{3}\left(\frac{m^2-1}{m^2+2}\right)^2+16\pi\epsilon_0 a^6k^3\left(\frac{m^2-1}{\left(m^2+2\right)^3}\right)\chi_3|E\left(r,t\right)|^2 \tag{D.12}$$

In order to calculate the force acting on the particle is:

$$\left\langle F\left(r,t\right)\right\rangle=\left(p\left(r,t\right).\nabla\right)E\left(r,t\right)+\frac{1}{c}\frac{\partial p\left(r,t\right)}{\partial t}\times B\left(r,t\right) \tag{D.13}$$

This can also be written as [174, 175]:

$$\langle F(r,t)\rangle = Re\left[(p(r,t).\nabla)\right] Re\left[E(r,t)\right] + \frac{1}{c} Re\left[\frac{\partial p(r,t)}{\partial t}\right] \times Re\left[B(r,t)\right] \quad \text{(D.14)}$$

Time-averaged force can be written as:

$$\langle F(r,t)\rangle = \frac{1}{2} Re\left[(p(r,t).\nabla) E(r,t) + ikp(r,t) \times B(r,t)\right] \quad \text{(D.15)}$$

where $k = \frac{\omega}{c}$ and this expression can be re written as:

$$\langle F(r,t)\rangle = \frac{1}{2} Re\left[\alpha\right] (E(r,t).\nabla) E(r,t) + ik\alpha^* E(r,t) \times B(r,t) \quad \text{(D.16)}$$

$$\begin{aligned} \langle F(r,t)\rangle = \frac{1}{2} & Re\left[\alpha\right] Re\left[(E(r,t).\nabla) E(r,t)\right] \\ & + Im\left[\alpha\right] Im\left[(E(r,t).\nabla) E(r,t)\right] \\ & + kIm\left[\alpha\right] Im\left[E^*(r,t) \times B(r,t)\right] \\ & - kRe\left[\alpha\right] Im\left[E^*(r,t) \times B(r,t)\right] \end{aligned} \quad \text{(D.17)}$$

To further simplify this equation we have used vector identity:

$$\begin{aligned} \langle F(r,t)\rangle = & \frac{1}{4} Re\left[\alpha\right] \nabla |E(r,t)|^2 + \frac{k}{2} Im\left[\alpha\right] Re\left[E^*(r,t) \times B(r,t)\right] \\ & + \frac{1}{2} Im\left[\alpha\right] Im\left[(E^*(r,t).\nabla) E(r,t)\right] \end{aligned} \quad \text{(D.18)}$$

The first term is the gradient force. The second term is the scattering or radiation-pressure force. The third term is unnamed in the literature [174, 176].
It can be rewritten using the following identity:

$$\nabla\left(\frac{1}{2}|E(r,t)|^2\right) = (E^*(r,t).\nabla) E(r,t) + E^*(r,t) \times \nabla \times E(r,t) \quad \text{(D.19)}$$

$$\nabla(a.b) = (a.\nabla) b + (b.\nabla) a + a \times (\nabla \times b) + b \times (\nabla \times a) \quad \text{(D.20)}$$

$$(a \times b) \times c = c \times (b \times a) \quad \text{(D.21)}$$

$$\begin{aligned}\frac{k}{2}Im\left(\alpha\right)Re\left[E\left(r,t\right)\times B\left(r,t\right)\right] &= \frac{1}{2}Im\left(\alpha\right)Im\left[E^{*}\left(r,t\right)\times\nabla\times E\left(r,t\right)\right]\\ &= \frac{1}{2}Im\left(\alpha\right)Im\left[E\left(r,t\right)\times\nabla\times E^{*}\left(r,t\right)\right]\end{aligned} \tag{D.22}$$

This can be further simplified as:

$$\begin{aligned}\frac{k}{\epsilon_0 c}Im\left(\alpha\right)\left\langle S\left(r,t\right)\right\rangle_{Orb} &= \frac{k}{\epsilon_0 c}Im\left(\alpha\right)\left(\left\langle S\left(r,t\right)\right\rangle+\frac{\epsilon_0 c}{2k}Im\left[\left(E^{*}\left(r,t\right).\nabla\right)E\left(r,t\right)\right]\right)\\ &= \frac{k}{\epsilon_0 c}Im\left(\alpha\right)\left(\frac{1}{2\mu_0\omega}Im\left(E\left(r,t\right)\times\left(\nabla\times E^{*}\left(r,t\right)\right)\right)\right)\\ &+\frac{\epsilon_0 c}{2k}Im\left[\left(E^{*}\left(r,t\right).\nabla\right)E\left(r,t\right)\right]\end{aligned} \tag{D.23}$$

Using above equations it can be written as:

$$\begin{aligned}\frac{k}{\epsilon_0 c}Im\left(\alpha\right)\left\langle S\left(r,t\right)\right\rangle_{Orb} &= \frac{k}{\epsilon_0 c}Im\left(\alpha\right)\left(\frac{\epsilon_0 c}{2k}Im\left(\nabla\left(\frac{1}{2}|E\left(r,t\right)|^{2}\right)\right)\right)\\ &-\frac{k}{\epsilon_0 c}Im\left(\alpha\right)\left(\left(E^{*}\left(r,t\right)\times\left(\nabla\times E\left(r,t\right)\right)\right)\right)\\ &+\frac{k}{\epsilon_0 c}Im\left(\alpha\right)\left(\frac{1}{2\mu_0\omega}Im\left(E\left(r,t\right)\times\left(\nabla\times E^{*}\left(r,t\right)\right)\right)\right)\end{aligned} \tag{D.24}$$

$$\begin{aligned}\frac{k}{\epsilon_0 c}Im\left(\alpha\right)\left\langle S\left(r,t\right)\right\rangle_{Orb} &= \frac{k}{\epsilon_0 c}Im\left(\alpha\right)\left(\frac{\epsilon_0 c}{2k}Im\left(\nabla\left(\frac{1}{2}|E\left(r,t\right)|^{2}\right)\right)\right)\\ &+\left(\frac{k}{2\mu_0\omega}+\frac{\epsilon_0 c}{2}\right)Re\left[E^{*}\left(r,t\right)\times B\left(r,t\right)\right]\end{aligned} \tag{D.25}$$

which implies,

$$\frac{k}{\epsilon_0 c}*\left(\frac{k}{2\mu_0\omega}+\frac{\epsilon_0 c}{2}\right)=\frac{k}{2\epsilon_0 c}\left(\frac{1}{\mu_0 c}+\epsilon_0 c\right)=\frac{k}{2\epsilon_0 c}\left(\frac{1+\mu_0\epsilon_0 c^{2}}{\mu_0 c}\right)=\frac{k}{2\epsilon_0 c}*\frac{2}{\mu_0 c}=k \tag{D.26}$$

Above equation becomes:

$$\begin{aligned}\frac{k}{\epsilon_0 c}Im\left(\alpha\right)\left\langle E\left(r,t\right)\right\rangle_{Orb} &= \frac{1}{2}Im\left(\alpha\right)Im\left[\left(E^{*}\left(r,t\right).\nabla\right)E\left(r,t\right)\right]\\ &-\frac{1}{2}Im\left(\alpha\right)Im\left[E^{*}\left(r,t\right)\times\left(\nabla\times E\left(r,t\right)\right)\right]\\ &+kIm\left(\alpha\right)Re\left[E^{*}\left(r,t\right)\times B\left(r,t\right)\right]\end{aligned} \tag{D.27}$$

This can be simplified as:

$$\begin{aligned}\frac{k}{\epsilon_0 c} Im\left(\alpha\right)\left\langle S\left(r,t\right)\right\rangle_{Orb} &= \frac{1}{2} Im\left(\alpha\right) Im\left[\left(E^{*}\left(r,t\right).\nabla\right) E\left(r,t\right)\right] \\ &- \frac{k}{2} Im\left(\alpha\right) Re\left[E^{*}\left(r,t\right)\times B\left(r,t\right)\right] \\ &+ kIm\left(\alpha\right) Re\left[E^{*}\left(r,t\right)\times B\left(r,t\right)\right]\end{aligned} \tag{D.28}$$

$$\begin{aligned}\frac{k}{\epsilon_0 c} Im\left(\alpha\right)\left\langle S\left(r,t\right)\right\rangle_{Orb} &= \frac{1}{2} Im\left(\alpha\right) Im\left[\left(E^{*}\left(r,t\right).\nabla\right) E\left(r,t\right)\right] \\ &+ \frac{k}{2} Im\left(\alpha\right) Re\left[E^{*}\left(r,t\right)\times B\left(r,t\right)\right]\end{aligned} \tag{D.29}$$

after rearranging the term it can be written as:

$$\begin{aligned}\left\langle F\left(r,t\right)\right\rangle &= \frac{1}{4} Re\left[\alpha\right]\nabla|E\left(r,t\right)|^{2} + \frac{k}{2} Im\left[\alpha\right] Re\left[E^{*}\left(r,t\right)\times B\left(r,t\right)\right] \\ &+ \frac{1}{2} Im\left[\alpha\right] Im\left[\left(E^{*}\left(r,t\right).\nabla\right) E\left(r,t\right)\right]\end{aligned} \tag{D.30}$$

It can be seen that the first term is gradient and the second term is scattering force and the third term doesn't have much of the contribution to the total force compare to gradient and scattering force [176]. Here polarizability is:

$$\begin{aligned}\alpha &= Re\left[\alpha\right] + Im\left[\alpha\right] \\ &= 4\pi\epsilon_0 a^{3}\left(\frac{m^{2}-1}{m^{2}+2}\right) + i\frac{8\pi\epsilon_0 a^{6}k^{3}}{3}\left(\frac{m^{2}-1}{m^{2}+2}\right)^{2} \\ &+ \left[\frac{12\pi\epsilon_0 a^{3}}{\left(m^{2}+2\right)^{2}} + i16\pi\epsilon_0 a^{6}k^{3}\left(\frac{m^{2}-1}{\left(m^{2}+2\right)^{3}}\right)\right]\chi_3|E\left(r,t\right)|^{2}\end{aligned} \tag{D.31}$$

$$\begin{aligned}\left\langle F_{grad}\left(r,t\right)\right\rangle_{T} &= \frac{1}{4} Re\left[\alpha\right]\nabla|E_0|^{2} \\ &= \pi\epsilon_0 a^{3}\left(\left(\frac{m^{2}-1}{m^{2}+2}\right) + \frac{3}{\left(m^{2}+2\right)^{2}}\chi_3|E\left(r,t\right)|^{2}\right)\nabla|E\left(r,t\right)|^{2}\end{aligned} \tag{D.32}$$

$$\begin{aligned}\left\langle F_{scattering}\left(r,t\right)\right\rangle_{T} &= \frac{k}{2} Im\left[\alpha\right] Re\left[E_0^{*}\times B_0\right] \\ &= \left[\frac{8\pi a^{6}k^{4}n_w}{3c}\left(\frac{m^{2}-1}{m^{2}+2}\right)^{2} + 6\left(\frac{m^{2}-1}{\left(m^{2}+2\right)^{3}}\right)\chi_3|E\left(r,t\right)|^{2}\right] I\left(r\right)\end{aligned} \tag{D.33}$$

Method 2

In this method, polarizability is considered in terms of RI instead of susceptibility and corresponding expression can be expressed as:

$$\alpha = 4\pi\epsilon_0 a^3 \left(\frac{m^2-1}{m^2+2}\right) = 4\pi\epsilon_0 a^3 \left(\frac{n_p^2-n_w^2}{n_p^2+2n_w^2}\right) \tag{D.34}$$

In the above expression substitute $n_p = n_0^p + n_2^p I\left(r,t\right)$ and $n_w = n_0^w + n_2^w I\left(r,t\right)$

$$\alpha = 4\pi\epsilon_0 a^3 \left(\frac{\left(n_0^p + n_2^p I\left(r,t\right)\right)^2 - \left(n_0^w + n_2^w I\left(r,t\right)\right)^2}{\left(n_0^p + n_2^p I\left(r,t\right)\right)^2 + 2\left(n_0^w + n_2^w I\left(r,t\right)\right)^2}\right) \tag{D.35}$$

Neglecting higher order term we can rewrite it as:

$$\alpha = 4\pi\epsilon_0 a^3 \left(\frac{\left(n_0^p\right)^2 - \left(n_0^w\right)^2 + 2\left(n_0^p n_2^p - n_0^w n_2^w\right) I\left(r,t\right)}{\left(n_0^p\right)^2 + 2\left(n_0^w\right)^2 + 2\left(n_0^p n_2^p + 2n_0^w n_2^w\right) I\left(r,t\right)}\right) \tag{D.36}$$

Let us consider $M = m^2 - 1$; where m is the ratio of particle RI to medium RI.

$$\alpha = 4\pi\epsilon_0 a^3 \left(\frac{\left(n_0^w\right)^2 M + 2\left(n_0^p n_2^p - n_0^w n_2^w\right) I\left(r,t\right)}{\left(n_0^w\right)^2 \left(M+3\right)\left(1 + \frac{2\left(n_0^p n_2^p - n_0^w n_2^w\right)}{\left(n_0^w\right)^2 (M+3)} I\left(r,t\right)\right)}\right) \tag{D.37}$$

After Taylor expansion:

$$\alpha = 4\pi\epsilon_0 a^3 \left(\frac{M}{M+3} + \frac{6\left(n_0^p n_2^p - n_0^w n_2^w\left(M+1\right)\right) I\left(r,t\right)}{\left(n_0^w\right)^2 \left(M+3\right)^2}\right) \tag{D.38}$$

In the above expression $n_0^p n_2^p \gg n_0^w n_2^w$

$$\alpha = 4\pi\epsilon_0 a^3 \left(\frac{m^2-1}{m^2+2} + \frac{6 n_0^p n_2^p I\left(r,t\right)}{\left(n_0^w\right)^2 \left(m^2+2\right)^2}\right) \tag{D.39}$$

Force acting on the particle is:

$$F_{grad}\left(r,t\right) = \left[p\left(r,t\right).\nabla\right] E\left(r,t\right) \tag{D.40}$$

$$\left\langle F_{grad}\left(r,t\right)\right\rangle_T = \pi\epsilon_0 a^3 \left(\frac{m^2-1}{m^2+2} + \frac{3}{\left(m^2+2\right)^2} \frac{2n_0^p n_2^p I\left(r\right)}{\left(n_0^w\right)^2}\right) \nabla |E_0|^2 \tag{D.41}$$

$$\langle F_{scattering}\left(r,t\right)\rangle_T = \frac{8\pi k^4 a^6 n_w}{3c}\left(\left(\frac{m^2-1}{m^2+2}\right)^2 + 6\left(\frac{m^2-1}{\left(m^2+2\right)^3}\right)\frac{2n_0^p n_2^p I\left(r\right)}{\left(n_0^w\right)^2}\right) I\left(r\right) \tag{D.42}$$

Hence, either we incorporate nonlinearity through susceptibility or RI both the methods gives the approximately similar force expresssions.

Appendix E: Fano-resonance

E

Fano-resonances occur due to the interference between two scattering amplitudes: scattering amplitude of resonance and background. If the scattering amplitudes of the resonance and the background are of comparable magnitude, the cross-section of the Fano resonance follows an asymmetric line shape. Fano-resonance helps to achieve negative optical scattering force (NOSF) for nanoparticles. Fano-resonance is characterized by the asymmetric Lorentz spectral profile and symmetry breaks inside the system where there is non-uniform electromagnetic environment. An asymmetric scattering (Lorentz spectral profile) appears, when forward scattering is significantly enhanced, while the backscattered light is reduced, leading to considerable attenuation of forwarding scattering force along the direction of light propagation and resulting in a net NOSF [130, 135, 177, 178]. The role of Fano-resonance is important in modifying the longitudinal optical scattering force in which the Lorentz shape of scattering force shows reversal nature (positive to negative), either with the phase shift changes or due to higher frequencies. This reversal nature of scattering force occurs only when we lie in the Fano-dip regime [130, 135]. Fano resonance is a prominent effect in the case of the metallic particle but we have done our simulations for dielectric nanoparticles [178, 179]. Researchers have explored the Fano-resonance phenomena for core-shell (metal-dielectric; Au-ZnS, Au-CdS, Au-silica) and hollow dielectric (CdS, ZnS, and silica) nanoparticles. They have observed that Fano-resonance occurs due to strong interference between the plasmonic resonance of metallic core and background scattering of dielectric shell. They found that in the case of Au-ZnS, Fano-resonance peak is obtained at 556 nm, and full-width half maxima of the peak is $\sim$ 66 nm. With an increase in the gap between core and shell, a blue shift is observed in the Fano-resonance peak. Consequently, for hollow ZnS, Fano-resonance peak is observed at 380 nm. Similarly, for Au-CdS and Au-silica, the peaks are obtained $\sim$ 627 nm and $\sim$ 572 nm respectively. From reference [179], it can be seen that there is no Fano-resonance process occurring at $\sim$ 800nm, even for higher refractive index dielectric nanoparticles [179]. Since we are using 800nm wavelength, away from the resonance, these effects can be ignored for dielectric nanoparticles. The noticeable point here is that in this letter, we are discussing reversal nature (repulsive to attractive) of gradient force instead of scattering force, and this reversal nature of force occurs only when we

take nonlinearity into account for similar conditions. Another important point is that in the case of Fano-resonance this reversal nature occurs only along lateral direction because transverse optical force vanishes due to azimuthal symmetry [135]. However, including nonlinearity shows the reversal nature of the gradient force curve along both radial and axial directions. Along axial direction, we have two forces, one is gradient and another one is scattering force whereas along radial direction we have gradient force only.

Appendix F: Thermal nonlinearity

F

Nonlinearity is incorporated in a phenomenological way as:

$$n^{w/p} = n_0^{w/p} + n_2^{w/p} * I_{(peak/average)}(r,z) \tag{F.1}$$

here, $n_0^{(w/p)}$ and $n_2^{(w/p)}$ are the linear and nonlinear refractive index of medium/-particle, respectively. Nonlinear refractive index involves many processes such as electronic polarizability, molecular reorientation, electrostrictive, and thermal effects, and all these can be expressed as [180]

$$n_2^{w/p} = n_{2,\,electronic}^{w/p} + n_{2,\,molecular\,re-orientation}^{w/p} + n_{2,\,electrostrictive}^{w/p} + n_{2,\,thermal}^{w/p} \tag{F.2}$$

In case of water and polystyrene, the major contribution in nonlinear refractive index is from electronic polarizability and thermal effects as compared to other effects, on that account the effect of molecular reoriention and electrostrctive can be ignored. In addition, it is well known that thermal effect contribute significantly when the time delay between two pulses is less than thermal diffusion time ($t_c = \frac{\omega_0^2}{4D}$; ω_0 is beam spot size and D is thermal diffusion coefficient), and in our experiment $t_c \sim 3\mu s$ and $t_{pulse} \sim 12ns$. Therefore, thermal effects contribution can not be ignored. Also, the contribution of electronic polarizability in nonlinear refractive index for water is very small as compared to the polystyrene, even at the high average power ($\sim 100mW$) near geometric focus, the effect is negligible; consequently, it can be neglected for both CW/pulsed excitations. From the previously done experiments, it has been observed that while trapping the main contribution of thermal nonlinearity or heaing is due to surrounding medium, therefore the minor contribution from the trapped particle can be ignored [92]. The change in refractive index due to thermal nonlinearity can be expresses as: $\frac{dn}{dT}\Delta T$; where, $\frac{dn}{dT}$ is thermo-optic coefficient, and ΔT is change in temperature. In our simulations, we considered $n^w \approx n_0^w$ & $n^p \approx n_0^w$ for CW excitation and $n^w = n_0^w + \frac{dn}{dT}\Delta T$ & $n^p = n_0^p + n_2^p * I_{peak}(r,z)$ for pulsed excitation, respectively. The change in temperature (ΔT) can be calculated using following relation [92]:

$$\Delta T = \frac{\alpha P_{peak}}{2\pi C}\left(ln\left(2\pi R/\lambda\right) - 1\right) \tag{F.3}$$

here, α is the absorption factor, C is thermal conductivity, λ is the wavelength of trapping beam, and R is the distance of the bead from coverglass slide.

Bibliography

1. Ashkin, A. Acceleration and Trapping of Particles by Radiation Pressure. *Phys. Rev. Lett.* **24 (4),** 156–159. eprint: https://link.aps.org/doi/10.1103/PhysRevLett.24.156 (1970) (cit. on pp. 1–5).

2. Yan, J., Skoko, D. & Marko, J. F. Near-field-magnetic-tweezer manipulation of single DNA molecules. *Phys. Rev. E* **70 (1),** 011905. eprint: https://link.aps.org/doi/10.1103/PhysRevE.70.011905 (2004) (cit. on pp. 1, 9).

3. Yu, Y., Qiu, W., Chiu, B. & Sun, L. Feasibility of Multiple Micro Particle Trapping A Simulation Study. *Sensors* **15,** 4958–4974. eprint: http://www.mdpi.com/1424-8220/15/3/4958 (2015) (cit. on p. 1).

4. Son, M., Choi, S., Ko, K. H., *et al.* Characterization of the Stiffness of Multiple Particles Trapped by Dielectrophoretic Tweezers in a Microfluidic Device. *Langmuir* **32.** PMID: 26734855, 922–927. eprint: https://doi.org/10.1021/acs.langmuir.5b03677 (2016) (cit. on p. 1).

5. Zhou, Y., Basu, S., Wohlfahrt, K. J., *et al.* A microfluidic platform for trapping, releasing and superresolution imaging of single cells. *Sensors and Actuators B: Chemical* **232,** 680–691. eprint: https://www.sciencedirect.com/science/article/pii/S0925400516304257 (2016) (cit. on p. 1).

6. Ashkin, A. & Dziedzic, J. Optical trapping and manipulation of viruses and bacteria. *Science* **4795.** eprint: https://science.sciencemag.org/content/235/4795/1517 (1987) (cit. on pp. 1, 5, 6, 8).

7. Buican, T. N., Smyth, M. J., Crissman, H. A., *et al.* Automated single-cell manipulation and sorting by light trapping. *Appl. Opt.* **26,** 5311–5316. eprint: http://ao.osa.org/abstract.cfm?URI=ao-26-24-5311 (1987) (cit. on p. 1).

8. Ashkin, A., Dziedzic, J. & Yamane, T. Optical trapping and manipulation of single cells using infrared laser beams. *nat* **330,** 769–771. eprint: http://adsabs.harvard.edu/abs/1987Natur.330..769A (1987) (cit. on pp. 1, 5, 6).

9. Berns, M. W., Wright, W. H., Tromberg, B. J., *et al.* Use of a laser-induced optical force trap to study chromosome movement on the mitotic spindle. *Proceedings of the National Academy of Sciences* **86,** 4539–4543. eprint: https://www.pnas.org/content/86/12/4539 (1989) (cit. on p. 1).

10. Block, S. M., Blair, D. F. & Berg, H. C. Compliance of bacterial flagella measured with optical tweezers. *Nature* **338,** 514. eprint: https://www.nature.com/articles/338514a0 (1989) (cit. on p. 1).

11. Ashkin, A & Dziedzic, J. M. Internal cell manipulation using infrared laser traps. *Proceedings of the National Academy of Sciences* **86,** 7914–7918. eprint: https://www.pnas.org/content/86/20/7914.full.pdf (1989) (cit. on p. 1).

12. Tadir, Y., Wright, W. H., Vafa, O., *et al.* Micromanipulation of sperm by a laser generated optical trap. *Fertility and sterility* **52(5),** 870–873. eprint: https://www.fertstert.org/article/S0015-0282(16)53057-X/fulltext (1989) (cit. on p. 1).

13. Bonder, E. Force production by swimming sperm analysis using optical tweezers. *Journal of Cell Biology* **111,** 421A. eprint: https://eurekamag.com/research/031/485/031485803.php (1990) (cit. on pp. 1, 6–8, 46, 82).

14. Ashkin, A, Schütze, K., Dziedzic, J., Euteneuer, U. & Schliwa, M. Force generation of organelle transport measured in vivo by an infrared laser trap. *Nature* **348,** 346. eprint: https://www.nature.com/articles/348346a0 (1990) (cit. on pp. 1, 6).

15. Block, S. M., Goldstein, L. S. & Schnapp, B. J. Bead movement by single kinesin molecules studied with optical tweezers. *Nature* **348,** 348. eprint: https://www.nature.com/articles/348348a0 (1990) (cit. on p. 1).

16. Cherney, D. P., Bridges, T. E. & Harris, J. M. Optical trapping of unilamellar phospholipid vesicles: investigation of the effect of optical forces on the lipid membrane shape by confocal-Raman microscopy. *Analytical chemistry* **76,** 4920–4928. eprint: https://pubs.acs.org/doi/10.1021/ac0492620 (2004) (cit. on p. 1).

17. Bendix, P. M. & Oddershede, L. B. Expanding the Optical Trapping Range of Lipid Vesicles to the Nanoscale. *Nano Letters* **11.** PMID: 22074221, 5431–5437. eprint: https://doi.org/10.1021/nl203200g (2011) (cit. on p. 1).

18. Collard, L., Perez-Guaita, D., Faraj, B. H., *et al.* Light Scattering By Optically Trapped Vesicles Affords Unprecedented Temporal Resolution Of Lipid Raft Dynamics. *Scientific reports* **7,** 8589. eprint: https://www.nature.com/articles/s41598-017-08980-1 (2017) (cit. on p. 1).

19. Heller, I., Hoekstra, T. P., King, G. A., Peterman, E. J. G. & Wuite, G. J. L. Optical Tweezers Analysis of DNA Protein Complexes. *Chemical Reviews* **114.** PMID: 24443844, 3087–3119. eprint: https://doi.org/10.1021/cr4003006 (2014) (cit. on p. 1).

20. Kudo, T. & Ishihara, H. Proposed Nonlinear Resonance Laser Technique for Manipulating Nanoparticles. *Phys. Rev. Lett.* **109,** 087402. eprint: https://link.aps.org/doi/10.1103/PhysRevLett.109.087402 (2012) (cit. on p. 2).

21. Ashkin, A. *Optical trapping and manipulation of neutral particles using lasers: a reprint volume with commentaries* (World Scientific, 2006) (cit. on pp. 2, 4, 5, 117, 123).

22. Hansen, P. M., Bhatia, V. K., Harrit, N. & Oddershede, L. Expanding the Optical Trapping Range of Gold Nanoparticles. *Nano Letters* **5.** PMID: 16218713, 1937–1942. eprint: https://doi.org/10.1021/nl051289r (2005) (cit. on pp. 2, 150).

23. Min, C., Shen, Z., Shen, J., *et al.* Focused plasmonic trapping of metallic particles. *Nature communications* **4,** 2891. eprint: https://www.nature.com/articles/ncomms3891 (2013) (cit. on p. 2).

24. Jauffred, L., Taheri, S. M.-R., Schmitt, R., Linke, H. & Oddershede, L. B. Optical Trapping of Gold Nanoparticles in Air. *Nano Letters* **15.** PMID: 26083715, 4713–4719. eprint: https://doi.org/10.1021/acs.nanolett.5b01562 (2015) (cit. on p. 2).

25. Lehmuskero, A., Johansson, P., Rubinsztein-Dunlop, H., Tong, L. & Käll, M. Laser Trapping of Colloidal Metal Nanoparticles. *ACS Nano* **9.** PMID: 25808609, 3453–3469. eprint: https://doi.org/10.1021/acsnano.5b00286 (2015) (cit. on p. 2).

26. Wang, X., Dai, Y., Zhang, Y., Min, C. & Yuan, X. Plasmonic Manipulation of Targeted Metallic Particles by Polarization-Sensitive Metalens. *ACS Photonics* **5,** 2945–2950. eprint: https://doi.org/10.1021/acsphotonics.8b00282 (2018) (cit. on p. 2).

27. *A brief History of Halley's Comet* eprint: http://www.ianridpath.com/halley/halley2.htm (cit. on p. 2).

28. *A Study of Two Comet Tails* eprint: http://adsabs.harvard.edu/full/1958ApJ...128...950 (cit. on p. 2).

29. Heidarzadeh, T. *A history of physical theories of comets, from Aristotle to Whipple* eprint: http://booksdescr.org/item/index.php?md5=22F38D9D2DA443ABBB50F7A460467BE1 (Springer Science and Business Media, 2008) (cit. on p. 2).

30. *A History of Johannes Kepler* eprint: https://en.wikipedia.org/wiki/JohannesKepler (cit. on p. 2).

31. Gabbey, A. Isaac Newton: The Principia: Mathematical Principles of Natural Philosophy, trans. by I. Bernard Cohen and Anne Whitman, assisted by Julia Budenz, *Isis* **94,** 719–721. eprint: https://doi.org/10.1086/386435 (2003) (cit. on p. 2).

32. Bartoli, A. Il calorico raggiante e il secondo principio di termodinamica. *Il Nuovo Cimento* **15,** 193–202 (1884) (cit. on p. 3).

33. Maxwell, J. *A Treatise on Electricity and Magnetism A Treatise on Electricity and Magnetism* **v. 2.** eprint: https://books.google.co.in/books?id=zJJEAQAAIAAJ (Oxford University Press, 1955) (cit. on p. 3).

34. Padgett, M. J., Molloy, J. & McGloin, D. *Optical Tweezers: methods and applications* eprint: https://www.crcpress.com/Optical-Tweezers-Methods-and-Applications/Padgett-Molloy-McGloin/p/book/9781420074123 (Chapman and Hall/CRC, 2010) (cit. on p. 3).

35. Lebedew, P. Untersuchungen über die Druckkräfte des Lichtes. *Annalen der Physik* **311,** 433–458. eprint: https://onlinelibrary.wiley.com/doi/abs/10.1002/andp.19013111102 (1901) (cit. on p. 3).

36. Nichols, E. F. & Hull, G. F. A Preliminary Communication on the Pressure of Heat and Light Radiation. *Phys. Rev. (Series I)* **13,** 307–320. eprint: https://link.aps.org/doi/10.1103/PhysRevSeriesI.13.307 (1901) (cit. on p. 3).

37. Nichols, E. F. & Hull, G. F. The Pressure Due to Radiation. (Second Paper.) *Phys. Rev. (Series I)* **17,** 26–50 (1903) (cit. on p. 3).

38. Nichols, E. F. & Hull, G. F. The Pressure Due to Radiation. (Second Paper.) *Phys. Rev. (Series I)* **17,** 91–104. eprint: https://link.aps.org/doi/10.1103/PhysRevSeriesI.17.91 (1903) (cit. on p. 3).

39. Ashkin, A., Dziedzic, J. M., Bjorkholm, J. E. & Chu, S. Observation of a single-beam gradient force optical trap for dielectric particles. *Opt. Lett.* **11,** 288–290. eprint: http://ol.osa.org/abstract.cfm?URI=ol-11-5-288 (1986) (cit. on pp. 4–6, 25, 26, 29, 152).

40. Gordon, J. P., Zeiger, H. J. & Townes, C. H. The Maser—New Type of Microwave Amplifier, Frequency Standard, and Spectrometer. *Phys. Rev.* **99,** 1264–1274. eprint: https://link.aps.org/doi/10.1103/PhysRev.99.1264 (1955) (cit. on p. 4).

41. Eddington, A. S. *The Internal Constitution of the Stars* eprint: http://library1.org/_ads/92b7ba3ac796c57b6ce1e0f078068ccc (Cambridge University Press, 1988) (cit. on p. 4).

42. *Invention of the LASER* eprint: https://www.aps.org/publications/apsnews/200312/history.cfm (cit. on p. 4).

43. R., W. How it all began. *Nature Photonics* **5,** 316. eprint: https://www.nature.com/articles/nphoton.2011.101 (2011) (cit. on p. 5).

44. Ashkin, A. Trapping of Atoms by Resonance Radiation Pressure. *Phys. Rev. Lett.* **40,** 729–732. eprint: https://link.aps.org/doi/10.1103/PhysRevLett.40.729 (1978) (cit. on p. 5).

45. Bjorkholm, J. E., Freeman, R. R., Ashkin, A. & Pearson, D. B. Observation of Focusing of Neutral Atoms by the Dipole Forces of Resonance-Radiation Pressure. *Phys. Rev. Lett.* **41,** 1361–1364. eprint: https://link.aps.org/doi/10.1103/PhysRevLett.41.1361 (1978) (cit. on p. 5).

46. Ashkin, A. & Gordon, J. P. Cooling and trapping of atoms by resonance radiation pressure. *Opt. Lett.* **4,** 161–163. eprint: http://ol.osa.org/abstract.cfm?URI=ol-4-6-161 (1979) (cit. on p. 5).

47. Gordon, J. P. & Ashkin, A. Motion of atoms in a radiation trap. *Phys. Rev. A* **21,** 1606–1617. eprint: https://link.aps.org/doi/10.1103/PhysRevA.21.1606 (1980) (cit. on p. 5).

48. Ashkin, A. & Gordon, J. P. Stability of radiation-pressure particle traps: an optical Earnshaw theorem. *Opt. Lett.* **8,** 511–513. eprint: http://ol.osa.org/abstract.cfm?URI=ol-8-10-511 (1983) (cit. on p. 5).

49. *Background information for the 1997 Nobel prize in physics for laser cooling* eprint: http://www.nobel.se/announcement-97/phyback97.html (cit. on p. 5).

50. Durfee, D. S. & Ketterle, W. Experimental studies of Bose-Einstein condensation. *Opt. Express* **2,** 299–313. eprint: http://www.opticsexpress.org/abstract.cfm?URI=oe-2-8-299 (1998) (cit. on p. 5).

51. Anderson, M. H., Ensher, J. R., Matthews, M. R., Wieman, C. E. & Cornell, E. A. Observation of Bose-Einstein Condensation in a Dilute Atomic Vapor. *Science* **269,** 198–201. eprint: https://science.sciencemag.org/content/269/5221/198.full.pdf (1995) (cit. on p. 5).

52. Davis, K. B., Mewes, M. O., Andrews, M. R., *et al.* Bose-Einstein Condensation in a Gas of Sodium Atoms. *Phys. Rev. Lett.* **75,** 3969–3973. eprint: https://link.aps.org/doi/10.1103/PhysRevLett.75.3969 (1995) (cit. on p. 5).

53. Bradley, C. C., Sackett, C. A. & Hulet, R. G. Bose-Einstein Condensation of Lithium: Observation of Limited Condensate Number. *Phys. Rev. Lett.* **78,** 985–989. eprint: https://link.aps.org/doi/10.1103/PhysRevLett.78.985 (1997) (cit. on p. 5).

54. Svoboda, K., Schmidt, C. F., Schnapp, B. J. & Block, S. M. Direct observation of kinesin stepping by optical trapping interferometry. *Nature* **365,** 721. eprint: https://www.nature.com/articles/365721a0 (1993) (cit. on p. 6).

55. Neuman, K. C. & Nagy, A. Single-molecule force spectroscopy: optical tweezers, magnetic tweezers and atomic force microscopy. *Nature methods* **5,** 491. eprint: https://www.nature.com/articles/nmeth.1218 (2008) (cit. on pp. 6, 7, 9).

56. Padgett, M. & Allen, L. Optical tweezers and spanners. *Physics World* **10,** 35. eprint: https://iopscience.iop.org/article/10.1088/2058-7058/10/9/22/meta (1997) (cit. on p. 6).

57. Simpson, N. B., Dholakia, K., Allen, L. & Padgett, M. J. Mechanical equivalence of spin and orbital angular momentum of light: an optical spanner. *Opt. Lett.* **22,** 52–54. eprint: http://ol.osa.org/abstract.cfm?URI=ol-22-1-52 (1997) (cit. on p. 6).

58. Xie, C., Dinno, M. A. & qing Li, Y. Near-infrared Raman spectroscopy of single optically trapped biological cells. *Opt. Lett.* **27,** 249–251. eprint: http://ol.osa.org/abstract.cfm?URI=ol-27-4-249 (2002) (cit. on p. 6).

59. Petrov, D. V. Raman spectroscopy of optically trapped particles. *Journal of Optics A: Pure and Applied Optics* **9,** S139–S156. eprint: https://iopscience.iop.org/article/10.1088/1464-4258/9/8/S06/meta (2007) (cit. on p. 6).

60. Redding, B., Schwab, M. J. & Pan, Y.-l. Raman Spectroscopy of Optically Trapped Single Biological Micro-Particles. *Sensors* **15,** 19021–19046. eprint: http://www.mdpi.com/1424-8220/15/8/19021 (2015) (cit. on p. 6).

61. Thurn, R. & Kiefer, W. Raman-Microsampling Technique Applying Optical Levitation by Radiation Pressure. *Appl. Spectrosc.* **38,** 78–83. eprint: http://as.osa.org/abstract.cfm?URI=as-38-1-78 (1984) (cit. on p. 6).

62. Xie, C., Li, Y.-q., Tang, W. & Newton, R. J. Study of dynamical process of heat denaturation in optically trapped single microorganisms by near-infrared Raman spectroscopy. *Journal of Applied Physics* **94,** 6138–6142. eprint: https://aip.scitation.org/doi/10.1063/1.1617359 (2003) (cit. on p. 6).

63. Ajito, K. & Torimitsu, K. Laser trapping and Raman spectroscopy of single cellular organelles in the nanometer range. *Lab Chip,* 11–14. eprint: http://dx.doi.org/10.1039/B108744B (2002) (cit. on p. 6).

64. Zhang, H. & Liu, K.-K. Optical tweezers for single cells. *Journal of the Royal Society interface* **5,** 671–690. eprint: https://doi.org/10.1098/rsif.2008.0052 (2008) (cit. on p. 6).

65. Alexander, T. A., Pellegrino, P. M. & Gillespie, J. B. *Near-infrared surface-enhanced-Raman-scattering (SERS) mediated detection of single optically trapped bacterial spores* in *Chemical and Biological Sensing IV* **5085** (2003), 91–101. eprint: https://journals.sagepub.com/doi/10.1366/000370203322554482 (cit. on p. 6).

66. Curtis, J. E., Koss, B. A. & Grier, D. G. Dynamic holographic optical tweezers. *Optics Communications* **207,** 169 –175. eprint: http://www.sciencedirect.com/science/article/pii/S0030401802015249 (2002) (cit. on p. 6).

67. Xing, Q., Mao, F., Chai, L. & Wang, Q. Numerical modeling and theoretical analysis of femtosecond laser tweezers. *Optics and Laser Technology* **36,** 635 –639. eprint: http://www.sciencedirect.com/science/article/pii/S0030399204000210 (2004) (cit. on p. 7).

68. Agate, B., Brown, C. T. A., Sibbett, W. & Dholakia, K. Femtosecond optical tweezers for in-situ control of two-photon fluorescence. *Opt. Express* **12,** 3011–3017. eprint: http://www.opticsexpress.org/abstract.cfm?URI=oe-12-13-3011 (2004) (cit. on pp. 7, 8, 77, 82, 203).

69. Righini, M., Zelenina, A. S., Girard, C. & Quidant, R. Parallel and selective trapping in a patterned plasmonic landscape. *Nature Physics* **3,** 477. eprint: https://www.nature.com/articles/nphys624 (2007) (cit. on p. 7).

70. Bosanac, L., Aabo, T., Bendix, P. M. & Oddershede, L. B. Efficient Optical Trapping and Visualization of Silver Nanoparticles. *Nano Letters* **8.** PMID: 18386911, 1486–1491. eprint: https://doi.org/10.1021/nl080490+ (2008) (cit. on p. 7).

71. Selhuber-Unkel, C., Zins, I., Schubert, O., Sönnichsen, C. & Oddershede, L. B. Quantitative Optical Trapping of Single Gold Nanorods. *Nano Letters* **8.** PMID: 18720978, 2998–3003. eprint: https://doi.org/10.1021/nl802053h (2008) (cit. on pp. 7, 150).

72. Braun, D. & Libchaber, A. Trapping of DNA by Thermophoretic Depletion and Convection. *Phys. Rev. Lett.* **89,** 188103. eprint: https://link.aps.org/doi/10.1103/PhysRevLett.89.188103 (2002) (cit. on p. 7).

73. Pang, Y. & Gordon, R. Optical Trapping of a Single Protein. *Nano Letters* **12.** PMID: 22171921, 402–406. eprint: https://doi.org/10.1021/nl203719v (2012) (cit. on p. 7).

74. Roy, D., Goswami, D. & De, A. K. Exploring the physics of efficient optical trapping of dielectric nanoparticles with ultrafast pulsed excitation. *Appl. Opt.* **54,** 7002–7006. eprint: http://ao.osa.org/abstract.cfm?URI=ao-54-23-7002 (2015) (cit. on pp. 7–9, 77, 82, 203).

75. Dasgupta, R., Verma, R. S., Ahlawat, S., Uppal, A. & Gupta, P. K. Studies on erythrocytes in malaria infected blood sample with Raman optical tweezers. *Journal of biomedical optics* **16,** 077009. eprint: https://www.spiedigitallibrary.org/journals/journal-of-biomedical-optics/volume-16/issue-7/077009/Studies-on-erythrocytes-in-malaria-infected-blood-sample-with-Raman/10.1117/1.3600011.full?SSO=1 (2011) (cit. on p. 7).

76. Paul, A., Padmapriya, P. & Natarajan, V. Diagnosis of malarial infection using change in properties of optically trapped red blood cells. *Biomedical Journal* **40,** 101 –105. eprint: http://www.sciencedirect.com/science/article/pii/S2319417016300804 (2017) (cit. on p. 7).

77. Shane, J. C., Mazilu, M., Lee, W. M. & Dholakia, K. Effect of pulse temporal shape on optical trapping and impulse transfer using ultrashort pulsed lasers. *Opt. Express* **18,** 7554–7568. eprint: http://www.opticsexpress.org/abstract.cfm?URI=oe-18-7-7554 (2010) (cit. on pp. 7, 8, 37, 43, 44, 77, 82, 101, 107, 203).

78. Wang, L.-G. & Zhao, C.-L. Dynamic radiation force of a pulsed Gaussian beam acting on a Rayleigh dielectric sphere. *Opt. Express* **15,** 10615–10621. eprint: http://www.opticsexpress.org/abstract.cfm?URI=oe-15-17-10615 (2007) (cit. on pp. 7, 8).

79. Wang, L.-G. & Chai, H.-S. Revisit on dynamic radiation forces induced by pulsed Gaussian beams. *Opt. Express* **19,** 14389–14402. eprint: http://www.opticsexpress.org/abstract.cfm?URI=oe-19-15-14389 (2011) (cit. on pp. 7, 8).

80. Devi, A. & De, A. K. Theoretical investigation on nonlinear optical effects in laser trapping of dielectric nanoparticles with ultrafast pulsed excitation. *Opt. Express* **24,** 21485–21496. eprint: http://www.opticsexpress.org/abstract.cfm?URI=oe-24-19-21485 (2016) (cit. on pp. 7, 8, 37, 44, 82, 107).

81. Liu, T.-H., Chiang, W.-Y., Usman, A. & Masuhara, H. Optical Trapping Dynamics of a Single Polystyrene Sphere: Continuous Wave versus Femtosecond Lasers. *The Journal of Physical Chemistry C* **120,** 2392–2399. eprint: https://doi.org/10.1021/acs.jpcc.5b09146 (2016) (cit. on pp. 7, 37, 44, 77, 82, 107, 109, 203).

82. De, A. K., Roy, D., Dutta, A. & Goswami, D. Stable optical trapping of latex nanoparticles with ultrashort pulsed illumination. *Appl. Opt.* **48,** G33–G37. eprint: http://ao.osa.org/abstract.cfm?URI=ao-48-31-G33 (2009) (cit. on pp. 7, 37, 82, 109, 203).

83. De, A. K. & Goswami, D. Towards controlling molecular motions in fluorescence microscopy and optical trapping: a spatiotemporal approach. *International Reviews in Physical Chemistry* **30,** 275–299. eprint: https://doi.org/10.1080/0144235X.2011.603237 (2011) (cit. on pp. 7, 8, 37, 82).

84. Tan, S., Lopez, H. A., Cai, C. W. & Zhang, Y. Optical Trapping of Single-Walled Carbon Nanotubes. *Nano Letters* **4,** 1415–1419. eprint: https://doi.org/10.1021/nl049347g (2004) (cit. on p. 8).

85. Gao, D., Ding, W., Nieto-Vesperinas, M., *et al.* Optical manipulation from the microscale to the nanoscale: fundamentals, advances and prospects. *Light: Science & Applications* **6,** e17039. eprint: https://www.nature.com/articles/lsa201739 (2017) (cit. on pp. 9, 117).

86. Cluzel, P., Lebrun, A., Heller, C., *et al.* DNA: An Extensible Molecule. *Science* **271,** 792–794. eprint: https://science.sciencemag.org/content/271/5250/792.full.pdf (1996) (cit. on p. 9).

87. Evans, E., Ritchie, K. & Merkel, R. Sensitive force technique to probe molecular adhesion and structural linkages at biological interfaces. *Biophysical Journal* **68,** 2580 –2587. eprint: http://www.sciencedirect.com/science/article/pii/S0006349595804418 (1995) (cit. on p. 9).

88. Smith, S., Finzi, L & Bustamante, C. Direct mechanical measurements of the elasticity of single DNA molecules by using magnetic beads. *Science* **258,** 1122–1126. eprint: https://science.sciencemag.org/content/258/5085/1122.full.pdf (1992) (cit. on p. 9).

89. Kim, S., Blainey, P. C., Schroeder, C. M. & Xie, X. S. Multiplexed single-molecule assay for enzymatic activity on flow-stretched DNA. *Nature methods* **4,** 397. eprint: https://www.nature.com/articles/nmeth1037 (2007) (cit. on p. 9).

90. Noy, A. *Handbook of Molecular Force Spectroscopy* eprint: https://books.google.co.in/books?id=L7zvAAAAMAAJ (Springer, 2008) (cit. on p. 9).

91. Jannasch, A., Demirörs, A. F., Van Oostrum, P. D., Van Blaaderen, A. & Schäffer, E. Nanonewton optical force trap employing anti-reflection coated, high-refractive-index titania microspheres. *Nature Photonics* **6,** 469. eprint: https://www.nature.com/articles/nphoton.2012.140.pdf (2012) (cit. on p. 9).

92. Peterman, E. J., Gittes, F. & Schmidt, C. F. Laser-induced heating in optical traps. *Biophysical journal* **84,** 1308–1316. eprint: https://www.ncbi.nlm.nih.gov/pmc/articles/PMC1302707/ (2003) (cit. on pp. 9, 285).

93. Abbondanzieri, E. A., Shaevitz, J. W. & Block, S. M. Picocalorimetry of Transcription by RNA Polymerase. *iophysical Journal* **89,** L61 –L63. eprint: http://www.sciencedirect.com/science/article/pii/S0006349505730095 (2005) (cit. on p. 9).

94. Harada, Y. & Asakura, T. Radiation forces on a dielectric sphere in the Rayleigh scattering regime. *Optics Communications* **124,** 529 –541. eprint: http://www.sciencedirect.com/science/article/pii/0030401895007539 (1996) (cit. on pp. 19, 25, 29, 37, 152).

95. Ashkin, A. Forces of a single-beam gradient laser trap on a dielectric sphere in the ray optics regime. *Biophysical Journal* **61,** 569 –582. eprint: http://www.sciencedirect.com/science/article/pii/S000634959281860X (992) (cit. on pp. 19, 26, 101, 117).

96. Callegari, A., Mijalkov, M., Gököz, A. B. & Volpe, G. Computational toolbox for optical tweezers in geometrical optics. *J. Opt. Soc. Am. B* **32,** B11–B19. eprint: http://josab.osa.org/abstract.cfm?URI=josab-32-5-B11 (2015) (cit. on pp. 19, 26, 101, 117).

97. Svoboda, K. & Block, S. M. Optical trapping of metallic Rayleigh particles. *Opt. Lett.* **19,** 930–932. eprint: http://ol.osa.org/abstract.cfm?URI=ol-19-13-930 (1994) (cit. on pp. 21, 149).

98. *Electric Dipole* eprint: http://bolvan.ph.utexas.edu/\~vadim/classes/17f/dipole.pdf (cit. on p. 22).

99. Hulst, H. C. & van de Hulst, H. C. Light scattering by small particles. *Quarterly Journal of the Royal Meteorological Society* **84,** 198–199. eprint: https://rmets.onlinelibrary.wiley.com/doi/pdf/10.1002/qj.49708436025 (1958) (cit. on pp. 24, 29, 78, 82, 89).

100. Born, M. & Wolf, E. *Principles of optics: electromagnetic theory of propagation, interference and diffraction of light* eprint: https://archive.org/details/PrinciplesOfOptics (Elsevier, 2013) (cit. on p. 27).

101. Hecht, E. *Optics 4th edition* eprint: http://adsabs.harvard.edu/abs/2001opt4.book.....H (2001) (cit. on p. 27).

102. Gr´ehan, G. *Nouveaux progr'esenth´eorie de Lorenz-Mie. Application 'a lamesure de diam'etre de particules dans des ´ecoulements* 1980. eprint: https://hal-centralesupelec.archives-ouvertes.fr/cel-01289012/document (cit. on p. 28).

103. Gouesbet, G. Partial-wave expansions and properties of axisymmetric light beams. *Appl. Opt.* **35,** 1543–1555. eprint: http://ao.osa.org/abstract.cfm?URI=ao-35-9-1543 (1996) (cit. on p. 28).

104. Wallace, T. P. The scattering of light and other electromagnetic radiation. *Journal of Polymer Science Part A-2: Polymer Physics* **8,** 813–813. eprint: https://onlinelibrary.wiley.com/doi/pdf/10.1002/pol.1970.160080514 (1970) (cit. on p. 28).

105. Davis, L. W. Theory of electromagnetic beams. *Phys. Rev. A* **19,** 1177–1179. eprint: https://link.aps.org/doi/10.1103/PhysRevA.19.1177 (1979) (cit. on p. 28).

106. Gouesbet, G, Maheu, B & Grehan, G. The order of approximation in a theory of the scattering of a Gaussian beam by a Mie scatter center. *Journal of Optics* **16,** 239–247. eprint: https://iopscience.iop.org/article/10.1088/0150-536X/16/2/004 (1985) (cit. on p. 28).

107. Gouesbet, G. & Gréhan, G. *Generalized lorenz-mie theories* eprint: https://doi.org/10.1016/j.jqsrt.2008.11.013 (Springer, 2011) (cit. on pp. 28, 29, 31, 89, 273, 274).

108. Grehan, G., Maheu, B. & Gouesbet, G. Scattering of laser beams by Mie scatter centers: numerical results using a localized approximation. *Appl. Opt.* **25,** 3539–3548. eprint: http://ao.osa.org/abstract.cfm?URI=ao-25-19-3539 (1986) (cit. on p. 29).

109. Gouesbet, G., Grehan, G. & Maheu, B. Computations of the gn coefficients in the generalized Lorenz-Mie theory using three different methods. *Appl. Opt.* **27,** 4874–4883. eprint: http://ao.osa.org/abstract.cfm?URI=ao-27-23-4874 (1988) (cit. on pp. 29, 82, 273).

110. Gouesbet, G., Maheu, B. & Gréhan, G. Light scattering from a sphere arbitrarily located in a Gaussian beam, using a Bromwich formulation. *J. Opt. Soc. Am. A* **5,** 1427–1443. eprint: http://josaa.osa.org/abstract.cfm?URI=josaa-5-9-1427 (1988) (cit. on pp. 29, 30).

111. Neto, P. A. M. & Nussenzveig, H. M. Theory of optical tweezers. *Europhysics Letters (EPL)* **50,** 702–708. eprint: https://iopscience.iop.org/article/10.1209/epl/i2000-00327-4 (2000) (cit. on pp. 30, 117).

112. Edmonds, A. *Angular Momentum in Quantum Mechanics* eprint: https://books.google.co.in/books?id=YEWPDAAAQBAJ (Princeton University Press, 2016) (cit. on p. 31).

113. LL.D., J. K. XL. A new relation between electricity and light: Dielectrified media birefringent. *The London, Edinburgh, and Dublin Philosophical Magazine and Journal of Science* **50,** 337–348. eprint: https://doi.org/10.1080/14786447508641302 (1875) (cit. on p. 33).

114. LL.D., J. K. LIV. A new relation between electricity and light: Dielectrified media birefringent (Second paper). *The London, Edinburgh, and Dublin Philosophical Magazine and Journal of Science* **50,** 446–458. eprint: https://doi.org/10.1080/14786447508641319 (1875) (cit. on p. 33).

115. Franken, P. A., Hill, A. E., Peters, C. W. & Weinreich, G. Generation of Optical Harmonics. *Phys. Rev. Lett.* **7,** 118–119. eprint: https://link.aps.org/doi/10.1103/PhysRevLett.7.118 (1961) (cit. on p. 33).

116. Boyd, R. Nonlinear Optics, Academic. *San Diego, Calif* **19922,** 39. eprint: https://www.scirp.org/(S(vtj3fa45qm1ean45vvffcz55))/reference/ReferencesPapers.aspx?ReferenceID=651512 (1992) (cit. on p. 34).

117. *Refractive index data base* eprint: https://refractiveindex.info/ (cit. on p. 35).

118. Jahja, M. *On nonlinear optical constants of polystyrene* in *International Symposium on Modern Optics and Its Applications* (2011) (cit. on p. 35).

119. Weber, M. J. *Handbook of optical materials* eprint: http://optics.sgu.ru/~ulianov/Students/Books/Applied_Optics/Marvin (CRC press, 2018) (cit. on p. 35).

120. Milam, D. Review and assessment of measured values of the nonlinear refractive-index coefficient of fused silica. *Applied optics* **37,** 546–550. eprint: https://www.osapublishing.org/ao/abstract.cfm?uri=ao-37-3-546 (1998) (cit. on p. 35).

121. Krauss, T. D. & Wise, F. W. Femtosecond measurement of nonlinear absorption and refraction in CdS, ZnSe, and ZnS. *Applied physics letters* **65,** 1739–1741. eprint: https://aip.scitation.org/doi/10.1063/1.112901 (1994) (cit. on p. 35).

122. Geints, Y. E., Kabanov, A., Zemlyanov, A., *et al.* Kerr-driven nonlinear refractive index of air at 800 and 400 nm measured through femtosecond laser pulse filamentation. *Applied Physics Letters* **99,** 181114. eprint: https://aip.scitation.org/doi/full/10.1063/1.3657774 (2011) (cit. on p. 35).

123. Dienerowitz, M. *Plasmonic effects upon Optical Trapping of metal nanoparticles* PhD thesis (University of St Andrews, 2010). eprint: https://research-repository.st-andrews.ac.uk/handle/10023/1634 (cit. on pp. 35, 151, 166).

124. Rativa, D., De Araujo, R. & Gomes, A. One photon nonresonant high-order nonlinear optical properties of silver nanoparticles in aqueous solution. *Optics express* **16,** 19244–19252. eprint: https://www.osapublishing.org/oe/abstract.cfm?uri=oe-16-23-19244 (2008) (cit. on p. 35).

125. Lenzner, M., Krüger, J., Sartania, S, *et al.* Femtosecond optical breakdown in dielectrics. *Physical review letters* **80,** 4076. eprint: https://journals.aps.org/prl/abstract/10.1103/PhysRevLett.80.4076 (1998) (cit. on p. 38).

126. Hu, Y., Nieminen, T. A., Heckenberg, N. R. & Rubinsztein-Dunlop, H. Antireflection coating for improved optical trapping. *Journal of Applied Physics* **103,** 093119. eprint: https://doi.org/10.1063/1.2919574 (2008) (cit. on p. 58).

127. Wang, N., Li, X., Chen, J., Lin, Z. & Ng, J. Gradient and scattering forces of anti-reflection-coated spheres in an aplanatic beam. *Scientific reports* **8,** 17423. eprint: https://www.nature.com/articles/s41598-018-35575-1 (2018) (cit. on p. 58).

128. Rahaman, M. H., Nazim, M. S. & Kemp, B. A. *Radiation pressure on core-shell nanoparticles in Rayleigh regime* in (2017). eprint: https://ieeexplore.ieee.org/document/7925345 (cit. on p. 65).

129. Donato, M. G., Messina, E., Foti, A., *et al.* Optical trapping and optical force positioning of two-dimensional materials. *Nanoscale* **10,** 1245–1255. eprint: http://dx.doi.org/10.1039/C7NR06465A (2018) (cit. on p. 75).

130. Limonov, M. F., Rybin, M. V., Poddubny, A. N. & Kivshar, Y. S. Fano resonances in photonics. *Nature Photonics* **11,** 543–554. eprint: https://doi.org/10.1038/nphoton.2017.142 (2017) (cit. on pp. 75, 95, 283).

131. Chen, H., Liu, S., Zi, J. & Lin, Z. Fano Resonance-Induced Negative Optical Scattering Force on Plasmonic Nanoparticles. *ACS Nano* **9.** PMID: 25635617, 1926–1935. eprint: https://doi.org/10.1021/nn506835j (2015) (cit. on p. 75).

132. Cordova, J. C., Reinemann, D. N., Laky, D. J., *et al.* Bioconjugated Core–Shell Microparticles for High-Force Optical Trapping. *Particle & Particle Systems Characterization* **35,** 1700448. eprint: https://onlinelibrary.wiley.com/doi/pdf/10.1002/ppsc.201700448 (2018) (cit. on p. 77).

133. Jiang, Y., Narushima, T. & Okamoto, H. Nonlinear optical effects in trapping nanoparticles with femtosecond pulses. *Nature Physics* **6,** 1005. eprint: https://www.nature.com/articles/nphys1776 (2010) (cit. on p. 78).

134. Bohren, C. F. & Huffman, D. R. *Absorption and scattering of light by small particles* eprint: https://onlinelibrary.wiley.com/doi/book/10.1002/9783527618156 (John Wiley & Sons, 2008) (cit. on pp. 89, 212).

135. Chen, H., Liu, S., Zi, J. & Lin, Z. Fano Resonance-Induced Negative Optical Scattering Force on Plasmonic Nanoparticles. *ACS Nano* **9.** PMID: 25635617, 1926–1935. eprint: https://doi.org/10.1021/nn506835j (2015) (cit. on pp. 95, 283, 284).

136. Pobre, R. & Saloma, C. Single Gaussian beam interaction with a Kerr microsphere: characteristics of the radiation force. *Appl. Opt.* **36,** 3515–3520. eprint: http://ao.osa.org/abstract.cfm?URI=ao-36-15-3515 (1997) (cit. on p. 101).

137. Tanaka, K. in *Springer Handbook of Electronic and Photonic Materials* (eds Kasap, S. & Capper, P.) 1–1 (Springer International Publishing, Cham, 2017). eprint: https://doi.org/10.1007/978-3-319-48933-9_42 (cit. on pp. 101, 109).

138. Qiu, C.-W., Ding, W., Mahdy, M., *et al.* Photon momentum transfer in inhomogeneous dielectric mixtures and induced tractor beams. *Light: Science & Applications* **4,** e278. eprint: https://www.nature.com/articles/lsa201551 (2015) (cit. on p. 117).

139. Akbarzadeh, A., Crosse, J. A., Danesh, M., *et al.* Interplay of Optical Force and Ray-Optic Behavior between Luneburg Lenses. *ACS Photonics* **2,** 1384–1390. eprint: https://doi.org/10.1021/acsphotonics.5b00352 (2015) (cit. on p. 117).

140. Akbarzadeh, A., Danesh, M., Qiu, C.-W. & Danner, A. J. Tracing optical force fields within graded-index media. *New Journal of Physics* **16,** 053035. eprint: https://iopscience.iop.org/article/10.1088/1367-2630/16/5/053035/meta (2014) (cit. on p. 117).

141. Maia Neto, P. A. & Nussenzveig, H. M. Theory of optical tweezers. *Europhys. Lett.* **50,** 702–708. eprint: https://doi.org/10.1209/epl/i2000-00327-4 (2000) (cit. on pp. 124, 203).

142. Friese, M. E. J., Rubinsztein-Dunlop, H., Heckenberg, N. R. & Dearden, E. W. Determination of the force constant of a single-beam gradient trap by measurement of backscattered light. *Appl. Opt.* **35,** 7112–7116. eprint: http://ao.osa.org/abstract.cfm?URI=ao-35-36-7112 (1996) (cit. on p. 124).

143. Molloy, J. E. & Padgett, M. J. Lights, action: Optical tweezers. *Contemporary Physics* **43,** 241–258. eprint: https://doi.org/10.1080/00107510110116051 (2002) (cit. on p. 149).

144. Ashkin, A. Applications of Laser Radiation Pressure. *Science* **210,** 1081–1088. eprint: https://science.sciencemag.org/content/210/4474/1081.full.pdf (1980) (cit. on p. 149).

145. Sasaki, K., Koshioka, M., Misawa, H., Kitamura, N. & Masuhara, H. Optical trapping of a metal particle and a water droplet by a scanning laser beam. *Applied Physics Letters* **60,** 807–809 (1992) (cit. on p. 149).

146. Maier, S. A. & Atwater, H. A. Plasmonics: Localization and guiding of electromagnetic energy in metal/dielectric structures. *Journal of Applied Physics* **98,** 011101. eprint: https://doi.org/10.1063/1.1951057 (2005) (cit. on p. 149).

147. Barnes, W. L., Dereux, A. & Ebbesen, T. W. Surface plasmon subwavelength optics. *nature* **424,** 824. eprint: https://www.nature.com/articles/nature01937 (2003) (cit. on p. 149).

148. Sasaki, K., Koshioka, M., Misawa, H., Kitamura, N. & Masuhara, H. Optical trapping of a metal particle and a water droplet by a scanning laser beam. *Applied Physics Letters* **60,** 807–809. eprint: https://doi.org/10.1063/1.107427 (1992) (cit. on p. 149).

149. Hajizadeh, F. & S.Reihani, S. Optimized optical trapping of gold nanoparticles. *Opt. Express* **18,** 551–559. eprint: http://www.opticsexpress.org/abstract.cfm?URI=oe-18-2-551 (2010) (cit. on p. 150).

150. Brzobohatý, O., Šiler, M., Trojek, J., *et al.* Non-spherical gold nanoparticles trapped in optical tweezers: shape matters. *Opt. Express* **23,** 8179–8189. eprint: http://www.opticsexpress.org/abstract.cfm?URI=oe-18-2-551 (2015) (cit. on p. 150).

151. Pelton, M., Liu, M., Kim, H. Y., *et al.* Optical trapping and alignment of single gold nanorods by using plasmon resonances. *Opt. Lett.* **31,** 2075–2077. eprint: http://ol.osa.org/abstract.cfm?URI=ol-31-13-2075 (2006) (cit. on p. 150).

152. Arias-González, J. R. & Nieto-Vesperinas, M. Optical forces on small particles: attractive and repulsive nature and plasmon-resonance conditions. *J. Opt. Soc. Am. A* **20,** 1201–1209. eprint: http://josaa.osa.org/abstract.cfm?URI=josaa-20-7-1201 (2003) (cit. on p. 150).

153. Toussaint, K. C., Liu, M., Pelton, M., *et al.* Plasmon resonance-based optical trapping of single and multiple Au nanoparticles. *Opt. Express* **15,** 12017–12029. eprint: http://www.opticsexpress.org/abstract.cfm?URI=oe-15-19-12017 (2007) (cit. on p. 150).

154. Messina, E., Cavallaro, E., Cacciola, A., *et al.* Plasmon-Enhanced Optical Trapping of Gold Nanoaggregates with Selected Optical Properties. *ACS Nano* **5.** PMID: 21207989, 905–913. eprint: https://doi.org/10.1021/nn102101a (2011) (cit. on p. 150).

155. Maier, S. A. *Plasmonics: fundamentals and applications* eprint: http://gen.lib.rus.ec/book/index.php?md5=52F8A73D3F2E6693959AAB7FE33B3620 (Springer Science & Business Media, 2007) (cit. on p. 150).

156. Johnson, P. B. & Christy, R. W. Optical Constants of the Noble Metals. *Phys. Rev. B* **6,** 4370–4379. eprint: https://link.aps.org/doi/10.1103/PhysRevB.6.4370 (1972) (cit. on p. 150).

157. Bendix, P. M., Reihani, S. N. S. & Oddershede, L. B. Direct Measurements of Heating by Electromagnetically Trapped Gold Nanoparticles on Supported Lipid Bilayers. *ACS Nano* **4.** PMID: 20369898, 2256–2262. eprint: https://doi.org/10.1021/nn901751w (2010) (cit. on p. 166).

158. Lehmuskero, A., Johansson, P., Rubinsztein-Dunlop, H., Tong, L. & Käll, M. Laser Trapping of Colloidal Metal Nanoparticles. *ACS Nano* **9.** PMID: 25808609, 3453–3469. eprint: https://doi.org/10.1021/acsnano.5b00286 (2015) (cit. on p. 166).

159. Huang, H, Sivayoganathan, M, Duley, W. & Zhou, Y. Efficient localized heating of silver nanoparticles by low-fluence femtosecond laser pulses. *Applied Surface Science* **331,** 392–398. eprint: https://www.sciencedirect.com/journal/applied-surface-science/vol/331/suppl/C (2015) (cit. on p. 166).

160. Rulliere, C. *et al. Femtosecond laser pulses* eprint: http://library1.org/_ads/2374EA8EDF76F4798000CA9127F337D1 (Springer, 2005) (cit. on pp. 185, 186, 200).

161. *Application Note : Prism Compression for Ultrashort Laser Pulses* eprint: https://www.newport.com/medias/sys_master/images/images/h25/h7f/8797242818590/Prism-Compressor-for-Ultrashort-Laser-Pulses-App-Note-29.pdf (cit. on p. 200).

162. Brakenhoff, G., Müller, M & Squier, J. Femtosecond pulse width control in microscopy by two-photon absorption autocorrelation. *Journal of Microscopy* **179,** 253–260. eprint: https://onlinelibrary.wiley.com/doi/abs/10.1111/j.1365-2818.1995.tb03638.x (1995) (cit. on p. 200).

163. *Physics tracker software* eprint: https://physlets.org/tracker/ (cit. on p. 202).

164. Vasilev, V. & Skidanov, R. Microexplosions polysterene microparticles on substrate covered by aluminum. eprint: http://ceur-ws.org/Vol-1900/paper10.pdf (cit. on p. 204).

165. Helmers, H. & Witte, W. Holographic study of laser-induced liquid surface deformations. *Optics Communications* **49,** 21 –23. eprint: http://www.sciencedirect.com/science/article/pii/0030401884900828 (1984) (cit. on p. 205).

166. Fan, X., Zheng, W. & Singh, D. J. Light scattering and surface plasmons on small spherical particles. *Light: Science & Applications* **3,** e179. eprint: https://www.nature.com/articles/lsa201460 (2014) (cit. on p. 212).

167. Richards, B. & Wolf, E. Electromagnetic diffraction in optical systems, II. Structure of the image field in an aplanatic system. *Proc. R. Soc. Lon. Ser. A* **253,** 358–379. eprint: https://royalsocietypublishing.org/doi/pdf/10.1098/rspa.1959.0200 (1979) (cit. on p. 212).

168. Liberal, I., Ederra, I., Gonzalo, R. & Ziolkowski, R. W. Superbackscattering from single dielectric particles. *Journal of Optics* **17,** 072001. eprint: https://iopscience.iop.org/article/10.1088/2040-8978/17/7/072001 (2015) (cit. on p. 212).

169. Novotny, L. & Hecht, B. *Principles of nano-optics* eprint: http://www.fulviofrisone.com/attachments/article/406/Principles\%20of\%20Nano-Optics.pdf (Cambridge university press, 2012) (cit. on p. 212).

170. Griffiths, D. J. *Introduction to electrodynamics* 2005. eprint: http://booksdescr.org/item/index.php?md5=635B96707ABD947654A466A3F6D9EDFD (cit. on pp. 267, 271).

171. Jackson, J. D. *Classical electrodynamics* 1999. eprint: http://library1.org/_ads/FC4200F46DA445E9D79EFFFDD82F1CE8 (cit. on p. 267).

172. Talebian, E & Talebian, M. A general review on the derivation of Clausius Mossotti relation. *Optik International Journal for Light and Electron Optics* **124,** 2324–2326. eprint: https://www.sciencedirect.com/science/article/pii/S0030402612005220 (2013) (cit. on p. 272).

173. Gong, L., Gu, B., Rui, G., *et al.* Optical forces of focused femtosecond laser pulses on nonlinear optical Rayleigh particles. *Photonics Research* **6,** 138–143. eprint: https://www.osapublishing.org/prj/abstract.cfm?uri=prj-6-2-138 (2018) (cit. on p. 275).

174. Albaladejo, S., Marqués, M. I., Laroche, M. & Sáenz, J. J. Scattering forces from the curl of the spin angular momentum of a light field. *Physical review letters* **102,** 113602. eprint: https://journals.aps.org/prl/pdf/10.1103/PhysRevLett.102.113602 (2009) (cit. on p. 277).

175. Wong, V. & Ratner, M. A. Explicit computation of gradient and nongradient contributions to optical forces in the discrete-dipole approximation. *JOSA B* **23,** 1801–1814. eprint: https://www.osapublishing.org/josab/abstract.cfm?uri=josab-23-9-1801 (2006) (cit. on p. 277).

176. Wong, V. & Ratner, M. A. Gradient and nongradient contributions to plasmon-enhanced optical forces on silver nanoparticles. *Physical Review B* **73,** 075416. eprint: http://citeseerx.ist.psu.edu/viewdoc/download?doi=10.1.1.459.9354&rep=rep1&type=pdf (2006) (cit. on pp. 277, 279).

177. Yang, Y., Li, J. & Li, Z.-Y. Fano resonance of the ultrasensitve optical force excited by Gaussian evanescent field. *Journal of Optics* **17,** 075004. eprint: https://iopscience.iop.org/article/10.1088/2040-8978/17/7/075004/meta (2015) (cit. on p. 283).

178. Liu, K., Xue, X., Sukhotskiy, V. & Furlani, E. P. Optical Fano Resonance in Self-Assembled Magnetic–Plasmonic Nanostructures. *The Journal of Physical Chemistry C* **120,** 27555–27561. eprint: https://doi.org/10.1021/acs.jpcc.6b09473 (2016) (cit. on p. 283).

179. Chen, H., Shao, L., Man, Y. C., *et al.* Fano Resonance in (Gold Core)(Dielectric Shell) Nanostructures without Symmetry Breaking. *Small* **8,** 1503–1509. eprint: https://onlinelibrary.wiley.com/doi/pdf/10.1002/smll.201200032 (2012) (cit. on p. 283).

180. eprint: https://shodhganga.inflibnet.ac.in/bitstream/10603/72334/3/chapter&\%204.pdf (cit. on p. 285).

List of Figures

List of Tables